

FINAL REPORT OF FUEL DYNAMICS TEST E7

by

R. C. Doerner, W. F. Murphy,
G. S. Stanford, and P. H. Froehle

BASE TECHNOLOGY



U of C - AUA - USERDA

ARGONNE NATIONAL LABORATORY, ARGONNE, ILLINOIS

Prepared for the U. S. ENERGY RESEARCH

AND DEVELOPMENT ADMINISTRATION

under Contract W-31-109-Eng-38

The facilities of Argonne National Laboratory are owned by the United States Government. Under the terms of a contract (W-31-109-Eng-38) between the U. S. Energy Research and Development Administration, Argonne Universities Association and The University of Chicago, the University employs the staff and operates the Laboratory in accordance with policies and programs formulated, approved and reviewed by the Association.

MEMBERS OF ARGONNE UNIVERSITIES ASSOCIATION

The University of Arizona	Kansas State University	The Ohio State University
Carnegie-Mellon University	The University of Kansas	Ohio University
Case Western Reserve University	Loyola University	The Pennsylvania State University
The University of Chicago	Marquette University	Purdue University
University of Cincinnati	Michigan State University	Saint Louis University
Illinois Institute of Technology	The University of Michigan	Southern Illinois University
University of Illinois	University of Minnesota	The University of Texas at Austin
Indiana University	University of Missouri	Washington University
Iowa State University	Northwestern University	Wayne State University
The University of Iowa	University of Notre Dame	The University of Wisconsin

NOTICE

This report was prepared as an account of work sponsored by the United States Government. Neither the United States nor the United States Energy Research and Development Administration, nor any of their employees, nor any of their contractors, subcontractors, or their employees, makes any warranty, express or implied, or assumes any legal liability or responsibility for the accuracy, completeness or usefulness of any information, apparatus, product or process disclosed, or represents that its use would not infringe privately-owned rights. Mention of commercial products, their manufacturers, or their suppliers in this publication does not imply or connote approval or disapproval of the product by Argonne National Laboratory or the U. S. Energy Research and Development Administration.

Printed in the United States of America
Available from
National Technical Information Service
U. S. Department of Commerce
5285 Port Royal Road
Springfield, Virginia 22161
Price: Printed Copy \$8.00; Microfiche \$3.00

ANL-77-25

ARGONNE NATIONAL LABORATORY
9700 South Cass Avenue
Argonne, Illinois 60439

FINAL REPORT OF FUEL DYNAMICS TEST E7

by

R. C. Doerner, W. F. Murphy,*
G. S. Stanford, and P. H. Froehle

Reactor Analysis and Safety Division

April 1977

TABLE OF CONTENTS

	<u>Page</u>
ABSTRACT	13
I. INTRODUCTION.	13
II. TEST FUEL	15
A. Pin Modifications	16
B. Fuel Composition	17
C. Nondestructive Examination	18
D. Preirradiation History	18
E. Axial Power Shape.	20
F. Fission-gas Distribution.	20
G. Radial power Shape and Calibration Factors.	22
III. TEST GEOMETRY	24
A. Fuel-pin Geometry	24
B. Axial Flow Channel	25
C. Thermal-neutron Filter	27
D. Monitor Wires	28
E. Thermocouples	28
F. TREAT Core Loading.	29
IV. TEST SUMMARY	30
A. Failure Threshold.	31
B. Fuel Motion at Failure	31
C. Postfailure Activity.	31
V. SIGNAL CONDITIONING	33
A. Analog Data Tapes.	33
B. Data Digitization.	33
C. Noise	34
D. Instrument Calibration Factors	34

TABLE OF CONTENTS

	<u>Page</u>
1. Temperature	34
2. Calibration of Lower Flow Detector	35
3. Pressure Transducers	35
4. Calibration of Upper Flow Detector	36
VI. TEST DATA	37
A. TREAT Transient	37
B. Temperature Data	44
C. Flow and Void Data	50
D. Pressure Data	57
E. Hodoscope Data	59
1. Supralinearity	60
2. Data Smoothing	62
3. Differential Hodographs	63
4. Postshutdown	76
F. Posttest Radiography	76
VII. POSTTEST EXAMINATION	78
A. Test-section Disassembly	78
B. Examination Results, General Features	80
C. Top and Bottom Blockages	85
D. Extent of Melting	86
E. Microstructures	87
F. Fuel-element Plenum Sections	92
VIII. CALCULATIONS	94
A. General Results of COBRA Calculations	95
B. Temperature Distribution at End of Preheat	95
C. Thermal History during Approach to Failure	97
D. Temperature Distribution at Failure	102
E. Damage Parameter	103

TABLE OF CONTENTS

	<u>Page</u>
IX. SUMMARY, DISCUSSION, AND CONCLUSIONS.	109
A. Flow Data	109
B. Fuel-failure Criteria	112
C. Flow-channel Voiding.	112
D. Early Fuel and Cladding Motion after Cladding Rupture	112
E. Fuel Motion after Holder Rupture.	117
F. Late Fuel Motion.	117
G. Chronology of Events	118
H. Conclusions	118
X. RELATION OF TEST E7 TO LMFBR CONDITIONS.	120
APPENDIXES	
A. Tabulation of Test Data	122
B. Thermal Constants and Geometry Used in COBRA Calculations	142
ACKNOWLEDGMENTS	147
REFERENCES	147

LIST OF FIGURES

<u>No.</u>	<u>Title</u>	<u>Page</u>
1.	Modified HEDL N-F Fuel Pin.	16
2.	Metallographic Cross Section of HEDL N-F Pin	18
3.	Comparison of Axial Power Shape of Peak-power FTR Pin, Sibling Pin in EBR-II Irradiation, and E7 Test Fuel	20
4.	Estimated Fission-gas Profile of Test Fuel in Test E7.	22
5.	Normalized Radial Power Distributions and Pin-sector Identification.	23
6.	Cross Section of Fuel Cluster with Pin Identification for Test E7.	25
7.	Detailed Axial Geometry of Flow Channel for Test E7, Showing One of Seven Identical Fuel Pins.	26
8.	Location of Test Instrumentation in Mark-II Loop for Test E7.	27
9.	TREAT Core Loading for Test E7.	29
10.	TREAT Summary Sheet for Test E7	30
11.	Cross-correlation between Outlet-flow Signal and Outlet Temperature.	36
12.	Power and Integrated-power Traces	39
13.	Lower-flow Data	39
14.	Upper-flow Data	40
15.	Pressure-transducer Response	40
16.	Inlet Temperatures	41
17.	Outlet Temperatures	41
18.	Sodium Temperatures at Pump Return.	42
19.	Temperatures above and below Sodium-free Surface	42
20.	TREAT Power and Energy.	43
21.	Motion of TREAT Rod 1	43
22.	Motion of TREAT Rod 2	44
23.	Response of Inlet Thermocouple TC1 during Failure Sequence	44
24.	Response of Inlet Thermocouple TC2 during Failure Sequence	45
25.	Response of Outlet Thermocouple TC3 during Failure Sequence	46
26.	Response of Outlet Thermocouple TC4 during Failure Sequence	46

LIST OF FIGURES

<u>No.</u>	<u>Title</u>	<u>Page</u>
27.	Temperature at Pump Return (TC5)	47
28.	Temperature of Downflow from Flow Channel (TC6) to 10 s.	48
29.	Temperature of Downflow (TC6) to 15 s	48
30.	Temperature of Upper Sodium Plenum (TC7) to 15 s	49
31.	Temperature of Upper Sodium Plenum (TC7) to 10 s	49
32.	Temperature of Plenum Cover Gas (TC8).	50
33.	Inlet-flow Data during Failure Sequence.	51
34.	Outlet-flow Data during Failure Sequence.	51
35.	Response of Inlet-flow Detector to Event at 7.834 s	52
36.	Response of Outlet-flow Detector to Event at 7.834 s	53
37.	Inlet-flow Data after Initial Failure.	54
38.	Outlet-flow Data after Initial Failure.	54
39.	Inlet-flow Data during Event at 10.95 s	55
40.	Outlet-flow Data during Event at 10.95 s	55
41.	Integrated Inlet and Outlet Flows since 7.0 s.	56
42.	Void Growth during Early Failure Stages	57
43.	Void to 8.0 s	57
44.	Inlet Pressure Data during Initial Failure	58
45.	Inlet Pressure Data during Event at 10.95 s	58
46.	Outlet Pressure Data during Initial Failure	59
47.	Outlet Pressure Data during Initial Failure, Averaged over 1 ms .	60
48.	Power Profile, as Indicated by Hodoscope Array Average and by TREAT Power Monitor	62
49.	Hodoscope Power Trace, with 15-cycle Averaging over the Peak .	63
50.	Hodoscope Summary and Array-averaged Power Trace	64
51.	Hodoscope Field of View	65
52.	Differential Hodograph for 5.73-7.39 s.	65
53.	Differential Hodograph for 7.39-7.59 s.	66
54.	Differential Hodograph for 5.73-7.59 s.	67

LIST OF FIGURES

<u>No.</u>	<u>Title</u>	<u>Page</u>
55.	Differential Hodograph for 7.59-7.72 s.	68
56.	Differential Hodograph for 5.73-7.72 s.	69
57.	Differential Hodograph for 7.63-7.77 s.	70
58.	R/P Curves for Certain Channels That Show Fuel Motion at 7.7 s	71
59.	Differential Hodograph for 7.72-7.81 s.	72
60.	Differential Hodograph for 5.73-7.81 s.	73
61.	Differential Hodograph for 7.81-8.05 s.	74
62.	Differential Hodograph for 8.05-8.41 s.	74
63.	Differential Hodograph for 5.73-8.41 s.	75
64.	Posttest Neutron Radiograph of Stripped Loop.	76
65.	Loop-cutting Plan for Posttest Examination	78
66.	Bottom End Plugs of Seven Elements with Some Stainless Steel Spatter.	80
67.	Melted Stainless Steel, Melted Fuel, and a Piece of UO ₂ Pellet Found among Bottom End Plugs	81
68.	Mirror-image Views of Split Section at Bottom of Fuel Columns .	81
69.	Mirror-image Views of Section at Bottom of Bellows	82
70.	Mirror-image Views of Split Section Showing Upper Two-thirds of Fuel-column Region	83
71.	Melted Fuel and UO ₂ Pellet at a Location about 1½ in. (3.8 cm) below Original Top of Fuel Column.	83
72.	Mirror-image Views of UO ₂ -insulator-pellet Region above the Fuel	84
73.	Three Views at Different Angular Orientations of Fuel-element Cluster Including Top of UO ₂ Stack and Reflector-rod Region (Section A3).	84
74.	View of Top of Elements Showing Relative Displacements	85
75.	Mirror-image View of Transverse Section of Fuel-element Cluster through UO ₂ Pellets Showing Stainless Steel and Fuel Blockage (Section A10)	86
76.	Cross Section of Fuel-element Cluster near Midlength of UO ₂ Stacks Showing Melted Steel around UO ₂ Pellets	86

LIST OF FIGURES

<u>No.</u>	<u>Title</u>	<u>Page</u>
77.	Transverse Section near Bottom of Fuel Column Showing Melting of Fluted Tube and Distribution of Melted Fuel.	88
78.	Enlargement of Section A15F Showing Porosity around Central Void in Fuel Pellets	89
79.	Fine Porosity in Melted Fuel	90
80.	Intergranular Porosity in Melted Fuel	90
81.	Fine, Uniform Dispersion of Metallic Particles in Melted Fuel . .	91
82.	Intrusive Melted Steel with Melted Fuel	91
83.	Solidified Stainless Steel Showing Effects of Rapid Cooling	92
84.	Fusion between Melted Fuel and a UO_2 Insulator Pellet.	93
85.	Isolated Particle of UO_2 Showing Grain-boundary Separation Found in Melted-fuel Region	93
86.	Generalized Radially Averaged Fuel-enthalpy/Temperature Results by Grain-structure Region	95
87.	Radial and Axial Temperature Distributions for Rod 1 at End of Preheat	98
88.	Radial and Axial Temperature Distributions for Rod 2 at End of Preheat	98
89.	Radial and Axial Temperature Distributions for Rod 3 at End of Preheat	99
90.	Radial and Axial Temperature Distributions for Rod 4 at End of Preheat	99
91.	Comparison of Radial Temperature Distributions of Test Fuel and High-power CRBR Rod	100
92.	Comparison of Axial Temperature Distributions of Test Fuel and High-power CRBR Rod	100
93.	Temperature and Energy History of Hottest Test Fuel Rod during Approach to Failure	101
94.	Energy Partitioning during Approach to Failure	101
95.	Axial Temperature Profiles and Radial Melt-front History during Approach to Failure	102
96.	Temperature Distributions at Failure of Hottest Test Fuel Pin . .	103
97.	Cladding Yield Strength as a Function of Midwall Temperature . .	105

LIST OF FIGURES

<u>No.</u>	<u>Title</u>	<u>Page</u>
98.	Damage Parameters for Rod 1	105
99.	Damage Parameters for Rod 2	106
100.	Damage Parameters for Rod 3	106
101.	Damage Parameters for Rod 4	107
102.	Detailed Flow Data into Individual Cladding-rupture Events with Corresponding Calculated Fuel Enthalpies.	109
103.	Response of Inlet Thermocouple TC1 at Failure	114
104.	Responses of Inlet Thermocouple TC2 and Outlet Thermo- couple TC3 at Failure	114
105.	Response of Outlet Thermocouple TC4 during Failure	115
106.	Temperature History of Return Flow during Failure	115
107.	Temperature History above and below Sodium-free Surface during Failure	116
108.	Inlet and Outlet Flow during Fuel-rod Failure	116
109.	Inlet and Outlet Pressure during Fuel-rod Failure	117
B.1.	Gap Conductance Used in COBRA Calculations	143
B.2.	Geometric Details Used in COBRA Calculations	145

LIST OF TABLES

<u>No.</u>	<u>Title</u>	<u>Page</u>
I.	Composition by Mass of Test Fuel Pin	17
II.	Isotopic Composition of Average Pin	17
III.	Burnup Calculations for HEDL N-F Pins Used in Test E7	19
IV.	Calibration Factors and Radial Power Distributions for Test E7	23
V.	Corrected and Uncorrected Flow Data	38
VI.	Measurements of Upper-plenum Pieces	94
VII.	Calculated Fuel Enthalpy and Cladding Temperatures	96
VIII.	Damage Parameters without Preheat Enthalpy.	108
IX.	Flow Surges during Cladding Ruptures	110
X.	Chronology of Events in Test E7	119
XI.	Comparison of Parameters in Test E7 to Reference Design Values of CRBR	120
A.1.	Instrument Signals	123
A.2.	Inlet and Outlet Flow Rates and Integrals, and Void	132
B.1.	Thermal Properties of Sodium	143
B.2.	Cladding and Duct-wall Thermal Properties	144
B.3.	Fuel Thermal Properties.	144
B.4.	Hydraulic Parameters Used in E7 COBRA Calculations.	144
B.5.	Forcing Functions Used in COBRA Calculations.	145
B.6.	Fuel-pin Properties for COBRA Calculations	146

FINAL REPORT OF FUEL DYNAMICS TEST E7

by

R. C. Doerner, W. F. Murphy, G. S. Stanford,
and P. H. Froehle

ABSTRACT

Test data from an in-pile failure experiment of high-power LMFBR-type fuel pins in a simulated $\$3/s$ transient-overpower (TOP) accident are reported and analyzed. Major conclusions are that (1) a series of cladding ruptures during the 100-ms period preceding fuel release injected small bursts of fission gas into the flow stream; (2) gas release influenced subsequent cladding melting and fuel release [there were no measurable FCI's (fuel-coolant interactions), and all fuel motion observed by the hodoscope was very slow]; (3) the predominant postfailure fuel motion appears to be radial swelling that left a spongy fuel crust on the holder wall; (4) less than 4-6% of the fuel moved axially out of the original fuel zone, and most of this froze within a 10-cm region above the original top of the fuel zone to form the outlet blockage. An inlet blockage ~ 1 cm long was formed and consisted of large interconnected void regions. Both blockages began just beyond the ends of the fuel pellets.

I. INTRODUCTION

In the series of tests with the Mark-II loop planned to simulate unprotected transient-overpower (TOP) accidents, E7 was the first to use a multipin cluster of high-burnup LMFBR-type fuel. Distinguishing features of this test were:

1. Seven nearly identical fuel pins previously irradiated in EBR-II at 10 kW/ft (33 kW/m) to a burnup of 4.2 at. % were used. Transient-power and fuel-temperature histories were characteristic of a $\$3/s$ unprotected TOP accident in the Fast Flux Test Facility (FFTF).

2. The only pressure pulse recorded during the test was small (~ 75 psi or 0.52 MPa) and occurred at the inlet 3.5 s after the initial failure. All fuel motion was slow and small in quantity.

3. Major conclusions of the test are that:

a. Incoherent cladding ruptures released bursts of fission gas that initiated flow-channel voiding, and molten-cladding/coolant thermal interactions maintained the void during fuel motion.

b. Fission-gas-induced fuel swelling formed a porous and spongy shell on the holder wall that served as a channel for molten-fuel flow.

c. Both fission-gas and coolant-vapor pressures remained below the threshold for significant fuel and coolant-slug ejections that have been found in other TOP accident simulations.

d. Flow-channel blockages were started by cladding and spacer-wire steel freezing to the colder upper and lower pin structure.

e. Boiling and vapor streaming at the inlet prevented formation of a solid plug.

4. Delayed events as late as 10 s after the initial failure suggest the possibility of fuel dispersal related to the postaccident heat-removal processes.

5. This was the first TOP test in which measurable quantities of fuel were found below the inlet of the test section.

Earlier reports of Test E7¹ were limited by the detail and extent to which the test data were and could be examined. Delayed events were not observed because the data did not extend beyond 8.2 s. Analysis of the test results was further limited by the interim nature of the thermophysical fuel constants used in the thermal-hydraulic calculations. A reevaluation of the test data was later compared to new and better calculations.² Reference 2 included comparisons between all the TOP tests and provided some insight into the failure threshold. Neither the results of the hodoscope-data analysis nor the posttest examinations were available at the time of these early reports. Both are included here. Advances and developments in both the modeling available in accident codes and a significantly extended capability for analyzing the test data since the test was performed (March 9, 1973), form the basis for this final report of Test E7. For this report, the original analog signals recorded on magnetic tape were redigitized and independently analyzed.

In the following sections, the fuel, the test geometry, and the test parameters are described. A number of mechanisms related to causes of fuel motion are identified in Sec. IV. Techniques used in "conditioning" the test signals are defined and discussed, and the test results are presented in Sec. V. Results of thermal-hydraulic calculations and an evaluation of the Baars-Scott-Culley³ damage parameter for fuel failure for each axial node of each test pin are presented in Sec. VIII. In Sec. IX, the test results are combined with the calculations to generate a scenario and a basis for the conclusions of the test. Evaluation of the input constants used in the calculations and tabular listings of the test data are presented in the appendixes.

The main conclusions of Test E7 are that two failure events can be identified: an initial breach of the cladding integrity, which releases small quantities of gas, and a "fuel-failure" event, producing severe flow anomalies. A series of incoherent cladding failures is identified by a 50-ms sequence of small surges in the flow signals. "Fuel failure" is identified by ejection of coolant from both ends of the flow channel. The flow surges were small ($0.9\text{--}3.5\text{ cm}^3$) and are interpreted as fission-gas releases. They are not accompanied by measurable pressure pulses, and they occur when various pins (or regions of a single pin) reach an enthalpy of 200 cal/g (837 J/g). Fuel release occurred after the flow channel was essentially voided. The picture of fuel motion that emerges is that individual pins swell as the solidus front approaches the gassy, unrestructured fuel region. As melting progresses, the cluster as a whole swells to form a spongy crust on the holder wall. The combined central void in the pins and the increased volume resulting from swelling are sufficient to reduce fission-gas pressures below the threshold for rapid ejection of molten fuel.

Blockages are formed as molten cladding freezes to the upper and lower pin structure. Later-arriving fuel does not penetrate the blockages and forms plugs of increasing fuel density toward the original fuel column. The inlet blockage forms after complete channel voiding. Some debris falls downward to form a fuel-steel deposit in the lower bend.

During the transition between individual pin swelling and cluster swelling, the upper pin structures drop downward, pushing the molten fuel outward and upward.

Near the end of the transient, the hottest region of the fuel crust at the axial midplane melts and moves both upward and outward into the adiabatic holder region.

Delayed reactions of relatively large magnitude are reminiscent of those observed in fresh-fuel tests in the S autoclave test series. Periods of coolant boiling at the inlet were observed 2-4 s after failure. Pressure of the sodium vapor may have dislodged and relocated some loose debris or partially molten fuel. At 16 s ($8\frac{1}{2}$ s after initial failure and $7\frac{1}{2}$ s after shutdown), the outlet-flow and temperature signals showed sodium penetrating the upper blockage. Vapor pressure appeared to relocate sufficient material to produce a rise in the outlet temperature with no measurable increase in the upper-head or pump-return temperatures. No later events were observed.

II. TEST FUEL

The seven fuel pins used in Test E7 were modified HEDL N-F pins that had been irradiated previously in Ring 5 of the X097 subassembly in EBR-II. A drawing of the pins is shown in Fig. 1, and their placement in the test is shown

in Figs. 6 and 8 below. Spacer wires were of 1.01 ± 0.01 -mm OD on a 0.3-m pitch. (FTR pins have 0.91-m-long fuel columns and use 1.4-mm spacer wires.) Except for the fuel and insulator pellets, and the Inconel reflector rod and spring material, all parts of the pins are made of Type 316 stainless steel.

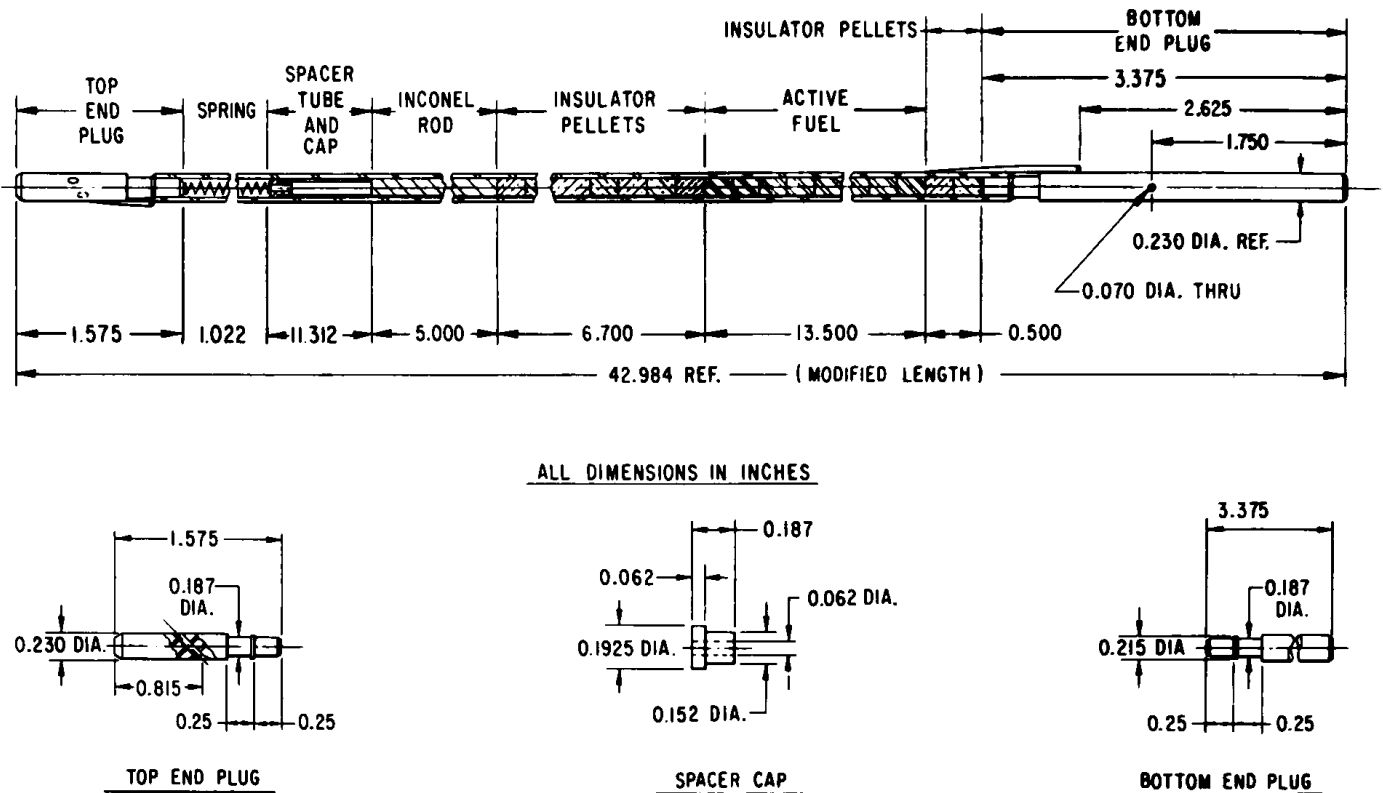


Fig. 1. Modified HEDL N-F Fuel Pin. Conversion factor: 1 in. = 2.54 cm. ANL Neg. No. 900-4383.

A. Pin Modifications

After irradiation in EBR-II, the spiral wire wraps were tack-welded to the solid end plug just below the cladding-plug weld, and the bottom 0.453 m of the 0.539-m-long solid lower end plugs were cut off. A 1.78-mm-dia hole was drilled through the plug 44 mm from the bottom. All axial dimensions of the fuel pin, the holder, the loop, and the instrumentation sections are relative to the bottom of the fuel pin, but are keyed to this hole.

As viewed from the bottom, the spacer wire is wound in a counter-clockwise direction. The location of the spacer wire at various axial elevations relative to the pump and hodoscope is shown below in Fig. 7. During the approach to failure, the pins can bow only in the direction allowed by the spacer wires. There is some slight evidence from the hodographs that initial bowing was toward the pump in the midregion of the fuel column and away from the pump at the ends. This motion is consistent with the angular location of the spacer wires shown in Fig. 7.

A 1.57-mm-dia pin through the 1.78-mm hole in the end plug provided the only axial support of the pins during the test. A limited amount of flow-induced vibration is possible, especially near the tops of the pins.

Cladding for the as-fabricated pins was of 5.86 ± 0.13 -mm-OD Type 316 stainless steel tubing with 20% cold work, having a wall thickness of 0.38 ± 0.02 mm and a length of 0.98 m. The yield strength is about three times as high as that of normal Type 316 stainless steel at temperatures below 550°C . This is important in predicting the necessary conditions for cladding failure.

B. Fuel Composition

Fuel was fabricated from preslugged, pressed, and sintered pellets of 25% PuO_2 enriched to 85% in ^{239}Pu and 25% UO_2 enriched to 77% in ^{235}U . Pellets, each about 6.3 mm long and of 4.94-mm diameter, were stacked into 344-mm-long fuel columns within the cladding tube. Weights of the oxides in individual pins are listed in Table I. Isotopic composition of an "average" pin before EBR-II irradiation is listed in Table II. Both tables reflect fresh, as-fabricated properties and assume homogeneous and isotropic distributions of material. Fuel-pellet density was 10.0 g/cm^3 .

TABLE I. Composition by Mass of Test Fuel Pin

Identification	Mass, g		
	Mixed Oxide	PuO_2	UO_2
N-104	63.64	15.92	47.72
N-115	63.88	15.98	47.90
N-153	64.57	16.16	48.41
N-092	65.18	16.22	48.96
N-069	64.19	16.06	48.13
N-185	63.76	15.95	47.81
N-081	64.15	16.05	48.10
Avg	64.196	16.048	48.147

TABLE II. Isotopic Composition of Average Pin

Isotope	Enrichment, %	Isotope Density, g/cm^3	Atom Density, $10^{24} \text{ atoms/cm}^3$	Total Mass in Pin, g
^{234}U	0.60	0.0387	9.9582×10^{-5}	0.253
^{235}U	76.88	4.9785	1.2760×10^{-2}	32.556
^{236}U	0.24	0.0156	3.9830×10^{-5}	0.102
^{238}U	22.28	1.4613	3.6980×10^{-3}	9.556
^{238}Pu	0.09	0.0019	4.9149×10^{-6}	0.0127
^{239}Pu	85.65	1.8560	4.6773×10^{-3}	12.137
^{240}Pu	11.51	0.2504	6.2856×10^{-4}	1.638
^{241}Pu	2.47	0.0539	1.3489×10^{-4}	0.358
^{242}Pu	0.28	0.0061	1.5291×10^{-5}	0.040
^{16}O		1.1543	4.3454×10^{-5}	7.549

Fuel-composition data after the EBR-II irradiation are not available. The major differences are expected to be the radial and axial distributions of material according to the grain structure. The grain structure of a sibling HEDL N-F pin (N-013) is shown in Fig. 2 and is discussed further in Sec. II.F.

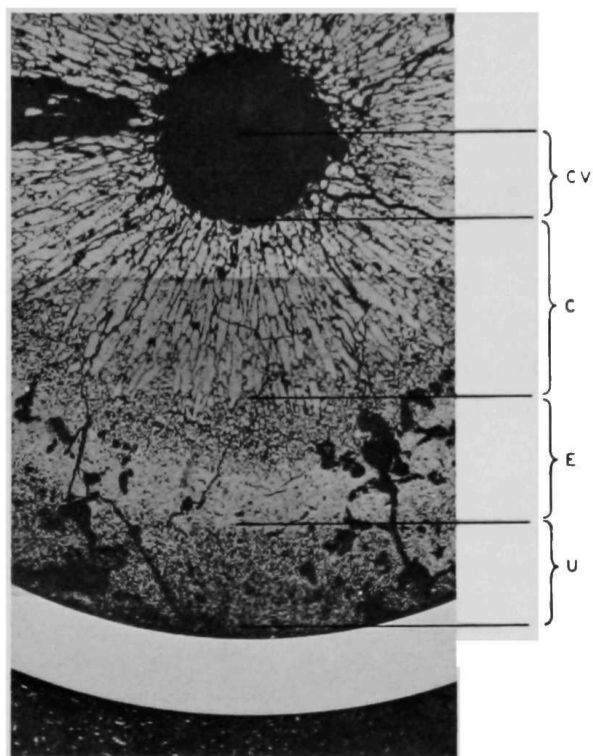


Fig. 2

Metallographic Cross Section of
HEDL N-F Pin. Mag. $\sim 28\times$.
ANL Neg. No. 900-4005.

CV: CENTRAL VOID E: EQUIAXED GRAIN REGION
C : COLUMNAR GRAIN U: UNRESTRUCTURED REGION
 REGION

C. Nondestructive Examination

The fuel pins were nondestructively inspected. The examination consisted of visual inspection and macrophotography, X radiography, helium leak testing, determination of element losses, condition of the wire wrap, gross and ^{137}Cs gamma scanning, and measurements of the weight, balance point, length, and diameter. The principal irregularity was that the spring in element N-092 (central pin in the test cluster) had 25 coils compared to 19 coils in the other elements. Posttest examination of the springs showed that some had 19 and others 20 coils. The difference is due to the pin orientation in the X-ray pictures.

D. Preirradiation History

Results of pin-surveillance calculations (by the VIGILANTE code) for the seven fuel pins used in Test E7 are listed in Table III. The sibling pin, N-013, that had been destructively examined, is included in the table. Fission-gas content is not known but can be back calculated from the pressures and temperatures listed in Table III. The calculated fission-gas fraction is 86.6% of the total gas volume.

TABLE III. Burnup Calculations for HEDL N-F Pins Used in Test E7

Pin No.	Beginning of Life				End of Life						
	Linear Power, kW/m	Coolant Temp, °C	Cladding Temp, °C	Plenum Pressure, MPa	Burnup, at. %	Fluence, 10^{22} nvt	Linear Power, kW/m	Coolant Temp, °C	Cladding Temp, °C	Fission Gas Generated, cm ³	Plenum Pressure, MPa
N013 (Sibling pin)	38.32	471	510	0.5141	4.760	4.138	37.01	467	505	61.02	3.810
N069	34.38	470	506	0.5067	4.291	3.705	33.33	466	502	55.03	3.436
W081	37.80	471	510	0.5067	4.695	4.079	36.48	468	506	60.17	3.209
N092	33.60	468	504	0.4913	4.141	3.570	32.60	465	500	53.87	3.352
N104	33.46	459	495	0.4960	4.202	3.622	32.47	456	491	53.42	3.290
N115	33.43	468	504	0.5026	4.188	3.609	32.43	465	500	53.45	3.332
N153	33.10	466	501	0.5004	4.167	3.590	32.13	462	498	52.92	3.292
N185	32.81	463	492	0.4959	4.121	3.547	31.83	455	489	52.50	3.241

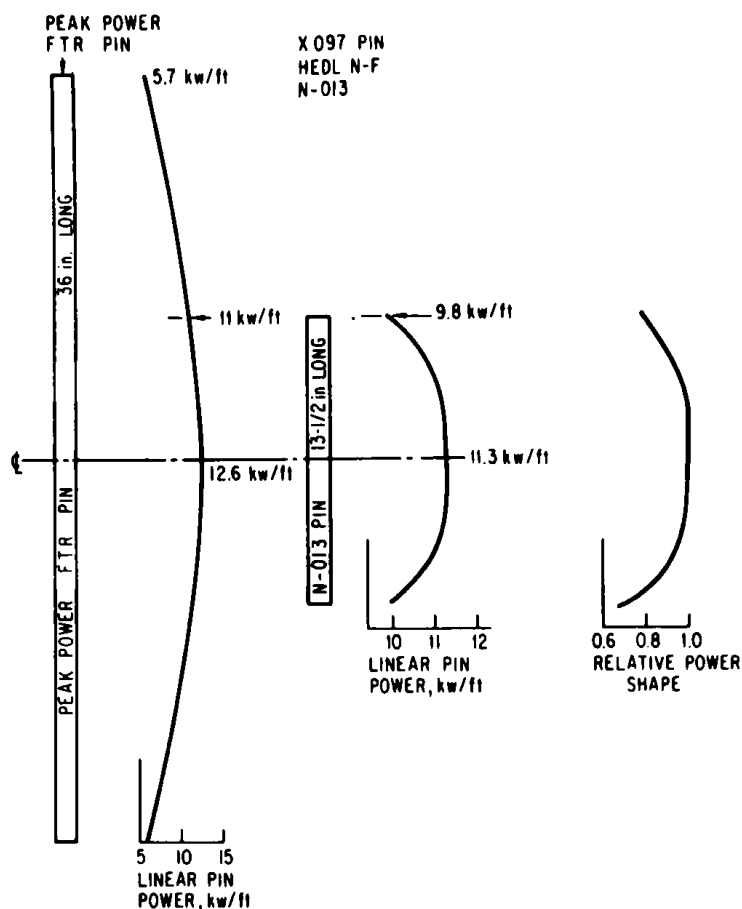


Fig. 3. Comparison of Axial Power Shape of Peak-power FTR Pin, Sibling Pin in EBR-II Irradiation, and E7 Test Fuel. Conversion factors: 1 kW/ft = 3.281 kW/m, 1 in. = 2.54 cm.

E. Axial Power Shape

Figure 3 compares the axial power shape of the test fuel during the E7 transient to that of a high-power FTR pin. This figure is an adaptation of Fig. 9 of Ref. 4. The 37-kW/m power level during the EBR-II preirradiation creates a void in the center of the test pin. The void size in an FTR pin will be somewhat larger at the same burnup because of the higher linear power. Thus, the test pin will have about the same fission-gas content as a 4.2%-burnup FTR pin, but a slightly smaller central void. Axially, the central void extended nearly to the end of each pin.

A relative axial power shape was determined from foil irradiations on fresh fuel pins during steady-state calibration measurements for Test H3.⁵ Results of these measurements are further discussed in Sec. II.G. The axial power shape during the E7 transient

test, shown at the right side of Fig. 3, is assumed to be the same as the steady-state H3 results. Differences between transient and steady-state measurements of the fuel calibration factors vary by as much as 20%. Most or all of this difference can be accounted for by detailed differences in core loading and rod settings between the low-power run and the test transient. On the basis of pretransient power calibration runs made for H3,⁵ the axial power shape as shown in Fig. 3 did not undergo similar changes during the transient. Only minor differences can be attributed to the differences between the fresh fuel of the H3 calibration measurements and the irradiated fuel of Test E7. Loop outfitting, including the flux-shaping filters, were the same for Tests H3 and E7.

F. Fission-gas Distribution

A sibling pin (HEDL N-F pin N-013) from the same EBR-II subassembly in which the E7 test pins were irradiated was destructively examined at the axial midplane and at the ends of the fuel columns for grain structure, but not for particle size or fission-gas distributions. The grain-structure regions as seen in Fig. 2 are well defined. The central void extends to 0.585 mm, the

columnar grains to 1.6 mm, and the unrestructured region to 2.52 mm, compared to the 2.46-mm radius of the fresh as-fabricated pellets. More extensive examinations for fission-gas distributions were performed on a PNL-17 sibling pin that had undergone a similar total irradiation, but at two different linear power levels.

A fission-gas retention profile was estimated⁶ from a comparison of the operating temperature, the observed structural morphology, and the total fission-gas release. The fission-gas distribution in the N-013 pin was estimated as follows:

The temperature distribution during EBR-II irradiation was determined from the average cladding temperature obtained from VIGILANTE data. To this was added a gap temperature drop using a gap conductance of 85 W/m²·°C to obtain the fuel surface temperature. The fuel-temperature profile was obtained from the $\int k(\theta)d\theta$ equation for fuel containing a central void.

A temperature profile obtained in this way for the PNL-17 pin was similar to that calculated by the LIFE-II code. The measured radial distribution of retained fission gas in the PNL-17 pin was compared to the calculated temperature profile. This result was then applied to the HEDL N-F pins.

Total gas release from the N-013 sibling pin was 40.73 cm³. (The pin was put in a vacuum chamber of known volume, and the cladding was punctured by a laser beam. The release volume was then determined from the equilibrium chamber pressure.) Of the released gas volume, 86.8% or 35.3 cm³ was fission gas. The remaining fission-gas volume (5.4 cm³) is retained within the fuel microstructure. Laser sampling measurements of the PNL-17 pin gave volume fractions of retained fission gas by structure regions (see Fig. 2). These were:

Columnar-grain region	3.9%
Equiaxed region	32.1%
Unrestructured region	64.1%

An estimated profile for the retained fission gas in the HEDL N-F pins based on these data is shown in Fig. 4. Examination of samples taken from the top and bottom pellets of the N-013 pin indicated the axial variation of the inner radii of the different grain regions approximately as follows:

<u>Axial Position</u>	<u>Void, mm</u>	<u>Columnar, mm</u>	<u>Equiaxed, mm</u>
Ends	None		
6.3 mm from ends	0.46	1.4	1.95
Central 250 mm	0.58	1.6	2.06

This distribution is a direct reflection of the axial power shape during the EBR-II irradiation (see Fig. 3).

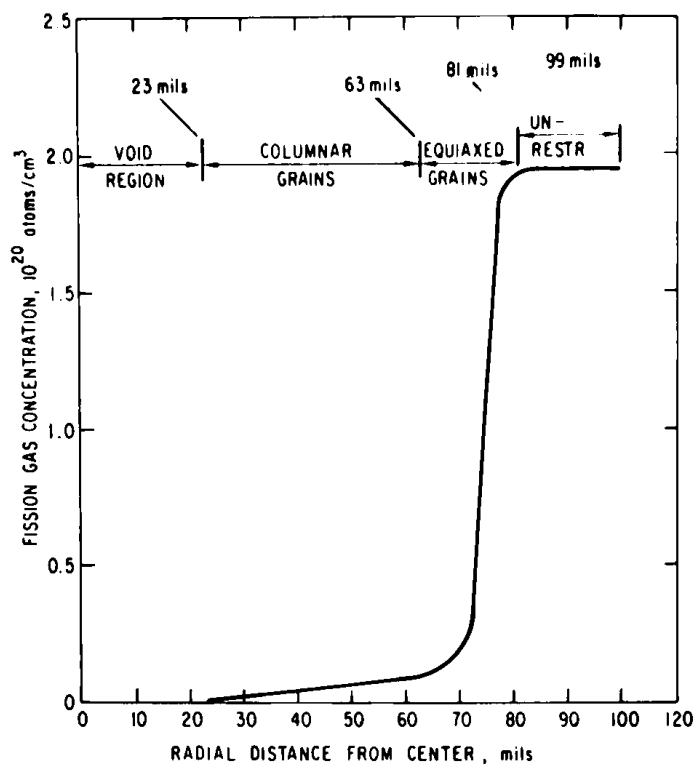


Fig. 4

Estimated Fission-gas Profile of Test Fuel in Test E7. Conversion factor:
1 mil = 0.00254 mm.

G. Radial Power Shape and Calibration Factors

Power distributions within each pin and among pins within the cluster are important, both as input information to calculations and as a factor bearing on fuel motion. The distributions are determined by a combination of neutronics calculations⁷ and experiments. Separation into axial and radial components is assumed, both of which can be adjusted, within limits, to meet certain criteria.

A series of transient calibration measurements was performed with both fresh pins in a pretest calibration study and fresh and irradiated PNL-type pins for Test H3.^{5,8} Enriched-uranium foils measured the surface power density at several angular orientation and axial locations.⁹ Some of the fuel pellets were destructively analyzed for the radially averaged power density. Two-dimensional transport calculations, normalized to the pellet-averaged and surface power densities, were used to obtain detailed distributions through the cluster.^{10,11} Monitor-wire activities were used to normalize cluster powers to TREAT power.

Power distributions within the cluster are characterized by a superposition of an axisymmetric radial distribution within the central pin and a gradient across the cluster arising from flux depression on the pump side of the loop. Each peripheral pin is taken to have the same intrapin distribution relative to the pin average power. Corrections were made to account for redistribution relative to the pin average power. Small corrections of a few percent were made to account for redistribution of fissile material during EBR-II preirradiation. These corrections include the migration of fission

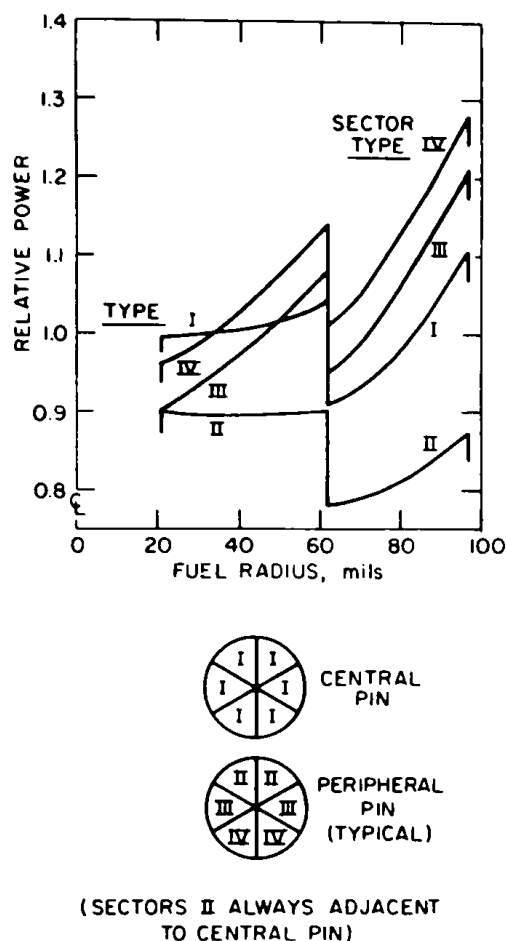


Fig. 5. Normalized Radial Power Distributions and Pin-sector Identification. Conversion factor: 1 mil = 0.00254 mm.

gas toward the center and the displacement of fuel outward to produce the different densities within the various structure zones. The correction calculations were supplied by HEDL.¹² The resulting intrapin power shapes are shown in Fig. 5. Four types of power shapes are shown. Type I distributions apply to all azimuthal sectors of the central pin. Type II-IV distributions are used for the peripheral pins as shown in the lower drawing of Fig. 5. Type II distributions are used for pin sectors whose adjacent flow channel is bounded by two additional pins. Type III distributions are towards flow channels bounded by a single additional pin, and Type IV distributions are for the pin sectors that face the holder wall.

The sharp decrease in calculated power density per unit volume in the unstructured regions is based on fuel-density measurements in the sibling PNL-17 pin. These volumetric power changes result from an average pellet density of 93% TD before irradiation, changing locally to 78% TD in the unstructured fuel region after irradiation. Calculations of the radial power shape as made by HEDL correctly predict the central-void growth and consequent fuel densification in the columnar-grain region.

No correction in the power shape was made to account for loss of fuel resulting from burnup and the addition of fission-product poisons.

Absolute pin calibration factors determined from the combined foil and pellet measurements in the H3 calibration measurements and the two-dimensional transport calculations are listed in the top left of Table IV. Intrapin distributions, corresponding to the four types shown in Fig. 5, are listed in the lower portion of Table IV. The relative axial power shape, shown at the right of Fig. 3, is tabulated at the top right in Table IV.

TABLE IV. Calibration Factors and Radial Power Distributions for Test E7^a

Pin No.	Power Calibration, J/g·MW·s	Height from Bottom, in.	Relative Axial Power Shape
N-092	1.612		
N-081	1.650	0-1.917	0.810
		1.917-3.861	0.950
N-069	1.969	3.861-5.778	0.990
N-115		5.778-7.722	1.000
N-185	2.166	7.722-9.639	0.990
N-153		9.639-11.583	0.960
N-104	2.166	11.583-13.500	0.820

TABLE IV (Contd.)

Radius, in.		Radial Power Distribution			
Inner	Outer	Type I	Type II	Type III	Type IV
0.023	0.0326	0.995	0.896	0.914	0.967
0.0326	0.0422	0.990	0.894	0.951	0.998
0.0422	0.0519	1.001	0.894	0.992	1.047
0.0519	0.0615	1.019	0.896	1.044	1.100
0.0615	0.0711	0.912	0.785	0.958	1.014
0.0711	0.0808	0.948	0.800	1.019	1.082
0.0808	0.0904	1.009	0.829	1.094	1.171
0.0904	0.100	1.090	0.867	1.185	1.249

^aConversion factor: 1 in. = 2.54 cm.

III. TEST GEOMETRY

The Mark-II test loop,¹³ the Transient Reactor Test Facility (TREAT),¹⁴ and the hodoscope,^{15,16} are described in the literature. The basic design of the loop was to accommodate fuel pins and flow channels that were less than 0.787 m long. Pressure and flow instrumentation are at fixed locations on the loop. The 1.1-m-long test pins and flow channel in Test E7 extended beyond the upper instrument section. Pressure pulses in the flow channel were coupled to the transducer through a hole cut in the flow tube at the elevation of the upper pressure transducer. In addition, an Armco iron core was installed inside the loop at the upper flow detector to enhance the outlet-flow signal. Unfortunately, the iron flow "amplifier" appears to have enhanced the temperature sensitivity of the flow detector. Outlet flow spilled over the top of the flow channel and moved downward on the outside of the holder to the pump return tee. All parts of the loop within the 1.22-m active height of the TREAT core are coated with a thermal-neutron-filter material.

A. Fuel-pin Geometry

The seven HEDL N-F test pins were arranged in a hexagonal array surrounding the central pin, as shown in Fig. 6. A fluted flow tube provides the correct hydraulic simulation of seven pins within a much larger cluster, as well as providing the necessary constraint against radial motion of the fuel cluster. Although 0.5 mm of diametrical clearance is allowed for, the pins (with their spacer wires having identical orientations) fit snugly in the fluted tube at room temperature, because of pin bowing.

An outer shell tube surrounding the fluted tube provides a space that is filled with argon gas at 0.1 MPa (1 atm) and serves as a thermal insulator. By limiting the heat losses to the loop wall, the seven-pin cluster is thermodynamically similar to pins within a much larger assembly. Unlike a larger cluster,

however, the fluted wall fails by melting during the fuel-motion phase of the test. The insulating argon gas can then mix with the flow stream, and pressure pulses that may have been generated are attenuated by an unknown amount; their propagation velocity can change drastically, and the flow-detector response to two-phase flow is unknown.

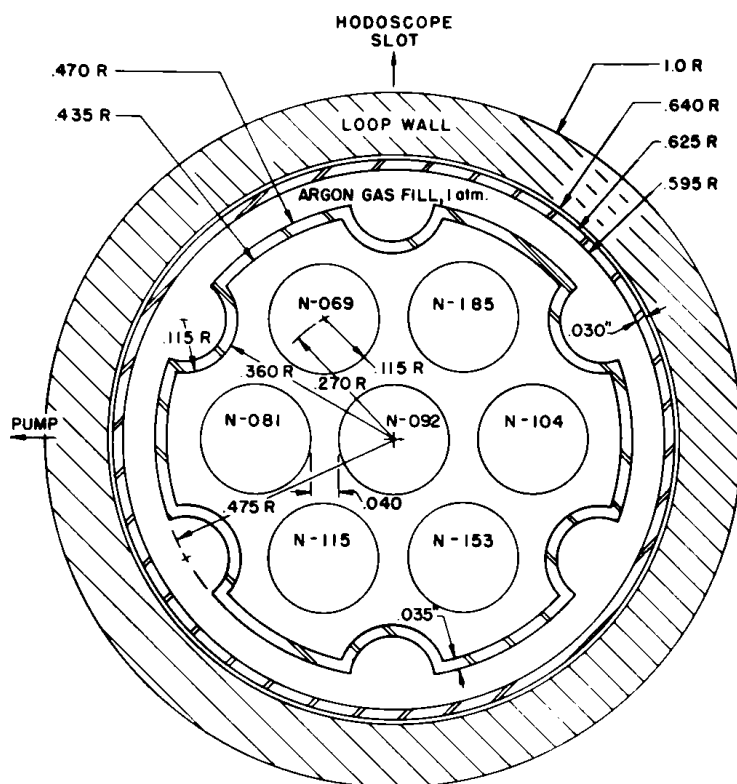


Fig. 6

Cross Section of Fuel Cluster with Pin Identification for Test E7. All dimensions in inches. Conversion factors: 1 in. = 2.54 cm; 1 atm = 0.1 MPa.

B. Axial Flow Channel

Axial motion of the fuel pins is constrained by the locking pin at the bottom (inlet) end of the flow channel. Details of the flow channel are shown in Fig. 7. Major points of interest in this figure are:

1. The substantial mass of steel exists in the inlet and outlet regions. These steel masses can act as heat sinks to rapidly cool the blockage material. Rapid cooling would account for the observed directional dendritic grain structure found in the remains.

2. The volume of argon gas that can be released when the fluted tube ruptures is 181 cm^3 (twice the volume of sodium in the same region) at a pressure of about 0.28 MPa (40 psi) at 380°C . This volume, plus that of the holder wall that melts and is carried away, can be occupied by sodium and complicates the calculation of voiding from the flow data.

3. Because of direct contact with the loop wall, radial heat transfer from upward-moving hot or molten debris increases dramatically above the adiabatic section (730 mm). Any debris entering this region is likely to freeze rapidly.

4. The tops of the fuel pins extend about 25 mm above the top of the flow channel, and the lowest sodium-slug baffle is about 13 mm above the tops of the fuel pins. Debris carried with an ejected sodium slug would impact the baffle.

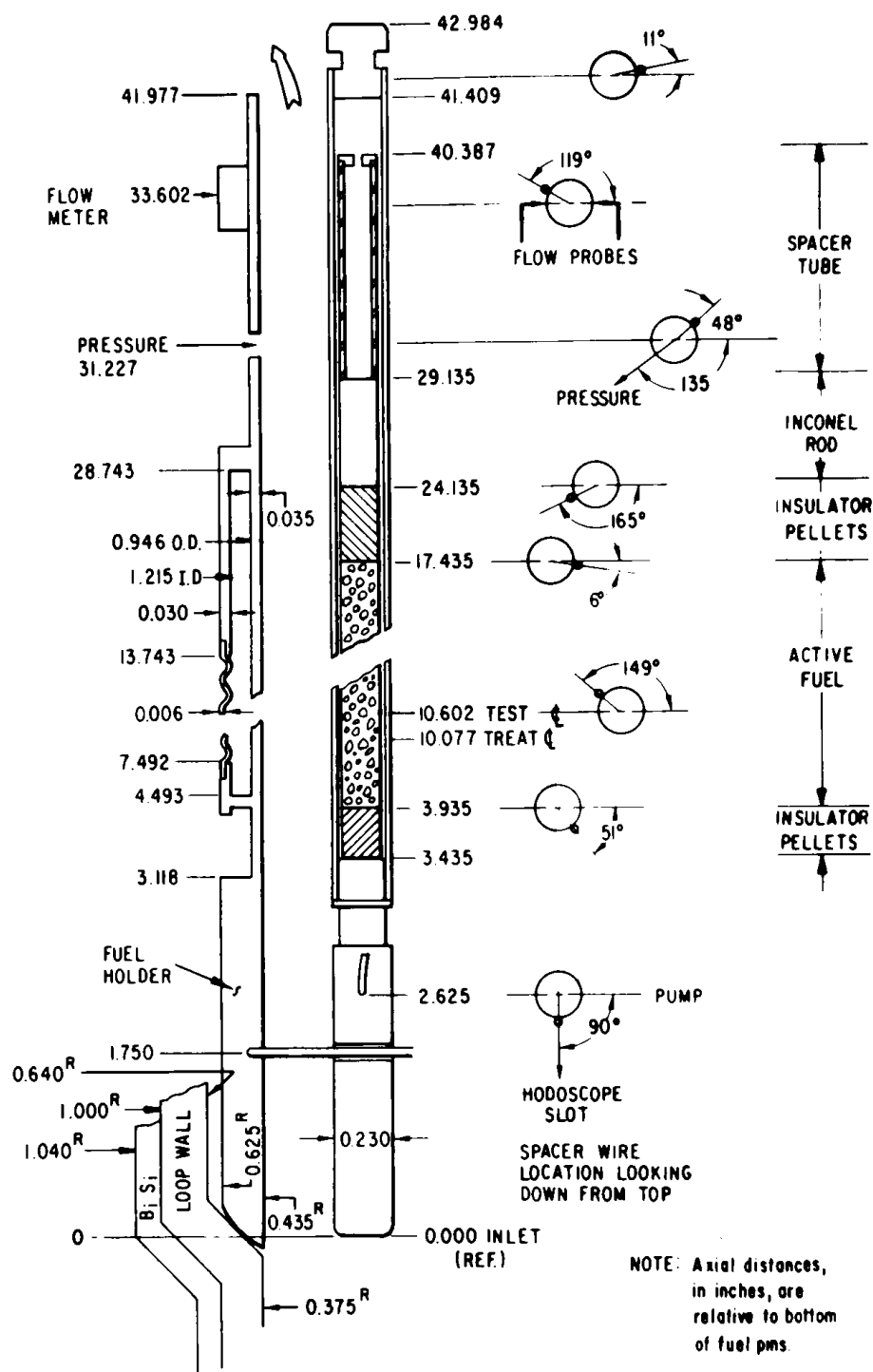


Fig. 7. Detailed Axial Geometry of Flow Channel for Test E7. Showing One of Seven Identical Fuel Pins. Conversion factor: 1 in. = 2.54 cm.

Inlet thermocouples, not shown in Fig. 7, pass through the gas in the adiabatic region of the fuel holder. When hot or molten fuel penetrates the holder wall, either inlet thermocouple can be destroyed by meltthrough of the sheath. Electrical signals from thermocouples that fail by sheath meltthrough

are uniquely different from those caused by hot debris melting the junction. Information on the time of holder-wall failure (determined from the time of failure of the inlet thermocouple by sheath melting) provides an important timing measurement in the analysis of fuel motion.

Figure 8 is a sketch of the loop, the test section, and the instrument locations. In the normal procedures for sodium filling, a slight excess is

allowed to spill over into the overflow pipe (at the location of TC6, Fig. 8), which is subsequently drained. Special filling procedures were followed in this test to establish the upper sodium head (165 mm above the overflow pipe). (Pretest volumetric displacement measurements indicated a total displacement of 22.6 cm^3 for the lower 1.18 m of the test train. This displacement volume was used to determine the required sodium-fill level that provides the 89-mm upper plenum head.)

C. Thermal-neutron Filter

All the TOP experiments in Mark-II loops that use high-enrichment mixed-oxide fuel have used thermal-neutron filtering to achieve an acceptably flat power distribution across the pin cluster.^{17,18} Filter material was a mixture of B_6Si and high-temperature Type HE Pyromark Paint.* This mixture is painted onto a 16-mesh Type 316 stainless steel screen that is tack-welded to the loop body. After air drying and baking by operating the loop at 370°C , the mesh filter has a thickness of 1.03 mm, consists of

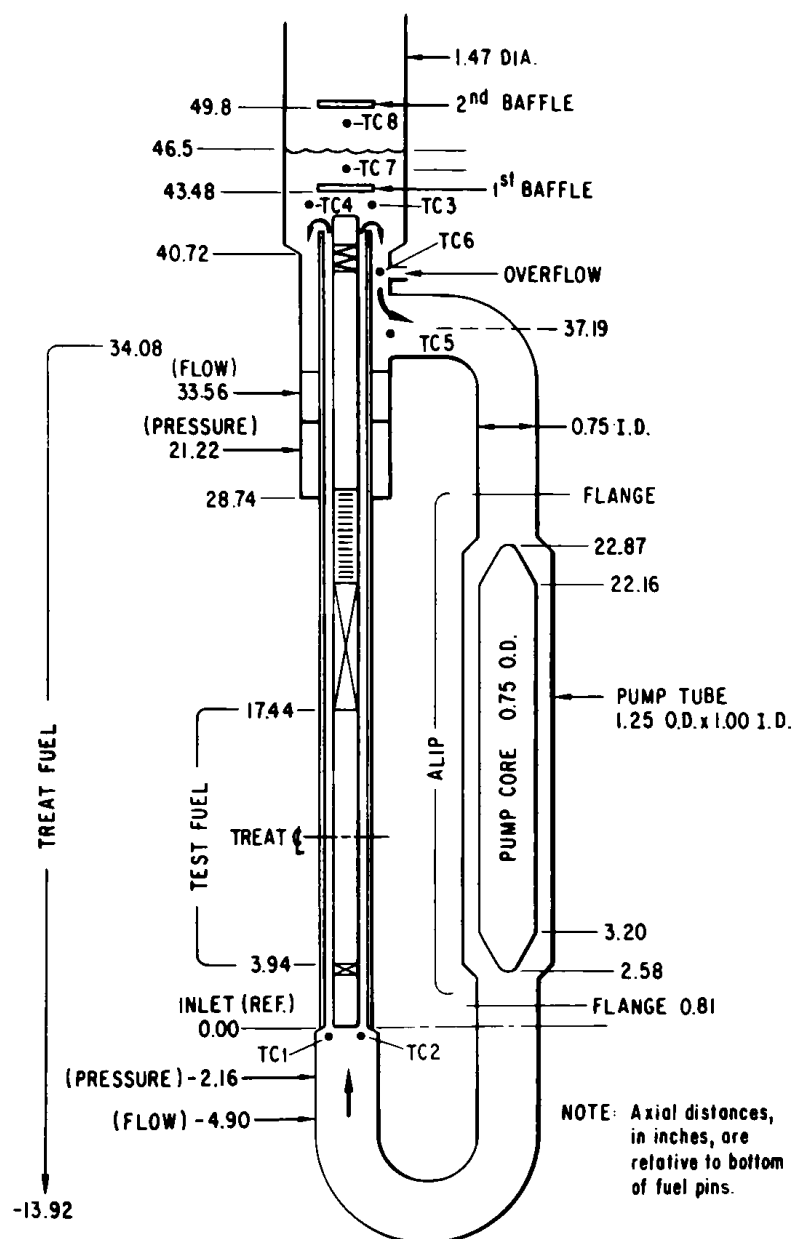


Fig. 8. Location of Test Instrumentation in Mark-II Loop for Test E7. Conversion factor: 1 in. = 2.54 cm.

25% steel and 75% B_6Si , and has a thermal-neutron absorption equivalent to 0.057 g/cm^2 of natural boron. (Effective thickness was determined by thermal and epi-cadmium neutron-transmission measurements of a plane filter.) Shaping collars at the ends of the fuel columns were used to reproduce the axial power shape during the EBR-II irradiation. The collars were made by overlaying layers of mesh and B_6Si material.

*Trademark, Tempil Corp., New York.

As a safety measure, all parts of the loop in which fuel could accumulate (as a result of sweepout or slumping after failure) are also coated with the filter material. Should a significant quantity of fuel freeze or attach to the loop wall before the transient is over, the filter limits the heat generation and prevents meltthrough. Skewing of the flux across the test pin cluster resulting from the asymmetric distribution of filter material is discussed in Sec. II.G.

D. Monitor Wires

Two monitor wires were used in Test E7 as additional checks on the fuel-pin calibration factors that were used to normalize the results of this test to others in the E and H series. Both wires were located at the axial midheight of the fuel column; one was between the fuel-holder walls, and the other was external to the loop between the overflow pipe and the pump.

Due to posttest delays in loop-handling operations, the internal monitor wire could not be reclaimed before the activity had decreased to a level too low for counting, and a direct verification of the calibration factors has not been made. The external monitor wire was removed and radiochemically analyzed for fissions within 11 days of the test. Results of this analysis, corrected to the test time, gave 3.85×10^{13} fissions per gram of wire. The wire consisted of 3.6 wt % uranium, enriched in ^{235}U to 93.118 wt %, and 96.4 wt % zirconium.

The integrated energy in the transient was 1457 MW·s. A similarly shaped 810-MW·s transient in the H3 calibration measurements gave 2.69×10^{13} fissions per gram of wire, and the 1244-MW·s transient of Test E6 gave 8.1×10^{13} fissions per gram. The obvious lack of consistency and correlation between the monitor-wire activations and the TREAT energy has not been resolved.

E. Thermocouples

Thermocouples in pairs were located at the inlet and outlet, respectively, as shown in Fig. 8. One thermocouple, TC7, was located about 85.4 mm above the first baffle to monitor bulk heating of the sodium in the upper head. Another, TC8, was located 25.4 mm above the free surface of the upper sodium head to monitor ejections of any coolant slugs. For the sodium and loop-wall temperatures at a nominal 390°C, the upper plenum-gas temperature is 250°C. The difference is due to heat loss by convection to the bayonet assembly and by conduction to the upper closure flange, top plate, and dome assemblies, all of which were at room temperature. Two thermocouples were located in the flow path: One was about 50 mm below the flow-channel outlet; the other was at the pump return.

Transient No.: 1499 Loading No.: 770 Date: 3-9-73 Time: 1423

Series No.: Mark II Sodium Loop Capsule No.: E-7

CALIBRATION FACTORS

- | | |
|---|---|
| 1. Safety #1: 0.162×10^{-7} A/MW | Safety #2: 0.335×10^{-7} A/MW |
| 2. Integrated Power #1: 0.069 CV/MW·s | Integrated Power #2: 0.098 CV/MW·s |
| Scram Settings #1: | Scram Settings #2: |
| 1400 MW·s 4.83 Trip Volt 20 Cap. | 1400 MW·s 6.86 Trip Volt 20 Cap.. |

SUMMARY RESULTS

- | | | | | | | | | | |
|--------------------------|---------------|-------------|--------|--------------|----------|---------------------------|----------|--|--|
| 1. Period: | 0.204 s | Reactivity: | 1.111% | | | | | | |
| 2. Reactor Temp: | TC #6 | Initial | 36 | Final | 323 | Int. Power (ΔT) | 921 MW.s | | |
| | | | | | | (287) | | | |
| 3. Integrated Power: | 1396 (tape) | | 1320 | | | | | | |
| | | | 1270 | | | MW.s | | | |
| 4. Peak Power: | 2468 (tape) | | 2370 | | | | | | |
| | | | 2800 | | | MW | | | |
| 5. Rod Position: | Critical | 43.15 #1 | 40 #2 | Pretransient | 59 #1 | 0.00 #2 | | | |
| | | 0 #3 | | | 15.26 #9 | | | | |
| 6. Primary Scram Signal: | Program Scram | | | | | | | | |

Fig. 10. TREAT Summary Sheet for Test E7

IV. TEST SUMMARY

A sequence of events that describes the results of Test E7 is divided into three time intervals:

1. An approach-to-failure interval characterized by well-defined fuel-pin and coolant heating rates, and by radial and axial temperature profiles that can be calculated with good accuracy. During this time, calculations of the prefailure threshold conditions of fuel temperatures and temperature gradients, the propagation of the fuel meltfront, and the cladding loading can be reliably predicted by a comparison between the calculated and the measured outlet temperature of the coolant. This interval ends with initial cladding rupture and fission-gas release.

2. An interval immediately following the failure threshold and lasting for several hundred milliseconds. During this interval, the flow channel voids, the peak temperatures are reached, and most of the cladding and fuel motions occur. Failures may occur incoherently among fuel pins. The hodoscope is

the only direct source of fuel-motion information. Coolant boiling at the inlet and the absence of flow recovery or correlated activity in the outlet during this interval are interpreted as the period of blockage formation.

3. A postfailure heat-removal and cooling interval that may last for tens of seconds. Flow and pressure data during this interval are too uncertain to provide quantitative information. However, there are indications in the test data that some coolant reentry does occur and leads to minor fuel/debris relocation.

A. Failure Threshold

An analysis of failure thresholds in fresh-fuel experiments¹⁹ (Tests H2 and E4) indicates that cladding overheating leads to boiling near the top of the fuel column. Coolant-film dryout occurs within 10-50 ms, and pin failure is by meltthrough near the top of the fuel column. There does not appear to be a strong dependence on heating rate, cladding strength, or fuel melt fraction. Fuel-coolant interactions (FCI's), although significant, are at least lower by an order of magnitude than is predicted by the parametric FCI model. Results of the present test indicate that the release of fission gas governs the dynamics of both coolant ejection and fuel motion. There was no evidence of explosive gas release in Test E7. Fuel enthalpy at failure, the extent of fuel melting, and the magnitude of the thermal interaction are all less in this test with irradiated fuel than with fresh fuel.

B. Fuel Motion at Failure

Little reliable experimental data useful in modeling the postfailure TOP fuel movement exists. Some out-of-pile experiments,²⁰ as well as the five TOP tests prior to E7, showed that hot or molten fuel and cladding preferentially move upward in the coolant channel. Freezing occurred over a distance of no more than several inches above the tops of the original fuel columns and formed an outlet blockage.

The observed distributions of fuel and steel in the E7 blockages, indicate that molten cladding was swept upward before any significant axial fuel motion occurred. Sodium was ejected from both ends of the flow channel, but at a lesser rate than has been observed in the three loop TOP failure tests with fresh fuel. Pressure-producing thermal interactions in the present test appear to be restricted to liquid films on the holder walls. Fission-gas release, sodium vaporization, and possibly fuel swelling are mechanisms that void the flow channel in this interval.

C. Postfailure Activity

The most significant flow activity occurred during the 200-ms period from 7.45 to 7.65 s, and the most rapid fuel motion was observed during the next 100-ms period. After 7.75 s, radial redistribution of fuel was observed,

but no significant axial motion. After 7.8 s, fuel began to appear in the adiabatic region of the fuel holder. A small but abrupt flow surge at 7.834 s indicated that an FCI did occur, but in a voided flow channel.

Slightly correlated flow oscillation, associated with boiling, at the inlet and outlet between 8 and 9 s, indicated that both blockages were still porous. A lesser correlation was observed for inlet flow oscillation from 10.5 to 12.5 s. The only pressure pulses measured during the test were at the inlet from 10.95 to 10.98 s, and these were less than 0.52 MPa (75 psi). A final "last blurp" occurred between 16.5 and 17 s when the outlet flow ceased and sodium in the outlet region was heated by some 93°C.

V. SIGNAL CONDITIONING

Except for the upper flow data, the signals as recorded on the magnetic tape are corrected only for the calibration factor and for instrument noise. The sequence of operations was as follows:

1. The analog tape was digitized, one channel at a time, with approximately 17 time channels between each millisecond time marker recorded on the tape.
2. Single-channel noise pulses were removed.
3. Digitized data were averaged over 1-ms time intervals.
4. Each datum so averaged was multiplied by the calibration factor to express temperature in °C, flow in cm³/s, and pressure in psi.
5. 60-Hz noise was removed.

A. Analog Data Tapes

Analog test data were recorded on 14-track, 2.54-cm-wide magnetic tape. Two simultaneous recordings were made, one with five of the eight thermocouples, the two flow and pressure signals, the TREAT power and integrated power, and the two transient rod positions. The remaining three thermocouples were recorded on a second tape. All signals were recorded at a tape speed of 152.4 cm/s (60 IPS) and a signal bandwidth of 20 kHz.

B. Data Digitization

Analog signals were digitized by a multiplexed ADC and written on a disk by a PDP-11 computer. The entire timing and command sequence is based on the 1-ms time markers recorded on tape channel 14. Errors due to differences in recording and playback speed and to tape flutter are effectively eliminated. The ADC digitized in time bins of about 50 μ s of real time, but with a variable and generally unknown time between bins. For a playback speed that is the same as the record speed, there are approximately 17 time bins between each pair of millisecond markers.

Data from the disk were written on seven-track 512 BPI tape, transferred to the IBM 370/195, "conditioned," and stored as archival files on nine-track 6250 BPI tapes. "Conditioning" included averaging the time bins between millisecond time markers, and multiplying by a constant that converts digital numbers to voltages and the voltages to practical units. The first conversion constant is determined by the dc calibrating voltages recorded on the tape just before the test transient. The second conversion constant is discussed in Sec. V.D. Removal of noise signals from the flow data is discussed in Sec. C below. The special case of the upper-flowmeter calibration is discussed in Sec. V.E.

C. Noise

Two types of noise signals exist on every data channel: a random or Gaussian noise and an instrument noise. Instrument noise consists of transient pulses in the recordings and periodic sine waves superimposed on the test signal. Transient pulses in the 50- μ s digitized data are treated as statistical "outliers" and are simply removed with no further analysis. They may be due to electrical transients in the power line or microscopic imperfections in the recording tape.

Instrument noise is primarily 60-Hz pickup and is especially predominant on the flow-detector signals. An unbiased estimate of the phase and amplitude of the 60-Hz signal was determined from a least-squares fit to a sine and cosine function of 60 Hz that was superimposed on a linear regression. Least-squares coefficients were determined during the period of "steady-state" flow from 5 to 7 s, and the resulting 60-Hz phase and amplitude was then removed from the data over the entire time span of 0-25 s.

D. Instrument Calibration Factors

Methods and/or measurements used to establish the relation between signal-voltage level and temperature, as well as between flow and pressure, are given in this section.

1. Temperature

All temperatures were measured relative to a 65.5°C (150°F) reference junction. A cubic equation of the form

$$T (^{\circ}\text{C}) = 65.55964 + 25.23399X - 0.09096279X^2 + 0.00166278X^3$$

was used to convert the detector signal X, in millivolts, to temperature, in $^{\circ}\text{C}$. Failure by sheath melting was expected at about 1400°C. Some out-of-pile measurements showed that failure by sheath meltthrough could be identified by an abrupt negative signal preceded by little or no increase above ambient response. The response of TC2 and TC3 in Test E7 suggests both of them failed by sheath meltthrough.

After assembly of the test train, but before fuel was loaded, each thermocouple was tested by touching a hot soldering iron to the junction and monitoring the output voltage of the corresponding terminals of the plug at the closure flange. This testing procedure verified the identification of each thermocouple relative to its pin numbers in the connecting plug, as well as the electrical isolation of each of the junctions. Nevertheless, the test data indicate a potential cross-connection between one of the inlet (TC2) and one of the outlet (TC3) thermocouples. A similar cross-connection between TC2 and TC3 has been suspected in other TOP and loss-of-flow experiments. In all these tests, the same pin numbers and loop-control-console terminals were used for these two thermocouples.

2. Calibration of Lower Flow Detector

Flow detectors were calibrated by an orifice installed in place of the fuel cluster in the test section. Inlet and outlet flow signals were measured as a function of upstream-downstream pressure drop across the orifice for different settings of the ALIP. Volumetric flow was then calculated from the standard orifice equations. The orifice discharge coefficient had previously been determined from absolute measurement for water flow.

Calibration by the orifice method gives the flow in terms of the pressure drop Δp as

$$Q \text{ (cm/s)} = K \frac{\beta^2}{(1 - \beta^2)\sqrt{1 + \beta^2}} C \sqrt{\frac{\Delta p}{\rho}},$$

where

β = ratio of orifice to pipe diameters,

ρ = $0.927 - 0.00238(^{\circ}\text{C} - 100)$ is the sodium density in g/cm^3 ,

C = 0.585 is the orifice discharge coefficient for a 12.1-mm orifice and sodium at 382°C ,

and

K = 1058 is a constant to convert head loss to psi, density to g/cm^3 , and flow to cm^3/s .

The measured slope of the flow signal versus the square root of the pressure drop for a 12.1-mm orifice in the E7 loop was $0.700 \text{ mV}/\sqrt{\text{psi}}$ ($266 \text{ mV}/\sqrt{\text{kPa}}$), and the calibration of the lower flow detector was

$$Q \text{ (cm}^3/\text{s)} = 501 \frac{E \text{ (mV)}}{\sqrt{\rho \text{ (g/cm}^3)}}.$$

3. Pressure Transducers

Fuel-failure tests of the type performed in the Mark-II loop have the potential for creating pressures and temperatures corresponding to the critical point of sodium. Although these conditions have not been realized in past tests, the pressure transducers are part of the primary containment and must meet the design-containment capability of the loop [5000 psi (34 MPa) at 530°C]. Statham Type PG732TC unbonded strain-bridge transducers with a full-scale range of 2500 psi (17 MPa) meet these requirements and were used on the E7 loop. Calibration in air by the manufacturer gave conversion factors of $6.715 \mu\text{V/psi}$ ($46.298 \mu\text{V/kPa}$) and $7.375 \mu\text{V/psi}$ ($50.849 \mu\text{V/kPa}$) for the upper and lower transducers, respectively. Calibration on the loop with sodium at 382°C gave a sensitivity of $7.410 \mu\text{V/psi}$ ($51.090 \mu\text{V/kPa}$).

Although the pressure transducers showed a definite response to TREAT power and integrated power, no attempt was made to correct for this response. As a consequence, the pressure data are limited to event timing and to verifying the magnitude of an impulse calculated from sodium-ejection velocities and accelerations.

In a previous analysis of Test E7, it was reported that no pulses were found in either the upper or lower pressure signals. Recent improvements in the techniques developed for analyzing test data now indicate small pressure pulses at 10.95 s.

4. Calibration of Upper Flow Detector

Test E7 contained a "magnetic amplifier" installed on the test train near the outlet-flow detector. The amplifier consisted of a 25-mm-long (3.8 mm thick) ARMCO iron shell fit between the flow tube and the loop wall. Slots were milled axially through the outer surface of the shell to allow passage of the thermocouples to the test section. Three nonmagnetic Type 304 stainless steel baffles above and below the iron shell prevented bypass flow. Direct contact of the ARMCO iron with the flow tube allowed the iron to heat according to the outlet sodium temperature to produce an undesired temperature-dependent flow-detector calibration factor.

After the loaded test train was inserted in the loop at HFEF, the ratio of lower- to upper-flow detector signals during steady-state flow was 3.82. A ratio of 2.94 was measured during the calibrations at ANL/East with a 12.1-mm orifice in place of the fuel bundle. However, the same ratio measured in TREAT just before the test transient was 2.29. Furthermore, during the steady-state flow conditions of the preheat period, the upper flow showed an almost linear rise in output while the lower flow remained constant. During the 2-s preheat period, a 21°C linear temperature rise was measured in the outlet flow. During this same period, the outlet-flow signal increased by 30%. This temperature dependence accounts for the differences between the inlet-outlet signal ratios measured at HFEF (sodium and magnetic amplifier at 204°C) and at TREAT (temperature of 382°C). Further verification of a temperature dependence was demonstrated by the cross-correlation between outlet flow and outlet temperature. The correlation function, shown in Fig. 11, shows a very strong correlation at lag times greater than 35 ms, the characteristic response time of the outlet thermocouple.

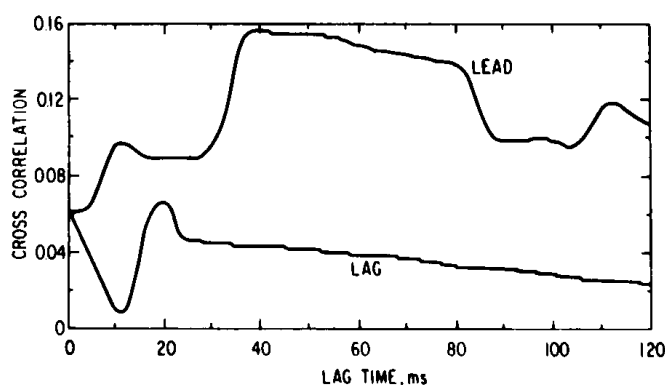


Fig. 11

Cross-correlation between Outlet-flow Signal and Outlet Temperature

Based on these observations, the outlet mass flow was set equal to the inlet mass flow from zero time to the end of the preheat period at 7 s. (Mass flows were used to properly account for sodium expansion during heating.) The measured outlet-flow data beyond 7 s were adjusted downward to match the steady-state flow before 7 s. No further temperature corrections were applied after 7 s. A tabular listing of the measured and corrected outlet flows is given in Table V. Included in the table are the inlet-flow data as well as the inlet and outlet temperatures.

VI. TEST DATA

Previous analysis of the test data was limited to times earlier than 8.2 s. For this report, test data were examined to 100 s. Little of significance was observed after 25 s. General features of the data are shown graphically in Figs. 12-19 and are tabulated in Appendix A. Two events are apparent from the inlet flow (see Fig. 13): the main failure at 7.5 s and a second event between 10 and 12 s. Both inlet thermocouples (see Fig. 16) and TC3 at the outlet (see Fig. 17) burned out during the initial failure sequence. A possible event, seen in Fig. 17 at 17 s, is interpreted as resulting from ejection of hot material toward the outlet of the flow channel. The initial slug ejection is observed in the response of TC8 (see Fig. 19), located above the sodium-free surface. The pressure transducers (see Fig. 15) showed a sensitivity to both reactor power and energy. Both transducers started and ultimately ended at 5 psig (0.034 MPa, gauge), the values expected at operating temperature. Reactor scram was at 8.7 s and shutdown at 9.5 s.

A. TREAT Transient

Irradiation of Test E7 in the TREAT reactor consisted of a 2.4-s preheat irradiation at 142 MW followed by a computer-controlled power ramp with a period of a 180 ms to a peak power of 2468 MW reached at 7.58 s. The transient was terminated by the prompt negative temperature coefficient of TREAT. Power into the fuel pins during the preheat period varied from 6.2 kW/m in the hottest edge pin to 4.6 kW/m in the central pin. Details of the power shape and energy are shown in Fig. 20.

TREAT Rod 2 was programmed to bring the reactor to the preheat level at 3.0 s. Rod 2 maintained constant power to 7 s. Rod 1 was then withdrawn to provide the specified 180-ms ramp until it was fully withdrawn. After 7.67 s, both rods remained in their least reactive state and the power fell off according to the negative temperature coefficient of reactivity. "Scram" was accomplished by driving the reactor control rods to their most (negative) reactive state at 8.59 s. Rod motions are shown in Figs. 21 and 22.

TABLE V. Corrected and Uncorrected Flow Data

TIME	TC1	LF	TC4	UP OLD	UP CORR	TIME	TC1	LF	TC4	UP OLD	UP CORR
SEC	DEGC	CC/SEC	DEGC	CC/SEC	CC/SEC	SEC	DEGC	CC/SEC	DEGC	CC/SEC	CC/SEC
0.225	390.	577.	389.	614.	577.	3.975	390.	576.	387.	613.	575.
0.275	391.	580.	389.	612.	580.	4.025	391.	579.	397.	616.	579.
0.325	391.	580.	388.	616.	579.	4.075	392.	579.	387.	619.	578.
0.375	390.	578.	388.	620.	578.	4.125	392.	579.	387.	611.	578.
0.425	390.	578.	388.	621.	578.	4.175	390.	578.	388.	607.	578.
0.475	391.	579.	388.	618.	579.	4.225	390.	577.	387.	620.	577.
0.525	391.	580.	388.	617.	579.	4.275	391.	582.	387.	612.	581.
0.575	390.	578.	388.	616.	577.	4.325	392.	580.	387.	607.	579.
0.625	390.	578.	387.	618.	577.	4.375	390.	575.	387.	614.	575.
0.675	391.	580.	387.	617.	580.	4.425	391.	578.	386.	614.	577.
0.725	391.	582.	387.	619.	581.	4.475	391.	580.	386.	617.	579.
0.775	390.	579.	386.	620.	579.	4.525	391.	580.	386.	609.	579.
0.825	390.	579.	386.	619.	578.	4.575	391.	576.	386.	619.	575.
0.875	391.	581.	386.	616.	580.	4.625	391.	578.	386.	623.	577.
0.925	391.	579.	386.	618.	578.	4.675	392.	581.	386.	615.	580.
0.975	390.	579.	386.	619.	578.	4.725	392.	580.	387.	597.	579.
1.025	390.	577.	385.	616.	576.	4.775	391.	579.	387.	610.	579.
1.075	391.	580.	386.	618.	580.	4.825	391.	578.	386.	612.	577.
1.125	391.	579.	385.	618.	578.	4.875	392.	581.	387.	632.	580.
1.175	390.	579.	385.	619.	578.	4.925	392.	578.	388.	638.	579.
1.225	390.	580.	384.	618.	579.	4.975	392.	578.	388.	633.	577.
1.275	391.	582.	384.	619.	581.	5.025	392.	580.	388.	621.	579.
1.325	391.	581.	384.	619.	580.	5.075	393.	581.	388.	638.	581.
1.375	390.	579.	384.	618.	578.	5.125	393.	582.	389.	645.	581.
1.425	390.	579.	384.	617.	578.	5.175	392.	578.	390.	639.	577.
1.475	391.	581.	383.	618.	580.	5.225	393.	580.	390.	658.	579.
1.525	391.	580.	384.	617.	578.	5.275	393.	582.	391.	669.	582.
1.575	390.	577.	384.	615.	576.	5.325	393.	580.	392.	667.	580.
1.625	390.	579.	384.	616.	578.	5.375	392.	578.	394.	679.	579.
1.675	392.	582.	384.	621.	581.	5.425	393.	579.	396.	689.	580.
1.725	391.	578.	384.	621.	577.	5.475	394.	581.	397.	708.	581.
1.775	390.	578.	384.	619.	577.	5.525	394.	581.	400.	717.	582.
1.825	390.	579.	384.	621.	578.	5.575	393.	579.	403.	714.	581.
1.875	391.	582.	384.	620.	581.	5.625	394.	580.	404.	731.	582.
1.925	391.	580.	384.	625.	579.	5.675	395.	580.	406.	732.	582.
1.975	390.	579.	384.	619.	578.	5.725	395.	579.	407.	749.	581.
2.025	390.	580.	384.	616.	579.	5.775	394.	577.	410.	758.	580.
2.075	391.	582.	384.	616.	581.	5.825	394.	580.	412.	760.	582.
2.125	391.	580.	385.	617.	579.	5.875	396.	581.	414.	766.	584.
2.175	390.	579.	385.	618.	578.	5.925	395.	580.	417.	774.	584.
2.225	390.	578.	385.	616.	577.	5.975	395.	577.	419.	780.	581.
2.275	391.	580.	385.	619.	579.	6.025	395.	578.	422.	791.	583.
2.325	391.	580.	385.	618.	579.	6.075	396.	580.	424.	790.	585.
2.375	390.	578.	386.	617.	577.	6.125	396.	580.	426.	791.	585.
2.425	390.	579.	386.	616.	578.	6.175	395.	577.	428.	803.	582.
2.475	391.	582.	386.	620.	581.	6.225	396.	578.	430.	816.	583.
2.525	391.	580.	387.	618.	579.	6.275	397.	580.	432.	805.	586.
2.575	390.	578.	387.	614.	578.	6.325	396.	580.	434.	817.	586.
2.625	390.	579.	387.	617.	578.	6.375	396.	579.	437.	817.	585.
2.675	391.	579.	387.	620.	579.	6.425	396.	576.	438.	827.	583.
2.725	391.	579.	387.	616.	578.	6.475	397.	579.	440.	836.	586.
2.775	390.	577.	388.	620.	577.	6.525	398.	579.	440.	827.	586.
2.825	390.	579.	388.	619.	578.	6.575	397.	577.	441.	831.	585.
2.875	391.	581.	388.	620.	580.	6.625	398.	577.	444.	837.	585.
2.925	391.	581.	388.	616.	580.	6.675	399.	579.	446.	849.	587.
2.975	390.	579.	389.	615.	579.	6.725	399.	580.	447.	852.	587.
3.025	391.	578.	389.	616.	578.	6.775	398.	576.	449.	842.	584.
3.075	392.	581.	389.	620.	581.	6.825	399.	576.	450.	850.	585.
3.125	391.	582.	389.	616.	581.	6.875	400.	577.	452.	852.	586.
3.175	390.	580.	388.	609.	580.	6.925	400.	578.	454.	856.	586.
3.225	390.	578.	388.	612.	577.	6.975	399.	576.	455.	857.	585.
3.275	391.	582.	389.	619.	581.	7.025	400.	577.	457.	848.	586.
3.325	391.	580.	388.	615.	579.	7.075	401.	578.	458.	847.	587.
3.375	390.	578.	389.	615.	578.	7.125	401.	574.	459.	861.	584.
3.425	391.	577.	388.	616.	577.	7.175	401.	572.	462.	863.	582.
3.475	392.	581.	388.	616.	580.	7.225	402.	573.	463.	872.	583.
3.525	391.	579.	388.	615.	578.	7.275	403.	573.	465.	876.	583.
3.575	391.	577.	388.	616.	576.	7.325	404.	573.	467.	877.	584.
3.625	390.	578.	388.	618.	578.	7.375	403.	570.	467.	907.	604.
3.675	391.	581.	388.	620.	580.	7.425	406.	561.	469.	933.	621.
3.725	392.	579.	388.	620.	579.	7.475	407.	538.	470.	987.	657.
3.775	390.	578.	388.	615.	578.	7.525	408.	452.	473.	1078.	717.
3.825	391.	577.	388.	616.	577.	7.575	409.	93.	475.	1481.	986.
3.875	391.	580.	388.	622.	580.	7.625	418.	-472.	481.	851.	566.
3.925	391.	581.	388.	609.	580.	7.675	475.	-388.	486.	323.	215.

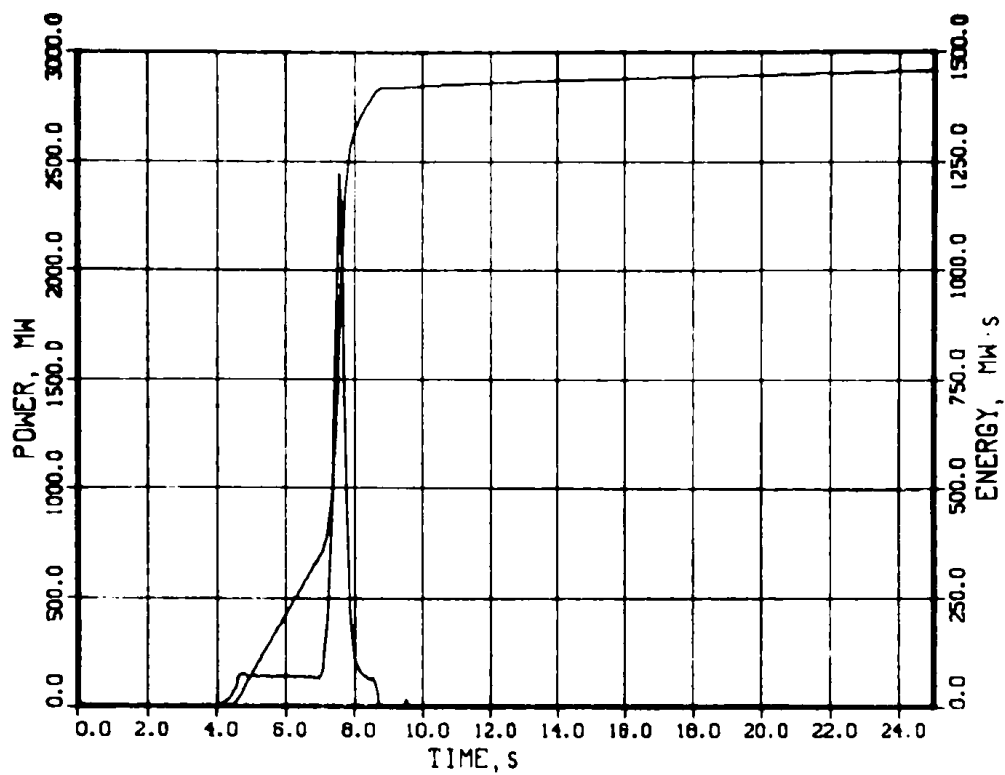


Fig. 12. Power and Integrated-power Traces

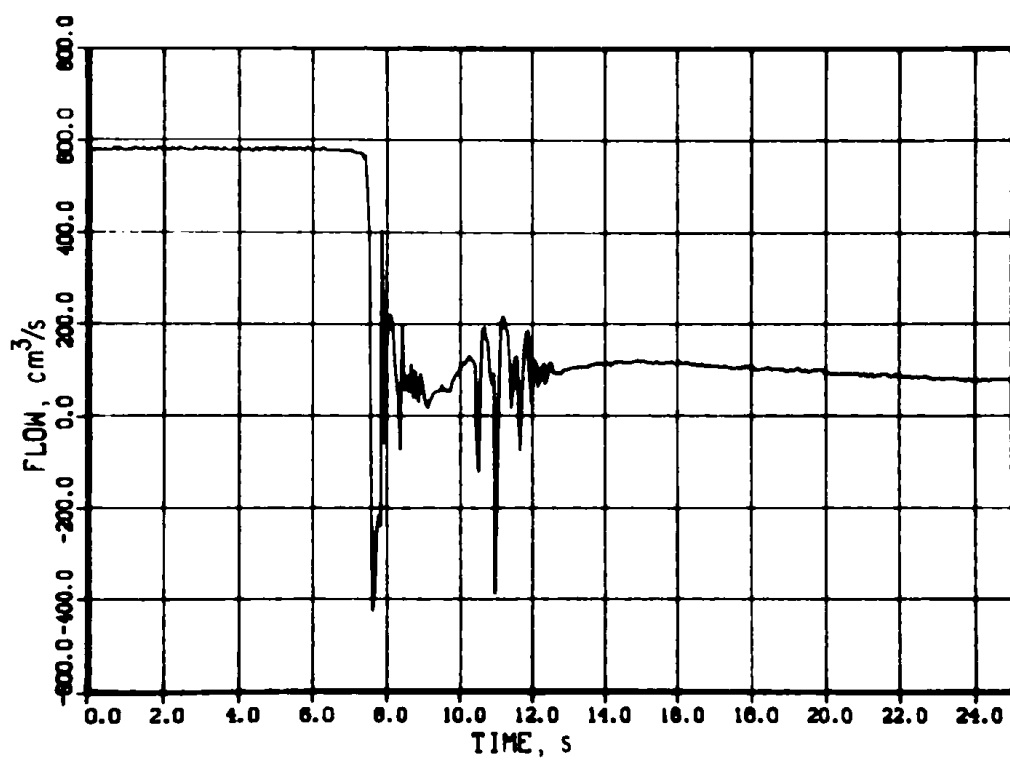


Fig. 13. Lower-flow Data

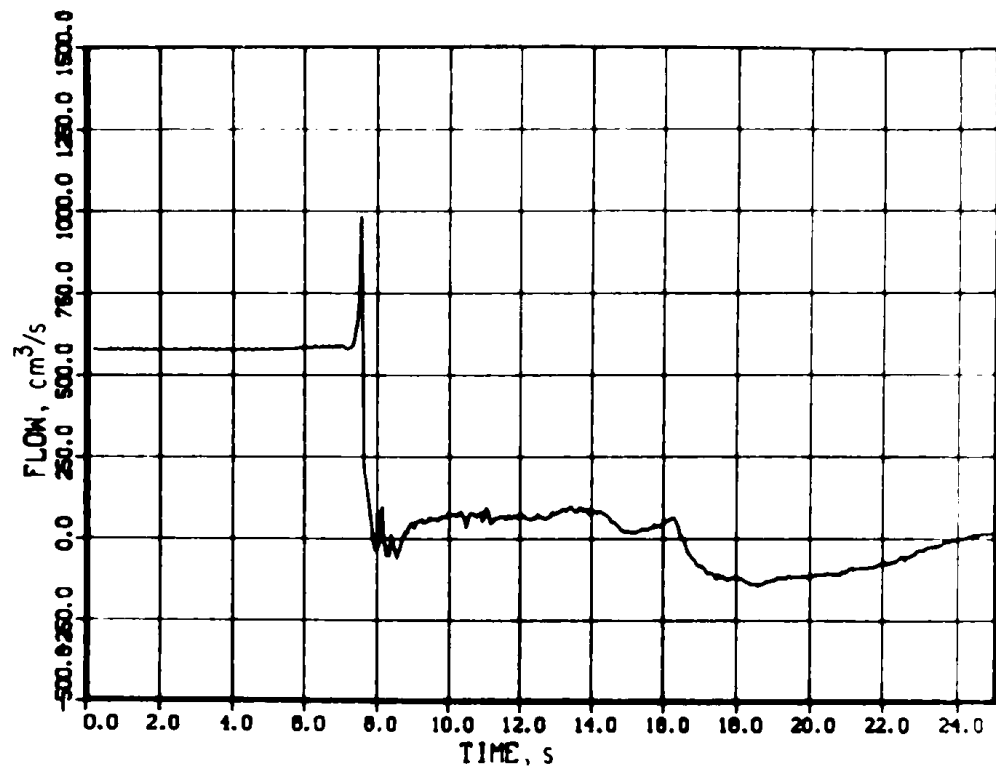


Fig. 14. Upper-flow Data

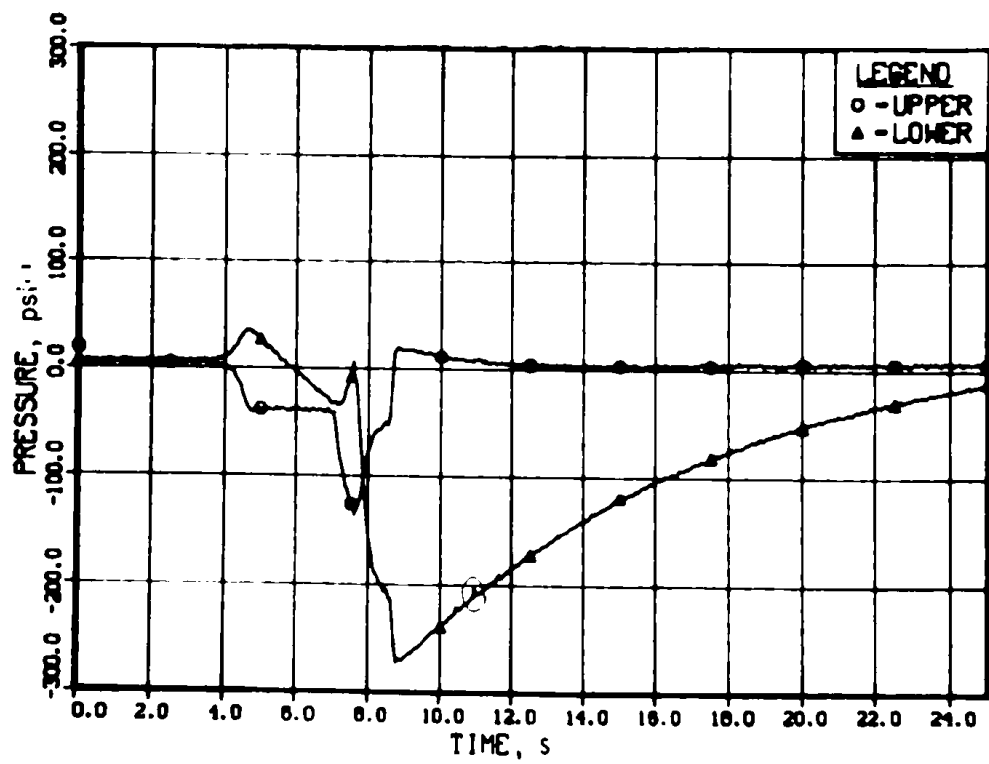


Fig. 15. Pressure-transducer Response. Conversion factor: 1 psi = 6.895 kPa.

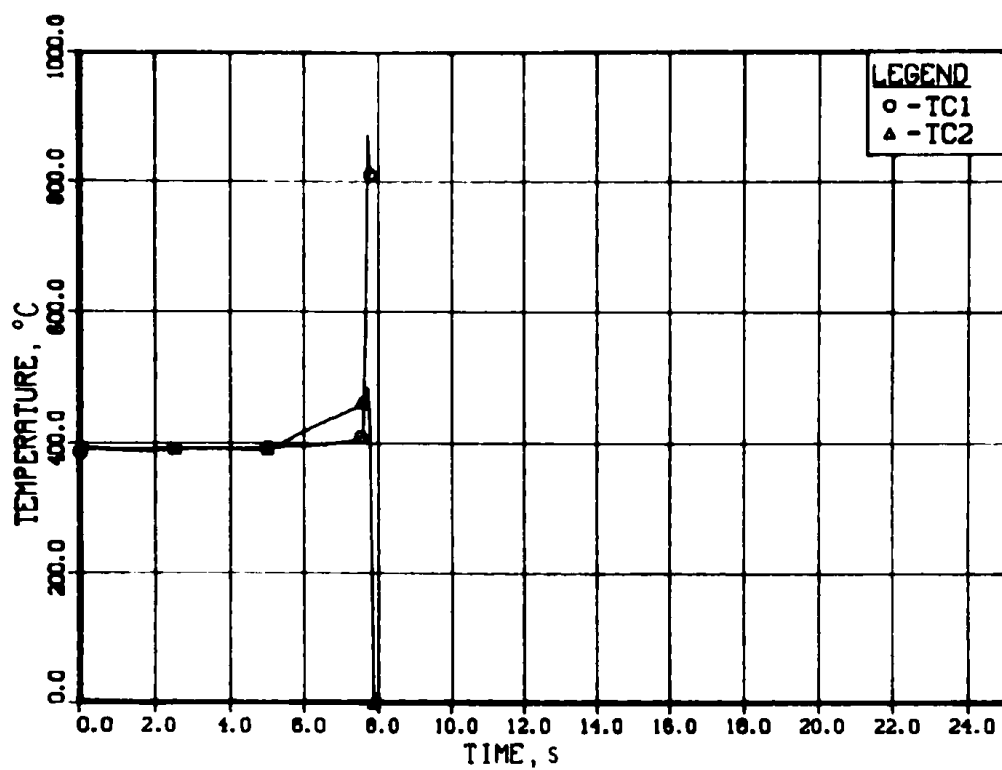


Fig. 16. Inlet Temperatures

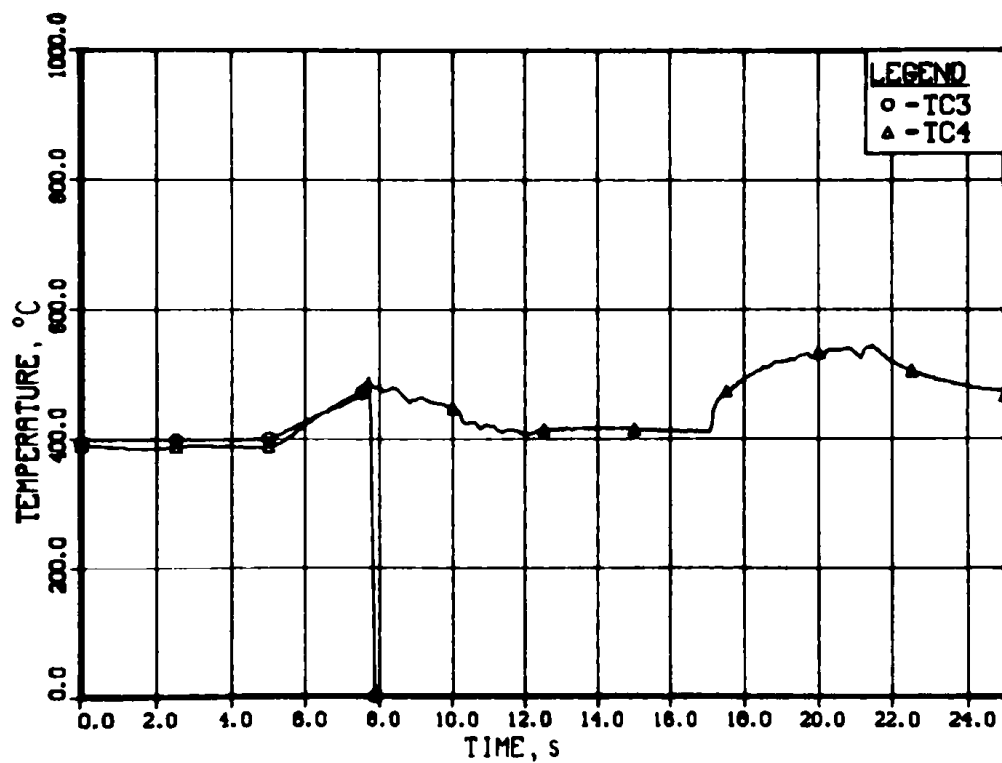


Fig. 17. Outlet Temperatures

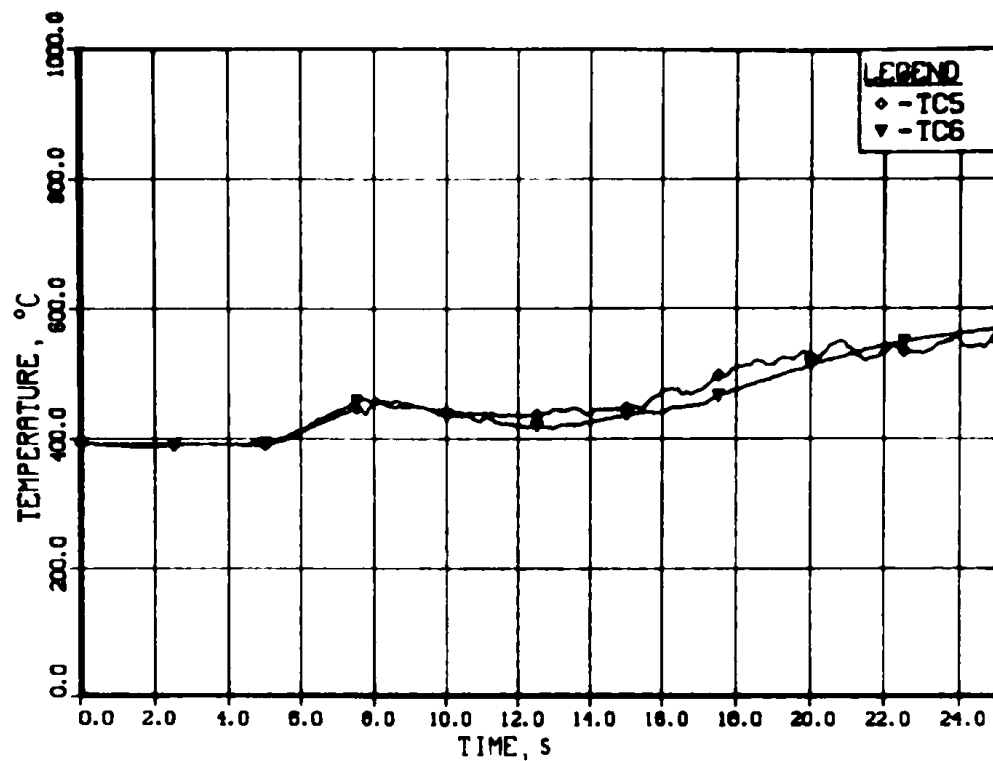


Fig. 18. Sodium Temperatures at Pump Return

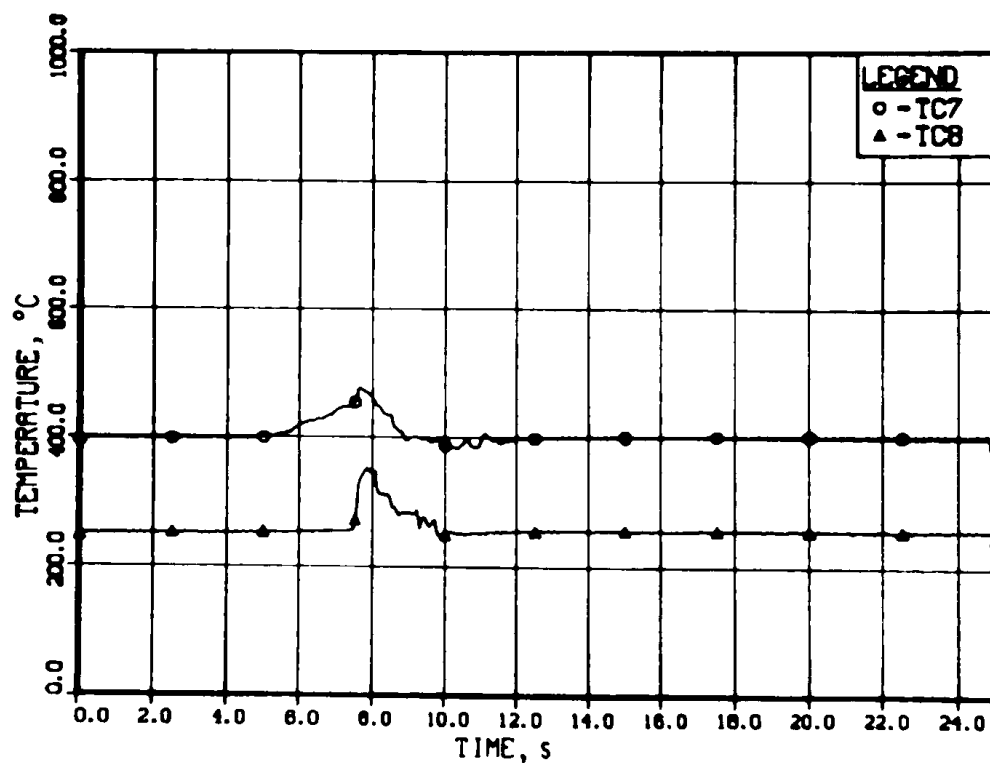


Fig. 19. Temperatures above and below Sodium-free Surface

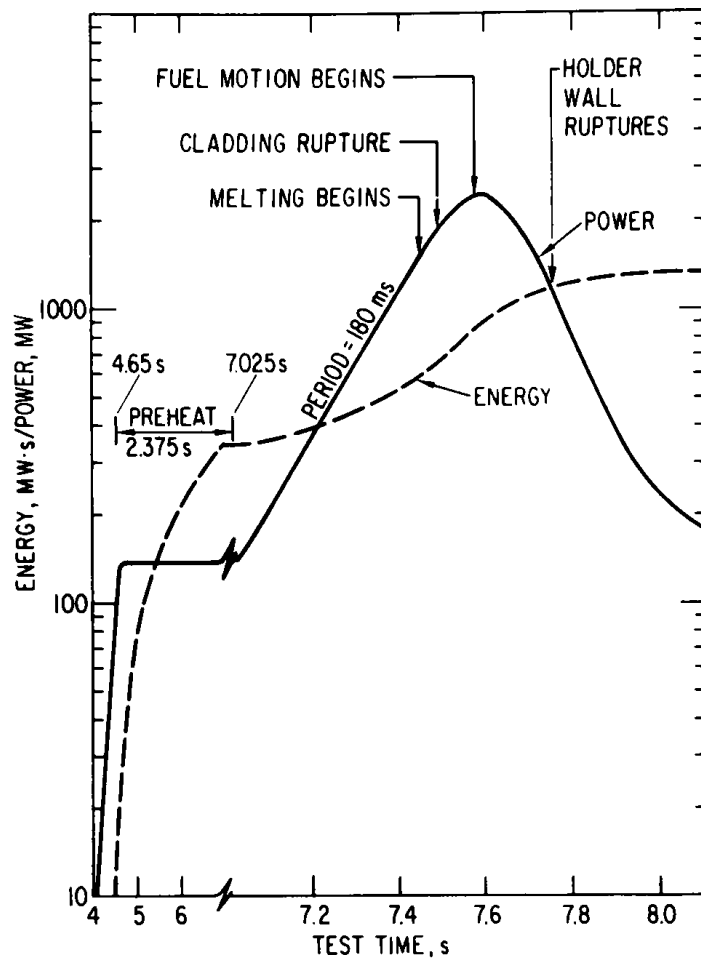


Fig. 20
TREAT Power and Energy

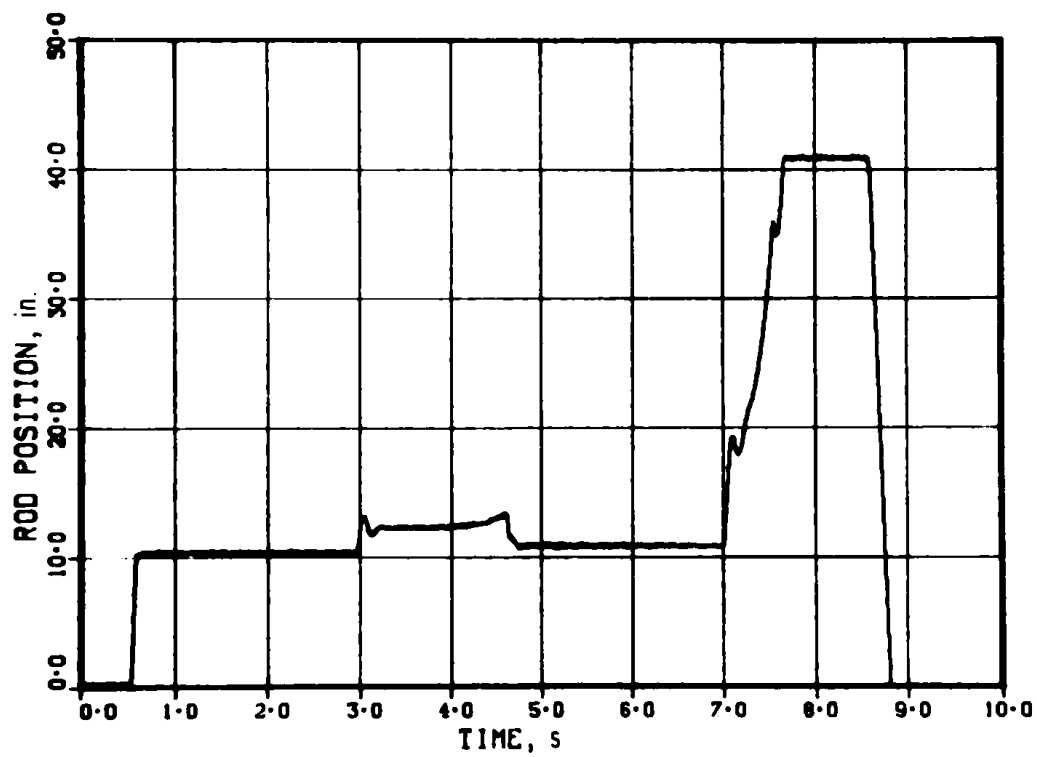


Fig. 21. Motion of TREAT Rod 1. Conversion factor: 1 in. = 2.54 cm.

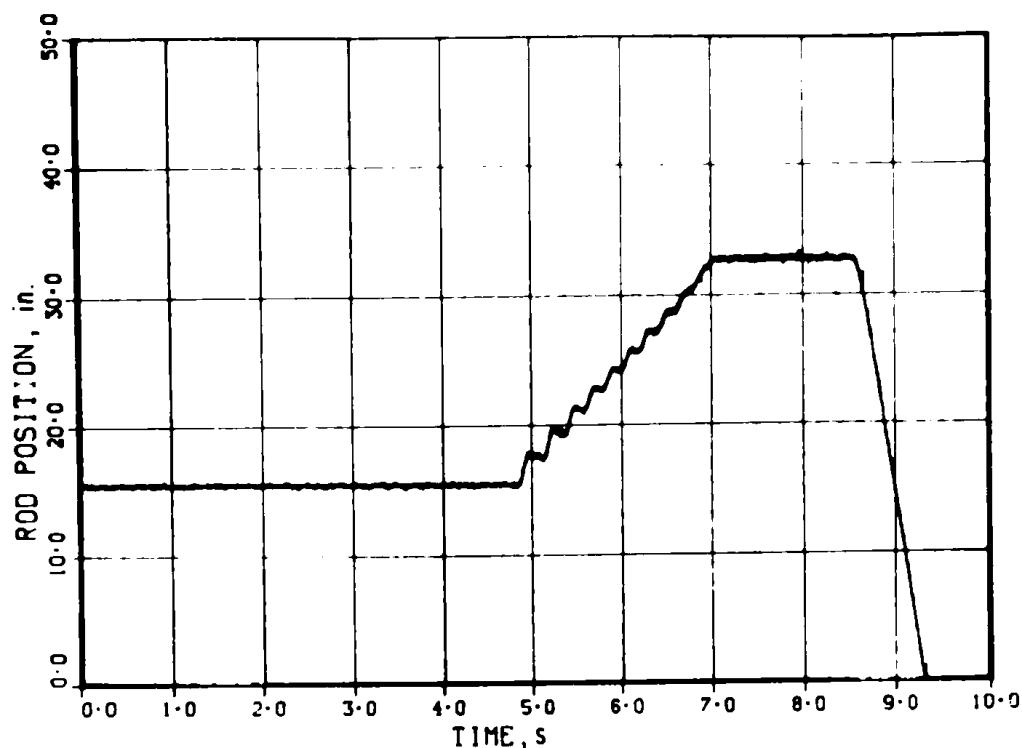


Fig. 22. Motion of TREAT Rod 2. Conversion factor: 1 in. = 2.54 cm.

B. Temperature Data

One of the two inlet thermocouples (TC1) showed a rise in inlet temperatures from its 390°C initial value to 1050°C at failure during the 200 ms after 7.6 s. The response, shown in Fig. 23, is characteristic of failure by

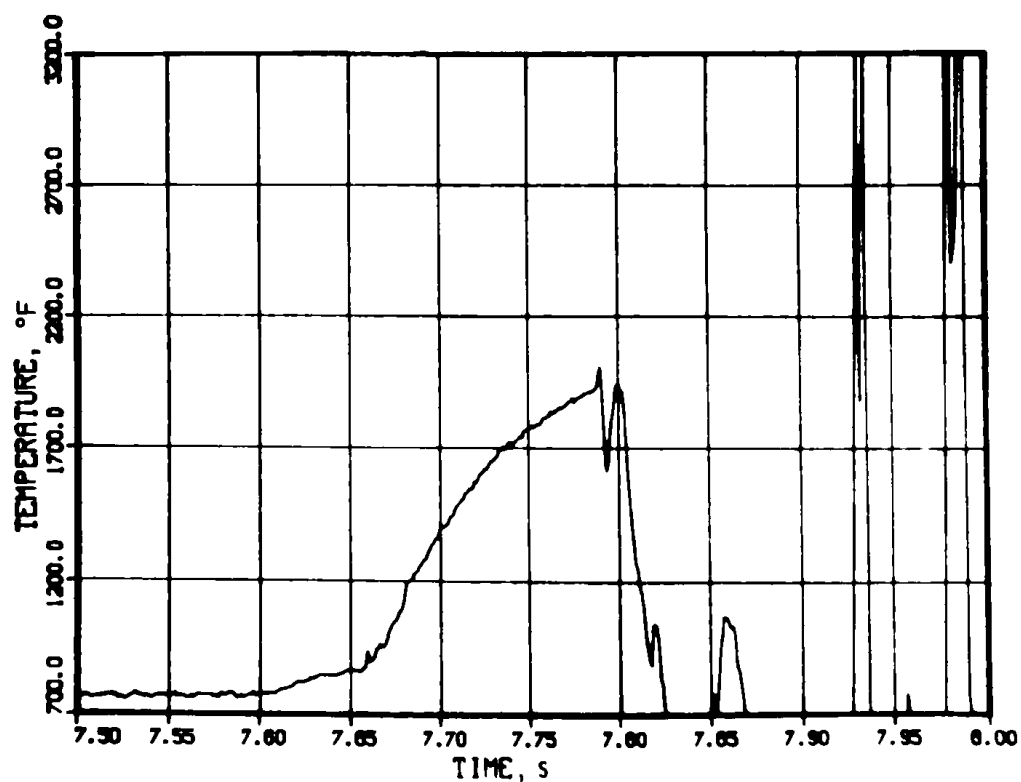


Fig. 23. Response of Inlet Thermocouple TC1 during Failure Sequence.
Conversion factor: $t (^{\circ}\text{C}) = [t (^{\circ}\text{F}) - 32]/1.8$.

meltthrough at the junction. Based on out-of-pile measurements, the rate of apparent temperature rise from 7.66 to 7.77 s suggests the failure was due to relatively hot material (2000°C) deposited on the junction. The estimated time of deposit is 7.66 s.

The second inlet thermocouple (TC2; see Fig. 24) showed a nearly identical response to the two outlet thermocouples (TC3, see Fig. 25; and TC4, see Fig. 26). Throughout the transient, TC3 was always 10°C hotter than TC2; neither reached the 1000-1100°C range expected for failure by meltthrough. Comparisons to out-of-pile measurements suggest that the response of TC2 is characteristic of meltthrough of the sheath. (Out-of-pile measurements do not show any measurable change in apparent temperature until the time of sheath meltthrough, whereas meltthrough at the junction is characterized by an increase in signal up to the time of failure.)

The test data suggests that TC3 and TC4 correctly monitored the outlet temperatures, but, due to some unknown causes, TC2 was cross-coupled to TC3. Thus, TC2 and TC3 would give essentially identical responses to TC4 up to failure by sheath meltthrough. The estimated time of sheath failure is 7.77 s. Failure of the sheath is accompanied or preceded by rupture of the fluted tube. (This is 65 ms earlier than estimated from the flow and hodoscope data.) Both inlet thermocouples passed through the holder wall space, but on opposite sides.

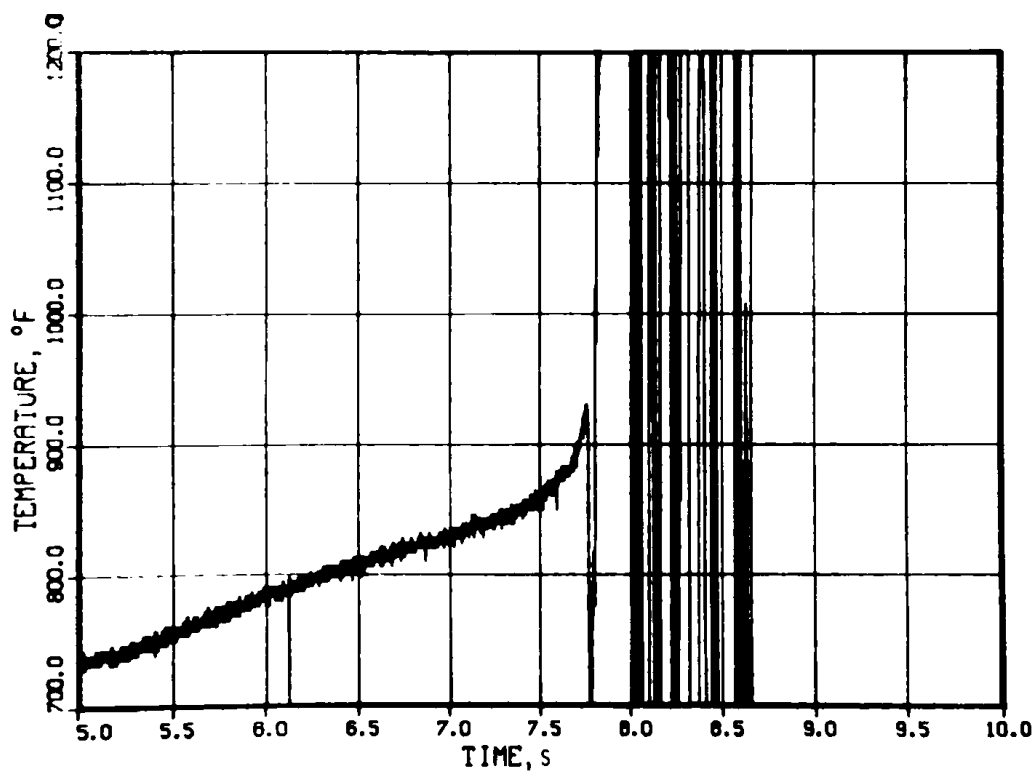


Fig. 24. Response of Inlet Thermocouple TC2 during Failure Sequence.

Conversion factor: $t (^{\circ}\text{C}) = [t (^{\circ}\text{F}) - 32]/1.8$.

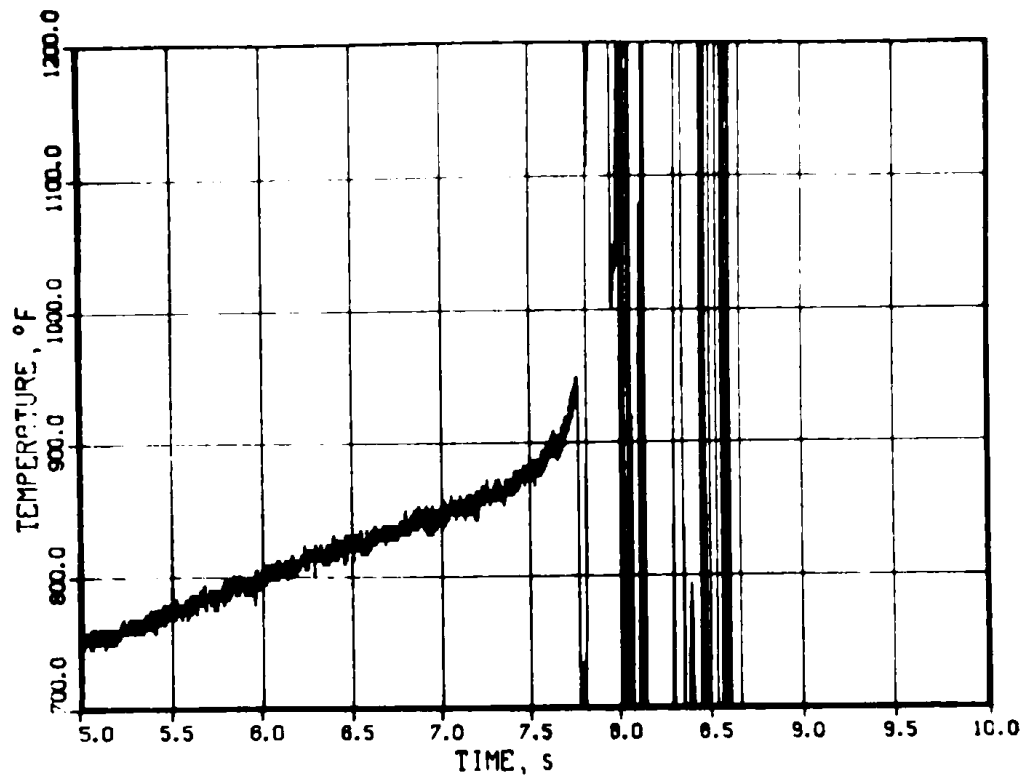


Fig. 25. Response of Outlet Thermocouple TC3 during Failure Sequence.
Conversion factor: $t (^{\circ}\text{C}) = [t (^{\circ}\text{F}) - 32]/1.8$.

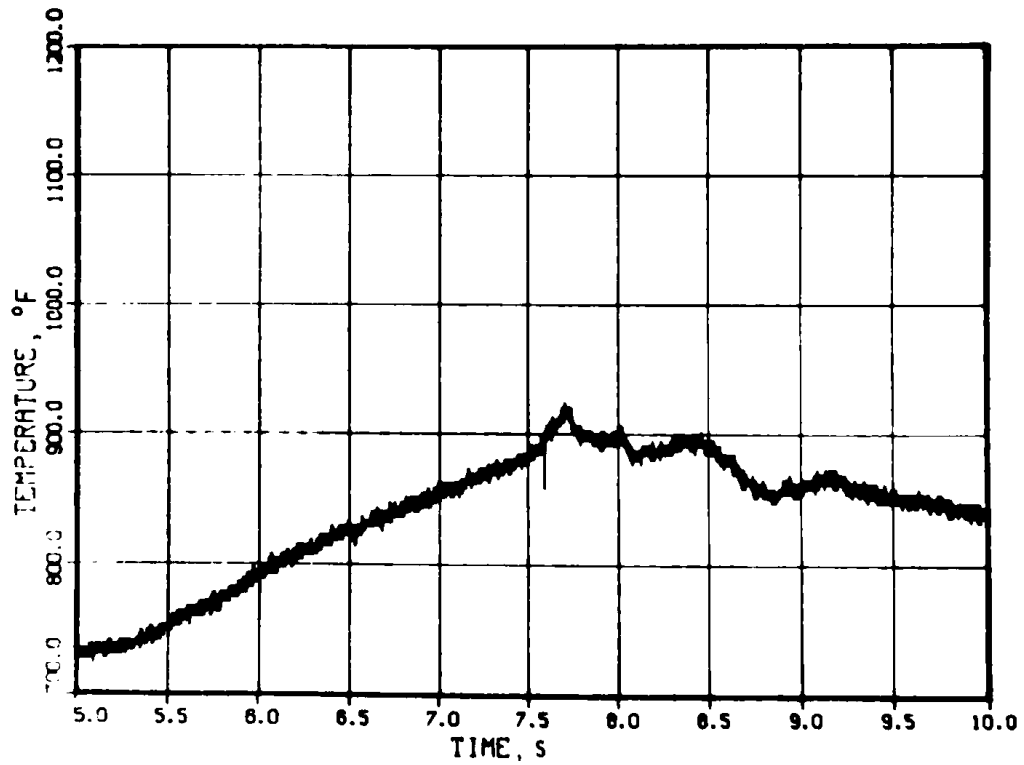


Fig. 26. Response of Outlet Thermocouple TC4 during Failure Sequence.
Conversion factor: $t (^{\circ}\text{C}) = [t (^{\circ}\text{F}) - 32]/1.8$.

Regions of interest for the remaining thermocouples are shown in Figs. 27-32. The following is noted from these temperature data:

1. Thermocouple TC5, at the pump return, showed the passage of a cold slug between 7.6 and 7.8 s. This corresponds to the time of reverse inlet flow. The cold slug represents liquid in the pump and inlet region at the beginning of reverse flow.
2. A larger response to the event at 10.95 s was observed on TC7 (above the first baffle) than from the outlet (TC4) or the pump return (TC5 and TC6).
3. The rapid cooling of TC7 after 7.7 s resulted from the effective mixing of the initially ejected slug (7.5-7.6 s, from Fig. 32) with upper-plenum sodium.
4. The ejected slug dynamics (see Fig. 32) may consist of a series of simple slug ejections at 7.5, 8.0, 9.2, and 9.7 s, and returns at 7.8, 8.1, 8.5, 9.3, 9.5, and 9.8 s. (Ejection corresponds to increase in temperature with respect to time; returns correspond to a drop in temperature.) Similar response was not observed on any other thermocouple.
5. A heat source appeared to approach the outlet at 17 s (see Fig. 17). The source is small and did not pass completely through the outlet region, since there was no apparent heating of either the upper sodium head (TC7) or the pump return (TC5) at this time.

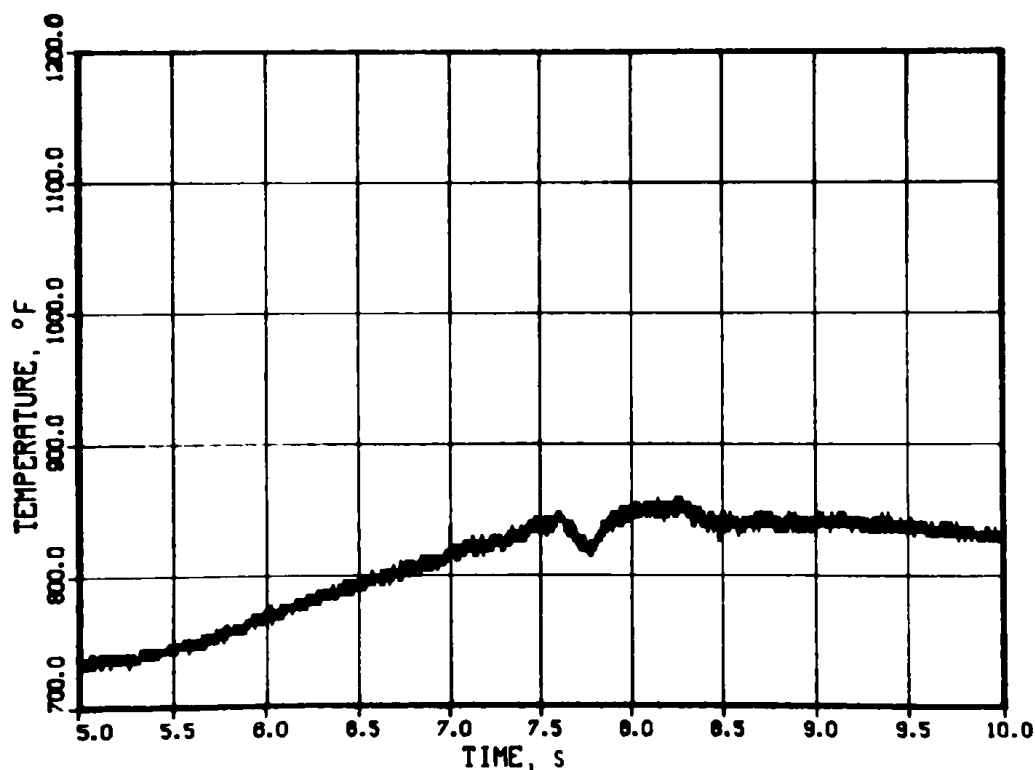


Fig. 27. Temperature at Pump Return (TC5). Conversion factor: $t (^{\circ}\text{C}) = [t (^{\circ}\text{F}) - 32]/1.8$.

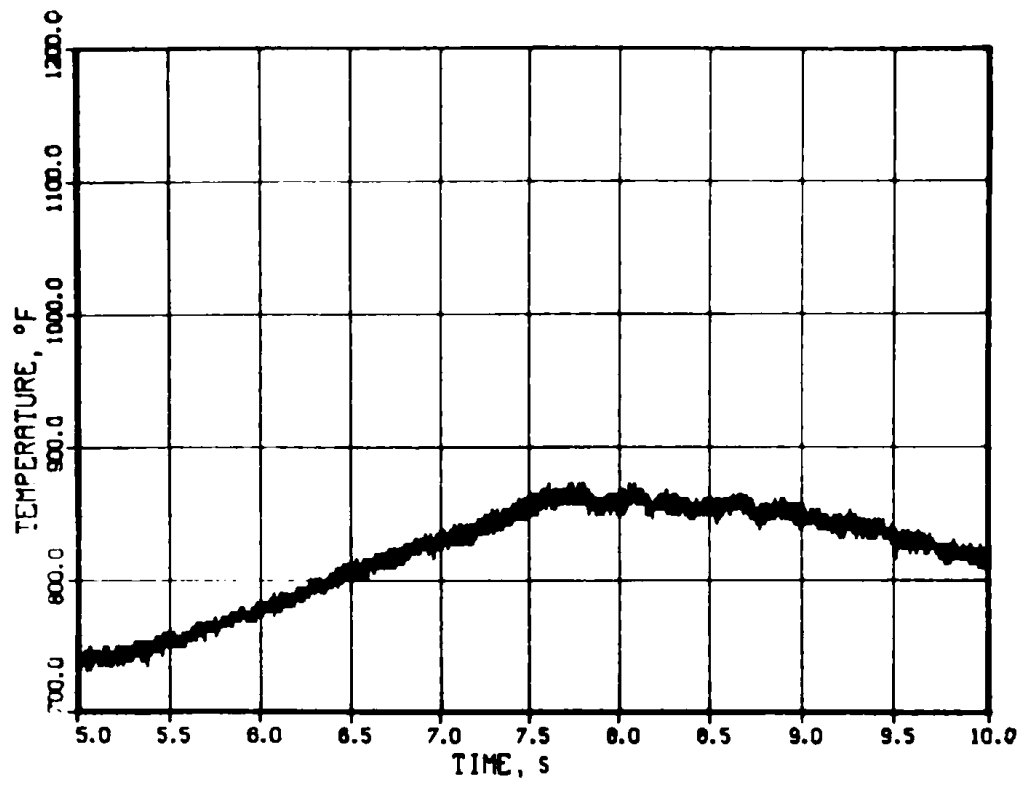


Fig. 28. Temperature of Downflow from Flow Channel (TC6) to 10 s. Conversion factor: $t (^{\circ}\text{C}) = [t (^{\circ}\text{F}) - 32]/1.8$.

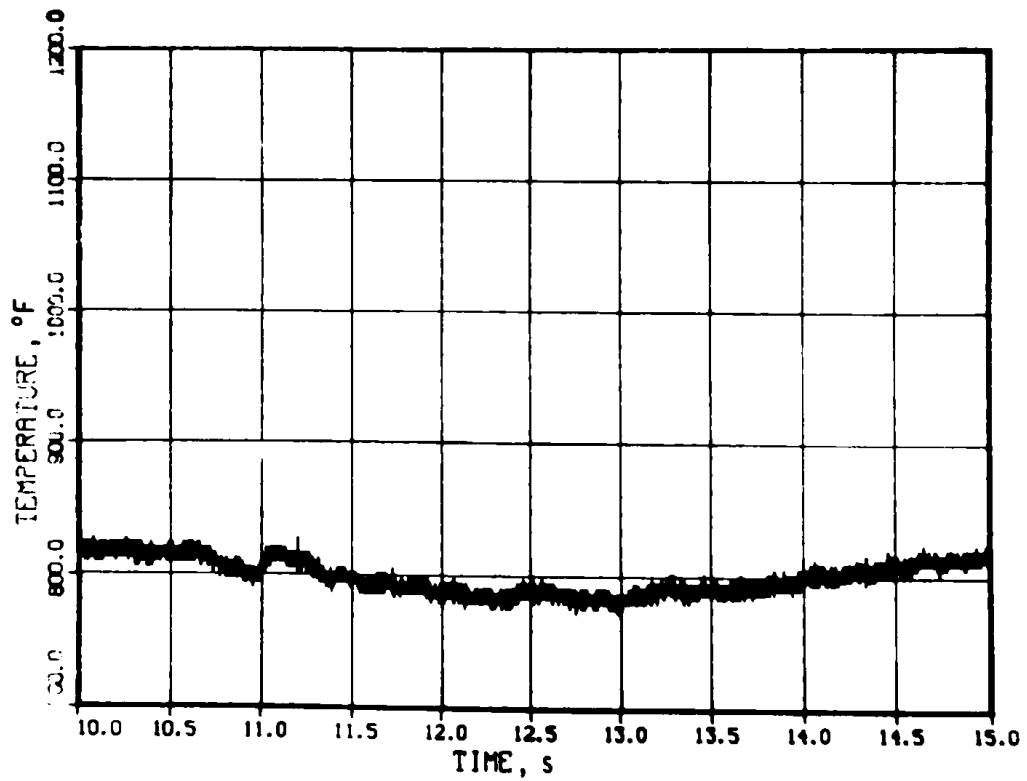


Fig. 29. Temperature of Downflow (TC6) to 15 s. Conversion factor: $t (^{\circ}\text{C}) = [t (^{\circ}\text{F}) - 32]/1.8$.

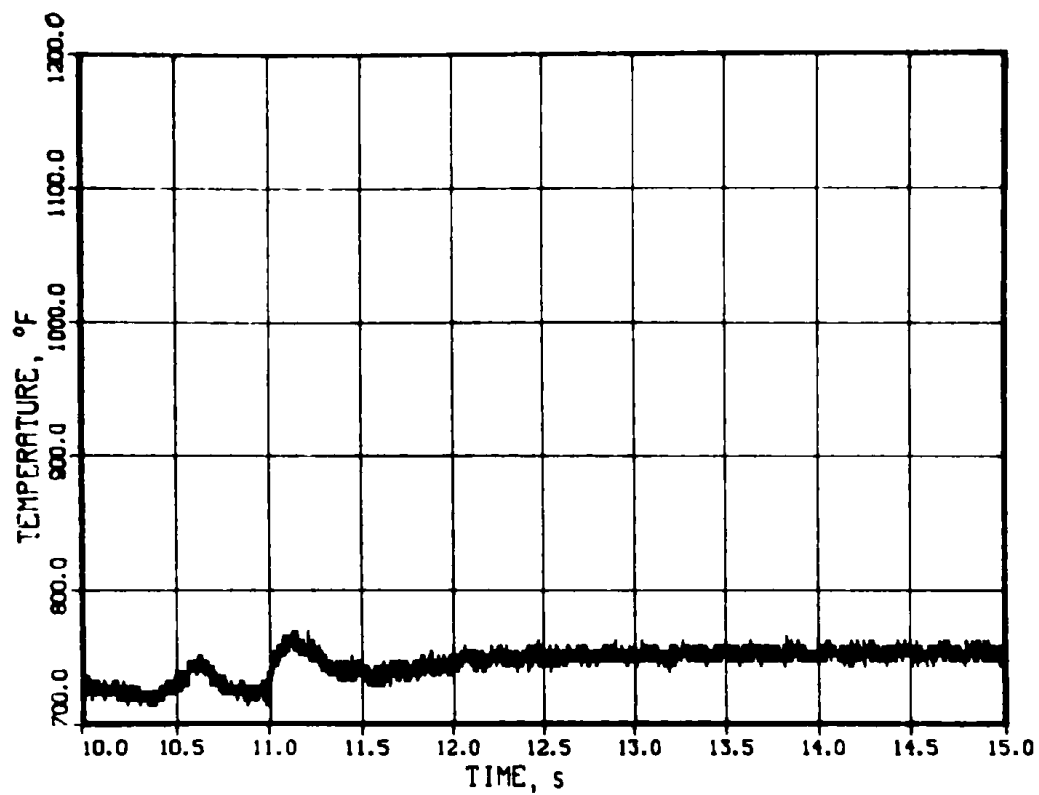


Fig. 30. Temperature of Upper Sodium Plenum (TC7) to 15 s.
Conversion factor: $t (^{\circ}\text{C}) = [t (^{\circ}\text{F}) - 32]/1.8$.

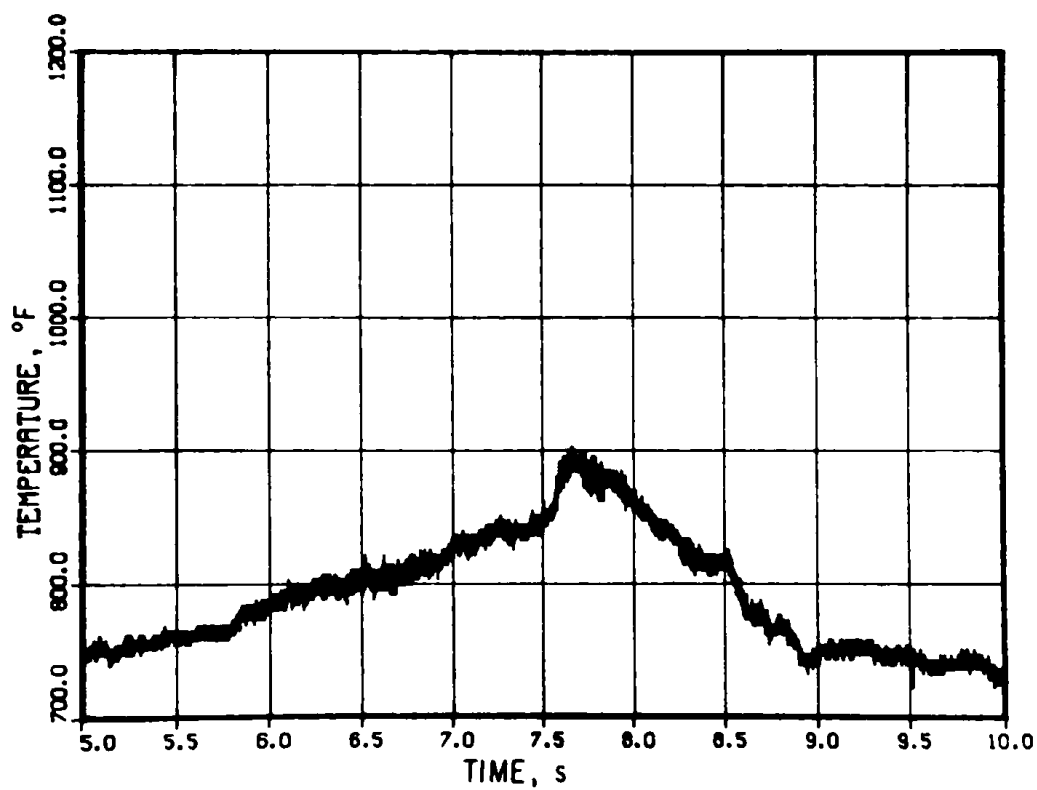


Fig. 31. Temperature of Upper Sodium Plenum (TC7) to 10 s.
Conversion factor: $t (^{\circ}\text{C}) = [t (^{\circ}\text{F}) - 32]/1.8$.

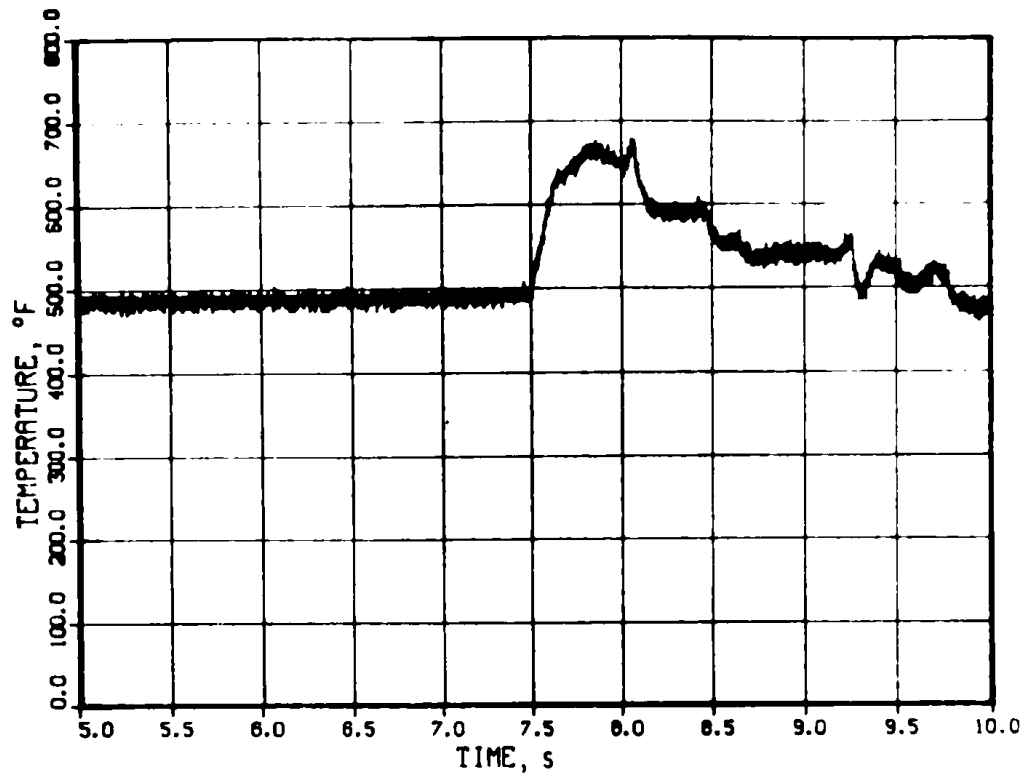


Fig. 32. Temperature of Plenum Cover Gas (TC8). Conversion factor: $t (^{\circ}\text{C}) = [t (^{\circ}\text{F}) - 32]/1.8$.

C. Flow and Void Data

Most comparisons between the calculated reactor accidents and test data from loop experiments are based on the flow data and void-growth rates. Flow velocity, particularly at the inlet, is the most accurate measure of dynamic behavior in the test.

All flow and void rates were calculated in units of grams of sodium per second and then converted to cm^3/s . In this way, thermal expansion during heating within the channel is properly accounted for.

Details of the inlet- and outlet-flow data from 7 to 8 s are shown in Figs. 33 and 34, respectively. Features of note at the inlet are:

1. The gradual flow reduction and reversal from 7.45 to 7.58 s.
2. Slowly decaying reverse flow for 260 ms (7.58 to 7.84 s).
3. An event at 7.834 s that is followed by a significant flow surge at the inlet. This event is shown in more detail in Fig. 35.
4. Small surge-type ejections at 7.46, 7.49, and 7.51 s, superimposed on the general flow reduction and reversal. These are discussed in more detail in Sec. IX.A.

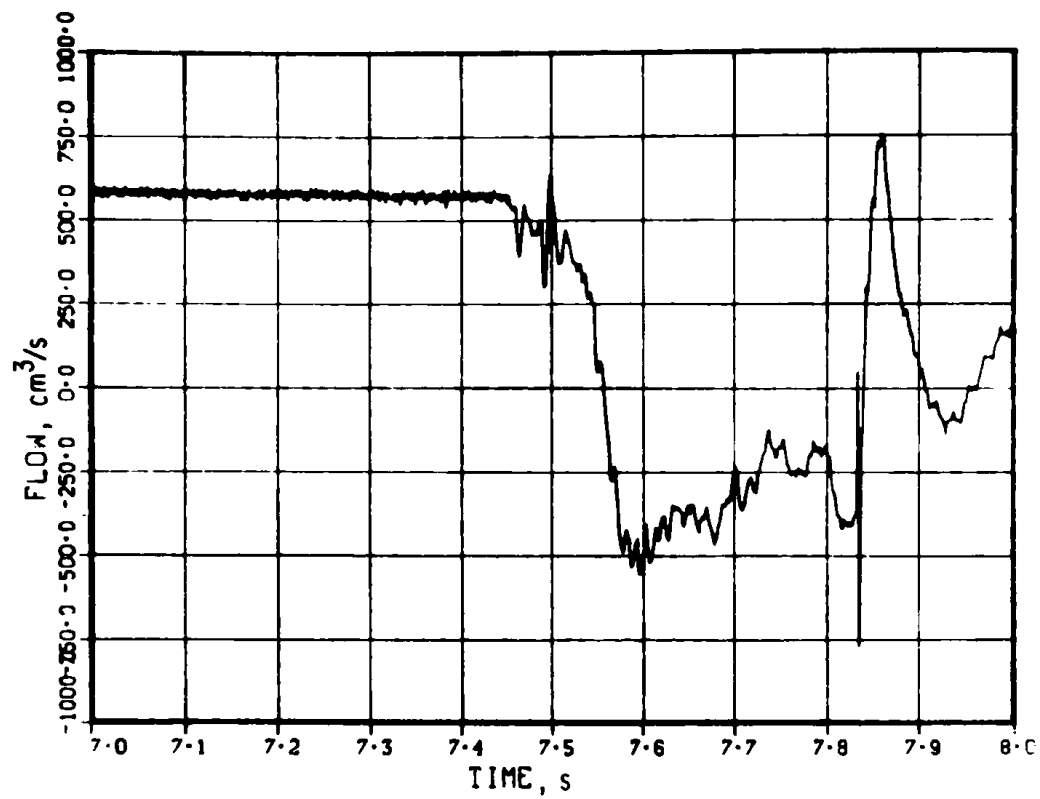


Fig. 33. Inlet-flow Data during Failure Sequence

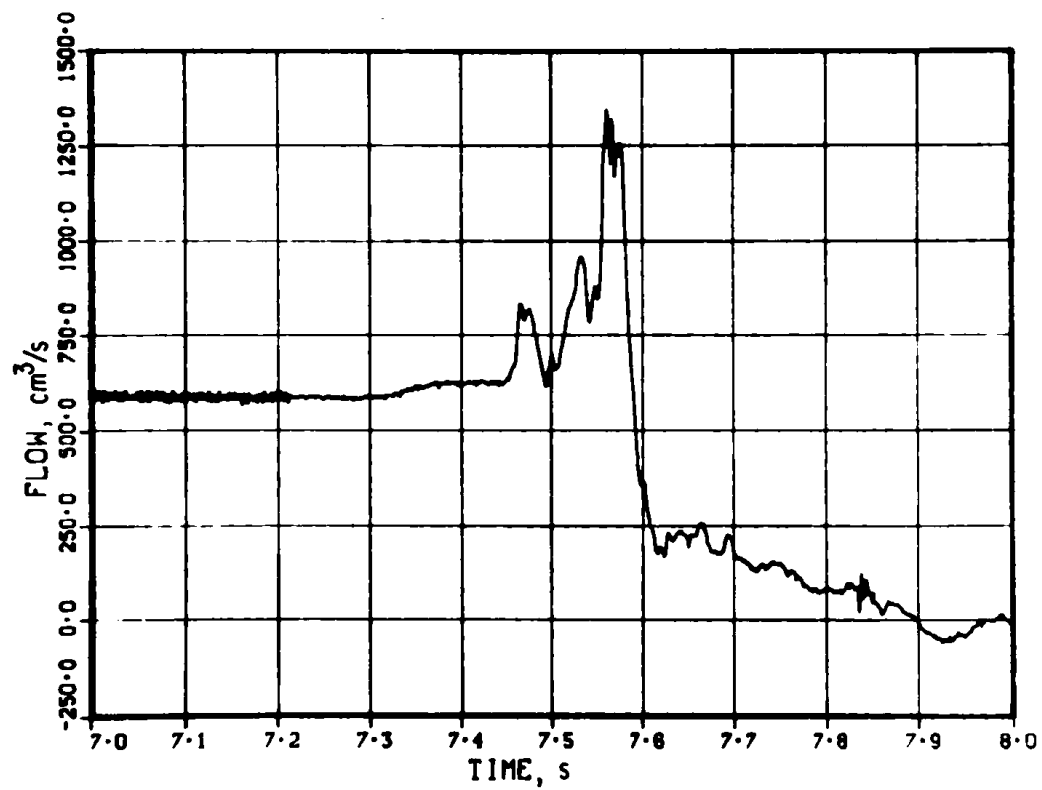


Fig. 34. Outlet-flow Data during Failure Sequence

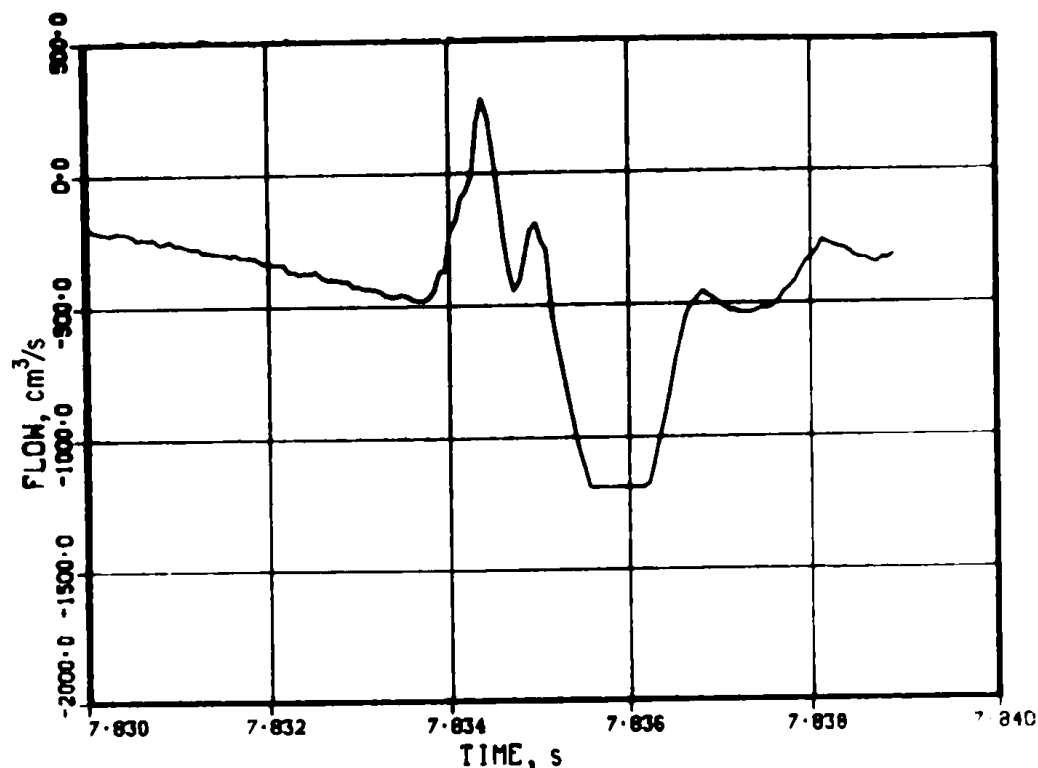


Fig. 35. Response of Inlet-flow Detector to Event at 7.834 s

Features of note in the outlet flow (see Fig. 34) are:

1. Successive ejections at 7.47, 7.53, and 7.56 s, superimposed on a general accelerated outlet flow. The first and third events appear to have multiple origins.
2. An abrupt drop in outlet flow at 7.58 s.
3. A small, but perceptible, increase in outlet flow from 7.32 to 7.45 s.

The apparent event at 7.834 s is shown on an expanded scale in Fig. 36. It is smaller in magnitude and narrower in time than the corresponding inlet event shown in Fig. 35. This could be the response of both detectors to a mild FCI-generated impulse, except that no pressure pulses were observed at this time. Absence of any significant reentry following the 7.834-s event corresponding to the substantial reentry at the inlet suggests isolation between the inlet and a partial blockage.

A number of interesting features are observed in the flow signals after 8 s. Inlet and outlet flow from 8 to 13 s are shown in Figs. 37 and 38.

1. At the inlet:

- a. Oscillations from 8.5 to 9 s and from 11.2 to 12.5 s are characteristic of boiling. Autopower-spectra calculations for these times display unique characteristics that confirm boiling. These characteristics are absent in the same calculations from 9 to 10 s and from 13 to 14 s.

b. A minor event occurred at 10.5 s and a significant ejection at 10.95 s. (Classification of events by magnitude is based on flow accelerations rather than on flow velocity.) The latter event is shown in more detail in Fig. 39.

2. At the outlet (see Fig. 38):

a. A minor ejection at 8.1 s did not have a strongly correlated response at the inlet.

b. Boiling from 8.3 to 8.8 s was very mild, if present at all.

c. The weak inlet ejection at 10.5 s was accompanied by a small outlet reentry. Normally, a pressure-producing event would cause ejection from both ends of the flow channel. Thus, this event appears as collapse of a vapor bubble. The relative inlet-to-outlet magnitudes indicate that some porosity still exists in the outlet plug.

d. The outlet-flow event at 10.95 s is correlated with the inlet-flow data. This would suggest that the blockages that did exist were spongy or porous, and the event was possibly of vapor origin. Flow during this event is shown on an expanded time scale in Fig. 40.

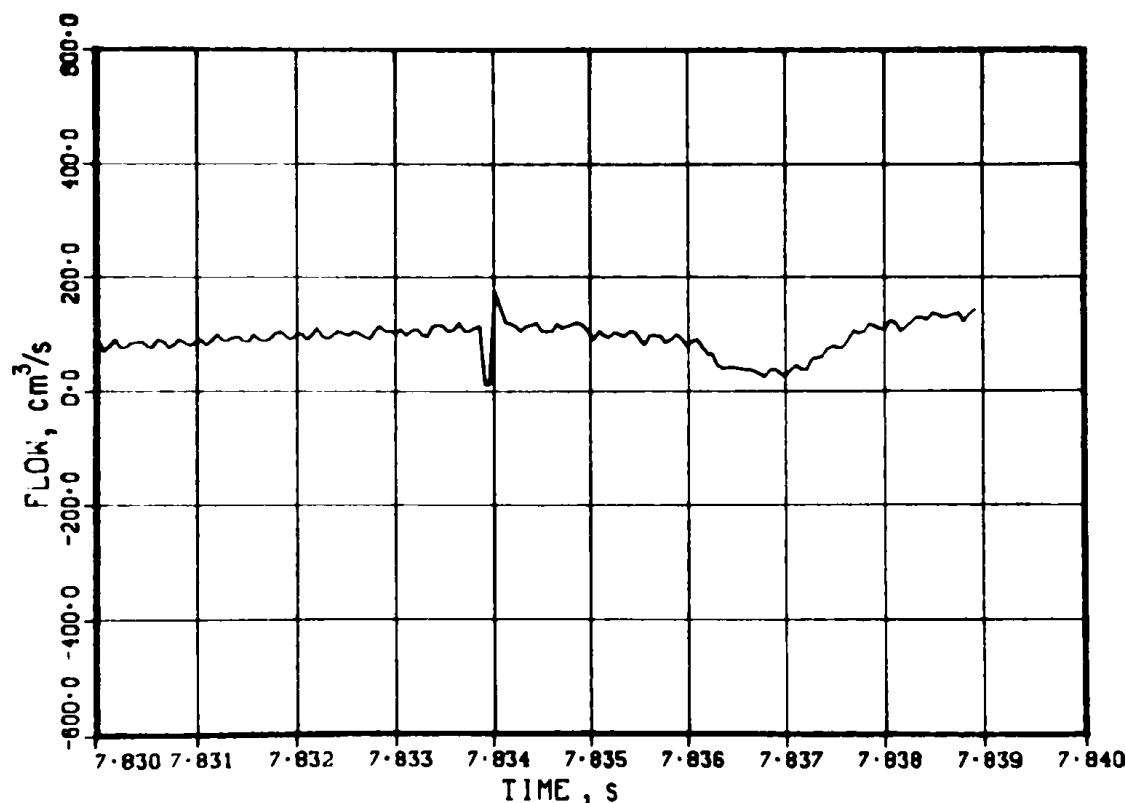


Fig. 36. Response of Outlet-flow Detector to Event at 7.834 s

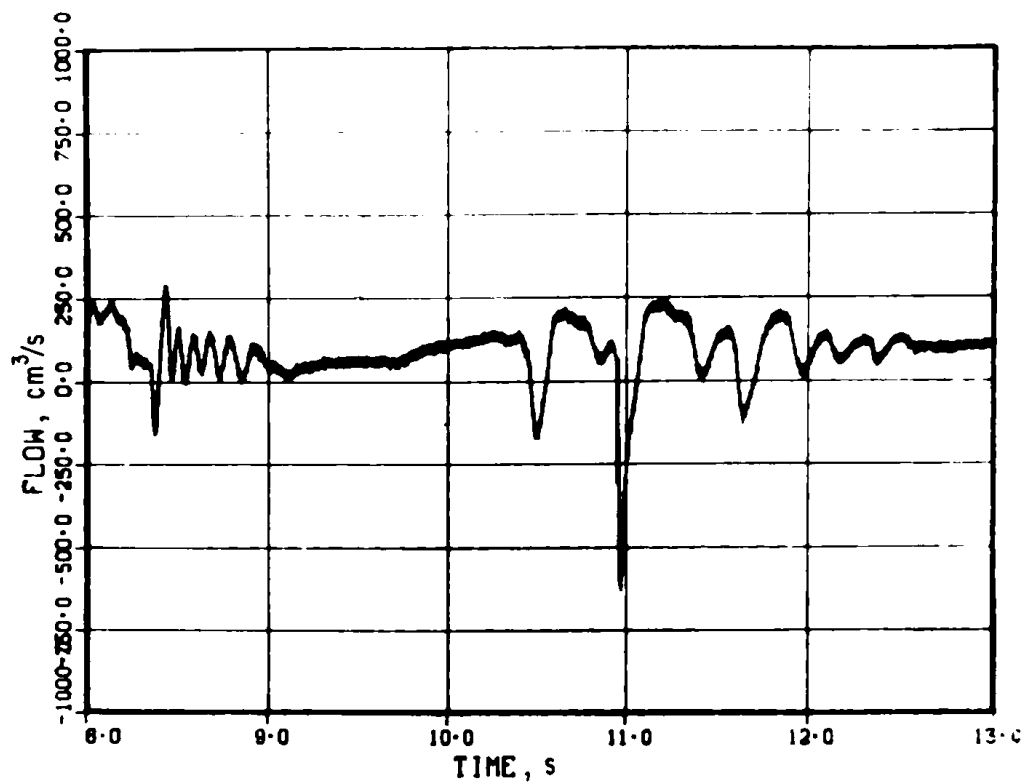


Fig. 37. Inlet-flow Data after Initial Failure

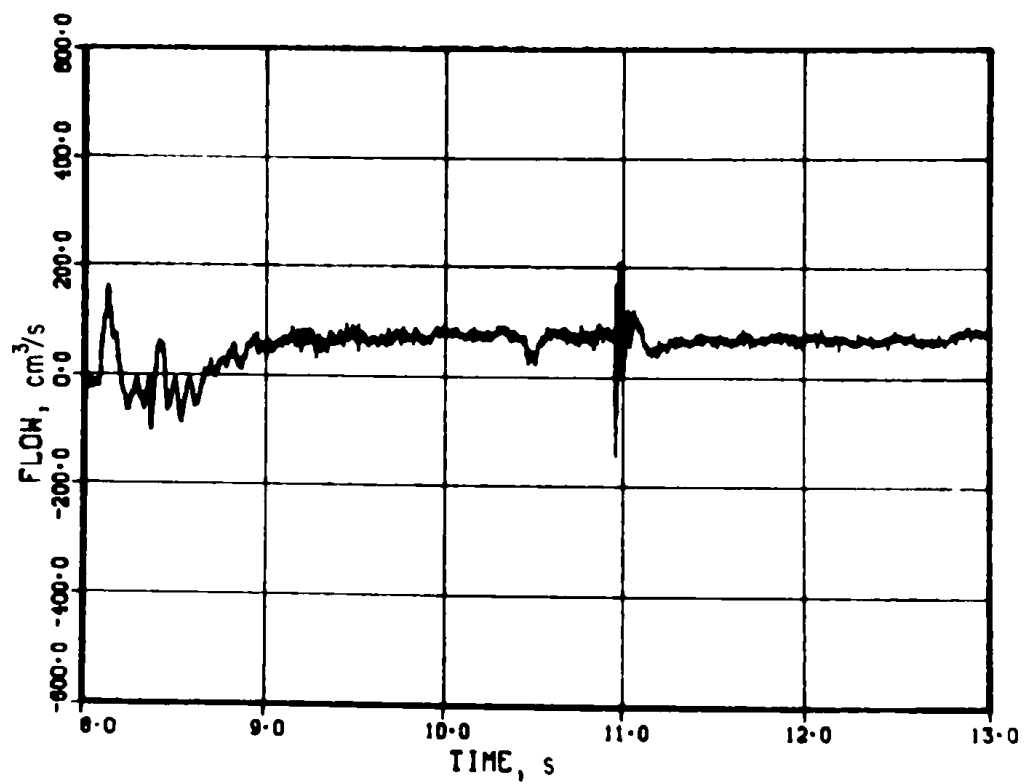


Fig. 38. Outlet-flow Data after Initial Failure

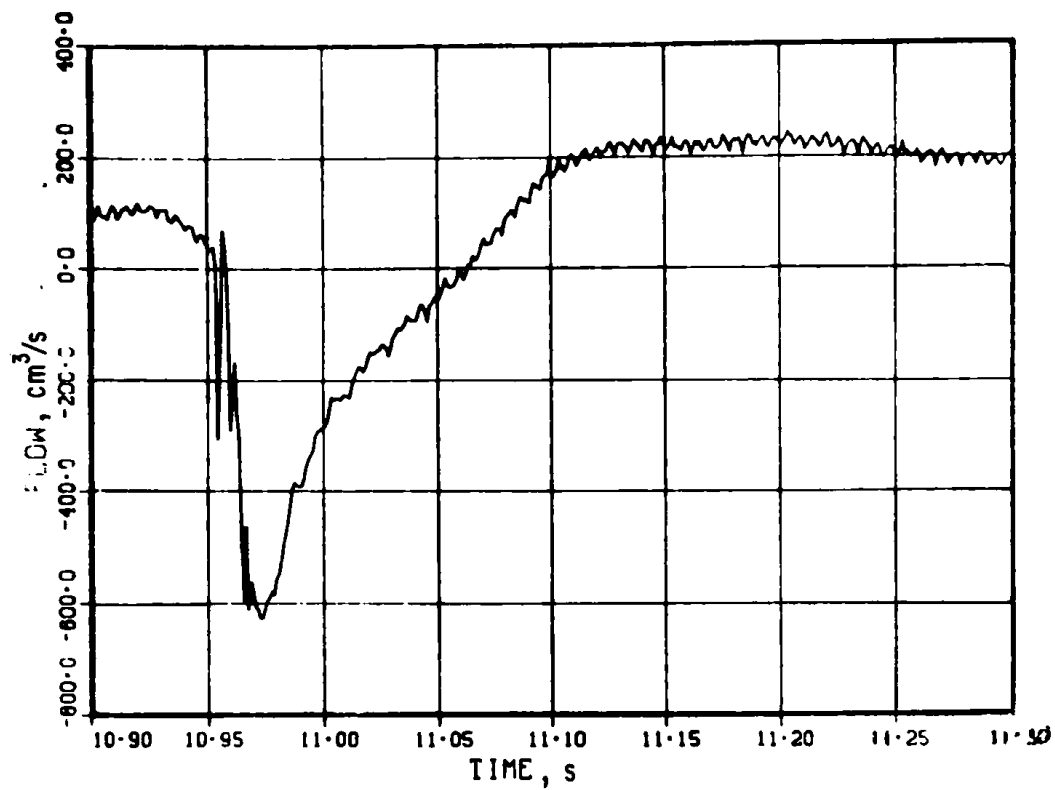


Fig. 39. Inlet-flow Data during Event at 10.95 s

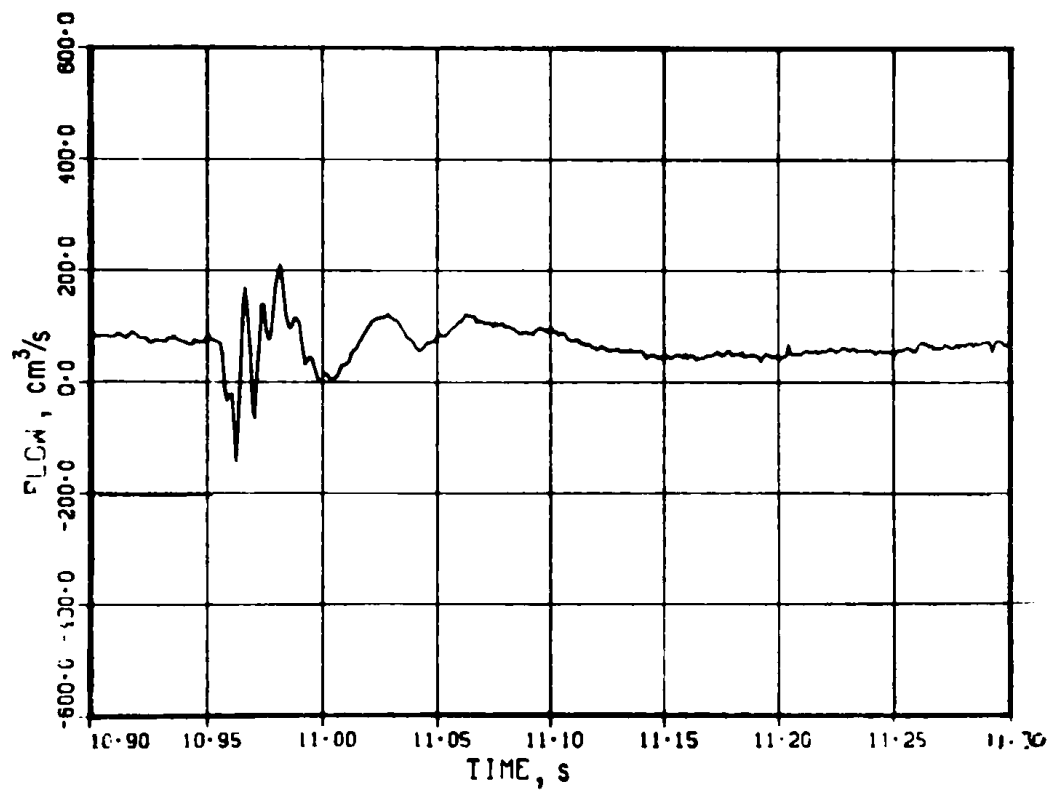


Fig. 40. Outlet-flow Data during Event at 10.95 s

Flow data are expected to be reasonably accurate during single-phase flow. Gas release from the fuel pins after cladding failure and from the adiabatic holder after fluted-tube rupture introduce noncondensable gases into the flow stream. Detector response as the two-phase flow is approached is uncertain. Additional uncertainties arise during production of vapor by sodium boiling. For these reasons, the void and liquid-interface calculations are of questionable reliability after about 7.8 s.

Early development of void interfaces is shown in Fig. 41. Data shown in Fig. 41 are the integrated inlet and outlet flows since 7.00 s. The difference between the two curves represents the total void volume between the two flow detectors. Before 7.45 s, the two curves should be the same. The finite difference (and consequent apparent void at 7.45 s) is a consequence of the temperature dependence of the ARMCO iron in the outlet-flow circuit. The void corresponding to these interfaces is shown in Fig. 42. The void to 8 s is shown in Fig. 43. The void calculations are tabulated in Appendix A.

After the test, no flow was detected through the test section. An upper limit of 5% flow is assigned to this determination.

Collapse of the outlet-flow slug at 7.58 s (see Fig. 34) and the relatively static inlet flow from 7.58 to 7.8 s is due to the combined effects of a vapor-bubble collapse and the passage of fission gas past the upper flow detector. The events at 7.834, 10.5 and 10.95 s are fuel-coolant interactions. At the times these FCI's occur, the flow channel is voided and a major response is not observed by the pressure transducers. The FCI at 10.95 s possibly occurs close to the inlet. A back calculation of the pressure from the mass of sodium in the slug (385 g) and the slug acceleration ($2.7 \times 10^4 \text{ cm/s}^2$) yields an expected pressure pulse of 0.69 MPa (100 psi), close to the measured pulse of 0.52 MPa (75 psi).

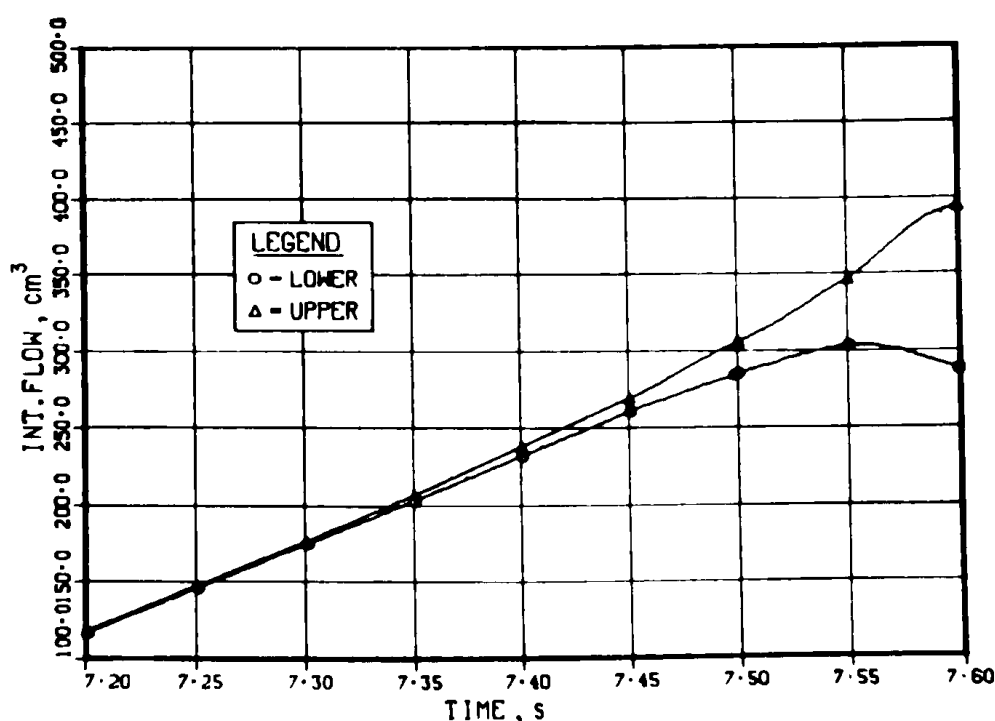


Fig. 41. Integrated Inlet and Outlet Flows since 7.0 s

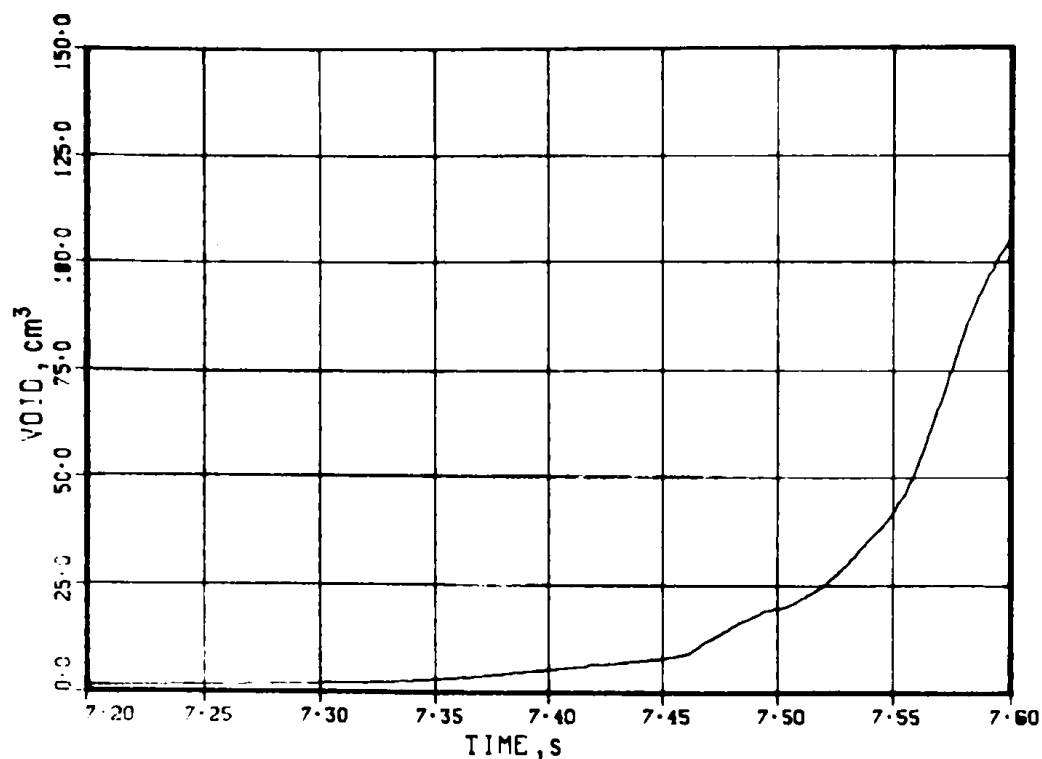


Fig. 42. Void Growth during Early Failure Stages

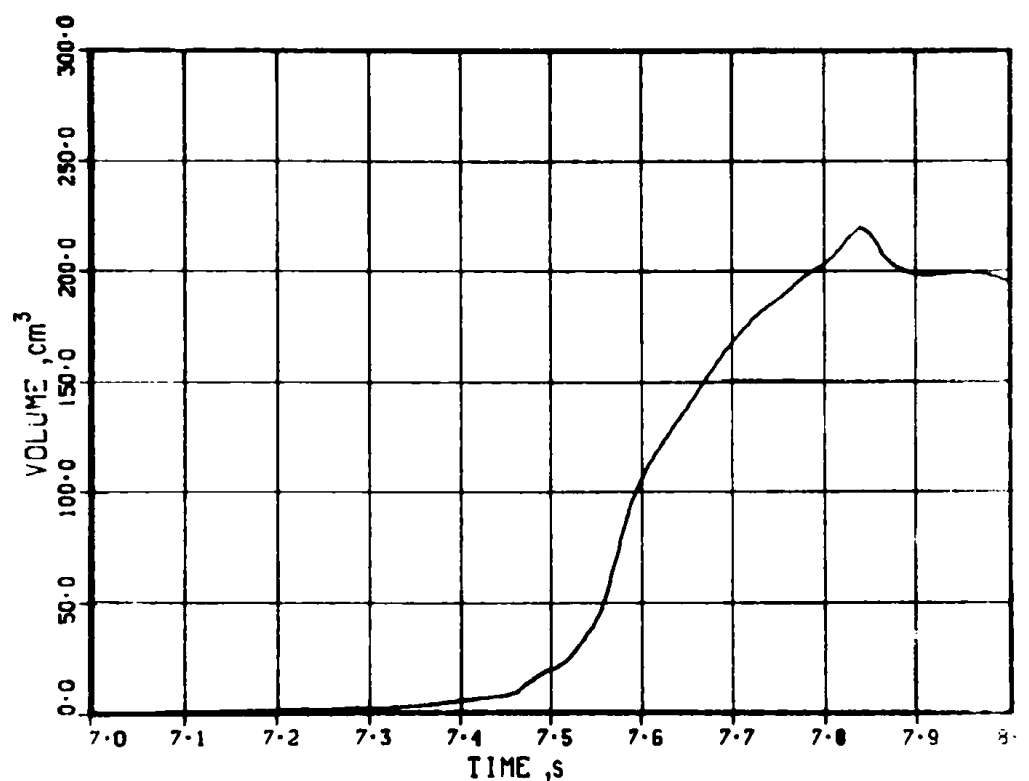


Fig. 43. Void to 8.0 s

D. Pressure Data

Pressure data at the inlet during the time of failure are of questionable statistical significance but, for reference, are shown in Fig. 44. Several small pulses [< 25 psi (0.17 MPa)] occurred between 7.55 and 7.58 s at the inlet. A 25-psi (0.1-MPa) pulse on a 2500-psi (172-MPa) gauge (1% of full scale) has

only marginal significance with respect to both the accuracy of the recorded data and the seven-bit ADC used to digitize the data. Both the significance of the data and the effect of seven-bit roundoff can be seen in Fig. 44. A more pronounced train of inlet pressure pulses is observed at 10.955-11.0 s (see Fig. 45). The largest of these is about 75 psi (0.52 MPa) and occurs at 10.96 s. No pressure pulses were found that correspond to the flow event at 7.834 s.

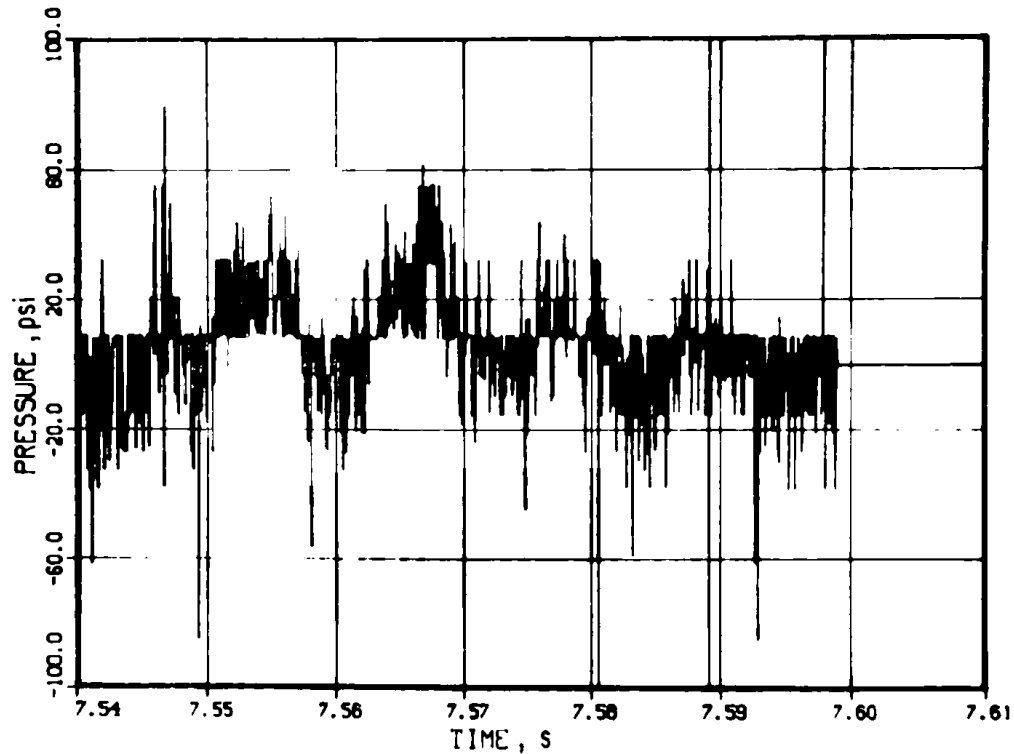


Fig. 44. Inlet Pressure Data during Initial Failure

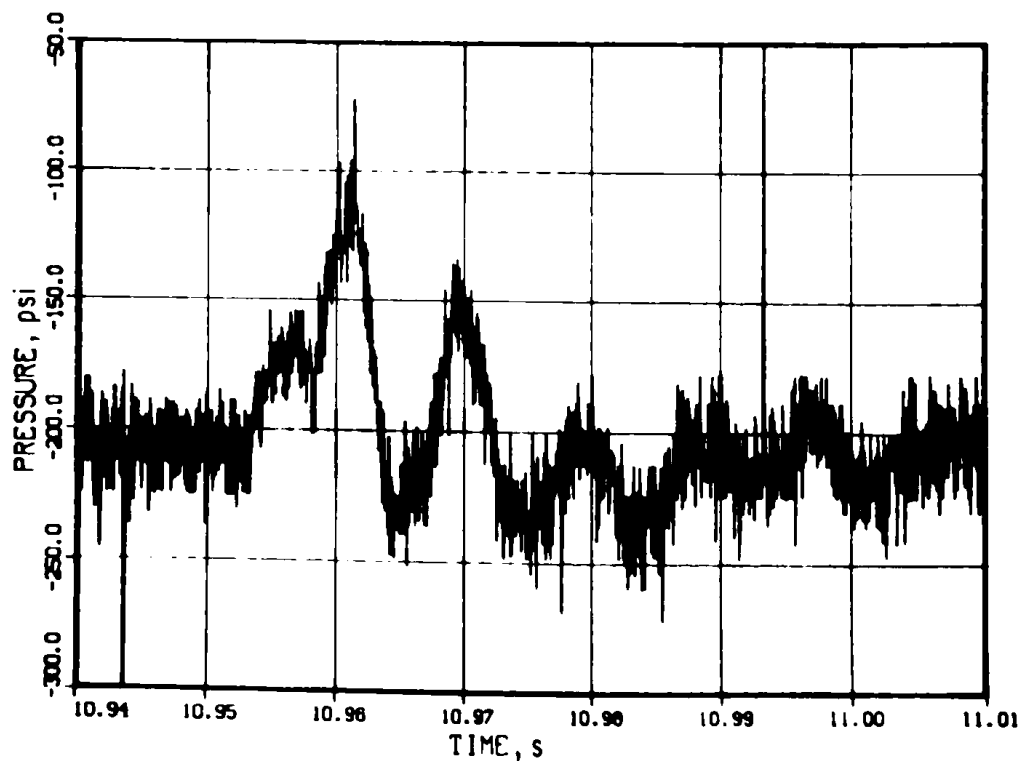


Fig. 45. Inlet Pressure Data during Event at 10.95 s.

Conversion factor: 1 psi = 6.895 kPa.

Pressure-producing events at the outlet were equally marginal. A series of what may be pressure pulses at the inlet is shown in Fig. 46. The first and largest of these (25 psi) occurred at 7.565 s, about 10 ms after the pressure event at the inlet. No pressure pulses were observed at the outlet during the flow event at 10.95 s.

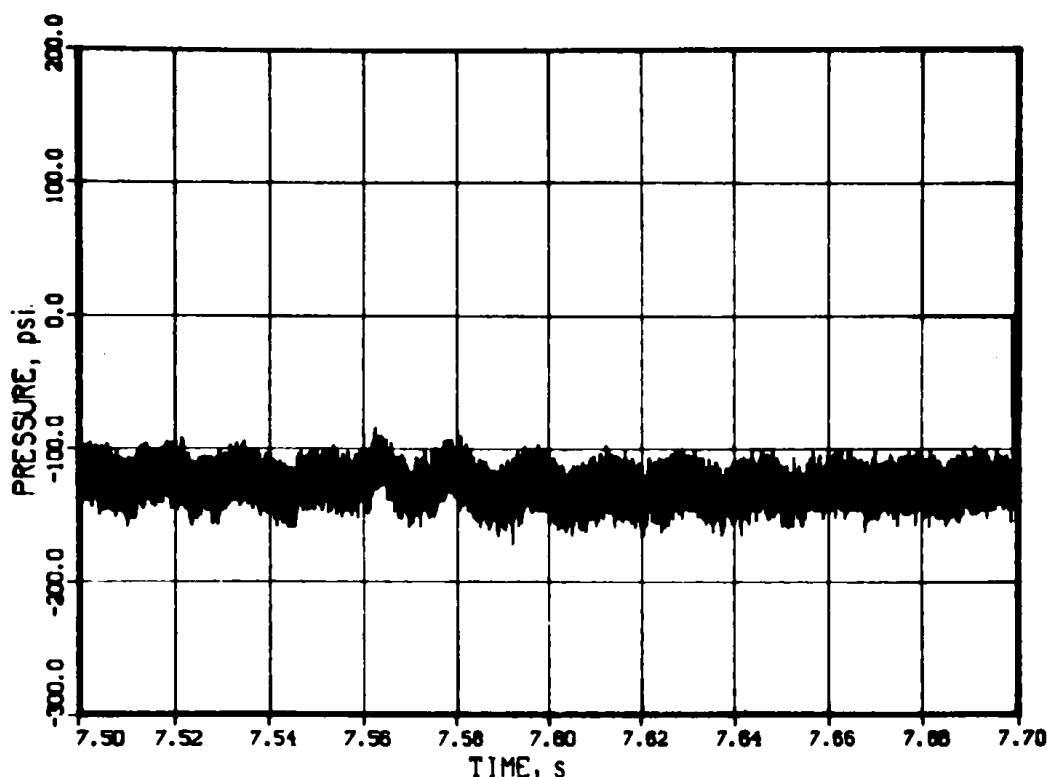


Fig. 46. Outlet Pressure Data during Initial Failure.
Conversion factor: 1 psi = 6.895 kPa.

No pressure pulses were found between 16 and 18 s for either pressure transducer.

Data shown in Figs. 44 and 45 have not had the noise pulses removed. Those shown in Fig. 46 have had "bad," or noise, points removed. All three plots are of "50- μ s" data. Results of averaging the data of Fig. 46 over 1-ms intervals is shown in Fig. 47. It would be difficult from this figure to identify pressure pulses from random variations in the signal. However, the same data in Fig. 46 are somewhat more suggestive. These data make it clear that no significant pressure-producing events (FCI's) occurred at the time of initial cladding rupture or fuel release.

E. Hodoscope Data

Fuel motion in E7 was analyzed on the basis of R/P plots of the hodoscope data, corrected for supralinearity effects (see Sec. 1 below). For the reference power P, the array-average counting rate (i.e., the average of the counting rates R of all the neutron-detecting channels) was used, because the statistics in those channels assigned as power monitors were insufficient to

produce a smooth curve. Using the array average for this purpose would clearly be wrong when fuel is lost from the field of view of the hodoscope (by traveling above Row 2 of the array of hodoscope detectors, or below Row 23), and for E7 the posttest radiograph shows that some fuel was expelled from the 460-mm field of view sooner or later. However, a careful comparison of the array average with the power-monitor average did not reveal any observable loss of fuel from the field of view prior to scram. A net loss of 8% or more would have been evident. A more detailed discussion of analysis details affecting this degree of sensitivity is given in Sec. 1 below. After scram the statistics were considerably worse, but probably a 25% loss would have shown up, and there was no consistent indication of such a loss prior to the time, about 2 s later (10.7 s), when the film recording the hodoscope data ran out.

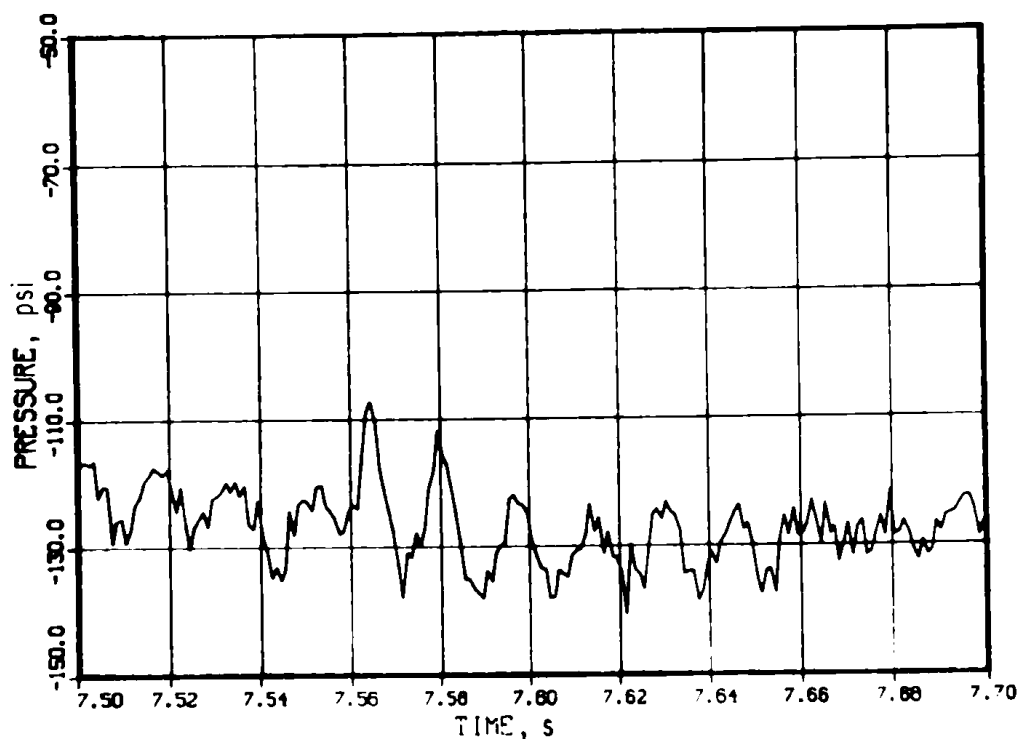


Fig. 47. Outlet Pressure Data during Initial Failure, Averaged over 1 ms. Conversion factor: 1 psi = 6.895 kPa.

It is pertinent to consider the effect on the analysis if a substantial amount of fuel were expelled from the field of view of the hodoscope. If this occurred, and if the analysis were based on the array-average counting rate rather than on true power monitors, the result would be an underestimate of the amount and extent of fuel voiding that occurred in connection with the expulsion. This should not lead to serious error, however, except in the unlikely event of loss of a fraction of the fuel rather evenly from a large volume. In the extreme case, a completely uniform loss of fuel would not show up at all if the power were assumed to be proportional to the array average, whereas it would appear as a uniformly distributed deficit with respect to a true power monitor.

1. Supralinearity

As with some of the in-core loop instruments in TREAT, the Hornyak buttons used as neutron detectors in the hodoscope show a nonlinear

response to TREAT power, both instantaneous and integrated. In the case of the Hornyak buttons, the response is supralinear. A computer code was used to correct the E7 hodoscope data for supralinear response to instantaneous power. The code uses a least-squares technique to generate a correction parameter for each detector, by comparing the detector response with the reactor power as given by the TREAT instrumentation. The comparison must, of course, be terminated before significant fuel motion takes place.

In E7, the cutoff time used for most of the scalers was 7.56 s, which is 20 ms before peak power. (In several cases it was necessary, for optimum fit, to use a larger dead time than the $0.5\ \mu\text{s}$ that suits most of the scalers; the largest dead time used was $10\ \mu\text{s}$.) Since there were possible indications of minor fuel motion during the last ~150 ms of this period, a second calculation was made, with the cutoff at 7.40 s. Time plots of R/P were made for both sets of supralinearity parameters and for all relevant scalers, and the pair of plots for each scaler was examined for evidence that the 7.56-s fit was obscuring indications of fuel motion. No such evidence could be seen, and in almost every case where there was a significant difference between the two plots, the supralinearity was handled better by the 7.56-s fit.

To distinguish between supralinearity effects and fuel motion, the principal criterion was symmetry about 7.58 s: If the R/P plot showed a dip or rise that was symmetrical about 7.58 s, supralinearity was assumed to be responsible, especially if adjacent channels did not show the same behavior. Although in principle this policy could suppress the indications of localized fuel oscillations that reverse at the time of peak power, such coincidences are unlikely. Nevertheless, this ambiguity will be inherent in the hodoscope data as long as the supralinearity problem exists.

At present, no correction is available for supralinear response to integrated reactor power (except insofar as the effect on the array average of power-monitor average approximates the effect on the individual scalers). Fortunately, the effect is small for most of the scalers and has not posed a major problem. The power shape as indicated by the array average is compared with that given by TREAT instrumentation in Fig. 48 where the supralinearity corrections are seen to have resulted in close agreement prior to 7.56 s. In the neighborhood of 7.0 s, the high hodoscope points are affected by film-scanning errors, so that the deviation is probably spurious. In the 300-ms interval following peak power, the hodoscope points are low by some 10%. One possible explanation is that about 10% of the test fuel disappeared from the field of view of the hodoscope at 7.6 s; to account for the subsequent agreement beyond 8 s, one would then have to invoke either time-dependent (integrated-power-dependent) supralinearity or the return of the expelled fuel.

As indicated later, however, other indications are lacking that a significant amount of fuel was lost to the field of view at 7.6 s, and it seems more likely that the discrepancy has some other explanation, such as residual

gamma-ray sensitivity in the compensated ion chamber that is used to measure the reactor power. Many scalers show evidence of a higher-order non-linearity than can currently be handled by SUPRA, even with scaler dead time as a floating parameter. In several cases, for example, the channel appears to saturate before peak power is reached; in others, the supralinearity appears to increase as maximum power is approached. This is one potential cause of poor-quality differential hodographs. Another is the general scatter in the data, due to counting statistics, film-scanning errors, or other sources or noise.

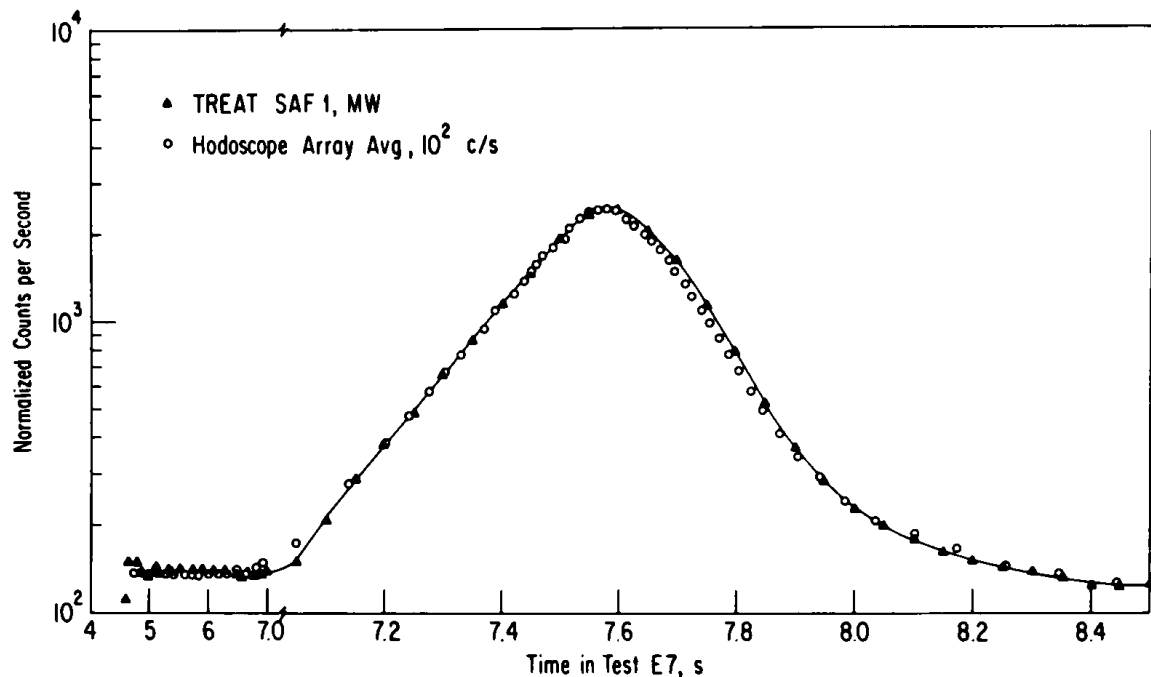


Fig. 48. Power Profile, as Indicated by Hodoscope Array Average and by TREAT Power Monitor

2. Data Smoothing

To optimize the data presentation, two steps were taken to smooth the data. First, the counting rates in the individual channels were averaged over as many cycles as seemed feasible--ranging from 15 cycles (45 ms) near the power peak to 150 cycles or more in the wings. The resulting time resolution is shown in Fig. 49. Second, individual data points were smoothed on the following basis: The time intervals to be used in analyzing the fuel motion were selected, and two R/P time plots for each scaler were made--one with 15-cycle averaging over the peak, and one with 5-cycle (15 ms) averaging (see Fig. 50). On the former, the points to be used for the differential hodographs are identified; when such a point appeared deviant, the latter plot was consulted in making the decision as to whether the point really deviated appreciably from the probable counting-rate curve. If it did, then the factor by which it deviated was determined and was used as a "manual-rate-adjustment" input for further data processing. This adjustment was used to compensate both for random deviations and for obvious residual nonlinearity at the power peak, and was equivalent to drawing a smooth curve through the data points.

3. Differential Hodographs

The point at 5.73 s, which is in the plateau preceding the power spike and before which there would have been no fuel motion, was chosen as the reference point for the undisturbed fuel configuration. Differential hodographs were constructed for most of the subsequent points with respect to this reference time and also for pairs of consecutive points. They are discussed in the sections that follow. In the differential hodographs, the solid circles represent a gain in (power-normalized) counting rate for the time period, and the hollow triangles a loss. The larger the symbol, the greater the gain or loss.

As a rough absolute calibration, the smallest symbol represents a change in fuel quantity amounting to ~ 0.4 g ($\sim 5\%$ of the fuel initially viewed by one of the central channels), and the largest to about 4 g. The minimum sensitivity value of 0.4 g is based on the analysis of the uncertainties discussed above. A blank square in the grid does not indicate lack of fuel, but merely that no net change in fuel quantity was observed at that location during the time period covered.

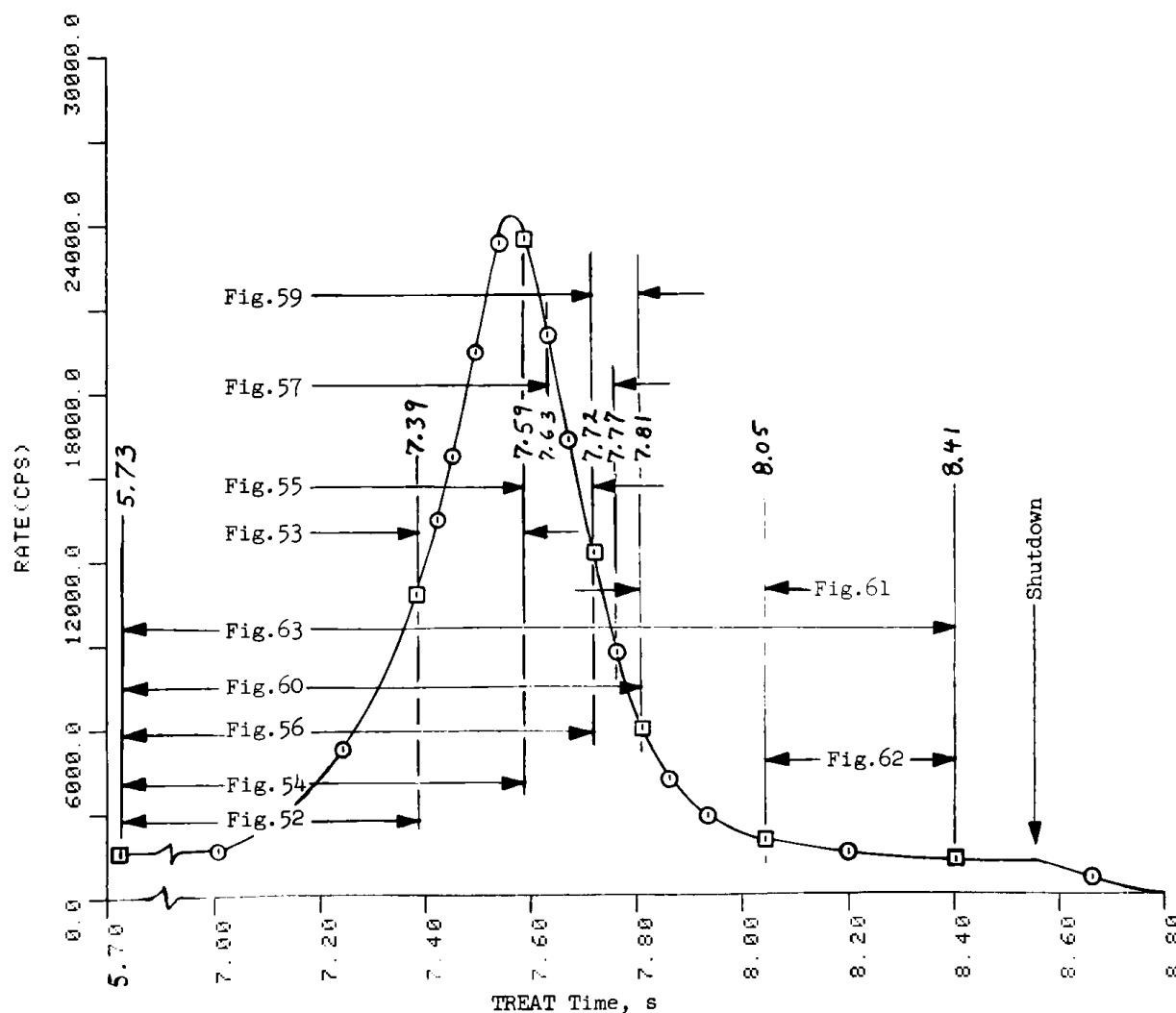


Fig. 49. Hodoscope Power Trace, with 15-cycle Averaging over the Peak. The times used in constructing the differential hodographs are indicated.

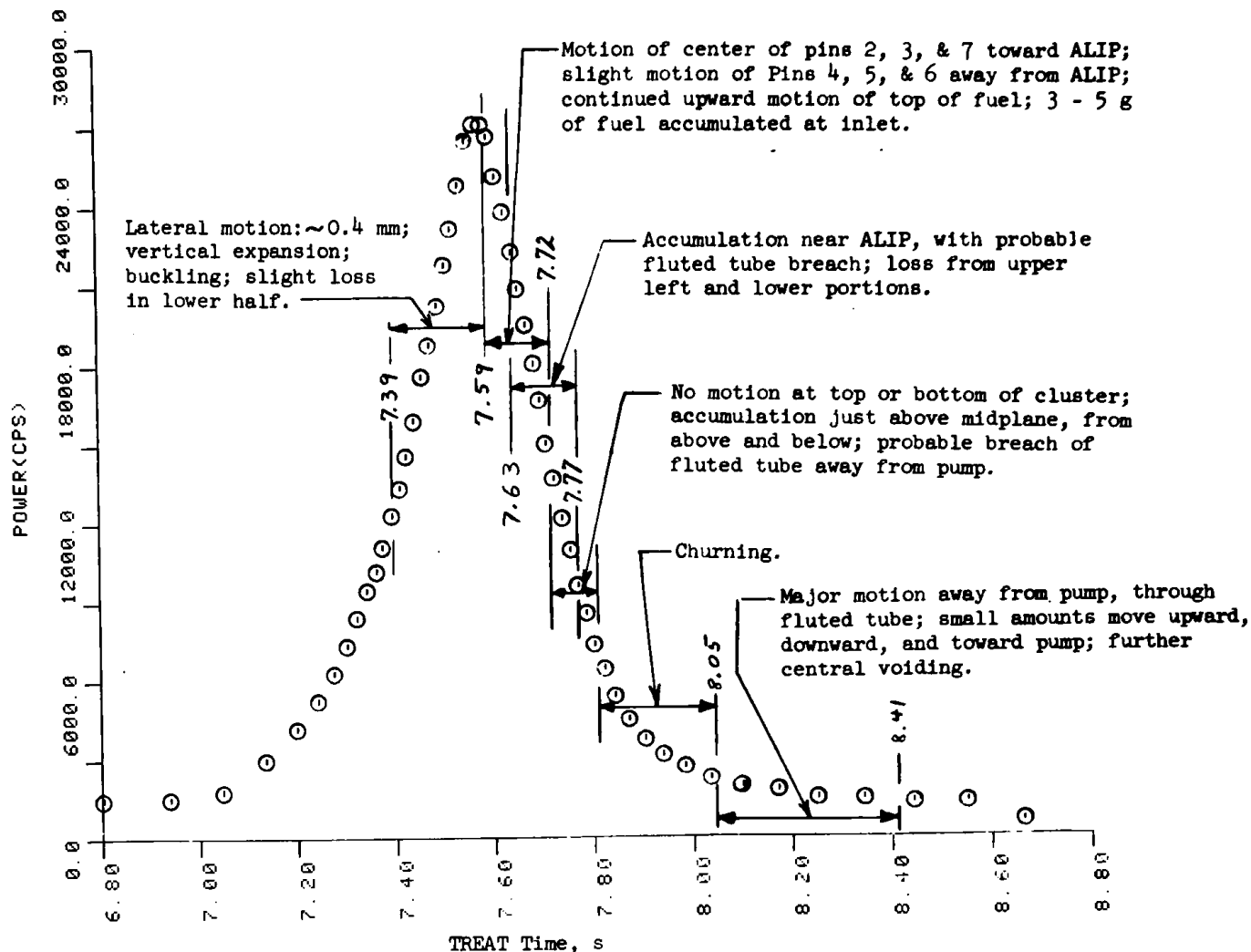
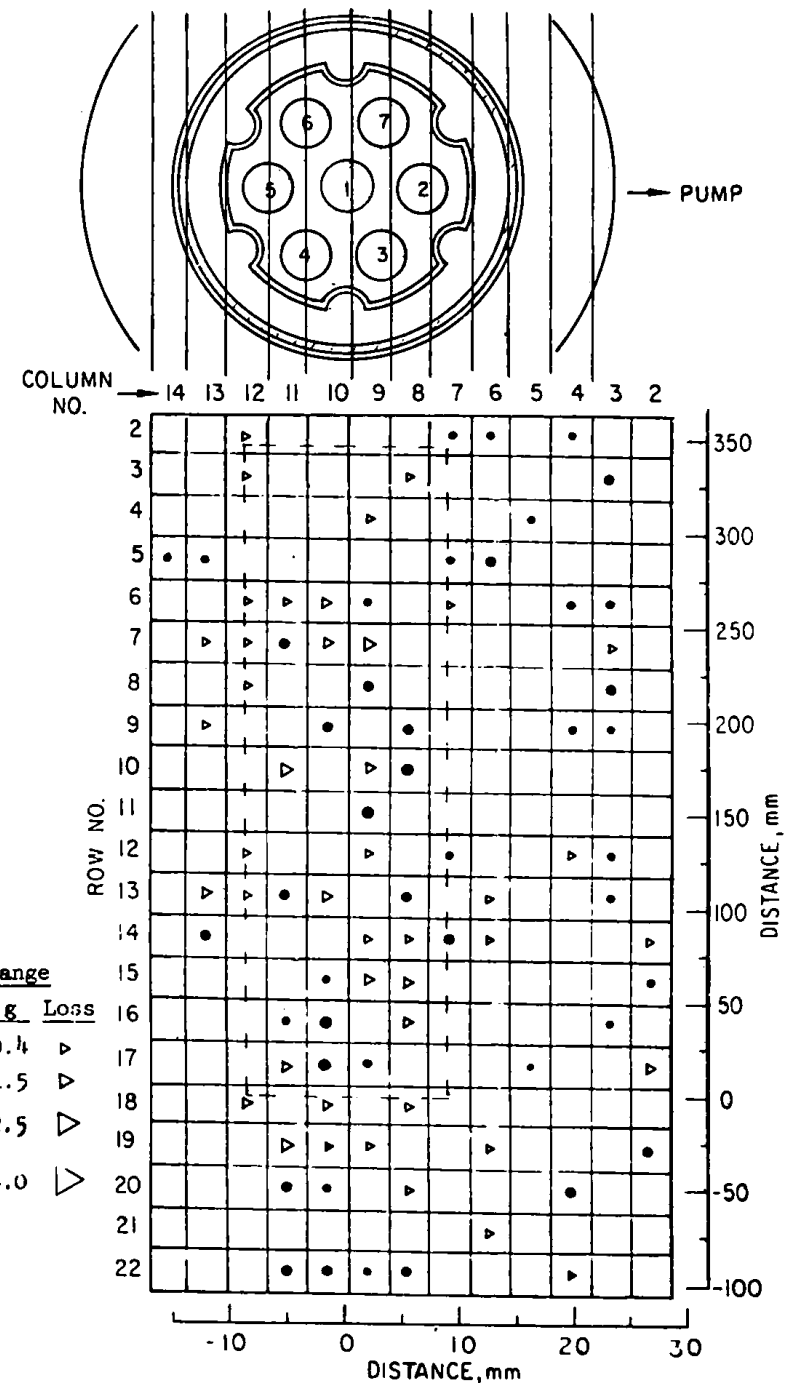
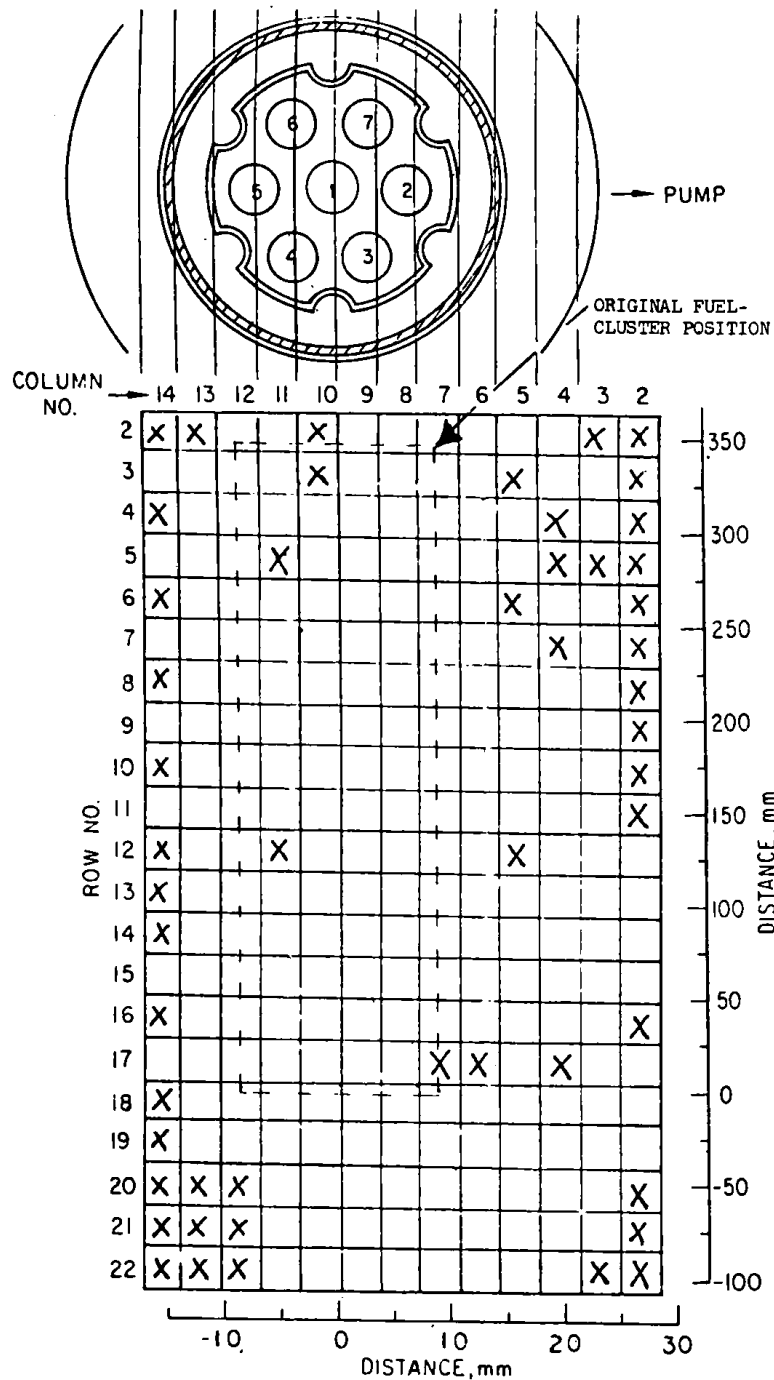


Fig. 50. Hodoscope Summary and Array-averaged Power Trace

Not all the hodoscope channels were used to monitor neutrons. Some were used to monitor gamma radiation, some were not equipped with detectors, and others were malfunctioning. Active channels and their viewing area relative to the E7 fuel cluster are shown in Fig. 51.

a. Fuel Motion at 5.73-7.39 s. The differential hodograph for the first time period, ending at 7.39 s, is shown in Fig. 52. Finding a pattern in this diagram is difficult, and the conclusion is that not much fuel motion took place before 7.39 s. The sprinkling of dots on the grid indicates the magnitude of the noise background in these differential hodographs. The string of four gains in Row 22 must be regarded as spurious, since it is too early for fuel to have travelled that far down and since the region immediately above shows no consistent sign of invasion by fuel.

b. Fuel Motion at 7.39-7.59 s. The 200-ms period immediately preceding peak power is covered in Fig. 53. Indications of fuel motion can be seen. In particular, small amounts of fuel have been displaced to the upper left, and possibly a smaller quantity to the lower right of the original fuel bundle. One can surmise that the fuel columns were expanding vertically and



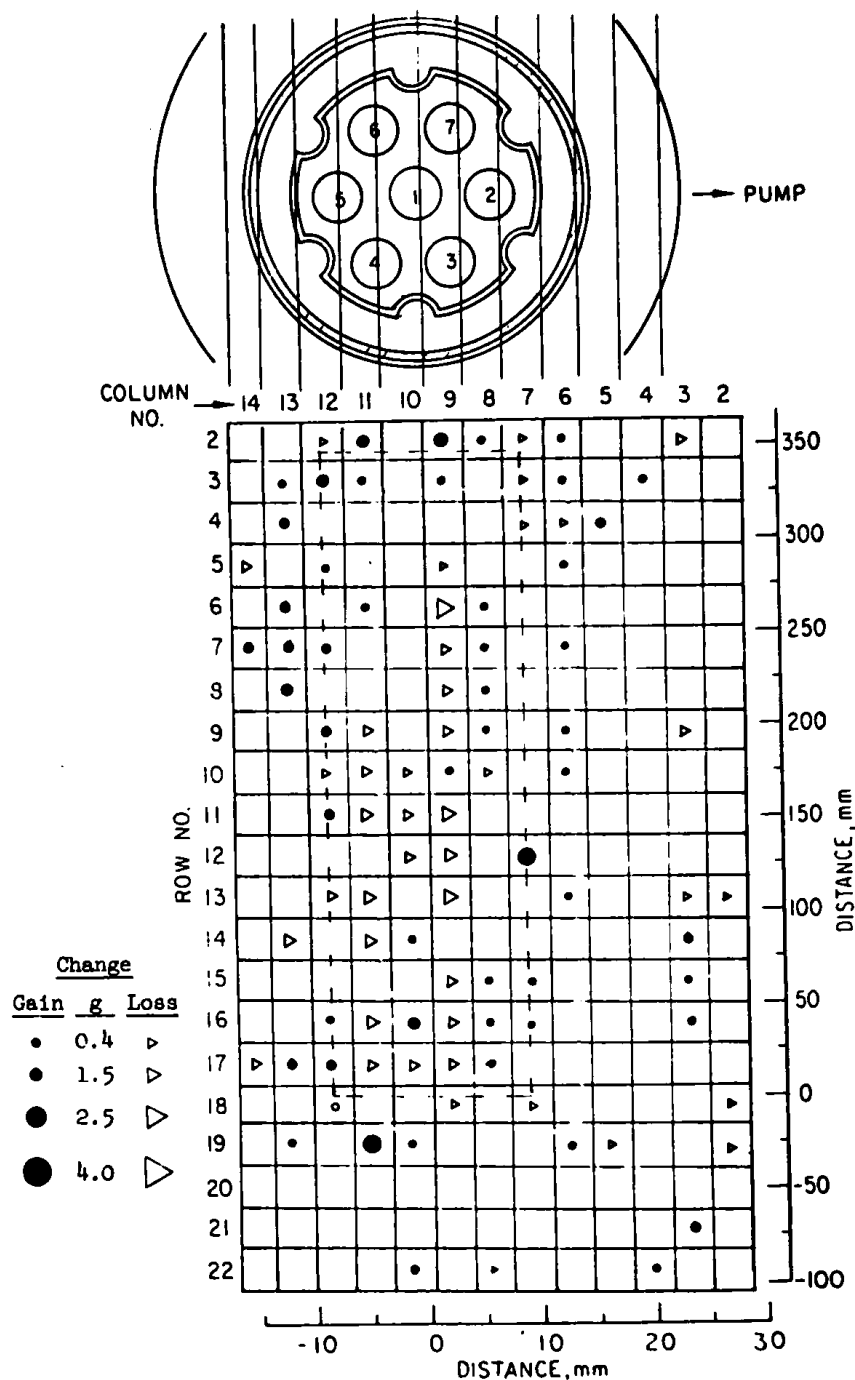


Fig. 53. Differential Hodograph for 7.39-7.59 s

buckling at this time, but they were not yet pressing against the fluted tube at the upper left by the end of the interval, since lateral motions of ~ 0.4 mm can account for the changes observed. This is consistent with the motion allowed by the spacer wires. (See Sec. II.A above.) (Note that an increase in signal from the Column-13 detectors does not necessarily mean the fuel was actually in the line of sight of those detectors: since the collimator walls are not completely opaque to fast neutrons, each detector is somewhat sensitive to fuel in adjacent column. Thus motion of pin 1 toward the left will produce a small increase in signal in Column 13 even before the fluted tube is reached.)

The relatively large increases shown in Row 12, Column 7, and Row 9, Column 11, are assumed to be spurious, since they are not confirmed by changes in adjacent channels. This emphasizes the point that isolated changes, even large ones, in single channels may be "noise," and are not to be trusted.

Figure 54 shows the configuration near peak power (at 7.58 s) with respect to the initial configuration. This picture is similar to Fig. 53, which is as it should be, since not much change had occurred by 7.39 s. The scattered points in Columns 2-5 are spurious.

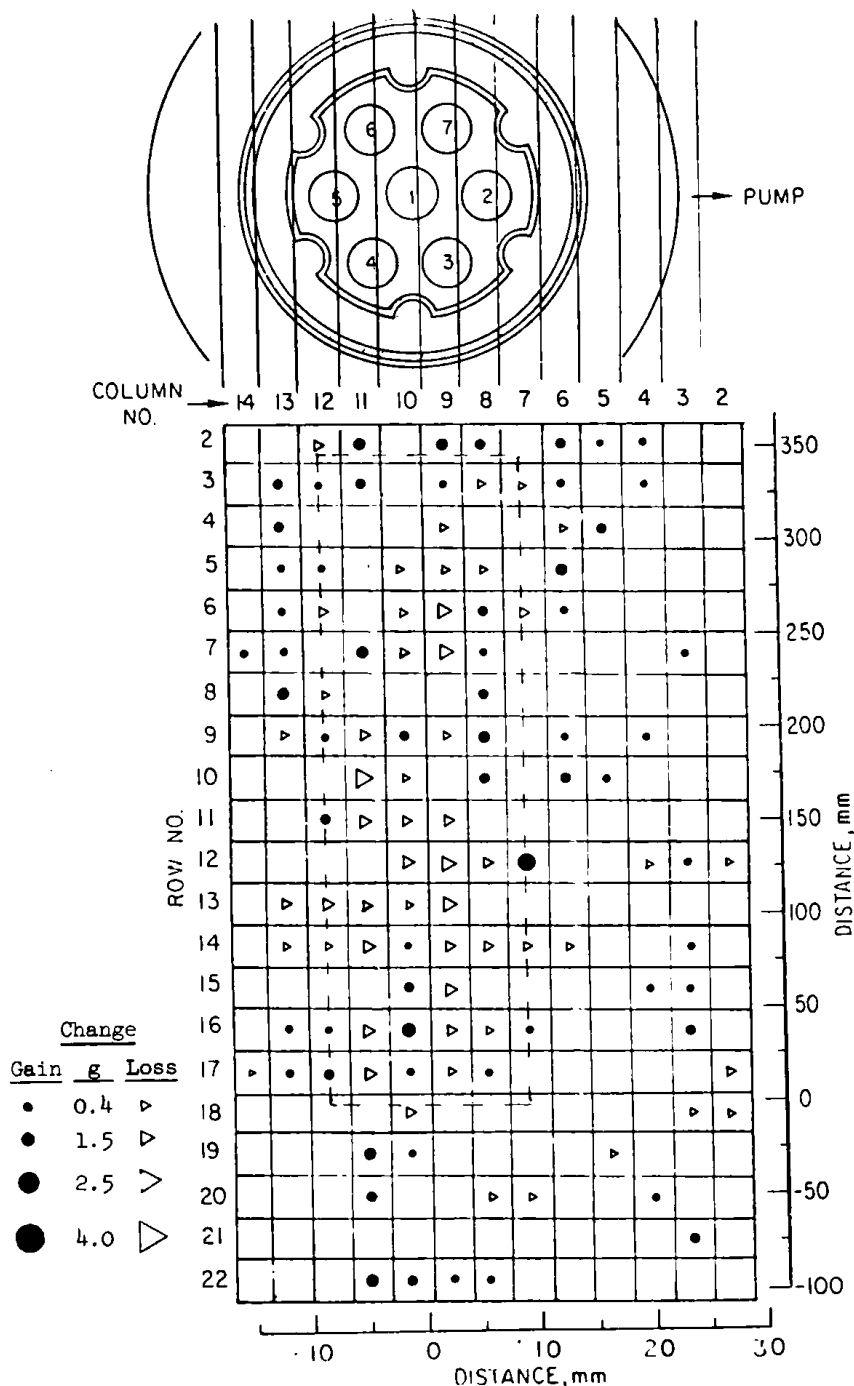


Fig. 54. Differential Hodograph for 5.73-7.59 s

Besides the motion towards the upper left, both figures indicate a slight net loss of fuel in the lower half of the fuel region, a slight upward motion of the upper boundary of the fuel, a possible slight motion of the upper portions of the right-hand pins toward the pump, and generally more action in the upper, hotter part of the fuel. For this time period, void growth was occurring; there are peaks in the flow rate of sodium at the outlet, and the inlet flow rate becomes negative at about 7.56 s.

c. Fuel Motion at 7.59-7.72 s. Figure 55 shows the changes during the 130-ms interval immediately following peak power. Most notable is the accumulation of gains at the central part of Column 7, with a corresponding deficit in Column 9. This is consistent with the interpretation that, with the continued squirming and buckling of the pins, the central portions of pins 5-7 have moved toward the pump by perhaps 0.5 mm. There is also indication that upward motion of the top of the fuel is continuing, and that slight leftward motion of pins 1-3 took place.

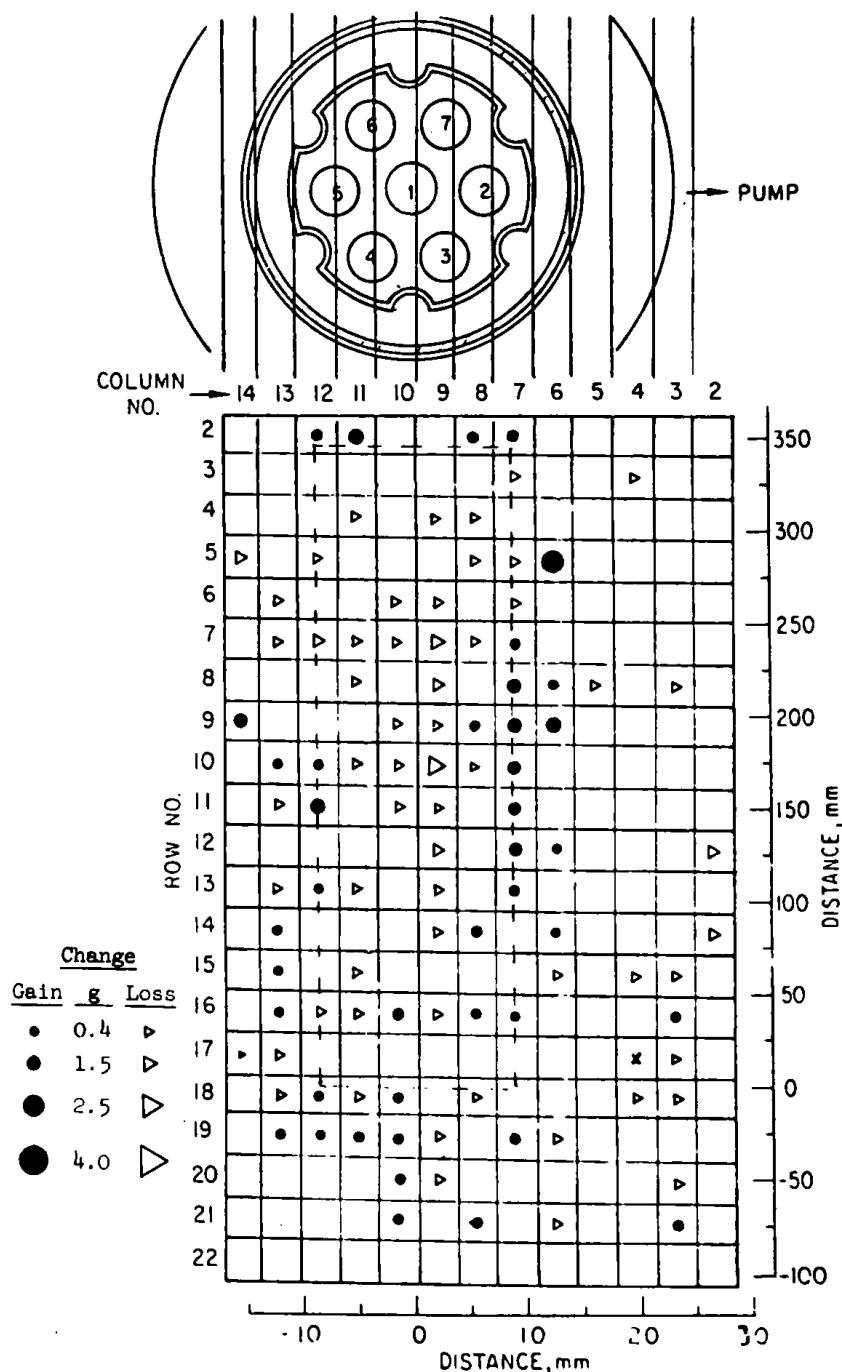


Fig. 55. Differential Hodograph for 7.59-7.72 s

The net change between the start of the transient and 7.72 s is shown in Fig. 56. In addition to the features already mentioned, there is the group of channels below the fuel column that show counting-rate increases. Such a consistent cluster is unlikely to be spurious. Accumulation here of 3-5 g of fuel is indicated.

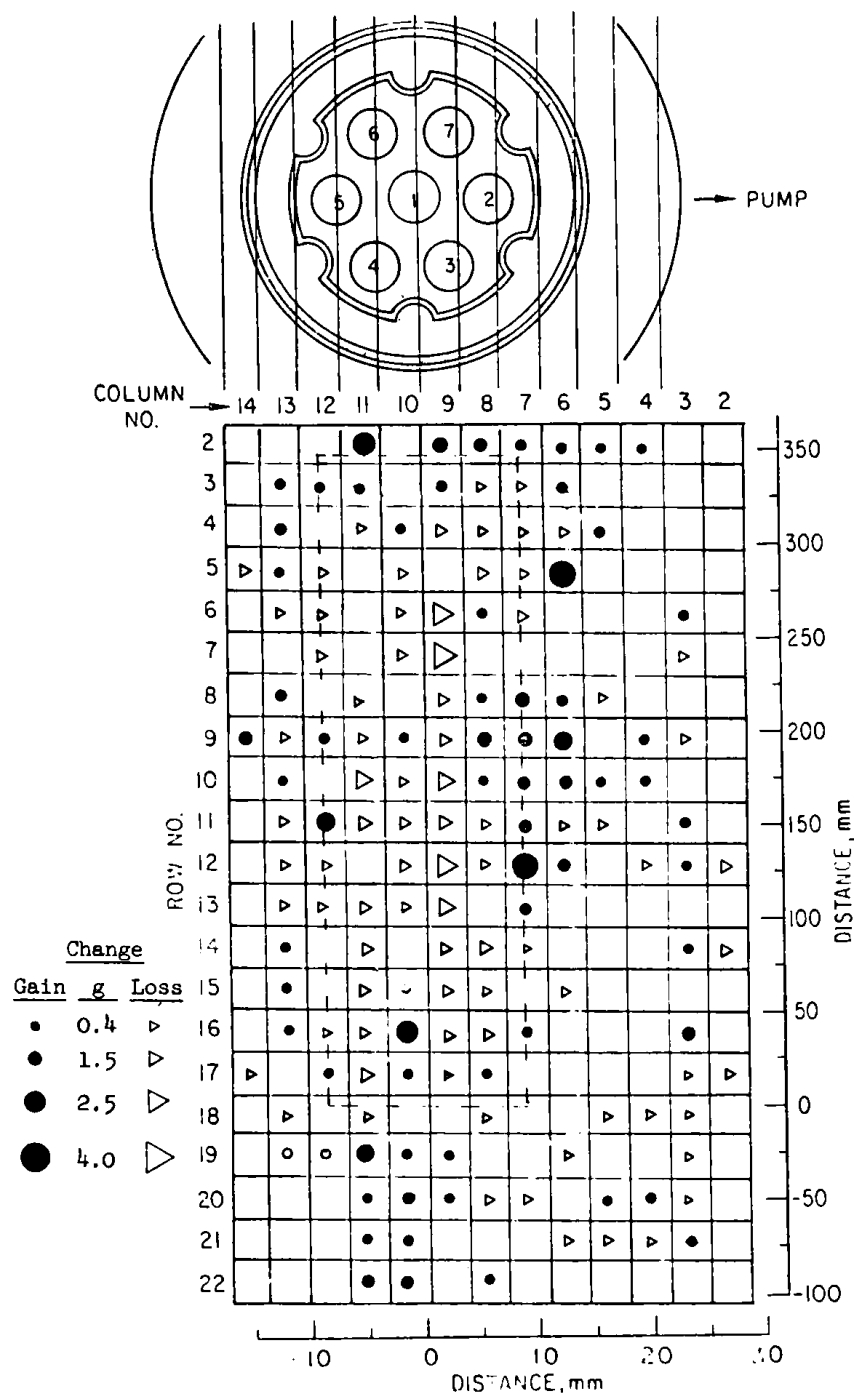


Fig. 56. Differential Hodograph for 5.73–7.72 s

As mentioned earlier, one possible deduction from Fig. 48 is that about 10% of the test fuel was expelled upward out of the field of view of the hodoscope before the end of this interval. Although Fig. 56 does not provide strong evidence either for or against this hypothesis, the counting-rate gains in Row 2 are not in general as large as one would expect if much fuel had moved upward, nor are the counting-rate gains below Row 18 compatible with massive downward motion of fuel. At the same time, the extrusion of, say, 5% of the test fuel above Row 2 and another 5% below Row 22 cannot be ruled out on the basis of Figs. 54 and 56.

d. Fuel Motion at 7.72 s. The most rapid fuel motion seen by the hodoscope during the transient occurred at about 7.72 s, with the reactor power

about halfway down the trailing edge of the peak. The change that occurred in the 140-ms interval bracketing this motion are shown in Fig. 57. (The time interval for Fig. 57 overlaps those for Figs. 55 and 59.) Prominent features in this picture are the accumulation of fuel on the pump side at Rows 7-12, quite possibly breaching the fluted tube; the loss of fuel from the upper left and lower portions of the original fuel zone; and the small increases in fuel content extending 100 mm or more below the bottom of the original test fuel region.

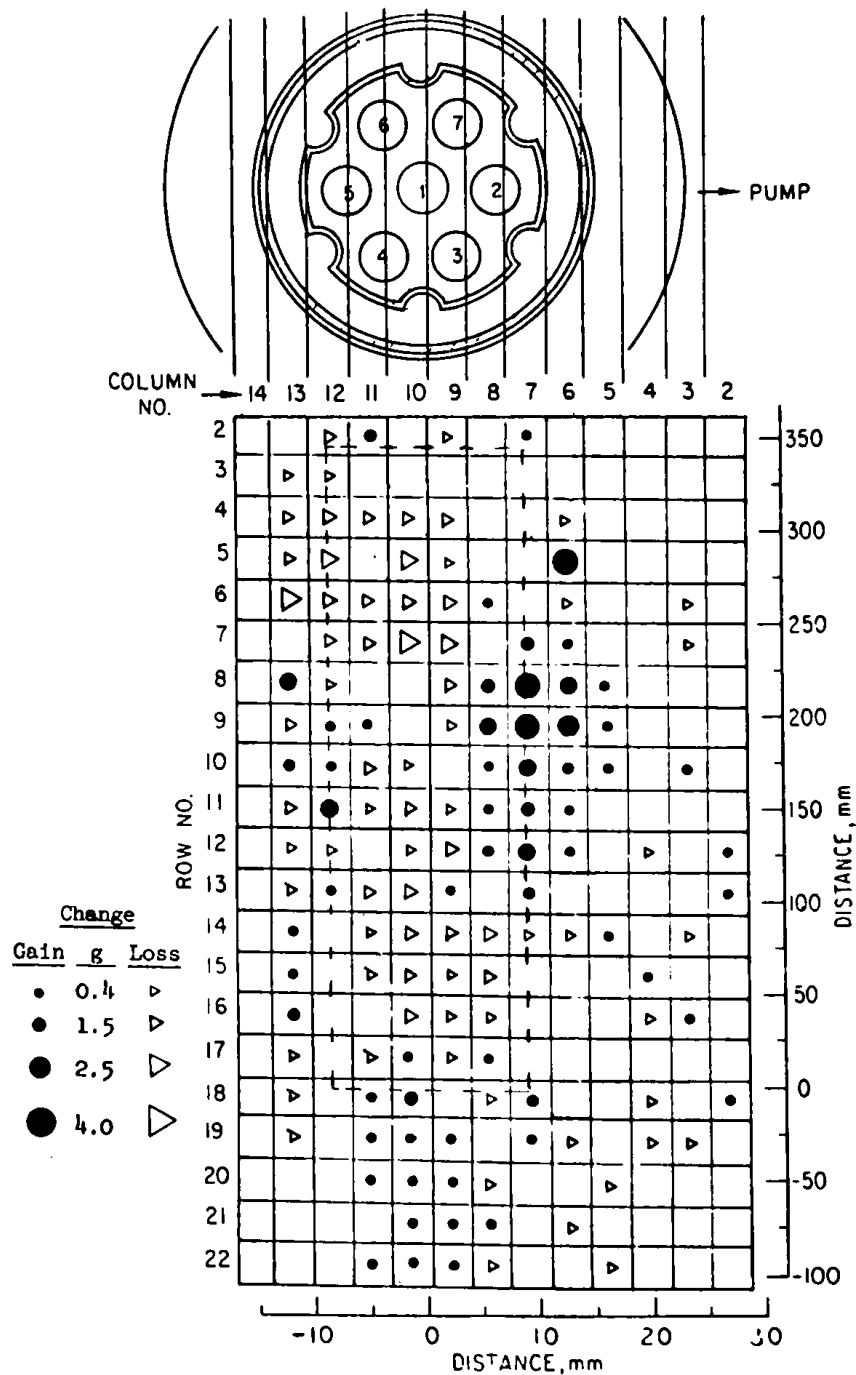


Fig. 57. Differential Hodograph for 7.63-7.77 s

Figure 58 shows the R/P curves for the 0.5-s interval from 7.5 to 8.0 s for selected channels with pronounced motion at or near 7.7 s. The two time bands indicated by the broken lines are the averaging intervals used

in constructing the differential hodograph of Fig. 57. The upper group of curves is from the upper left portion of the fuel zone, where a loss of fuel occurred, and the lower ones are from the right-hand parts of Rows 8-10, where fuel accumulated.

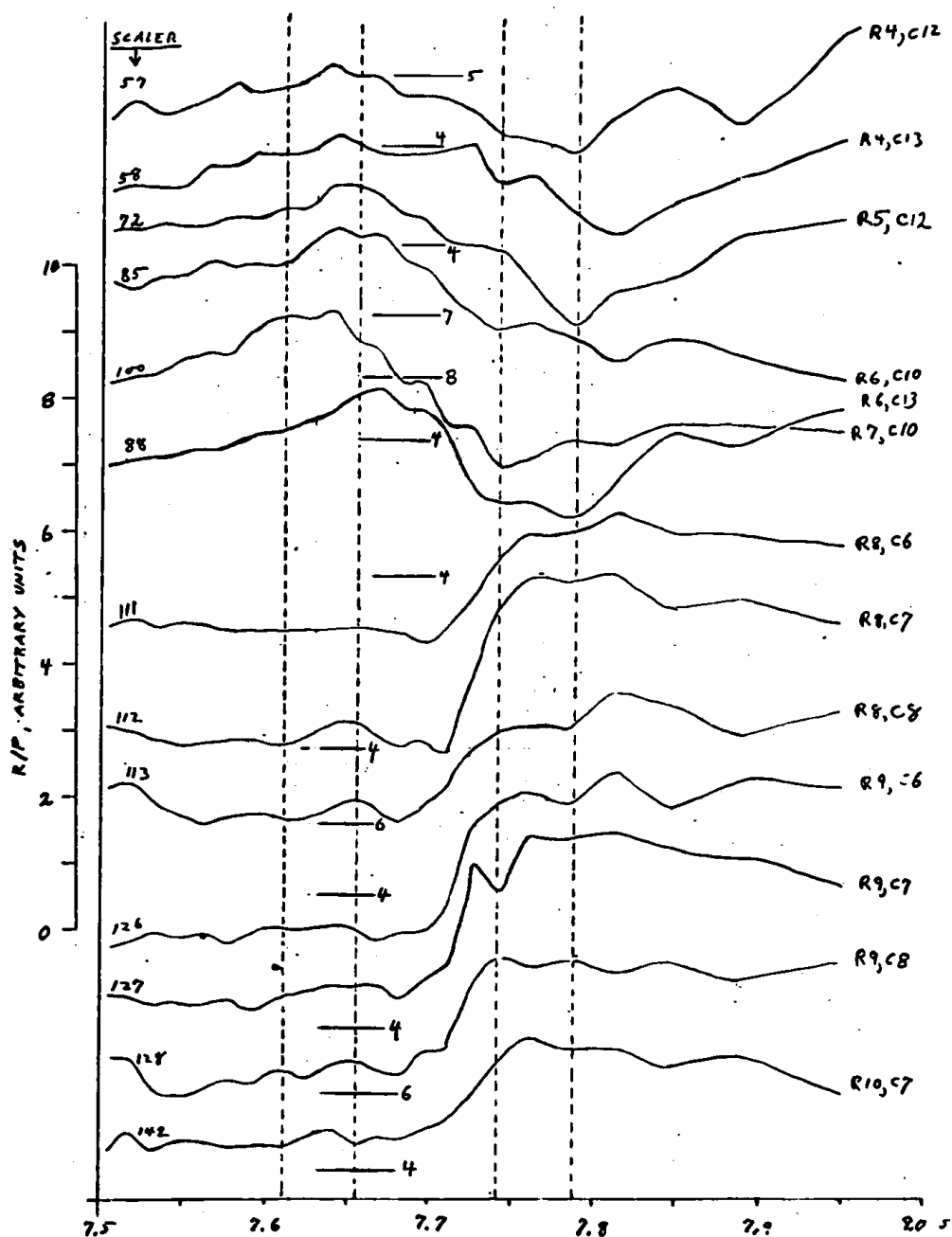


Fig. 58. R/P Curves for Certain Channels That Show Fuel Motion at 7.7 s. The broken lines indicate the time bands used in constructing the differential hodograph of Fig. 50. The horizontal lines, in conjunction with the scale at the left, show the absolute levels of the curves.

e. Fuel Motion at 7.72-7.81 s. Figure 59 shows the 90-ms interval from 7.72 to 7.81 s. Noteworthy here is the lack of fuel motion at the top and bottom edges of the fuel region. Instead, there is accumulation of fuel about a third of the way from the top, supplied both from above and below. Calculations indicate that most of the fuel is molten by this time. The lack of change at the upper and lower extremes of the fuel zone shows that the upper and lower boundaries of the fuel are not moving appreciably.

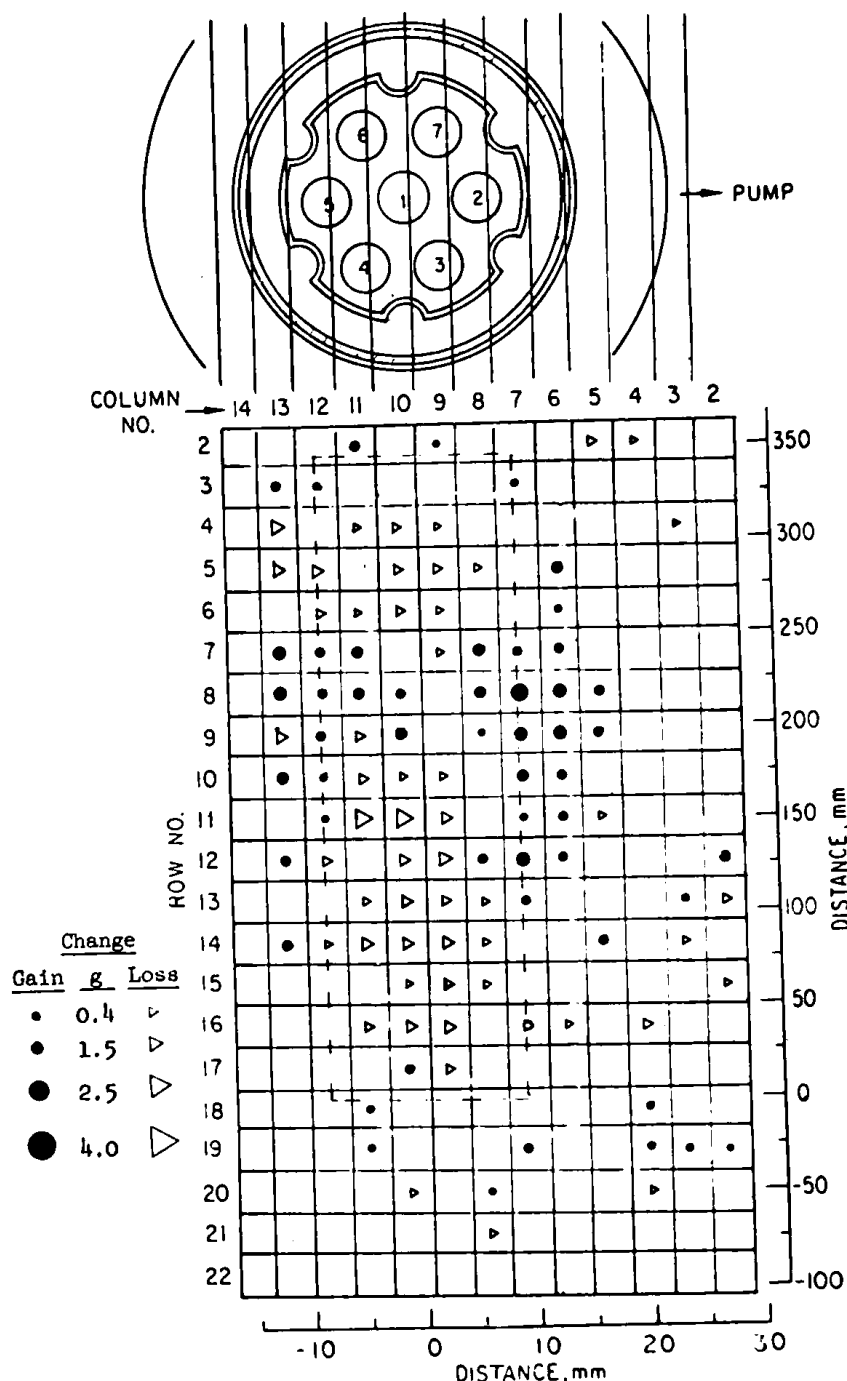


Fig. 59. Differential Hodograph for 7.72-7.81 s

The accumulated changes up to 7.81 s are shown in Fig. 60. Considering that fore-and-aft motion of fuel cannot be detected by the hodoscope, one can surmise from Fig. 60 that at 7.8 s there was an annulus of displaced fuel at the level of Rows 7-10, with a rather complete void at the original position of the central pin. Small amounts of fuel have moved above and below the original fuel boundaries. The fluted tube has probably been breached on the left (away-from-pump) side at Rows 7-9. On the pump side, the fuel from the upper portions of pins 5-7 is probably resting against the fluted tube, but does not appear to have penetrated it to any major extent. The fuel relocation depicted here did not occur rapidly; rather it took some 200 ms--from about 7.6 to 7.8 s--for the major part of the motion to occur.

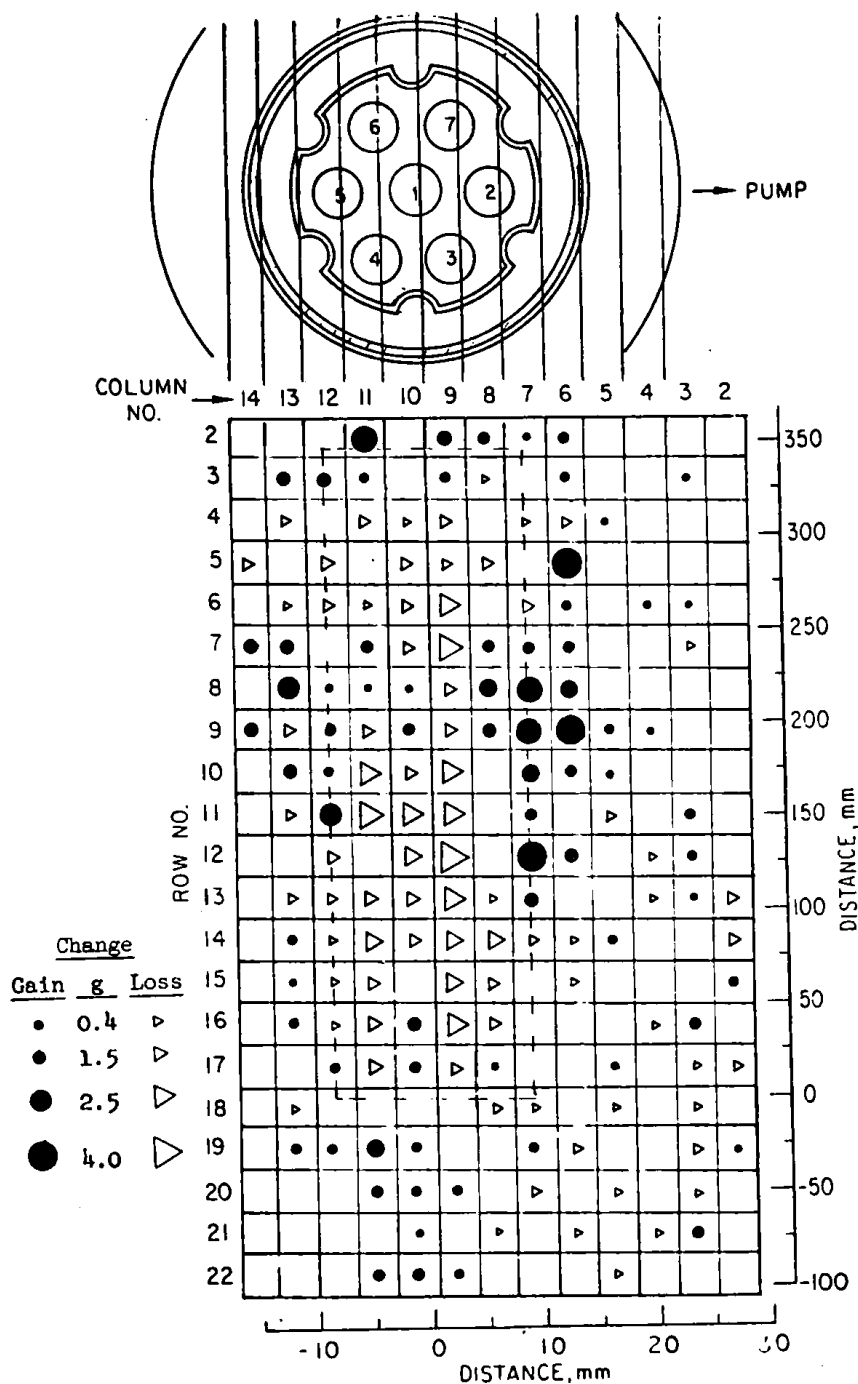


Fig. 60. Differential Hodograph for 5.73-7.81 s

f. Fuel Motion at 7.81-8.05 s. Figure 61 shows the changes during the 240-ms period from 7.81 to 8.05 s. Comparison with Fig. 59 reveals that the changes shown in that diagram are partially reversed in the current period, with decreases appearing where there had previously been increases, and vice versa. The fuel quantities involved are relatively small; clearly some churning is going on, but nothing dramatic.

g. Fuel Motion at 8.05-8.41 s. During the period from 8.05 to 8.41 s the power is very close to the preheat level (see Fig. 48). Some major leftward fuel motion occurs, as shown in Fig. 62, undoubtedly causing a major breach of the fluted tube on the side away from the pump. In addition, small quantities of fuel went up, down, and to the right--all at the expense of further voiding in the central regions.

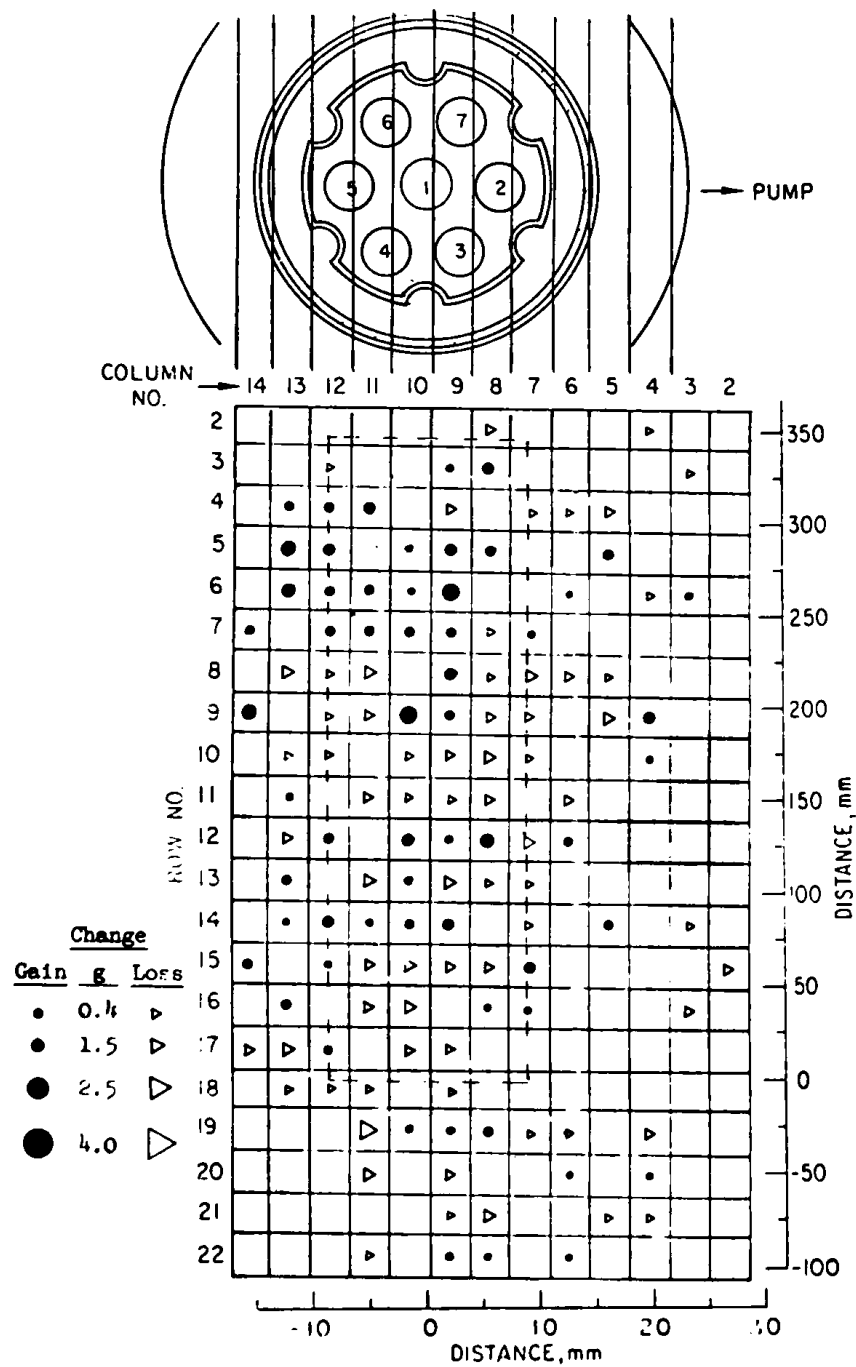


Fig. 61. Differential Hodograph for 7.81-8.05 s

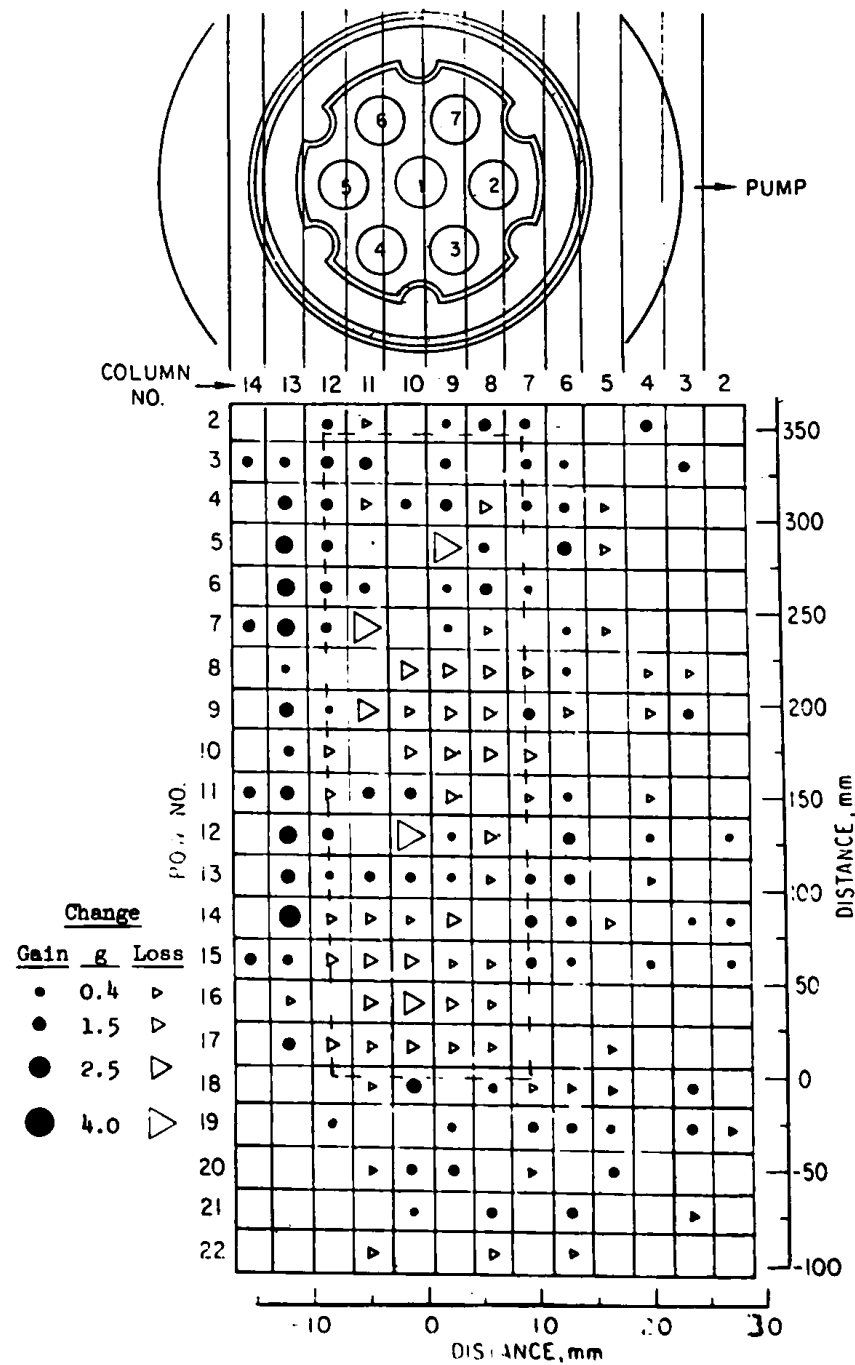


Fig. 62. Differential Hodograph for 8.05-8.41 s

The accumulated changes for the transient through 8.41 s are shown in Fig. 63. On the assumption that the fuel redistribution is radial, rather than just toward or away from the pump, we deduce that the lower two-thirds of the original fuel region is largely voided, that relatively small amounts of fuel have moved upward and downward, and that the fluted tube has been rather thoroughly breached on the side away from the pump. Some fuel has probably moved both upward and downward out of the field of view--but not much.

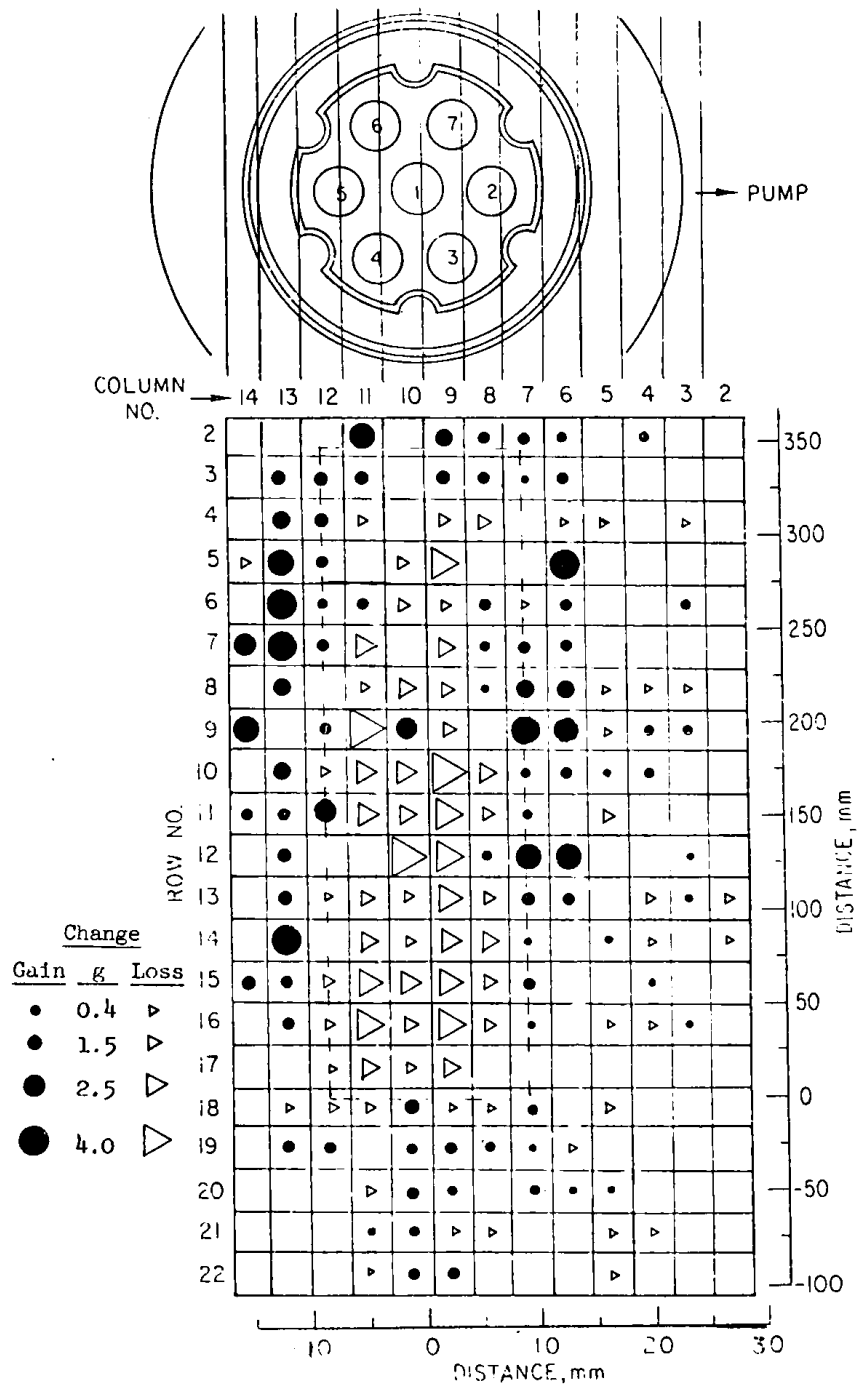


Fig. 63. Differential Hodograph for 5.73–8.41 s

Although the situation depicted in Fig. 63 does not correspond completely to the final fuel distribution as revealed by the posttest radiograph,

many of the same features are present in both. The radiograph (Fig. 64) shows a large, almost completely voided region near the midplane, whereas Fig. 63

shows some fuel still present at that level, at the periphery. Both the radiograph and the hodoscope show the general depletion of fuel concentration throughout most of the original fuel region, with fuel collected around much of the periphery.

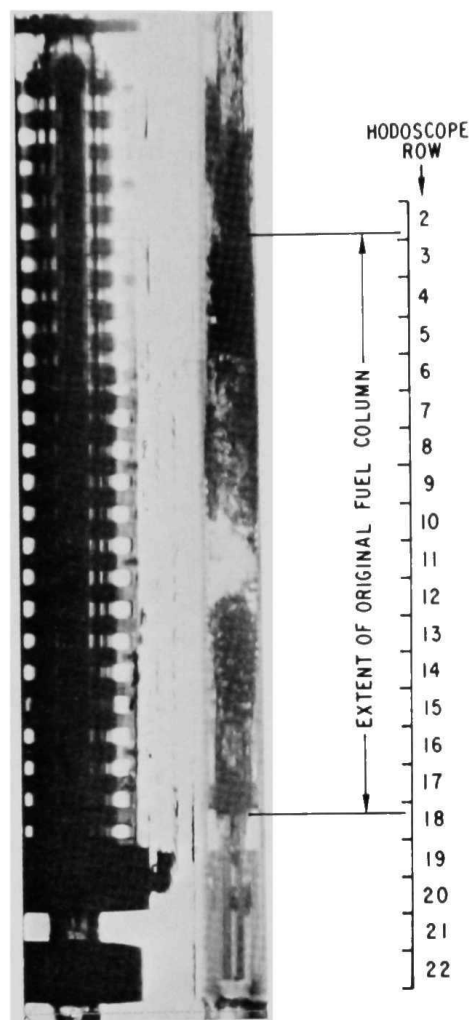


Fig. 64. Posttest Neutron Radiograph of Stripped Loop. Mag. $\sim 0.22X$.

The radiograph does not clearly reveal how much fuel was left above the original upper boundary of the fuel zone. The extra fuel that can be seen in Rows 2 and 3 of Fig. 63 amounts to about 20 g ($\sim 5\%$ of the original test fuel), and there is no reason to think there was not at least a small amount of fuel above the field of view. There is evidence, however, that not more than about 35 g could have been lost from the field before shutdown.

4. Postshutdown

Shutdown occurred at about 8.6 s, which was after the power had come down from the simulated excursion. Although the hodoscope film continued for about 2 s beyond shutdown, the combination of low statistics and film-scanning inaccuracies prevented detailed fuel-motion analysis in that region. Major fuel motion was occurring just before shutdown and presumably continued into the postshutdown period.

The loop instruments gave indications of disturbances at 10.96 and 17 s about which the hodoscope can shed no direct light, since the film ran out at 10.93 s--by which time the counting statistics were already too poor.

F. Posttest Radiography

The posttest neutron radiograph of the stripped loop, shown in Fig. 64, indicates that all the fuel elements had failed. Near the midlength of the original fuel columns a length of about 50 mm was practically empty of fuel. In this region, the fluted tube appeared to have melted entirely, and the bellows of the outer test section tube was partly melted. For about 121 mm below the empty region, the variations of density are indicative of a spongy or discontinuous mass of fuel. Within this region, radial motion of the fuel has been somewhat restrained by the fluted tube, which appears relatively intact toward the lower end. No complete pellets were in evidence at the bottom of the fuel columns, but the region of the last two pellets was masked by the presence of a stainless steel collar (see Fig. 7). A small amount of fuel and/or stainless steel was present among the bottom end plugs.

On the neutron radiograph, the presence of neutron-absorbing material in the bottom bend of the loop below the test section was masked by the remains of filter material on the outside of the tube. However, a subsequent determination using a gamma-radiation detector indicated a substantial local source of radiation in this region. Above the essentially fuel-free region near the mid-length of the fuel column, there is a region about 100 mm long of apparently spongy fuel. Since the fuel in this region appeared to be more dense on the periphery, it was probable that there was a hollow shell of spongy fuel.

Above this spongy fuel for about 63.5 mm (to the top of the original fuel columns) the neutron-absorbing material, presumably fuel, was quite dense. For the next 76.5 mm, above the top of the original fuel columns, much less dense regions of fuel and/or stainless steel were present. This last region included the upper part of the UO_2 stacks and the reflector rods of the elements.

In the plenum region of the elements, the neutron radiographs showed that the reflector rods and spacer tubes of some elements had dropped an appreciable distance as follows:

N-081	No drop
N-092	No drop
N-104	~63.5-mm drop
N-069}	One of these, 17.2 mm; the other, none.
N-115}	
N-185}	One of these, 57 mm; the other, 12 mm.
N-153}	

The UO_2 pellet stacks must have dropped as much as the spacer tubes and reflector rods, although the plenum components of several of the elements moved downward. The top end plugs of two of the elements appear to have moved upward: N-104, 6.4 mm, and either N-165 or N-153, 8 mm. The top of N-092, the center element, was covered by a structural member, and its position could not be determined. The sodium level appeared to be at the bottom of the test section opening to the upper sidearm to the pump.

VII. POSTTEST EXAMINATION

The E7 loop was stripped of its outer hardware in the HFEF-South at Argonne/West. After neutron radiography at TREAT, the loop was cut into sections at HFEF-South without removing the sodium. The following sections from the cutting operation were received at Argonne/East for further dis-

assembly and examination in the MSD Alpha-Gamma Hot Cell Facility (AGHCF): (1) a 910-mm length that contained the test section and fuel pins, (2) the upper and lower bends to the pump, (3) a small T-section with the bottom pressure-transducer port, and (4) the drain line from the bottom of the lower bend. Subsequent cuts and identification of the pieces are shown in Fig. 65.

A. Test-section Disassembly

Before disassembly of the loop test section in the AGHCF, an orientation groove was cut on the side of the loop toward the pump, from the outlet to the pump to the bottom of the test section. A transverse cut just below the upper pressure transducer separated the loop test section into two principal parts. The upper section, identified as A4, is shown in Fig. 65.

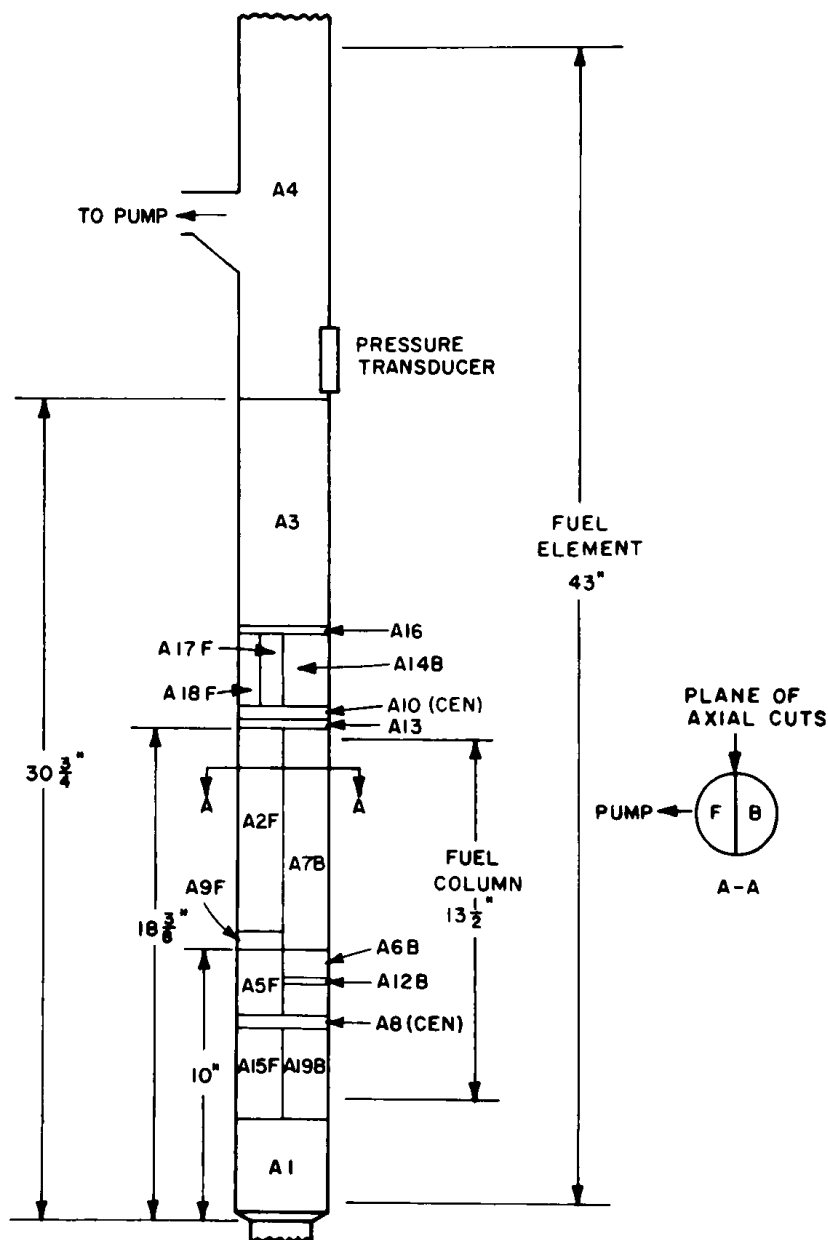


Fig. 65. Loop-cutting Plan for Posttest Examination.
Conversion factor: 1 in. = 2.54 cm.

lengthwise cuts were made through the loop wall for the full length of the section on opposite sides (180° apart) in a plane perpendicular to the plane of the pump and the test section. However, heating to melt the bonding sodium and moderate prying failed to separate the loop wall from the test section.

Transverse cuts were made on the loop to separate the sections in which the loop wall appeared to be fused to the underlying structure from

With some expectation that the loop wall could be removed from the part of the test section below A4, two

sections where such fusion was not obvious. By this approach the loop wall was removed from the test section from the bottom of section A13 to the top of A3, and from the bottom of section A1 to the top of A8, as well as from section A5F. The loop wall was still attached to sections A2F, A7B, and A6B.

After removal of the loop wall, the transverse sections A10 and A8, each 12 mm thick, were removed for subsequent analyses by the Chemical Engineering Division for postmeltdown mixing. Additional 12-mm-thick slices for analysis were subsequently cut as follows: A9F from the bottom of A2F, and A12B from the middle of section A6B.

Where possible, the outer test-section wall was removed from sections in a similar manner as the loop wall. The outer test-section wall was separated from sections A3, A14B, A17F, A18F, A15F, and A19B. The fluted tube was likewise removed from the sections of the elements in A3. The fuel-element end plugs in section A1 were unpinned and removed without difficulty.

Sodium samples for analysis were collected as follows: from the top of A1, from the top of A2F, from the bottom of A3, from the inside of the loop wall at sections A1 and A3, and from combined sections A5F and A6B.

Removal of sodium from the various sections was first attempted by melting and allowing the liquid sodium to run off. The sodium in section A7B would not run off. The sodium remaining on the pieces was reacted with ethyl alcohol, and the sections were then treated with a water-50% ethyl alcohol mixture and dried in a vacuum chamber.

The tops of the fuel elements were removed from section A4 by melting out the small amount of sodium. The loop part and the element sections were cleaned with ethyl alcohol to remove the remaining sodium. In the process of melting the sodium, the elements shifted position; their orientation, and hence identification, was lost.

The miscellaneous loop parts were also heated to melt out the sodium and then cleaned with alcohol.

The alcoholic liquors obtained from the reaction of ethyl alcohol with the sodium remaining on the sections after heating were separated from the insoluble residues by decantation. The residues were washed with water-50% ethyl alcohol and saved. The sodium melted out of the sections was also reacted with alcohol, and insoluble powder residues were saved. The recovered powders were separately saved for each principal section for later examination.

Photographs were taken during disassembly, as were photographs of sections after removing sodium. Sections containing fuel or insulator pellets were filled with epoxy to preserve the relationship between parts during

subsequent cutting operations. Specimens were cut from the epoxied sections for macroscopic examination and, in some cases, detailed examination of the microstructure.

B. Examination Results, General Features

In the parts received at the AGHCF, sodium was observed at the top flange to the pump, at the bottom of the test section, at both ends of the bottom bend, in the line to the pressure rupture disk, in the drain line before the freeze plug, and at the top and bottom of the T-section from below the test section. Sodium was not observed at the top of the test section, at the overflow line, at the upper pressure-transducer port, or at the outlet from the test section. Sodium was not observed in the drain line below the freeze-valve coil, on the pressure-transducer port of the T-section, or on the top end of the arm to the pump. The sodium that originally occupied these regions has drained into the adiabatic holder. The upper and lower pressure transducers were removed at HFEF, and holes were left in the sodium at their respective openings, thus accounting for the lack of sodium at the ports.

Since the sodium within the test section was disturbed by melting during the heating operation required to separate test-section parts, information on sodium reentry was not obtained.

After disassembly and sodium removal, the test-section parts were examined in some detail. A general description of the remains of the fuel elements from the bottom to the top follows.

The bottom end plugs were examined and photographed as shown in Fig. 66. Except for a small amount of steel spatter, the end plugs were quite clean. In the figure, the middle end plug (N-153) has more spatter along its

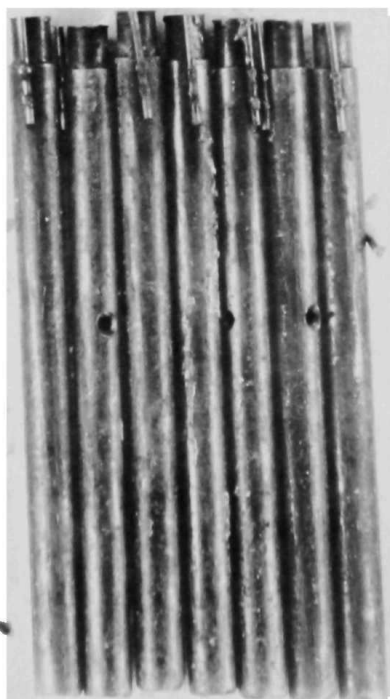


Fig. 66

Bottom End Plugs of Seven Elements with Some
Stainless Steel Spatter. Mag. $\sim 0.95X$. Neg.
No. MSD-169873.

length than the others. The material collected from among the end plugs is shown in Fig. 67. Globbs of melted stainless steel and melted fuel, and a piece of an unmelted UO_2 pellet, were present. It was not obvious that any of these pieces were bound to the end plugs either by fusion or mechanically. These pieces appeared to have been restrained from further downward movement by the roll pins locking the end plugs in place. The quantity of material recovered from among the end plugs was not sufficient to cause appreciable blockage to the flow of sodium through this region.

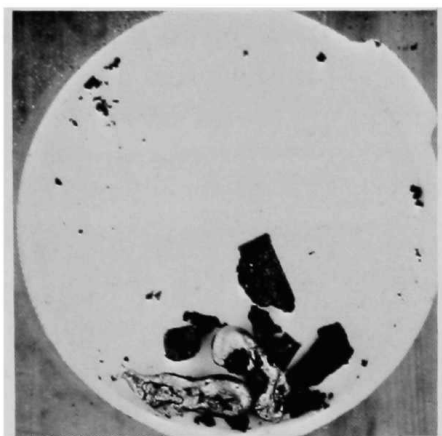


Fig. 67

Melted Stainless Steel, Melted Fuel, and a Piece of UO_2 Pellet Found among Bottom End Plugs. Mag. $\sim 6.80\times$. Neg. No. MSD-169874.

The 87-mm-long as-cut sections (A15F and A19B) immediately above the bottom end plugs in Fig. 65 originally contained a small part of the end plugs, 12 mm of UO_2 insulator pellets, and about nine fuel pellets per element. A cut on the long axis of this piece, in a plane almost perpendicular to the plane of the loop and the pump, separated the piece into two parts. The cut surfaces were photographed in a "light box," which resulted in mirror-image pictures as shown in Fig. 68. The F designation in section A15F identifies the piece nearest the pump, and the B in section A19B identifies the part away from the pump.

The UO_2 insulator pellets in this section at the bottom were cracked but otherwise intact. On the right side of section A19B (in the photograph), pieces of the insulator pellets fell out during the sodium-removal operation. Stainless steel appears to block the flow channels in the region of the UO_2 pellets on the side toward the hodoscope; fuel occupies channels on the



(a) Section A15F

(b) Section A19B

Fig. 68

Mirror-image Views of Split Section at Bottom of Fuel Columns. Mag. $\sim 0.98\times$. Neg. No. MSD-180130.

side away from the hodoscope. Where the melted fuel moved down in the channels around the UO_2 pellets, the cladding was melted away. Just above the insulator pellets, the fuel pellets have retained their shape, but the character of the fuel around the central void has changed from a dense columnar-grain structure to a spongy material. Parts of fuel pellets are identifiable to a height of about four pellets. Melted fuel appears to have flowed down among the partially intact fuel pellets. The cladding had melted almost completely off of the fuel pellets and relocated, partially downward. Above the region with the fuel pellets, fuel has completely melted and relocated. Some melted fuel moved downward, some may have moved upward, and some moved radially and resolidified as a spongy layer against the remnants of a badly melted fluted tube. At the upper end of this section, the fuel is located principally on the side (A19B) away from the pump.

A section 63 mm long (sections A5F and A6B in Fig. 65), starting 12 mm above the section shown in Fig. 68, is shown in Fig. 69. The lower part of the bellows is shown in which fuel and cladding have completely melted and relocated. Figure 69a shows combined sections A5F and A6B before sodium removal, with half the loop wall removed on side A5F. The mating half, section A6B, was fused to the loop wall. The interior of the bellows in sections A5F and A6B after sodium removal is shown in Figs. 69b and 69c. Some melted fuel lies against the partially melted bellows, chiefly on the side away from the pump. The fluted tube has completely melted in this region.

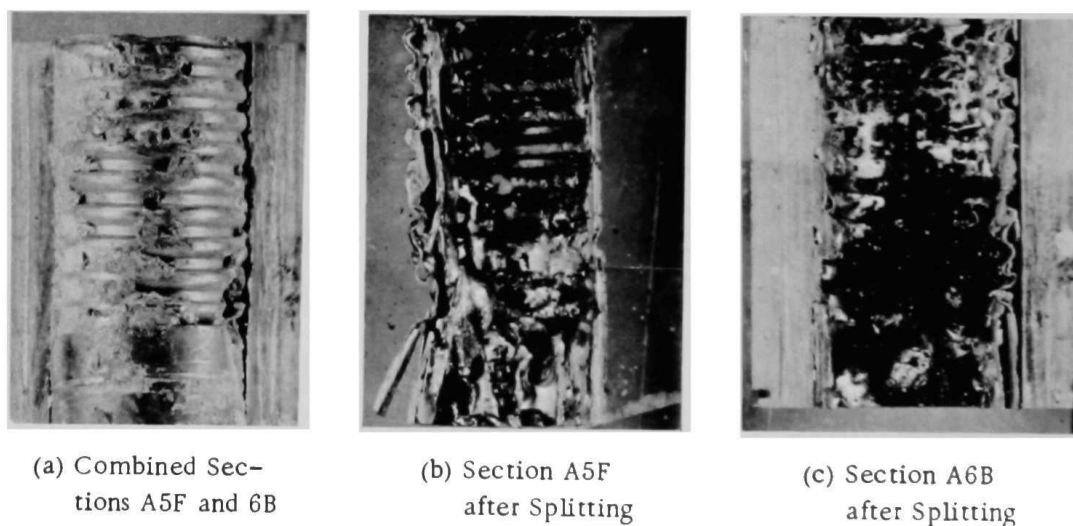
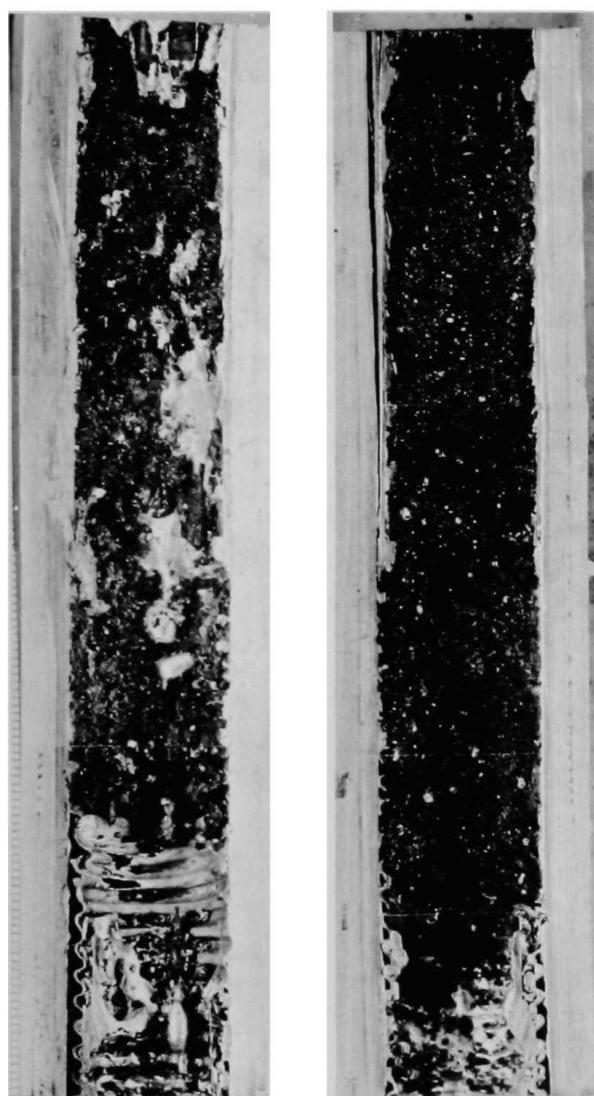


Fig. 69. Mirror-image Views of Section at Bottom of Bellows.
Mag. $\sim 0.70\times$. Neg. No. MSD-180854.

The bottom of combined sections A2F and A7B (see Fig. 70) is practically empty of fuel, confirming the evidence of the neutron radiograph. Some melted steel is present, however. Above this empty region, fuel forms a spongy layer ~ 76 mm long against the outer test-section tube, with the greater quantity of fuel on the side away from the pump. At the upper end of this 209-mm-long section, spongy fuel filled the cross section for ~ 90 mm. Portions of UO_2 insulator pellets were observed at the top of these sections

in some positions. Subsequently a UO_2 pellet was observed in a transverse section (see Fig. 71) through the fuel region about 38 mm below the top of the original fuel column. The location of the UO_2 pellet in the cross section appeared to correspond to either element N-104 or the adjacent element N-185. Some downward displacement of the stacks of UO_2 pellets had been inferred because of the downward shift of some of the Inconel reflector rods observed on the neutron radiographs. The outer test-section tube, except for the bellows, appeared to be intact, but fuel and steel inside had melted.



(a) Section A2F

(b) Section A7B

Fig. 70. Mirror-image Views of Split Section Showing Upper Two-thirds of Fuel-column Region. Mag. $\sim 0.58X$. Neg. No. MSD-169830.



Fig. 71. Melted Fuel and UO_2 Pellet at a Location about $1\frac{1}{2}$ in. (3.8 cm) below Original Top of Fuel Column. Mag. $\sim 7.14X$. Neg. No. MSD-180614.

Front and back views of section A14B after sodium removal are shown in Fig. 72. This 63-mm-long section was located 25 mm above the top of sections A2F and A7B (see Fig. 70). Stacks of UO_2 pellets occupied this region. Both melted fuel and melted steel were found among the stacks of pellets. The fuel was in greater quantity around the lower part of the UO_2 columns,

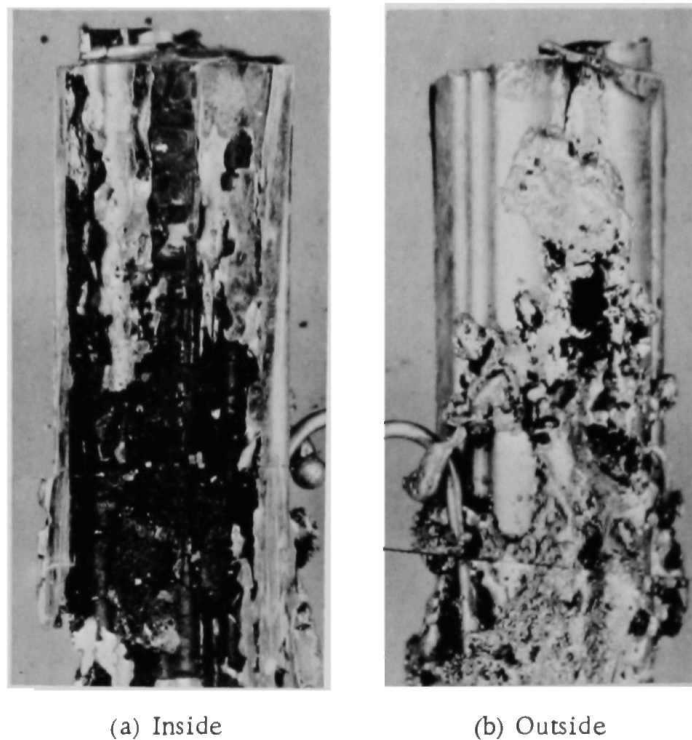


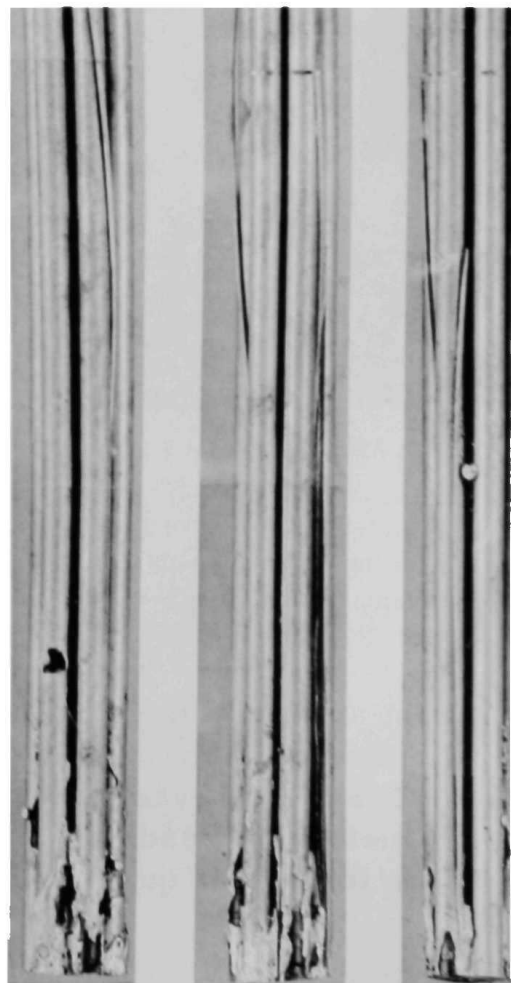
Fig. 72. Mirror-image Views of UO_2 -insulator-pellet Region above the Fuel. The fluted tube and two peripheral stacks of pellets were removed in view (a). Mag. $\sim 1.04X$. Neg. No. MSD-169831.

but melted steel was predominant toward the top of the section. Most of the cladding around the bottom of the UO_2 columns had melted off. Local melting of the cladding occurred mostly at the top. The removal of sodium also resulted in the removal of some melted fuel and the loss of some UO_2 pellets from this section. The general impression was that fast-moving melted fuel went up among the elements, melted the cladding around the UO_2 pellets, and tended to push the melted steel upward. (Probably small quantities of molten fuel were carried with the fast-moving vapor stream in the early stages of post-failure fuel movement prior to blockage.)

Three views of section A3 (see Fig. 65) at different rotations are shown in Fig. 73. The cluster

Fig. 73

Three Views at Different Angular Orientations of Fuel-element Cluster Including Top of UO_2 Stack and Reflector-rod Region (Section A3). Mag. $\sim 0.53X$. Neg. No. MSD-180853.



of seven elements was held together by melted stainless steel over a distance of 57 mm at the bottom, where extensive cladding melting had occurred. The element contained 75-90 mm of the 170-mm-long UO_2 pellet stacks, except for those with gross axial movement. Above the UO_2 pellets there was a 127-mm-long rod of Inconel 600. A hole melted through the cladding of a peripheral element at a place where there was a gap near the top of the pellet stack. Melting appeared to have occurred from the outside and the melted steel tended to move inward. The cause of the meltthrough was probably

melted fuel, which was subsequently moved or dislodged. The lack of a heat sink inside the cladding at this location may have contributed to the meltthrough. Since melted steel tended to move into the gap, the downward displacement of most of the stack of UO_2 pellets occurred before the meltthrough. The reason for the hang-up of the top UO_2 pellets in this element was not detected.

Figure 74 shows the relative displacement of the tops of the elements from section A4. The two that were raised by 6.3 mm were element N-104 and either N-185 or N-153, as noted from the neutron radiograph. The other elements, which include the center element N-092, were not significantly different in elevation and, hence, displacement. Fuel and stainless steel debris were not observed on these sections of elements.

C. Top and Bottom Blockages

The blockage at the bottom appeared to extend only over the 12-mm length of the UO_2 insulator pellets. Below this region, a small amount of melted fuel and melted steel was found among the end plugs as previously described. Above the insulator pellets, a jumble of fuel pellets and pellet parts, with practically no intermixed steel, was present. Channels for the flow of sodium appeared to exist in this region. The blockage around the insulator pellets (see Fig. 68) consisted of melted steel in some flow channels and melted fuel in others. Channels seemed to be associated with the spongy melted fuel, and a complete blockage to sodium flow seems doubtful at this location.

The top blockage was extensive in the axial direction. At its lower end, it consisted of a spongy mass of fuel near the top of the original fuel column. This spongy fuel filled the cross section of the outer test-section tube and was ~90 mm long. Above the fuel columns, the blockage consisted partly of melted fuel and partly of melted steel among the stacks of UO_2 pellets from which the cladding was melted. Figure 75 shows a transverse section (Section A10; see Fig. 65) near the bottom of the UO_2 stacks where the flow channels are occupied largely by melted fuel on the side away from the pump,

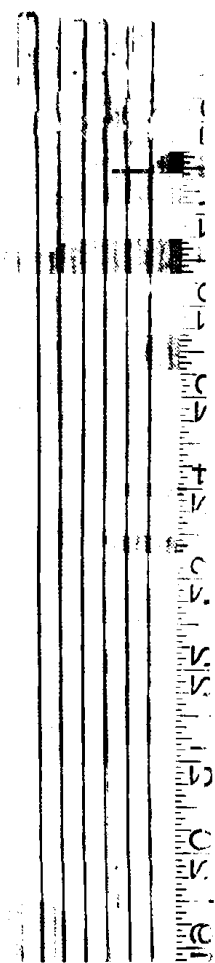


Fig. 74

View of Top of Elements
Showing Relative Dis-
placements. Mag. ~0.42X.
Neg. No. MSD-181391.

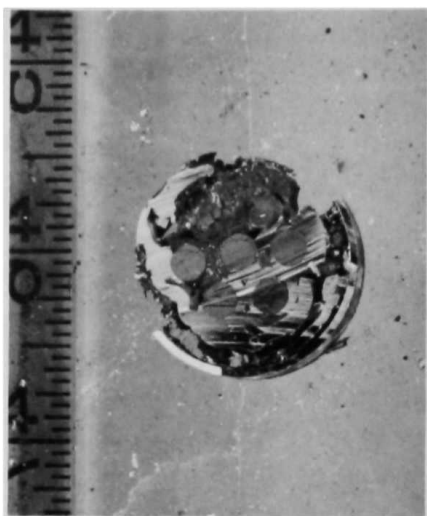


Fig. 75

Mirror-image View of Transverse Section of Fuel-element Cluster through UO_2 Pellets Showing Stainless Steel and Fuel Blockage (Section A10). Mag. $\sim 0.88X$. Neg. No. MSD-169698.

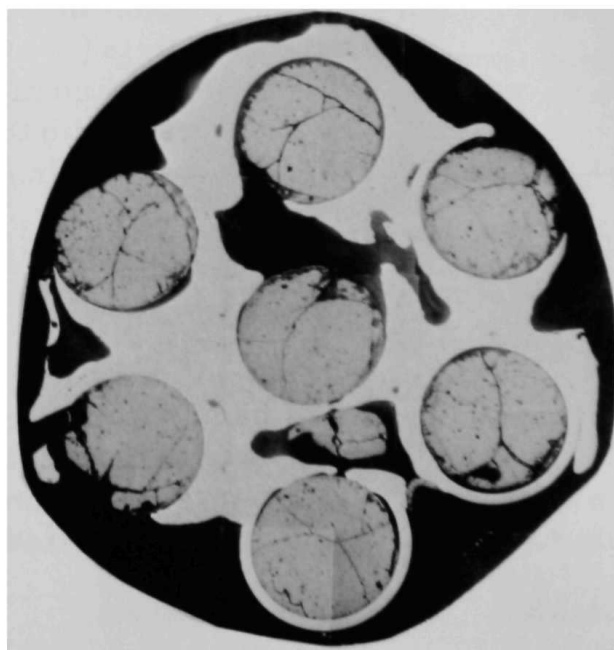
and by melted steel on the side toward the pump. Beginning about 57 mm above section A10 (see Fig. 75) for ~ 12 mm upward, the flow channels were mostly occupied by melted steel. Figure 76 shows the degree of blockage formed by melted steel at this location (bottom of section A3 in Fig. 65). Some fuel is also evident at this location, which was 95 mm above the top of the original fuel column. Scattered regions of melted steel were also evident for an additional few centimeters upward (see Fig. 73). Even where melted fuel or stainless steel occupied most of the available cross section, holes were evident that may have been interconnected and, hence, may have constituted channels for vapor streaming through porous plugs at inlet and outlet.

D. Extent of Melting

On the side away from the pump, fusion of the test section to the inside of the loop wall was general over the length of the bellows. On the side toward the pump, fusion to the loop wall occurred only at the top of the bellows. Below the bellows, melting of the outer test-section tube did not occur, and above the bellows, the tube was intact except for one location near the joint to the bellows. The extent of melting of the bellows is shown in Figs. 69 and 70. Melting of the bellows seems to have occurred to a somewhat greater extent on the side opposite the hodoscope in these mirror-image photographs. In Figs. 69a and 69b, perforations through the inward-projecting parts of the bellows are noted to occur on a somewhat vertical alignment. These melt-throughs appear to have formed from the inside out as a result of contact with melted fuel. Melted steel has solidified in the flutes of the bellows at some locations.

Fig. 76

Cross Section of Fuel-element Cluster near Midlength of UO_2 Stacks Showing Melted Steel around UO_2 Pellets. Mag. $\sim 3.45X$. Neg. No. MSD-181231.



Melting of the fluted tube occurred from the bottom of the fuel column to almost the top of section A14 (~90 mm above the top of the original fuel column). At the ends, melting was only partial, as can be seen in Figs. 68 and 72, and in a transverse section from just above the bottom header, near the foot of the fuel column, as shown in Fig. 77. Over most of the length of the fuel column, the fluted tube has completely melted.

Cladding and spacer wires have melted from the bottom of the fuel column to well above the top of the fuel column into the stacks of UO_2 pellets. The hole in the one element of Fig. 73 represents the highest location of cladding melting.

Except for ~20 mm at the bottom, the fuel column melted completely. The UO_2 pellets at the bottom were not melted, but some UO_2 pellets at the top had dropped into melted fuel and had fused superficially on the surface.

E. Microstructures

At the end of the preirradiation, a few pellets at the bottom of the fuel stacks did not melt or melted only partially. Microscopic examination of these pellets at high magnification was planned, but the pellets fell out before they could be epoxied. Consequently, an enlargement of part of Fig. 68 was made, as shown in Fig. 78, to show an intermediate stage between the irradiated pellet and melted fuel. Two of the bottom fuel pellets in the stack on the left have a dense outer shell of fuel with increasing porosity or sponginess toward the central void. Fission gases appear to have moved to the central void as the path of least resistance in fuel that was not melted but was probably close to the solidus temperature.

At all locations above the bottom four pellets, melting of fuel appeared complete. The structures of the melted fuel were generally equiaxed grains, but columnar grains indicating directional solidification were sometimes observed. Generally the melted fuel was closely associated with stainless steel and presumably the solid fission products. Porosity ranged upward from approximately 1- μm bubbles observed within grains, as shown in Fig. 79. Figure 79a is fuel from the top of the fuel column, and Fig. 79b is fuel from among the bottom end plugs (see Fig. 67). The grain boundaries of the fuel in Fig. 79b are much broader than observed in any other melted fuel samples and may contain a second phase. Intergranular voids are shown in Fig. 80. The large voids in Fig. 80b are ~200 μm long. The fuel in Fig. 80a is from the same transverse section as the fuel in Fig. 79a. The fuel in Fig. 80b is from the section shown in Fig. 71, ~38 mm below the top of the fuel column. Still larger voids can be seen in the spongy material in Figs. 71 and 77. The wide distribution of pore size appears to be a general feature of the melted fuel.

A general feature observed from the top to the bottom of the distributed fuel is the presence of small globules of metallic material, which from its

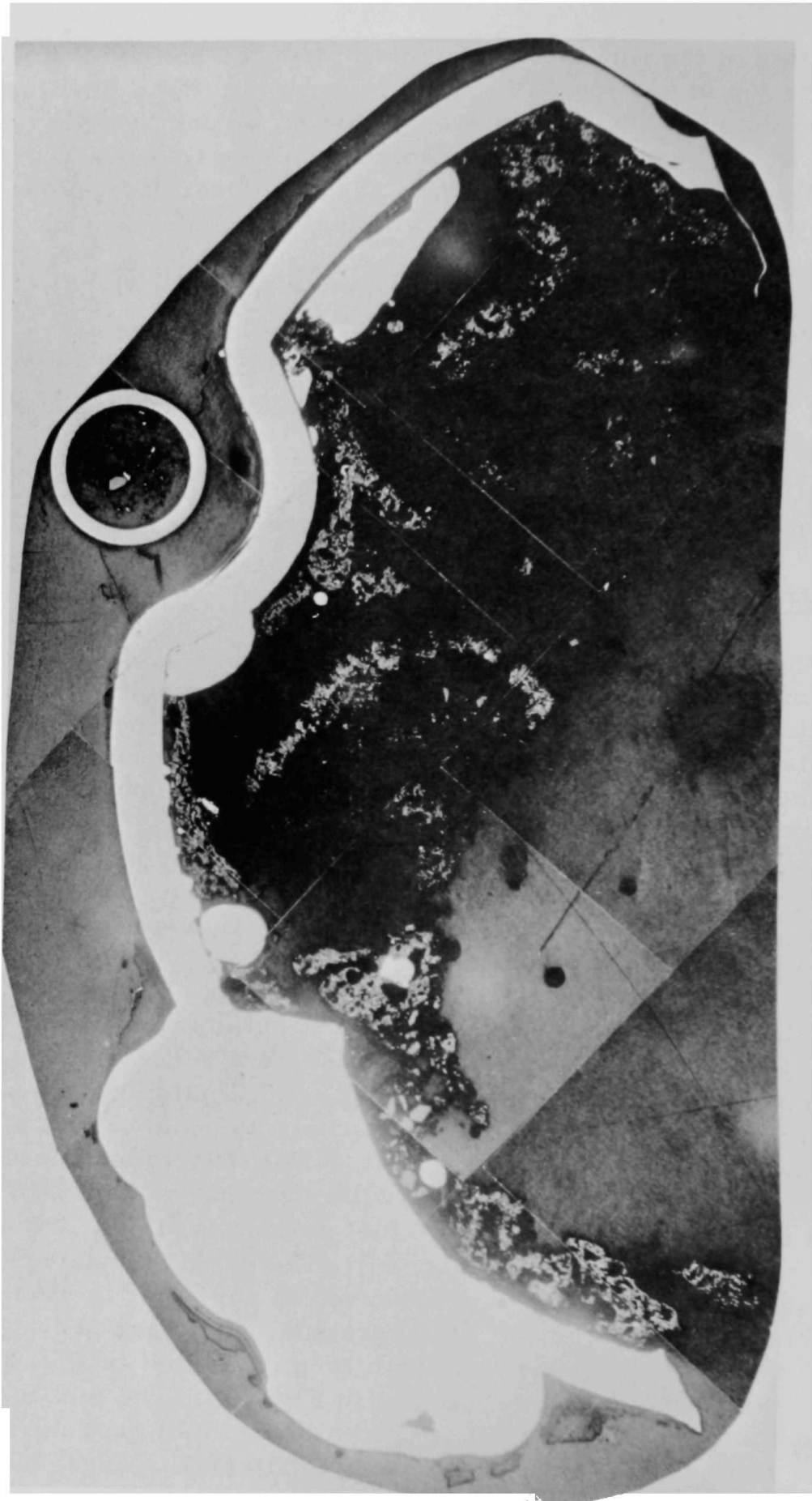
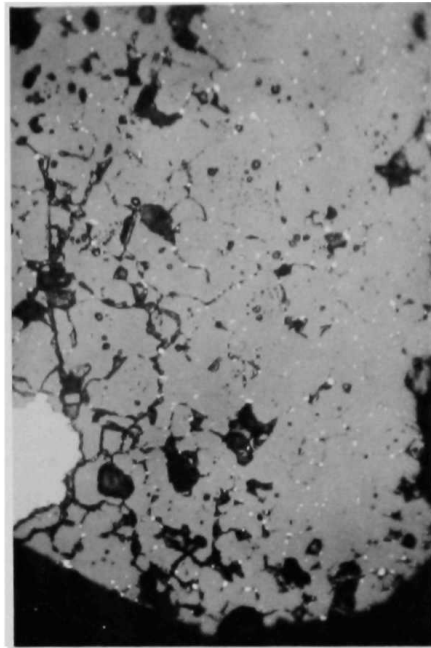


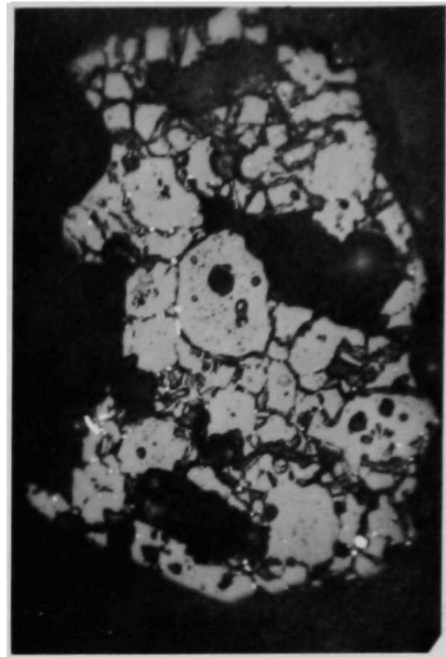
Fig. 77. Transverse Section near Bottom of Fuel Column Showing Melting of Fluted Tube and Distribution of Melted Fuel. Mag. $\sim 9.14X$. Neg. No. MSD-181706.



Fig. 78. Enlargement of Section A15F (see Fig. 68a) Showing Porosity around Central Void in Fuel Pellets.
Mag. $\sim 3.5X$. Neg. No. MSD-169876.



(a) From Top of Fuel Column.
Mag. $\sim 250\times$. Neg. No.
MSD-180777.

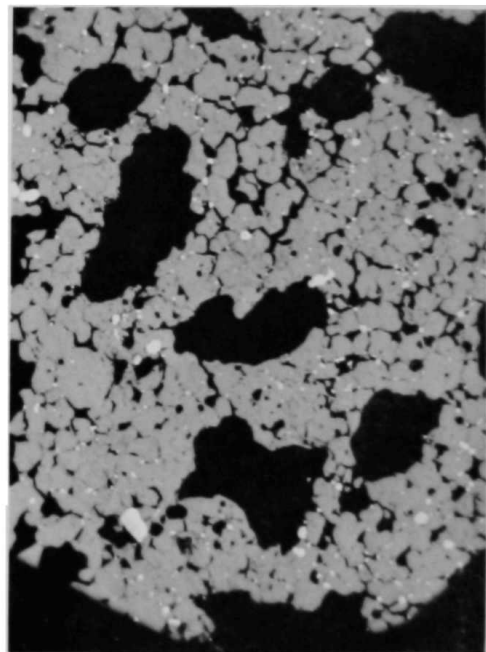


(b) From Debris among Bottom
End Plugs. Mag. $\sim 250\times$.
Neg. No. MSD-180765.

Fig. 79. Fine Porosity in Melted Fuel



(a) Mag. $\sim 125\times$. Neg.
No. MSD-180775.



(b) Mag. $\sim 100\times$. Neg.
No. MSD-180800.

Fig. 80. Intergranular Porosity in Melted Fuel

abundance is concluded to be stainless steel, perhaps in association with some fission products. Figure 79b (bottom) shows small, 1-2- μm particles of metal, few in number and randomly dispersed, mostly on grain boundaries. A very uniform dispersion of a large number of 1-2- μm metallic particles is shown

in Fig. 81. This type of dispersion was unique and occurred in rather dense fuel in the insulator-pellet region shown in Fig. 76. Other metallic dispersions are shown in Figs. 71, 77, 79, and 80a. The large globs of steel in melted fuel probably were intrusions after the fuel had solidified. Intrusive melted steel is shown in Fig. 82 as a dendritic structure in intimate association with fuel. It is from the same transverse section as in Fig. 71. Stainless steel dispersed in fuel generally has a wide range of particle sizes depending on its history.

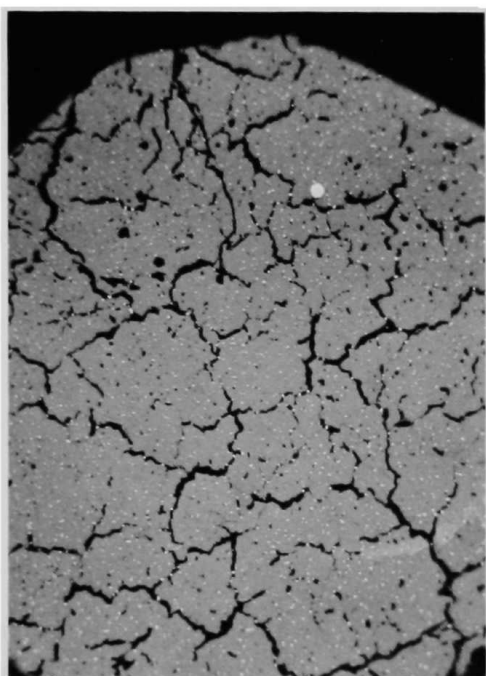


Fig. 81

Fine, Uniform Dispersion of Metallic
Particles in Melted Fuel. Mag. $\sim 100\times$.
Neg. No. MSD-180833.

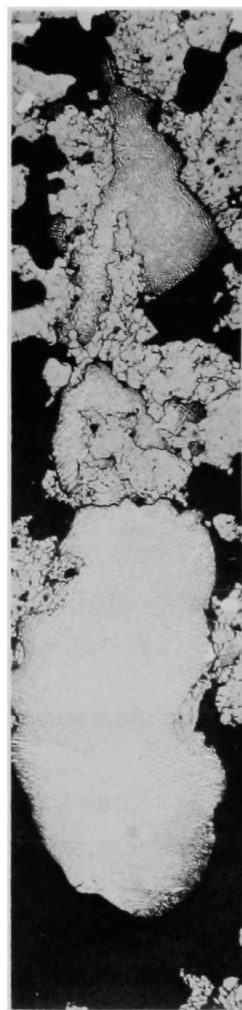
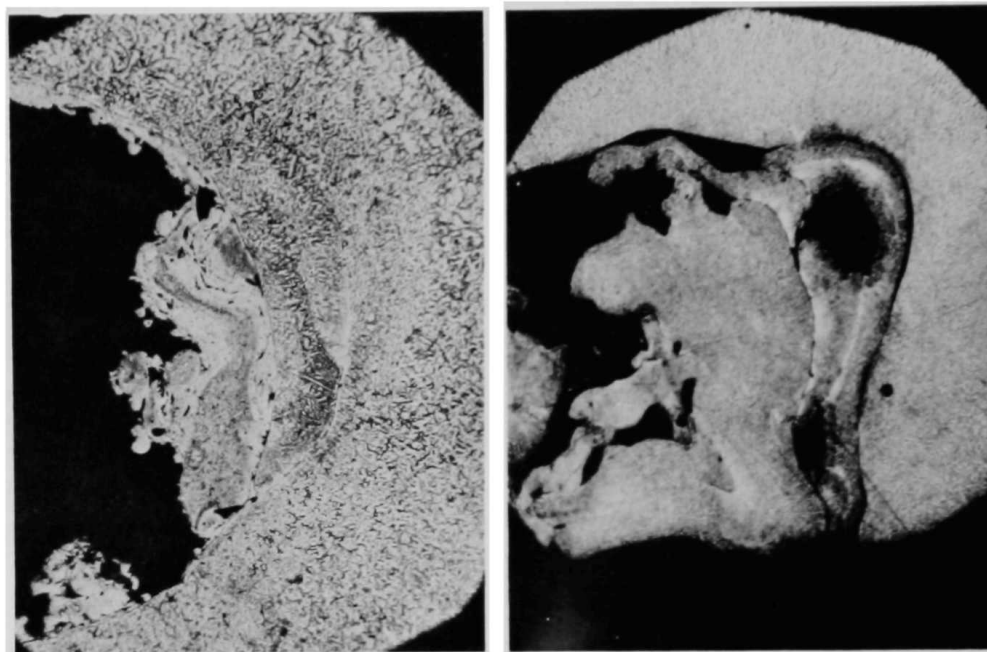


Fig. 82

Intrusive Melted Steel with
Melted Fuel. Etched, Oxalic
acid. Mag. $\sim 25\times$. Neg. No.
MSD-180863.

On melting, stainless steel may become intimately associated with fuel to a degree partly dependent on temperature. Figure 71 shows large globules of melted stainless steel in a matrix of spongy fuel. Although most of the steel seems to have moved radially or upward ahead of the fuel, some did become trapped in the melted fuel. The previous discussion on fuel showed the intimacy of mixtures of fuel and steel. On the periphery of the cluster of elements, where melted steel has solidified and has located among the bottom

plugs, the solidified steel appears in many instances to have frozen very rapidly. Typical contorted structures of stainless steel are shown in Fig. 83. Structures of this type were not observed in loss-of-flow Tests L2-L4. The generally finer dendritic structure of the steel in Fig. 83b (from among the end plugs) implies a faster rate of cooling compared to the steel in Fig. 83a (from the top of the fuel column near the outer wall).



(a) Etched, oxalic acid. Mag. $\sim 50\times$.
Neg. No. MSD-180772.

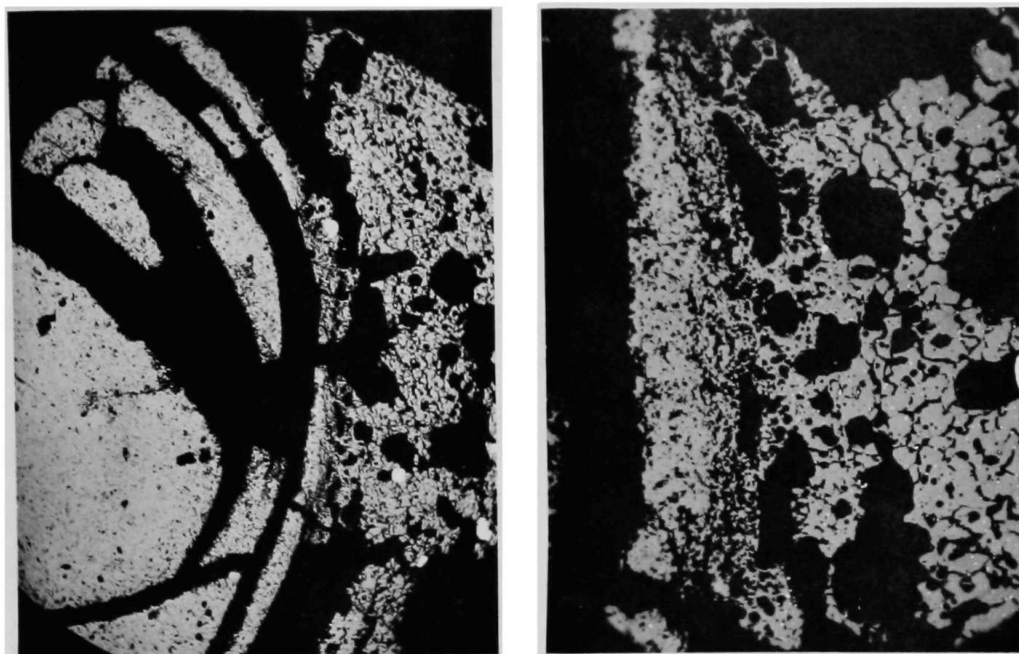
(b) Etched, CuCl_2 . Mag. $\sim 25\times$.
Neg. No. MSD-180766.

Fig. 83. Solidified Stainless Steel Showing Effects of Rapid Cooling

Except for cracking, the UO_2 pellets were generally unaffected by the transient, unless they were in intimate contact with melted fuel. Figure 84 shows a UO_2 pellet that dropped into the melted fuel at the top of the fuel column. Segments of arcs of UO_2 have spalled off of the pellet. The UO_2 has fused to the fuel around it, as shown in Fig. 84b at higher magnification. Metallic particles are present in the fuel, but not in the UO_2 . A small isolated particle of UO_2 was found in a region of melted fuel in the same region as shown in Fig. 71. This particle is shown in Fig. 85. Cracks are evident, and grain-boundary separation with the development of attendant porosity has occurred. Gases in the as-fabricated pellets contribute to the development of porosity.

F. Fuel-element Plenum Sections

The tops of the fuel elements were removed from section A4. Identification numbers on the top end plugs were tube numbers, but these numbers could not be correlated with the element number on the bottom plugs with the information at hand. The top section of element N-092, the central element, was identified by the spring with 25 coils, compared to 19-20 coils for all the other springs. The plenum sections of the elements are shown in Fig. 74.



(a) Mag. $\sim 25X$. Neg.
No. MSD-180617.

(b) Mag. $\sim 100X$. Neg.
No. MSD-180615.

Fig. 84. Fusion between Melted Fuel and a UO_2 Insulator Pellet

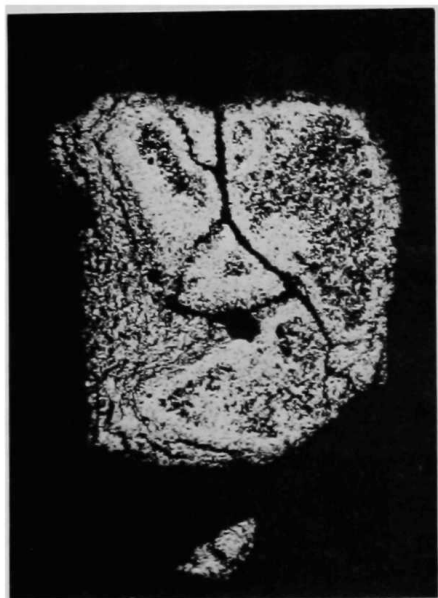


Fig. 85

Isolated Particle of UO_2 Showing Grain-boundary Separation Found in Melted-fuel Region. Mag. $\sim 45X$. Neg. No. MSD-180616.

Diameters of each element section were measured at 25-mm intervals and at 0 and 90° on the circumference for a total of 14 measurements per element. The average diameter and the range of diameters were 5.813 ± 0.023 mm. The diameter specified on the fuel-element drawing was $5.77-5.82$ mm. The posttest diameters are slightly on the low side. Diameter changes or the generation of ovality in the plenum region of the fuel element do not appear to have occurred from Test E7.

The spacer tubes and springs were removed from the plenum sections after heating to melt sodium. Sodium was found between the spacer tubes and

cladding, and up around some of the springs. A comparison of the lengths of the springs and the spacer tubes with the length of cladding indicated that, in some cases, considerable free space existed above the spacer tube. This was in accord with the evidence of the neutron radiographs. Data are shown in Table VI.

TABLE VI. Measurements of Upper-plenum Pieces

Top-plug Identification	Spring Length, mm	Overall Length of Section, mm	Coils per Spring	Gap in Plenum Region, mm
N-022	27.4	339.5	20	63.3
N-029	27.4	338.0	19	67.4
N-015	26.7	334.0	19	11.9
N-057	-	333.6	25	4.8
N-078	26.7	333.2	19	8.9
N-014	26.9	333.2	20	-0.3
N-061	26.9	332.4	19	-3.5

The relative gaps in the plenum corresponded in a general way with the amount of downward movement of the reflector rods and spacer tubes as determined from the neutron radiographs. However, differences as measured were greater than expected from the nature of the procedures used. Handling during the early attempts to remove the split loop from the test section by melting the sodium probably resulted in some movement of the parts.

Five of the section lengths were 339.5 ± 3.2 mm, and the other two elements were about 6.2 mm longer. On the basis of the neutron radiographs and these measurements, the N-022 top plug can be paired with element N-104, and top plug N-029 with either element N-185 or -153. By comparison with the results of Test L4, which was of similar geometry, the tops of the two longer-plenum sections appear to have moved upward as a result of the transient.

The spring constants were measured for two springs with the following results: N-014, 1.05 kN/m (6.0 lb/in.), and N-078, 1.03 kN/m (5.9 lb/in.) as compared with the as-fabricated specification of 0.70-0.84 kN/m (4.0-4.8 lb/in.). Irradiation hardening probably occurred during irradiation in EBR-II and may have resulted in a stiffer spring. These pretest results for spring constants compare with values of 0.93-1.17 kN/m (5.3-6.7 lb/in.) for similar elements in Test L4.

VIII. CALCULATIONS

Test instrumentation on the loop monitored flow, pressure, and temperature conditions at the inlet and outlet of the fuel-pin bundle. Detailed

conditions within the cluster must be estimated through calculations. The COBRA-3H code was used to calculate fuel, cladding, and holder-wall temperatures as functions of radius, azimuthal sector, and axial elevation. Details of these calculations are given in Appendix B.

Output from the thermal-hydraulic COBRA calculations include detailed fuel enthalpies and clad temperatures. These are then used in the Damage Parameter Model of Baars, Scott, and Culley³ to predict the time and location of initial cladding failure.

A. General Results of COBRA Calculations

To a good approximation, the results of the COBRA calculations yield the same temperature distributions for all pins in the cluster at a given radially averaged fuel enthalpy. This is shown in Fig. 86. These results apply to all axial zones and azimuthal sectors. Melting of the columnar grains begins at 0.837 MJ/kg (200 cal/g) and reaches the equiaxed-grain region as the fuel enthalpy reaches 0.987 MJ/kg (236 cal/g).

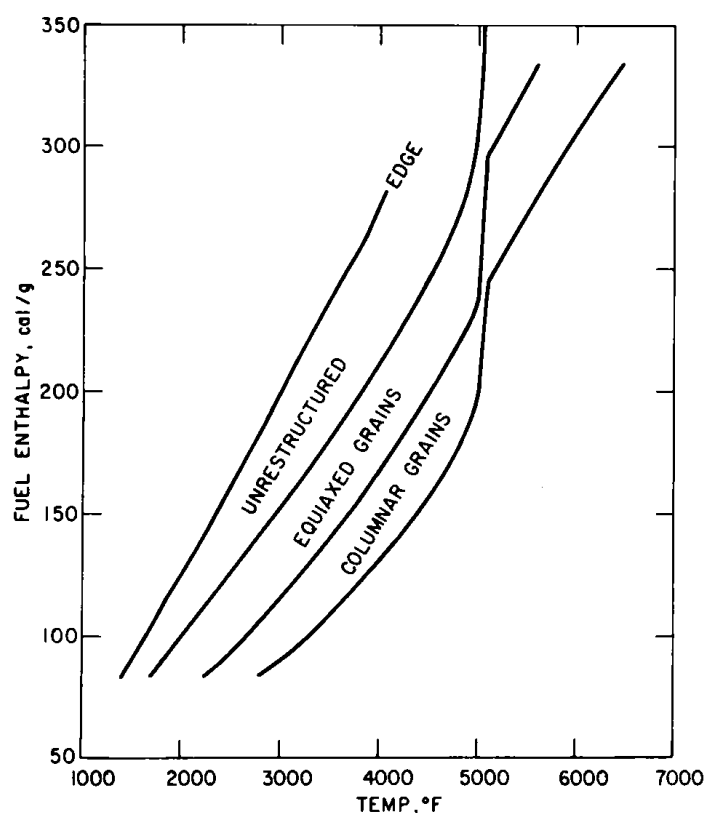


Fig. 86

Generalized Radially Averaged Fuel-enthalpy/
Temperature Results by Grain-structure Region.
Conversion factors: 1 cal/g = 4.184 x
10⁻³ MJ/kg; $t (^{\circ}\text{C}) = [t (^{\circ}\text{F}) - 32]/1.8$.

The results for the four fuel rods included in the calculations are listed in Table VII. Examination of the data in the table shows that the axial "hot spot" moves from the top third of the pin toward the center as the transient progresses.

B. Temperature Distribution at End of Preheat

Four pin cases were calculated: the central pin, the pin closest to the ALIP, a pin representing each of the three pins opposite the ALIP, and a pin

TABLE VII. Calculated Fuel Enthalpy and Cladding Temperatures

ROD 1 ENTHALPY								ROD 3 ENTHALPY							
TIME	AXIAL ZONE							TIME	AXIAL ZONE						
	1	2	3	4	5	6	7		1	2	3	4	5	6	7
3.300	0.0	0.0	0.0	0.0	0.0	0.0	0.0	3.300	0.0	0.0	0.0	0.0	0.0	0.0	0.0
4.600	35.40	37.50	38.10	38.30	38.20	37.78	35.76	4.600	35.92	38.07	38.70	38.88	38.76	38.33	36.23
5.400	61.85	68.09	70.14	70.96	70.92	69.97	64.07	5.400	63.30	69.74	71.85	72.69	72.66	71.69	65.59
6.200	76.92	84.52	87.79	89.88	91.01	91.00	84.69	6.200	78.63	86.29	89.62	91.78	92.99	93.01	86.70
7.000	84.16	91.84	96.07	99.02	101.30	102.60	98.10	7.000	85.73	94.22	98.75	101.60	103.40	104.50	100.10
7.100	85.83	93.85	98.29	101.30	103.50	104.80	100.40	7.100	87.42	96.47	101.20	104.20	105.90	106.80	102.40
7.200	90.68	100.00	104.90	108.00	110.00	111.00	106.00	7.200	92.56	103.10	106.20	111.20	112.90	113.50	108.10
7.300	101.40	113.20	118.70	122.00	123.90	124.40	116.90	7.300	104.00	116.90	122.70	126.00	127.60	127.70	119.60
7.350	110.50	124.30	130.30	133.80	135.50	135.60	126.30	7.350	113.60	128.50	134.80	138.30	139.80	139.50	129.40
7.400	123.10	139.30	146.10	149.70	151.40	151.00	139.10	7.400	126.80	144.20	151.30	155.00	156.40	155.60	143.00
7.440	136.20	154.90	162.40	166.30	167.90	166.90	152.60	7.440	140.50	160.60	168.50	172.40	173.60	172.30	157.10
7.480	152.60	174.40	182.90	187.10	188.40	186.90	169.60	7.480	157.70	181.00	189.60	194.00	195.10	193.10	174.80
7.500	162.20	165.80	194.70	199.10	200.30	198.40	179.40	7.500	167.70	192.60	202.20	206.60	207.50	205.20	185.10
7.520	172.60	198.20	207.80	212.30	213.40	211.20	190.20	7.520	178.70	205.80	215.80	220.40	221.20	218.50	196.40
7.540	184.10	211.80	222.00	226.70	227.70	225.00	202.00	7.540	190.70	220.00	230.70	235.40	236.20	233.00	208.80
7.560	196.30	226.30	237.20	242.10	243.00	239.90	214.70	7.560	203.50	235.20	246.60	251.60	252.20	248.50	222.00
7.580	209.00	241.30	252.90	258.00	258.90	255.30	227.80	7.580	216.70	250.90	263.00	268.20	268.70	264.60	235.70
7.600	221.50	256.10	268.40	273.80	274.50	270.50	240.70	7.600	229.80	266.40	279.30	284.70	285.10	280.50	249.30

ROD 1 CLAD TEMPERATURE								ROD 3 CLAD TEMPERATURE							
TIME	AXIAL ZONE							TIME	AXIAL ZONE						
	1	2	3	4	5	6	7		1	2	3	4	5	6	7
3.800	720.	721.	721.	721.	722.	722.	722.	3.800	720.	721.	721.	721.	722.	722.	722.
4.600	735.	740.	744.	748.	751.	754.	755.	4.600	736.	740.	744.	748.	751.	754.	755.
5.400	770.	797.	822.	846.	868.	887.	898.	5.400	771.	798.	823.	847.	869.	888.	899.
6.200	803.	851.	896.	941.	988.	1020.	1042.	6.200	805.	853.	899.	943.	985.	1022.	1044.
7.000	830.	884.	934.	987.	1041.	1090.	1124.	7.000	832.	883.	934.	988.	1041.	1093.	1126.
7.100	839.	891.	941.	994.	1048.	1100.	1134.	7.100	841.	891.	941.	994.	1048.	1101.	1137.
7.200	859.	909.	960.	1014.	1068.	1123.	1161.	7.200	857.	909.	961.	1014.	1068.	1121.	1165.
7.300	879.	939.	998.	1057.	1114.	1168.	1218.	7.300	877.	939.	998.	1057.	1113.	1168.	1216.
7.350	893.	961.	1026.	1089.	1150.	1206.	1254.	7.350	892.	961.	1026.	1089.	1149.	1206.	1252.
7.400	911.	990.	1063.	1133.	1198.	1258.	1304.	7.400	911.	990.	1063.	1133.	1198.	1257.	1303.
7.440	930.	1019.	1100.	1177.	1248.	1310.	1356.	7.440	929.	1018.	1099.	1176.	1247.	1309.	1355.
7.480	952.	1053.	1145.	1230.	1308.	1375.	1420.	7.480	951.	1052.	1144.	1230.	1307.	1374.	1419.
7.500	964.	1073.	1170.	1261.	1342.	1412.	1458.	7.500	963.	1072.	1169.	1260.	1341.	1411.	1457.
7.520	977.	1094.	1198.	1295.	1380.	1454.	1501.	7.520	976.	1093.	1197.	1294.	1379.	1452.	1499.
7.540	991.	1117.	1228.	1331.	1421.	1499.	1547.	7.540	990.	1116.	1227.	1330.	1420.	1497.	1545.
7.560	1006.	1141.	1261.	1371.	1466.	1548.	1597.	7.560	1005.	1140.	1259.	1369.	1465.	1546.	1595.
7.580	1022.	1167.	1295.	1412.	1515.	1601.	1651.	7.580	1020.	1165.	1294.	1411.	1513.	1599.	1649.
7.600	1038.	1193.	1331.	1456.	1566.	1657.	1708.	7.600	1036.	1191.	1329.	1454.	1564.	1655.	1706.

ROD 2 ENTHALPY								ROD 4 ENTHALPY							
TIME	AXIAL ZONE							TIME	AXIAL ZONE						
	1	2	3	4	5	6	7		1	2	3	4	5	6	7
3.800	0.0	0.0	0.0	0.0	0.0	0.0	0.0	3.800	0.0	0.0	0.0	0.0	0.0	0.0	0.0
4.600	33.92	35.73	36.27	36.42	36.32	35.96	34.19	4.600	37.15	39.51	40.20	40.40	40.26	39.78	37.47
5.400	57.33	62.95	64.77	65.44	65.34	64.44	59.11	5.400	66.84	73.68	75.92	76.84	76.83	75.82	69.35
6.200	71.75	79.04	81.95	83.61	84.33	84.00	77.78	6.200	82.33	89.99	93.39	95.63	97.04	97.29	91.17
7.000	79.50	87.10	90.77	93.34	95.11	95.87	90.68	7.000	88.97	100.00	105.00	107.80	109.20	109.20	104.10
7.100	81.12	88.87	92.62	95.29	97.15	98.02	92.89	7.100	90.92	102.70	107.80	110.70	112.10	112.10	106.40
7.200	85.61	93.91	97.95	100.70	102.60	103.40	98.06	7.200	96.95	110.10	115.60	118.60	120.00	119.70	112.50
7.300	94.61	105.10	109.70	112.60	114.30	114.70	108.00	7.300	109.80	125.40	131.70	135.00	136.30	135.50	125.60
7.350	102.40	114.50	119.70	122.70	124.30	124.30	115.90	7.350	120.50	138.20	145.10	148.60	149.70	148.60	136.60
7.400	113.20	127.50	133.30	136.60	138.00	137.50	127.00	7.400	135.20	155.60	163.30	167.10	168.10	166.40	151.70
7.440	124.50	141.10	147.50	150.90	152.30	151.40	138.60	7.440	150.40	173.70	182.20	186.20	187.10	184.80	167.30
7.480	138.80	158.00	165.30	168.90	170.10	168.70	153.30	7.480	169.40	196.20	205.80	210.10	210.80	207.80	186.90
7.500	147.00	167.80	175.60	179.40	180.50	178.70	161.80	7.500	180.50	209.20	219.50	226.90	224.50	221.20	198.20
7.520	156.10	178.70	186.90	190.90	191.80	189.80	171.20	7.520	192.60	223.60	234.50	239.20	229.60	235.80	210.70
7.540	166.10	190.50	199.30	203.40	204.30	201.80	181.40	7.540	205.80	239.20	250.90	255.70	256.00	251.80	224.40
7.560	176.70	203.10	212.50	216.80	217.60	214.80	192.50	7.560	220.00	256.00	268.40	273.50	273.70	268.90	238.90
7.580	187.70	216.20	226.20	230.70	231.40	228.20	203.80	7.580	234.60	273.00	286.50	291.80	291.90	286.60	254.00
7.600	198.60	229.10	239.80	244.40	245.00	241.40	215.10	7.600	249.10	290.40	304.40	310.00	309.90	304.20	269.00

ROD 2 CLAD TEMPERATURE								ROD 4 CLAD TEMPERATURE							
TIME	AXIAL ZONE							TIME	AXIAL ZONE						
	1	2	3	4	5	6	7		1	2	3	4	5	6	7
3.800	720.	721.	721.	721.	722.	722.	722.	3.800	720.	721.	721.	721.	722.	722.	722.
4.600	734.	738.	742.	745.	748.	750.	752.	4.600	736.	741.	745.	749.	752.	755.	756.
5.400	764.	787.	809.	829.	848.	865.	875.	5.400	774.	803.	828.	852.	874.	893.	902.
6.200	794.	835.	874.	912.	948.	930.	1001.	6.200	811.	860.	905.	951.	993.	1029.	1049.
7.000	820.	870.	917.	963.	1007.	1049.	1079.	7.000	836.	887.	938.	991.	1044.	1095.	1132.
7.100	828.	879.	926.	971.	1016.	1059.	1088.	7.100	844.	894.	945.	998.	1051.	1103.	1143.
7.200	846.	901.	948.	995.	1042.	1085.	1112.	7.200	853.	913.	965.	1019.	1072.	1124.	1170.
7.300	873.	926.	982.	1033.	1083.	1132.	1168.	7.300	881.	945.	1004.	1062.	1119.	1172.	1217.
7.350	885.	949.	1007.	1062.	1115.	1165.	1209.	7.350	896.	967.	1032.	1096.	1156.	1211.	1255.
7.400	901.	974.	1040.	1101.	1158.	1211.	1254.	7.400	916.	997.	1070.	1140.	1205.	1264.	1307.
7.440	917.	999.	1073.	1140.	1202.	1258.	1300.	7.440	935.	1027.	1108.	1185.	1255.	1317.	1361.
7.480	936.	1030.	1113.	1183.	1255.										

representing each of the remaining two. The radial and axial temperature profiles for fuel and cladding for these cases are shown in Figs. 87-90. Radial distributions are shown at the bottom and center of the fuel columns in each figure. Axial temperature profiles are shown at the centroid of the innermost radial node ($\bar{r} = 0.71$ mm), for the centroid of the outer region of the equiaxed grains ($\bar{r} = 1.92$ mm), for the centroid of the edge node ($\bar{r} = 2.4$ mm), and for the cladding midpoint ($\bar{r} = 2.62$ mm). The abrupt decrease in temperature at the top of the pin reflects the absence of axial heat transport by conduction to the upper structure. Cladding temperatures in the upper pin-structure region remain relatively constant, reflecting the effects of axial heat convection from the upward-moving sodium stream. The three-dimensional temperature pattern is summarized in the figures.

It is of interest to compare the degree to which thermal "prototypicality" was achieved in Test E7. Figure 91 shows the calculated radial temperature distribution for a high-power pin in the CRBR²¹ and those of the E7 fuel pins at the end of the preheat period (7 s). The dashed line refers to the CRBR. The agreement for Rod 4 (and 5) is excellent, although cladding temperatures in Test E7 are 25-50°C hotter than in the CRBR.

The corresponding comparison of the axial temperature profiles is shown in Fig. 92. In this comparison, Rod 4 (and 5) of Test E7 is nearly equivalent to a half-scale CRBR high-power pin. The flux-shaping collars on the loop were specified to produce an axial power profile characteristic of that in EBR-II (see Sec. III.C).

The axial elevations in Fig. 92 were chosen so that the cladding temperatures (figures to the right) in Test E7 matched reasonably well with those of CRBR. To do this requires the bottom of the E7 cladding to match the CRBR cladding at 178 mm up from the bottom.

It is concluded from these comparisons that the radial temperature profiles in the hottest pins of Test E7 (N-185, -104, and -153; see Fig. 6) at the end of the preheat period are indeed "prototypic" of high-power pins in CRBR near the end-of-life (EOL) cycle (see Fig. 91). Axial temperature distributions at the clad midpoint were equally prototypic. However, axial fuel temperatures in Test E7 look like 915-mm-long prototypic pins compressed into a 342-mm region starting 100 mm above the bottom of the core.

C. Thermal History during Approach to Failure

Figures 93 and 94 show thermal energies and temperatures during the approach to failure for the hottest pins (N-158 and -104). The other pins follow this same history, but at delayed times. This is a consequence of their lower calibration factors within the cluster. During the short period of the transient (580 ms), the heating of individual pins is nearly adiabatic.

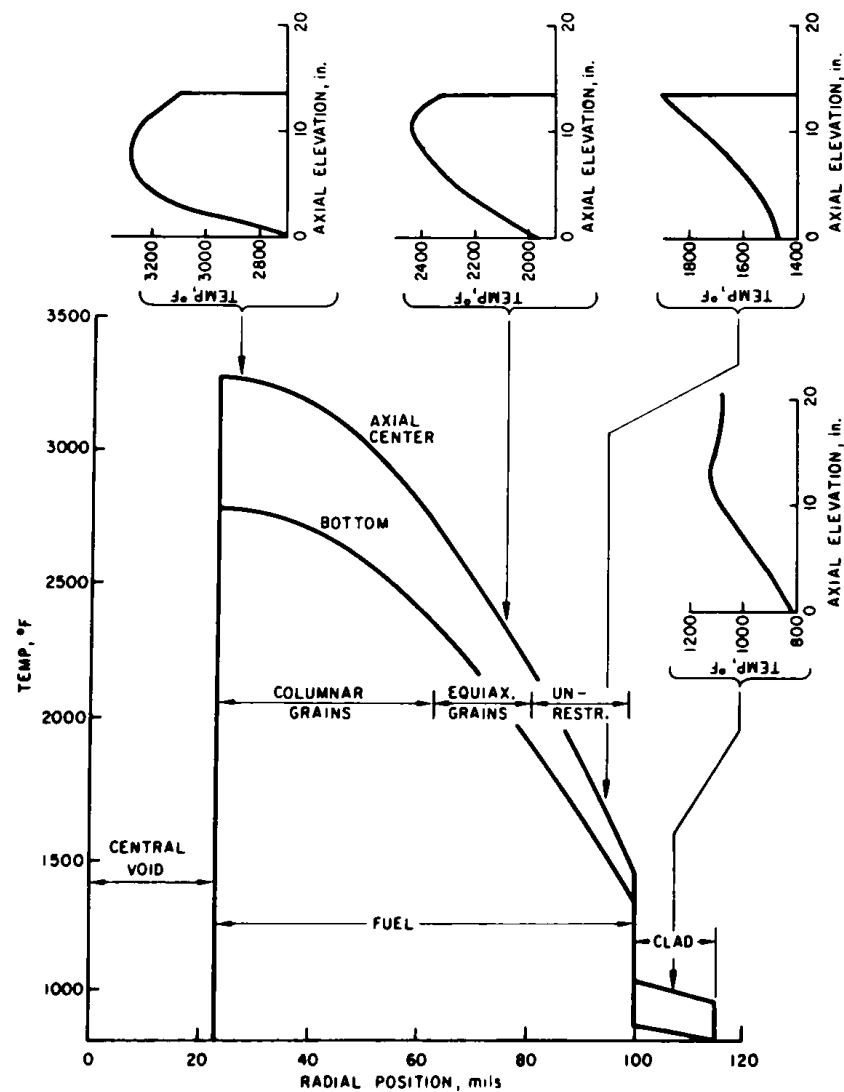


Fig. 87. Radial and Axial Temperature Distributions for Rod 1 at End of Preheat. Conversion factors: $t (^{\circ}\text{C}) = [t (^{\circ}\text{F}) - 32]/1.8$; 1 in. = 2.54 cm; 1 mil = 0.0254 mm.

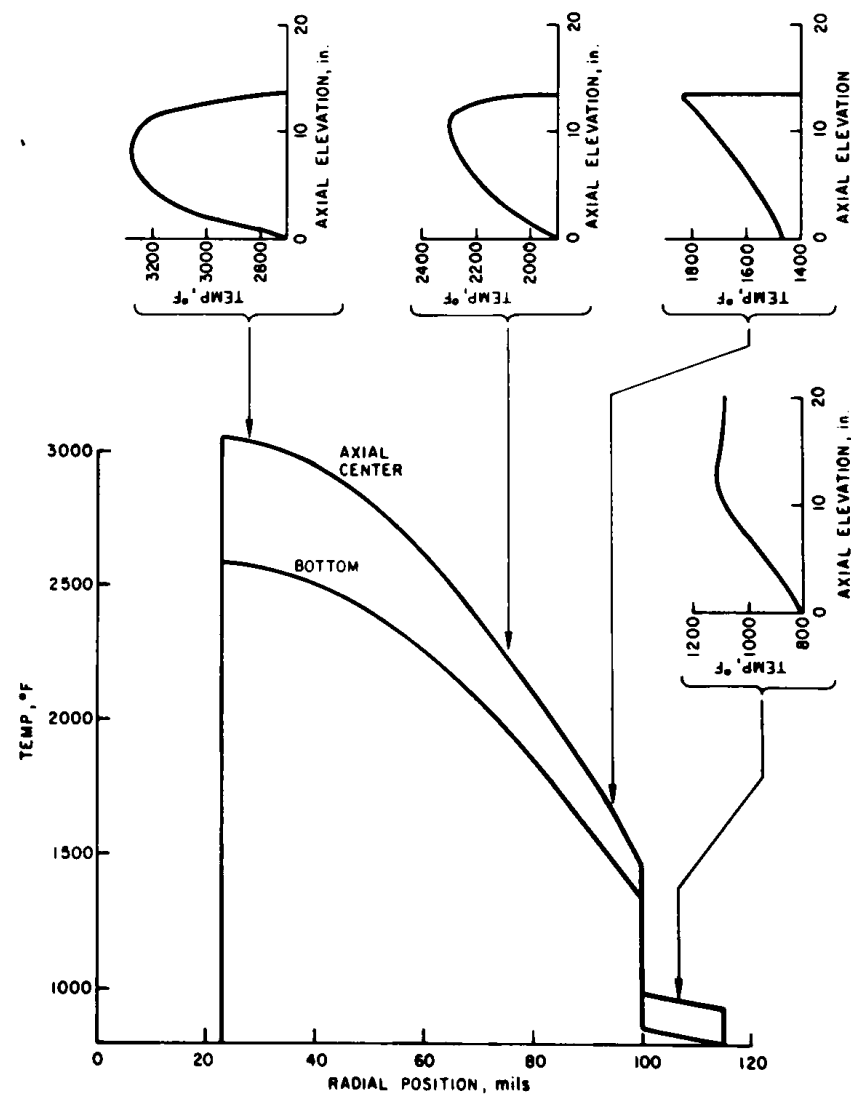


Fig. 88. Radial and Axial Temperature Distributions for Rod 2 at End of Preheat. Conversion factors: $t (^{\circ}\text{C}) = [t (^{\circ}\text{F}) - 32]/1.8$; 1 in. = 2.54 cm; 1 mil = 0.0254 mm.

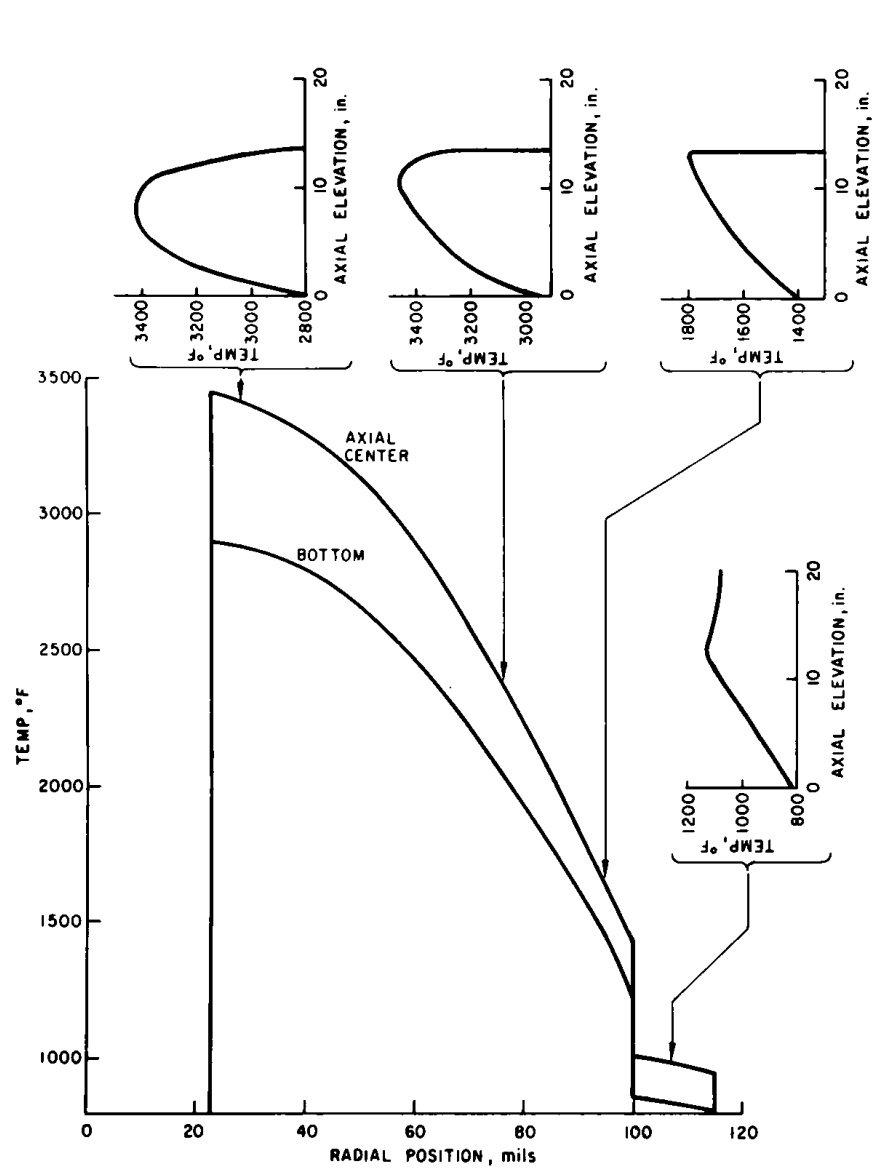


Fig. 89. Radial and Axial Temperature Distributions for Rod 3 at End of Preheat. Conversion factors: $t (^{\circ}\text{C}) = [t (^{\circ}\text{F}) - 32]/1.8$; 1 in. = 2.54 cm; 1 mil = 0.0254 mm.

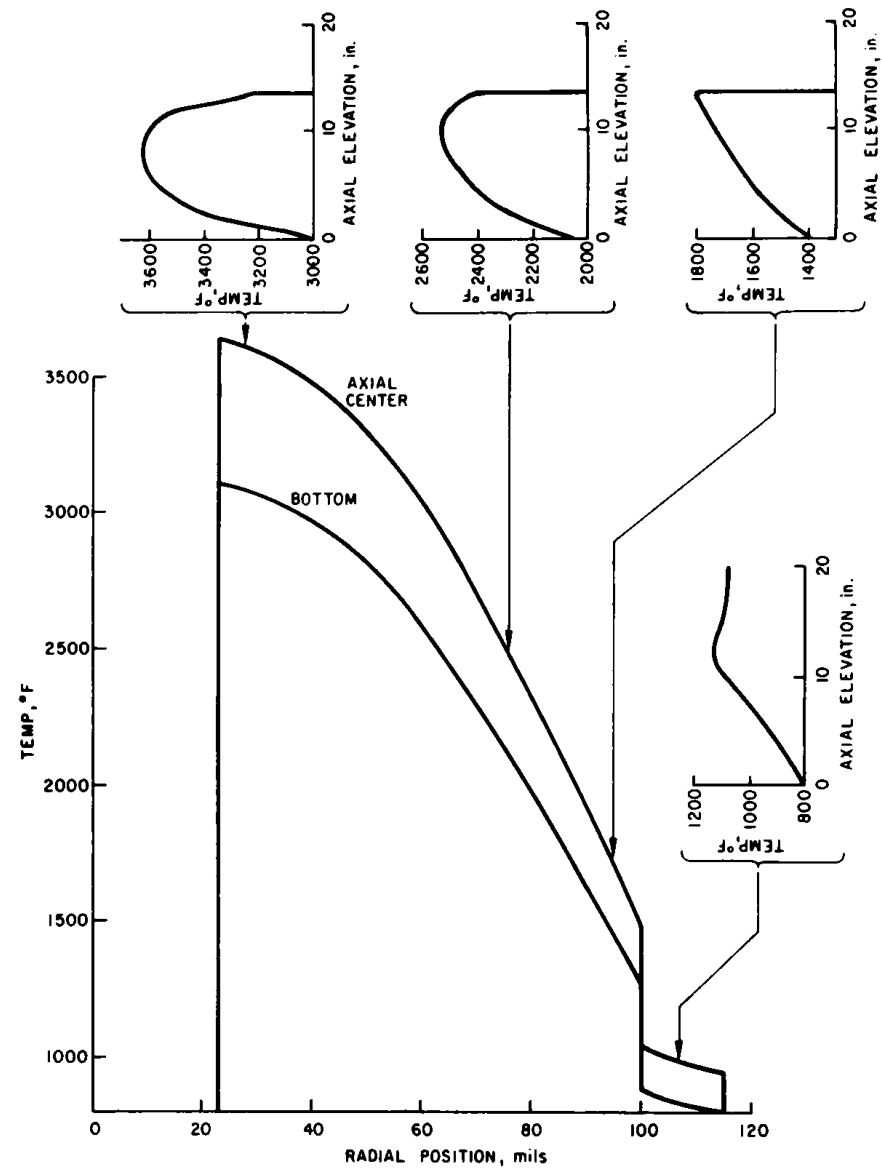


Fig. 90. Radial and Axial Temperature Distributions for Rod 4 at End of Preheat. Conversion factors: $t (^{\circ}\text{C}) = [t (^{\circ}\text{F}) - 32]/1.8$; 1 in. = 2.54 cm; 1 mil = 0.0254 mm.

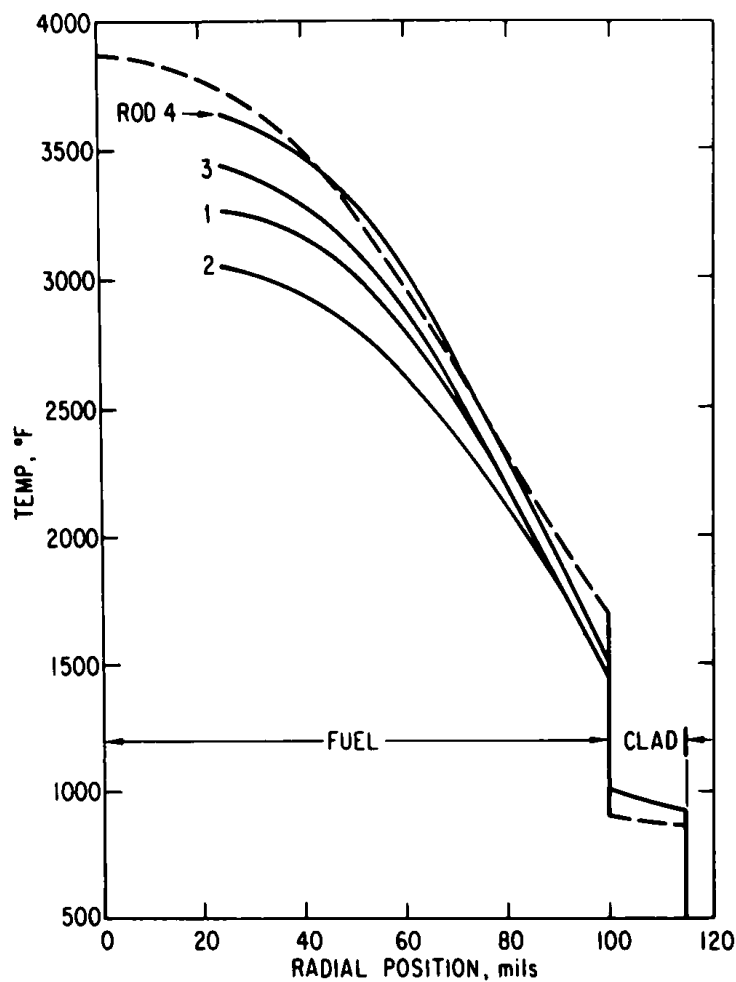


Fig. 91

Comparison of Radial Temperature Distributions of Test Fuel and High-power CRBR Rod. Conversion factors: $t (^{\circ}\text{C}) = [t (^{\circ}\text{F}) - 32]/1.8$; 1 mil = 0.0254 mm.

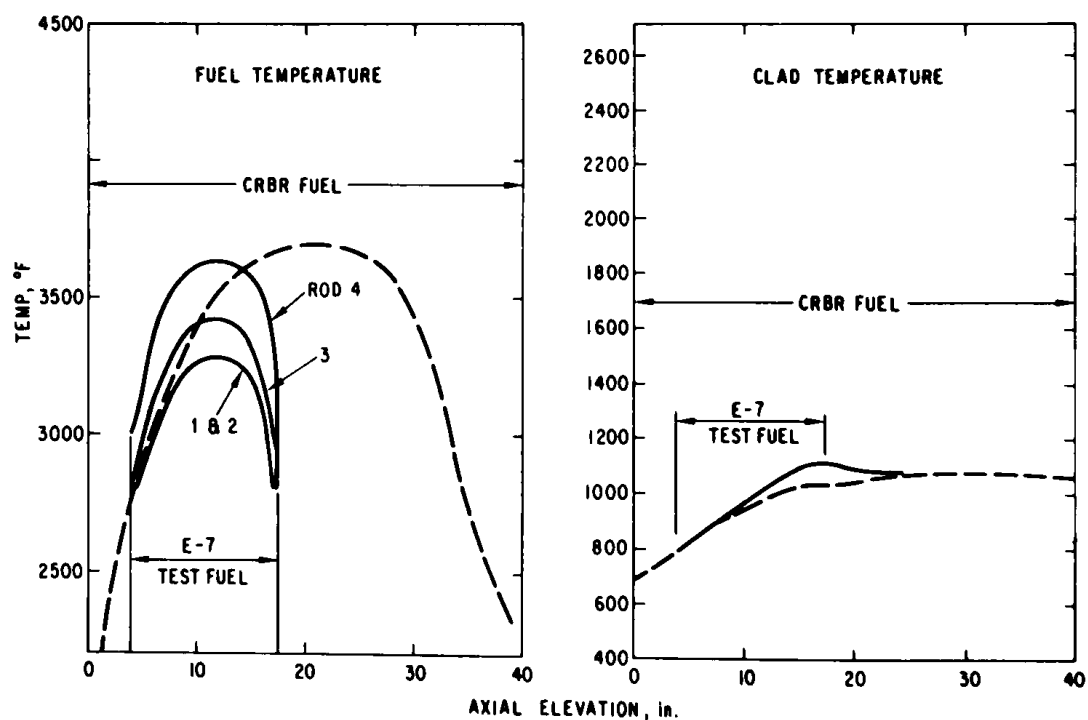


Fig. 92. Comparison of Axial Temperature Distributions of Test Fuel and High-power CRBR Rod. Conversion factors: $t (^{\circ}\text{C}) = [t (^{\circ}\text{F}) - 32]/1.8$; 1 in. = 2.54 cm.

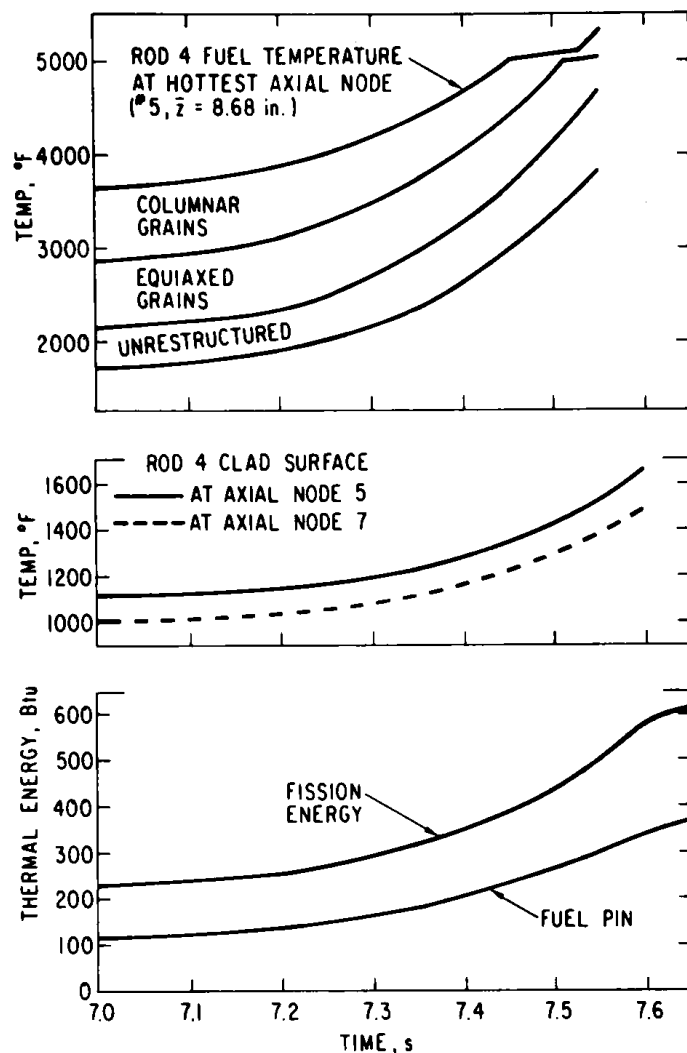
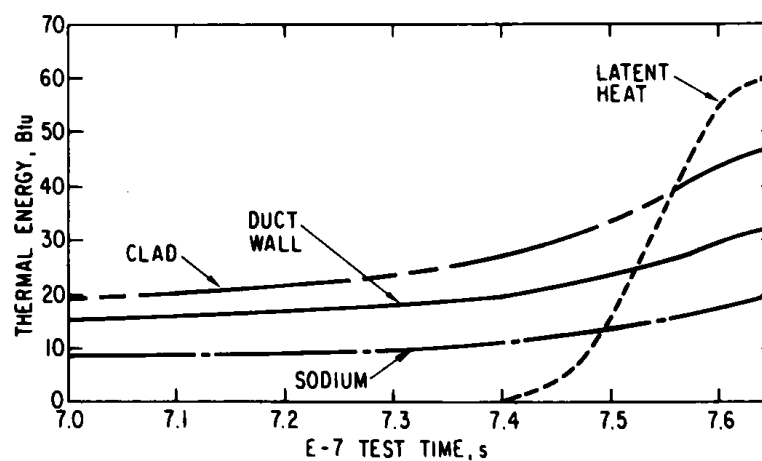


Fig. 93

Temperature and Energy History of Hottest Test Fuel Rod during Approach to Failure. Conversion factors: $t (^{\circ}\text{C}) = [t (^{\circ}\text{F}) - 32]/1.8$; 1 in. = 2.54 cm; 1 Btu = 1.055 kJ.

Fig. 94

Energy Partitioning during Approach to Failure. Conversion factor: 1 Btu = 1.055 kJ.



Fuel temperatures are shown by grain regions in the top curves of Fig. 93 for the hottest axial node (node 5 from 196 to 245 mm) of Rod 4. Cladding surface temperatures are shown in the middle two curves. The upper of these is the peak surface temperature that occurs at the top of the fuel column (344 mm) and is the same, within 10°C , as the maximum coolant temperature. The lower curve is the cladding surface at the hottest fuel node (node 5).

The bottom set of the curves in Fig. 93 show the total fission energy generated by the seven fuel pins and the total retained in the fuel, integrated over the entire fuel pin. Figure 94 shows partitioning of the total energy into cladding, sodium, and duct-wall enthalpy as well as the latent heat of fusion.

The lower portion of Fig. 95 shows the radial propagation of the solidus and liquidus fronts. Positions of the various grain-structure interfaces are shown as the lines A-D. The corresponding axial temperature distributions along these interfaces are shown for selected times at the top of the figure. With increasing time into the transient, the axial temperatures tend to become quite flat through the central region of the pin, compared to the nearly bell-shaped distribution at the end of the preheat (see Figs. 87-90).

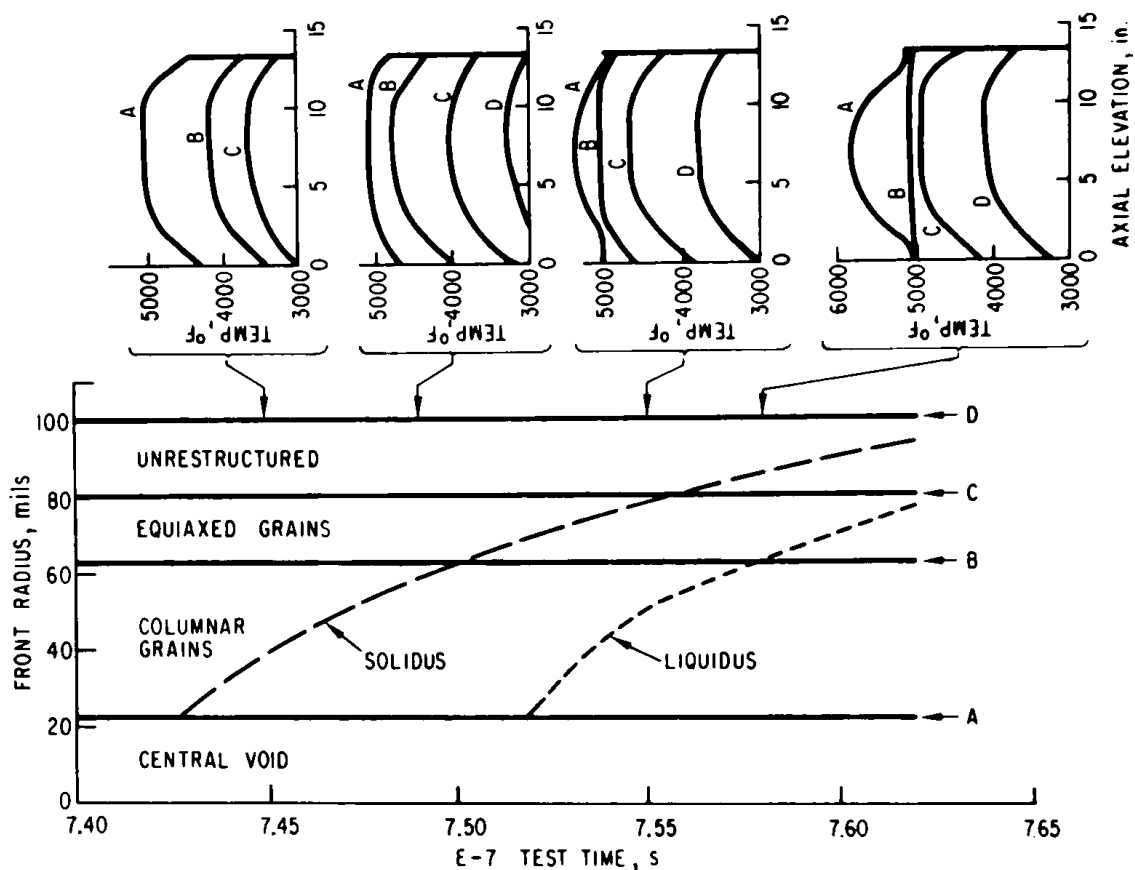


Fig. 95. Axial Temperature Profiles and Radial Melt-front History during Approach to Failure. Conversion factors: $t (^{\circ}\text{C}) = [t (^{\circ}\text{F}) - 32]/1.8$; 1 mil = 0.0254 mm; 1 in. = 2.54 cm.

D. Temperature Distribution at Failure

The sequence of events related to initial fuel-pin failure begins with a series of cladding ruptures at 7.45 s and ends with ejection of a sodium slug at 7.55 s. Fuel motion observed by the hodoscope during this time interval is attributed to pin bowing and squirming rather than motion within the flow channel. Figure 96 shows the calculated temperature profiles for the hottest pin (N-153, see Fig. 6) at the middle of this interval. The average pin enthalpy is 854 J/g (204 cal/g). Pins N-069, -092, and -081 reach this enthalpy at 7.52, 7.53, and 7.56 s, respectively. Figure 96 shows that the melt front has just entered the equiaxed grain region, the outside surface of the fuel pellets is some 1100°C below the melting temperature, and the temperature gradient is in excess of 644°C/cm (1635°C/in.).

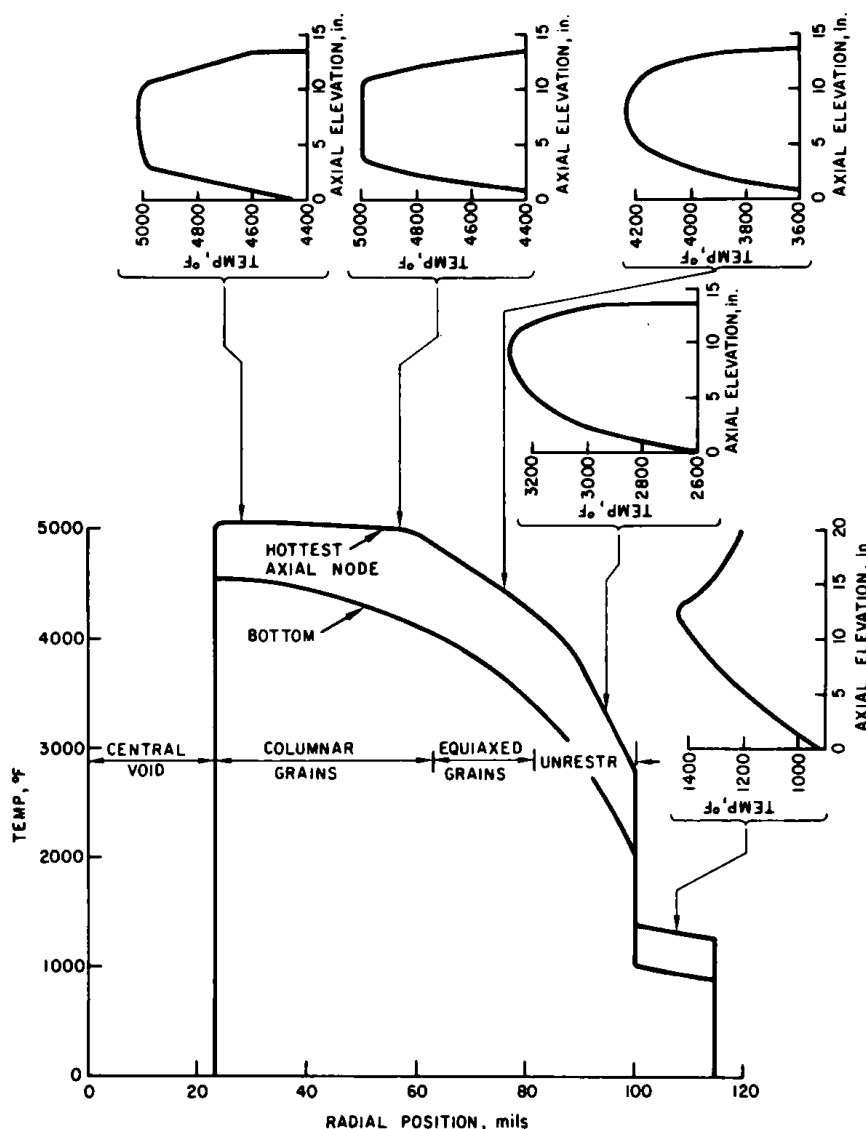


Fig. 96. Temperature Distributions at Failure of Hottest Test Fuel Pin. Conversion factors: $t (^{\circ}\text{C}) = [t (^{\circ}\text{F}) - 32]/1.8$; 1 in. = 2.54 cm; 1 mil = 0.0254 mm.

E. Damage Parameter

Scott and Baars originally proposed a single parameter⁴ that would characterize restructured fuel at the time of failures. Their so-called "damage parameter" was an empirical approach to predicting incipient failure due to cladding loading from thermal expansion, fission-gas release, and fuel swelling. A revised damage parameter³ with an explicit "time-into-the-transient" term is used here.

The Scott-Baars damage parameter is defined as

$$DP = \left(\frac{\Delta H}{y} \right)_{\text{eff}} (1 + C) V_f \sqrt{t},$$

where

$\left(\frac{\Delta H}{y}\right)_{\text{eff}}$ = the effective mean fuel enthalpy per unit cladding yield strength at time t_i into the transient

$$= \frac{\sum_{i=1}^m \frac{\Delta H_i}{Y_i} \Delta t_i}{\sum_{i=1}^m \Delta t_i},$$

ΔH_i = the change in enthalpy between two time steps (t_{j+1} and t_j) weighted by the time into the transient ($t_i - t_j$)

$$= \sum_{j=1}^{i-1} (H_{j+1} - H_j) \exp[-(t_i - t_j)/2],$$

C = the fission-gas concentration averaged over the fuel pin (cm^3/g),

and

V_f = the volume fraction of unrestructured fuel.

The \sqrt{t} term accounts for the experimentally observed rate of thermal-energy addition and the final severity of conditions at failure. An exponential weighting of early enthalpy additions corresponds to a "memory" at failure time of the cladding loading effects at earlier times.

The damage parameter has been calculated for each axial zone of each fuel rod. Yield strengths used in these calculations were for 20% cold-worked Type 316 stainless steel; these were taken from Ref. 22 and are shown in Fig. 97. Fuel enthalpies were those calculated by COBRA and listed in Table VII.

Results of the calculations are shown in Figs. 98-101 for each rod. Scott and Baars reported a value of 3.8×10^{-3} , with a 5-10% deviation, for the damage parameter at the threshold of failure. Correlations were studied for fast and slow transients in both Mark-II loop and HEDL static capsule failure tests. Use of these criteria for Test E7 suggests failures at 7.51, 7.55, 7.51, and 7.50 s for Rods 1-4, respectively. Further, all failures are predicted to occur at the top axial node of the fuel pins. This is the region of highest cladding temperature and lowest yield strength, but not necessarily of maximum internal clad loading.

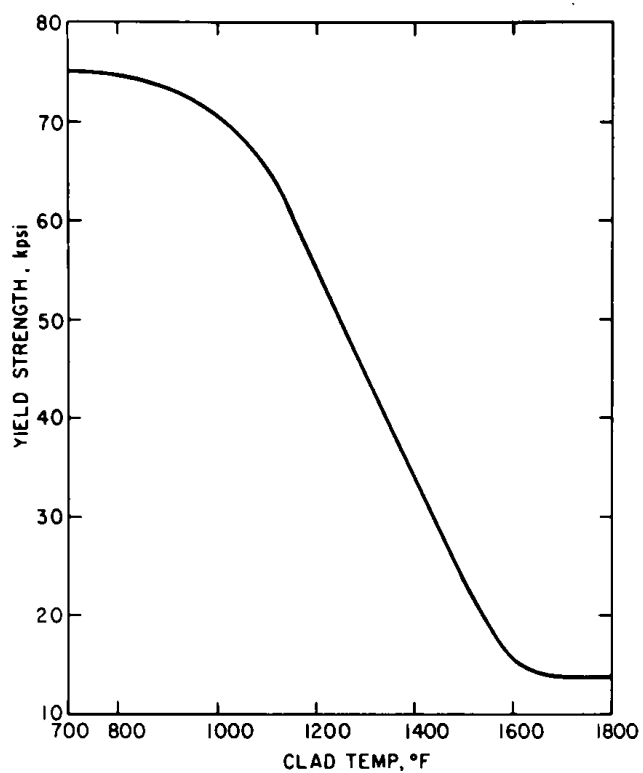


Fig. 97

Cladding Yield Strength as a Function of Mid-wall Temperature. Conversion factors: 1 psi = 6.895 kPa; $t (^{\circ}\text{C}) = [t (^{\circ}\text{F}) - 32]/1.8$.

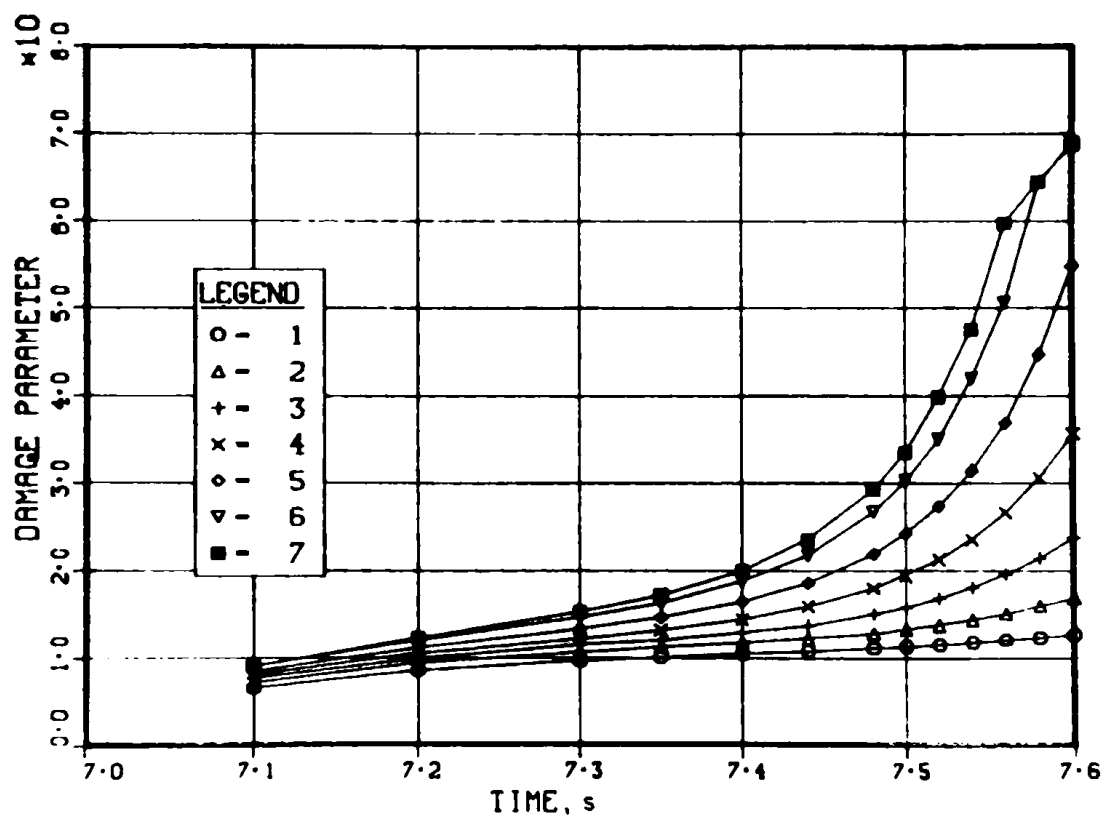


Fig. 98. Damage Parameters for Rod 1

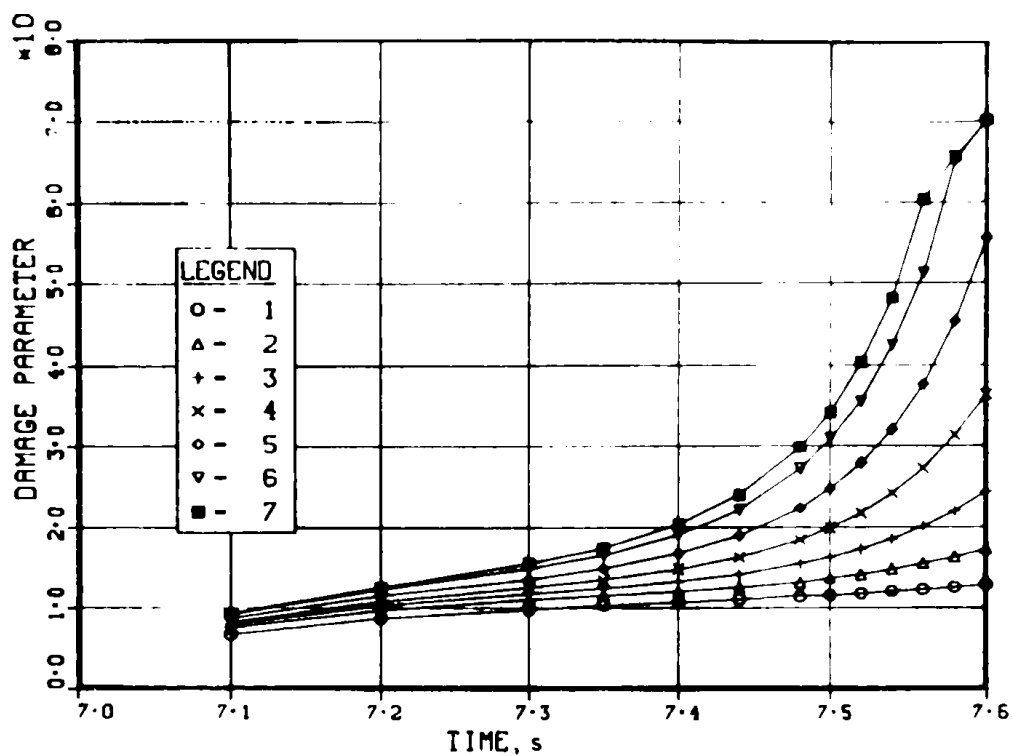


Fig. 99. Damage Parameters for Rod 2

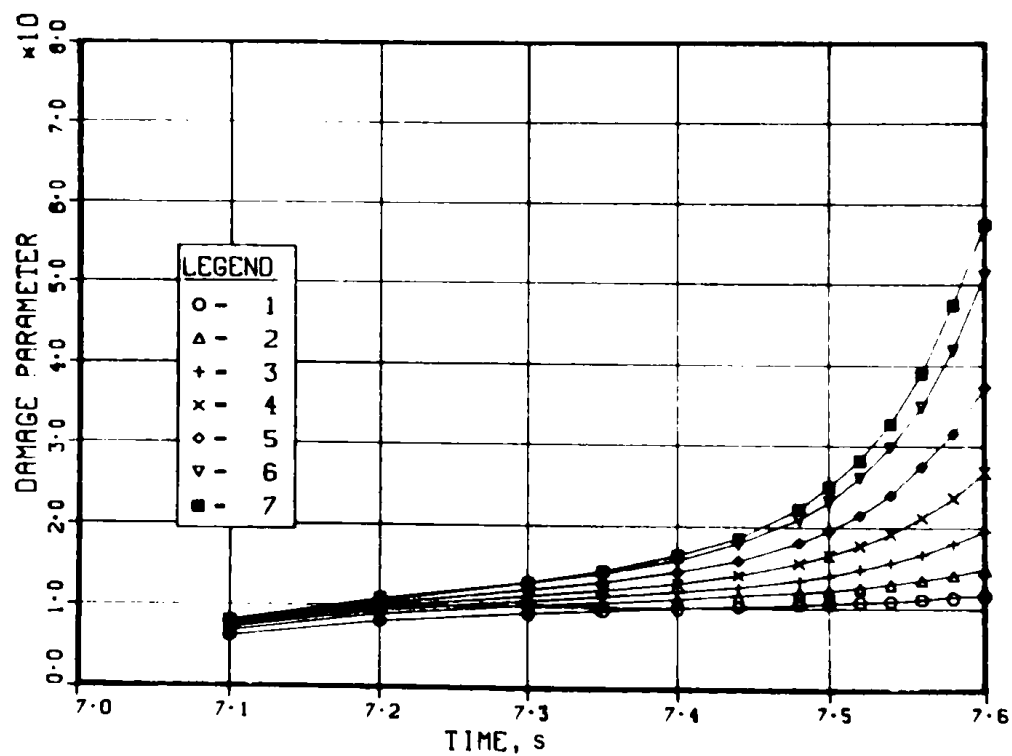


Fig. 100. Damage Parameters for Rod 3

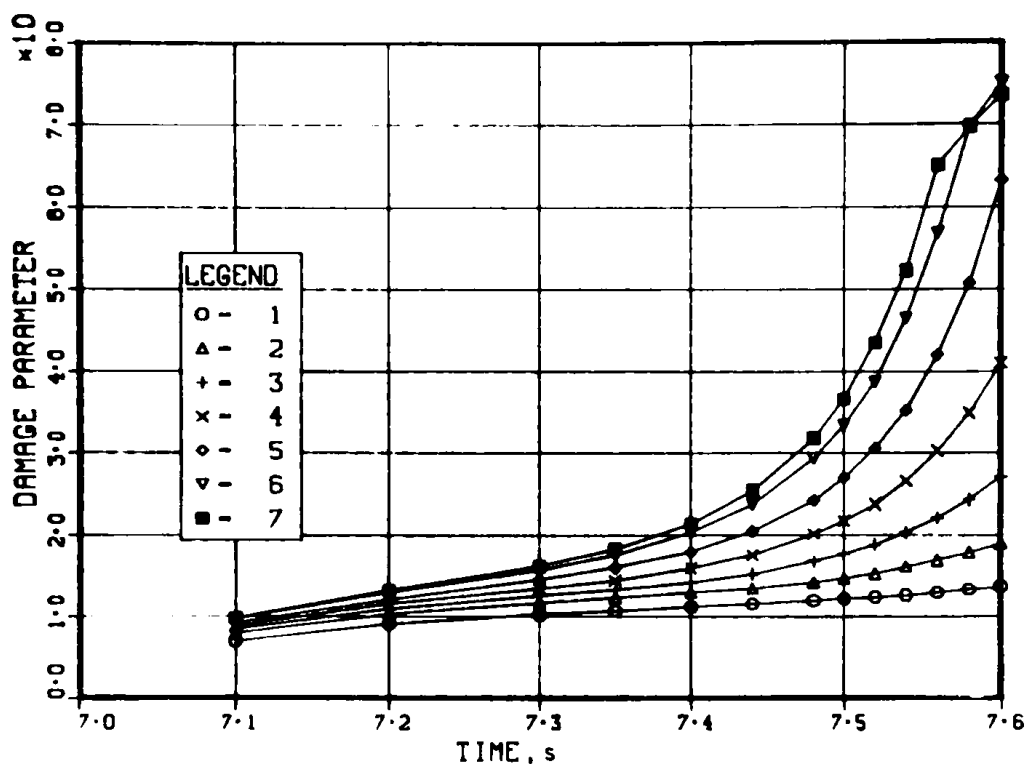


Fig. 101. Damage Parameters for Rod 4

The curves in Figs. 98-101 also show the rate at which failure can propagate downward. These results presume that the COBRA calculations of fuel enthalpy and cladding temperature are correct. The COBRA calculations predict an outlet temperature of about 570°C at the end of the preheat (7.0 s). Temperature monitored by the outlet thermocouples was 450°C. Part of this difference can be accounted for by the inability of COBRA to correctly calculate the heat loss to the structure above the adiabatic region of the fuel holder (see Fig. 7).

At the end of the preheat period, fuel enthalpies varied from 80 to 110 cal/g (335 to 460 J/g) (see Table VII). This energy, exponentially weighted to the time of potential failure, was included in the damage-parameter calculations. If the preheat enthalpy had not been included, the damage parameter for Rod 1, for example, would be 1×10^{-4} at 7.51 s, and the failure would be predicted between axial zones 5 and 6 rather than in zone 7.

If the hottest pin (Rod 4) were to fail at 7.50 s as predicted above, a damage parameter of 1×10^{-4} would predict failure at the bottom of axial zone 7. Results of damage parameter calculations that do not include the preheat enthalpy are listed in Table VIII.

TABLE VIII. Damage Parameters without Preheat Enthalpy

DAMAGE PARAMETERS FOR ROD 1												
TIME	AXIAL ZONES											
	1	2	3	4	5	6	7					
7 100	1 36E-05	1 66E-05	1 86E-05	1 94E-05	1 92E-05	2 03E-05	2 23E-05					
7 200	4 70E-05	5 90E-05	6 50E-05	6 75E-05	6 78E-05	7 03E-05	7 15E-05					
7 300	1 18E-04	1 49E-04	1 62E-04	1 69E-04	1 75E-04	1 83E-04	1 77E-04					
7 350	1 67E-04	2 09E-04	2 27E-04	2 39E-04	2 51E-04	2 64E-04	2 52E-04					
7 400	2 35E-04	2 94E-04	3 20E-04	3 44E-04	3 66E-04	3 90E-04	3 71E-04					
7 440	3 05E-04	3 81E-04	4 19E-04	4 52E-04	4 97E-04	5 37E-04	5 12E-04					
7 480	3 94E-04	4 94E-04	5 53E-04	6 17E-04	6 88E-04	7 63E-04	7 34E-04					
7 500	4 43E-04	5 57E-04	6 30E-04	7 12E-04	8 03E-04	9 03E-04	8 73E-04					
7 520	4 98E-04	6 29E-04	7 20E-04	8 26E-04	9 49E-04	1 08E-03	1 06E-03					
7 540	5 60E-04	7 12E-04	8 27E-04	9 66E-04	1 13E-03	1 33E-03	1 30E-03					
7 560	6 38E-04	8 08E-04	9 54E-04	1 14E-03	1 37E-03	1 65E-03	1 65E-03					
7 580	7 04E-04	9 16E-04	1 10E-03	1 36E-03	1 69E-03	2 10E-03	2 05E-03					
7 600	7 87E-04	1 04E-03	1 28E-03	1 64E-03	2 12E-03	2 61E-03	2 50E-03					
DAMAGE PARAMETERS FOR ROD 2												
TIME	AXIAL ZONES											
	1	2	3	4	5	6	7					
7 100	1 32E-05	1 46E-05	1 54E-05	1 65E-05	1 75E-05	1 90E-05	2 01E-05					
7 200	4 42E-05	4 97E-05	5 29E-05	5 53E-05	5 79E-05	6 11E-05	6 25E-05					
7 300	1 06E-04	1 25E-04	1 34E-04	1 39E-04	1 45E-04	1 52E-04	1 51E-04					
7 350	1 48E-04	1 76E-04	1 88E-04	1 97E-04	2 06E-04	2 17E-04	2 11E-04					
7 400	2 06E-04	2 48E-04	2 66E-04	2 82E-04	2 98E-04	3 14E-04	3 04E-04					
7 440	2 66E-04	3 22E-04	3 49E-04	3 73E-04	4 00E-04	4 25E-04	4 09E-04					
7 480	3 43E-04	4 17E-04	4 58E-04	4 99E-04	5 44E-04	5 83E-04	5 67E-04					
7 500	3 85E-04	4 70E-04	5 21E-04	5 73E-04	6 29E-04	6 86E-04	6 64E-04					
7 520	4 33E-04	5 31E-04	5 94E-04	6 60E-04	7 34E-04	8 10E-04	7 86E-04					
7 540	4 86E-04	5 99E-04	6 78E-04	7 65E-04	8 63E-04	9 68E-04	9 43E-04					
7 560	5 44E-04	6 77E-04	7 77E-04	8 91E-04	1 03E-03	1 17E-03	1 15E-03					
7 580	6 09E-04	7 66E-04	8 93E-04	1 05E-03	1 23E-03	1 44E-03	1 43E-03					
7 600	6 79E-04	8 65E-04	1 03E-03	1 23E-03	1 49E-03	1 79E-03	1 79E-03					
DAMAGE PARAMETERS FOR ROD 3												
TIME	AXIAL ZONES											
	1	2	3	4	5	6	7					
7 100	1 38E-05	1 86E-05	2 05E-05	2 21E-05	2 19E-05	2 12E-05	2 24E-05					
7 200	4 89E-05	6 46E-05	7 00E-05	7 30E-05	7 46E-05	7 48E-05	7 26E-05					
7 300	1 25E-04	1 60E-04	1 72E-04	1 81E-04	1 89E-04	1 95E-04	1 81E-04					
7 350	1 76E-04	2 03E-04	2 40E-04	2 55E-04	2 69E-04	2 80E-04	2 60E-04					
7 400	2 48E-04	3 12E-04	3 39E-04	3 64E-04	3 91E-04	4 13E-04	3 84E-04					
7 440	3 21E-04	4 04E-04	4 42E-04	4 84E-04	5 28E-04	5 67E-04	5 32E-04					
7 480	4 15E-04	5 22E-04	5 83E-04	6 51E-04	7 28E-04	8 04E-04	7 63E-04					
7 500	4 67E-04	5 88E-04	6 63E-04	7 50E-04	8 49E-04	9 51E-04	9 08E-04					
7 520	5 25E-04	6 63E-04	7 57E-04	8 69E-04	1 00E-03	1 14E-03	1 10E-03					
7 540	5 89E-04	7 50E-04	8 69E-04	1 02E-03	1 20E-03	1 39E-03	1 36E-03					
7 560	6 61E-04	8 50E-04	1 00E-03	1 20E-03	1 45E-03	1 73E-03	1 71E-03					
7 580	7 40E-04	9 63E-04	1 16E-03	1 43E-03	1 78E-03	2 19E-03	2 13E-03					
7 600	8 27E-04	1 09E-03	1 35E-03	1 71E-03	2 22E-03	2 73E-03	2 60E-03					
DAMAGE PARAMETERS FOR ROD 4												
TIME	AXIAL ZONES											
	1	2	3	4	5	6	7					
7 100	1 59E-05	2 23E-05	2 35E-05	2 47E-05	2 54E-05	2 69E-05	2 26E-05					
7 200	5 70E-05	7 43E-05	7 89E-05	8 22E-05	8 54E-05	8 90E-05	7 61E-05					
7 300	1 43E-04	1 81E-04	1 93E-04	2 03E-04	2 15E-04	2 25E-04	1 97E-04					
7 350	2 01E-04	2 51E-04	2 69E-04	2 86E-04	3 05E-04	3 22E-04	2 95E-04					
7 400	2 22E-04	3 50E-04	3 79E-04	4 09E-04	4 41E-04	4 73E-04	4 26E-04					
7 440	3 64E-04	4 52E-04	4 95E-04	5 43E-04	5 96E-04	6 45E-04	5 92E-04					
7 480	4 69E-04	5 84E-04	6 53E-04	7 32E-04	8 23E-04	9 18E-04	8 55E-04					
7 500	5 26E-04	6 58E-04	7 43E-04	8 44E-04	9 62E-04	1 09E-03	1 02E-03					
7 520	5 91E-04	7 43E-04	8 50E-04	9 80E-04	1 14E-03	1 31E-03	1 24E-03					
7 540	6 63E-04	8 41E-04	9 77E-04	1 15E-03	1 36E-03	1 60E-03	1 54E-03					
7 560	7 43E-04	9 54E-04	1 14E-03	1 36E-03	1 65E-03	1 99E-03	1 94E-03					
7 580	8 32E-04	1 08E-03	1 31E-03	1 62E-03	2 04E-03	2 52E-03	2 41E-03					
7 600	9 28E-04	1 23E-03	1 52E-03	1 96E-03	2 57E-03	3 12E-03	2 93E-03					

IX. SUMMARY, DISCUSSION, AND CONCLUSIONS

Loop-instrument signals as originally recorded on analog tape were independently redigitized and analyzed. The resulting TREAT power and inlet temperatures were used as driving functions in thermal-hydraulic calculations. Calculated fuel enthalpies as a function of space and time were used to evaluate a damage parameter. The use of the Scott-Baars recommended value of 3.8×10^{-3} for the damage parameter leads to a prediction of failure in the hottest pin of Test E7 at 7.50 s and of the coldest at 7.55 s. This is in reasonably good agreement with the observed flow dynamics, which imply failures about 50 ms earlier.

In the following sections, the test data, including the hodoscope observations and posttest-examination results, are interpreted in terms of physical phenomena taking place during the failure sequence.

A. Flow Data

Measured flow has been decomposed into a series of bursts superimposed on a general trend between 7.44 and 7.55 s with slug ejection at 7.56 s. Details of these data are shown at the top of Fig. 102.

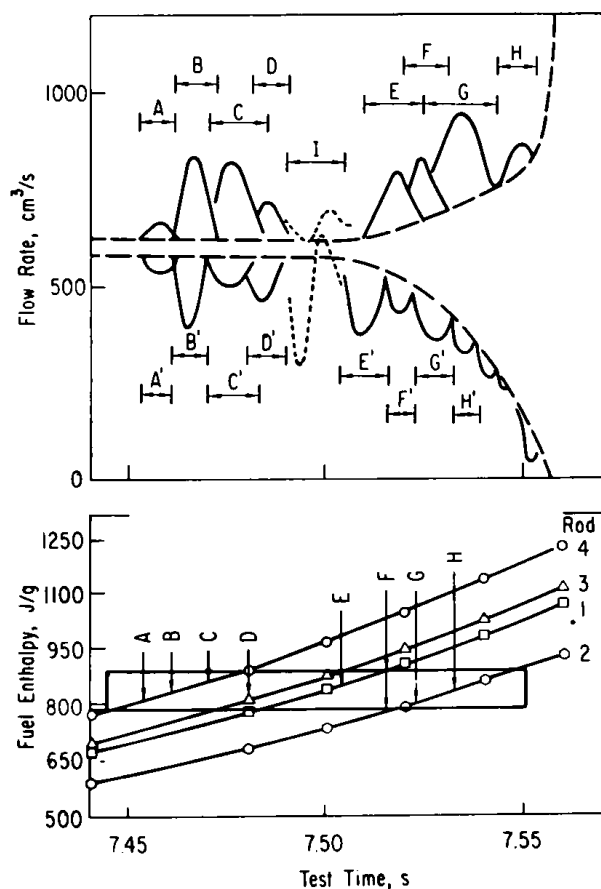


Fig. 102. Detailed Flow Data into Individual Cladding-rupture Events with Corresponding Calculated Fuel Enthalpies. ANL Neg. No. 900-76-431.

During the 100-ms period before 7.44 s, the average steady-state flow rate was $571 \text{ cm}^3/\text{s}$ at the inlet and $626 \text{ cm}^3/\text{s}$ at the outlet. The difference leads to an apparent void of 8.0 cm^3 at 7.45 s. Originally, this void was thought to be real and due to a pin-hole leak in one or more of the claddings. It is now believed to be the result of the anomalous response of the upper flow detector due to the temperature dependence of the internal Armco iron magnetic amplifier. The true inlet and outlet flow rates to the time of the first flow surge are $571 \text{ cm}^3/\text{s}$.

In Fig. 102, individual flow pulses or "bursts" are labeled A-H. Unprimed letters refer to outlet events, and a prime denotes the inlet bursts. We postulate that each of the early bursts is associated with one or more cladding ruptures that release bubbles of fission gas into the flow stream. Successive bursts at the outlet are successively more delayed and of increasing duration in comparison to the corresponding inlet bursts. This would

suggest that each gas release remains as an isolated bubble that is carried upstream with the flow to produce a compressible upper slug, assuming a uniform 1.5-cm^2 cross-sectional flow area along the entire flow channel. The first gas bubble released reached the upper flow detector in about 100 ms. Therefore, interpretation of the flow signal after 7.55 s is subject to large uncertainties. The individual flow surges, their duration, and the total volume of displaced sodium are listed in Table IX.

TABLE IX. Flow Surges during Cladding Ruptures

Identification	Time, s	Duration, ms	Displaced Volume, cm^3
A	7.453	7	0.9
B	7.460	11	3.3
C	7.471	10	3.3
D	7.481	9	2.2
E	7.505	11	3.2
F	7.516	12	3.1
G	7.528	17	9.7
H	7.545	15	13.0
I	7.491	9	2.2

The relatively large surge I at the inlet is interpreted as a local reaction between molten cladding and the lower liquid slug. The effect is not strongly coupled to the outlet because of vapor and fission-gas cushioning between the two liquid slugs. As the vapor from the early part of event I condenses, the inertia of the lower slug compresses the separating vapor between slugs and causes the observed response during the last half of event I. This would account for the slight hole in the void curve (see Fig. 42) from 7.49 to 7.50 s.

Surges after 7.505 s were generally larger and lasted longer. They may have been additional ruptures in colder pins or the colder axial regions of already ruptured pins, or thermal interactions between molten cladding and the inlet slug. By 7.51 s, sufficient gas had been released (13 cm^3) to effectively blanket most of the fuel pins above the rupture sites. The fuel-liquidus front had just reached the equiaxed gains, and the calculated cladding temperatures at the top of the fuel zone were $\sim 900^\circ\text{C}$. Voiding of the flow channel would have given rise to higher cladding temperatures than were calculated, so that melting at 7.5 s was quite possible.

Calculated radially averaged fuel enthalpies at the hottest axial zone during the period from 7.44 to 7.55 s are shown in the lower half of Fig. 102.

The first cladding rupture at 7.45 s is associated with the hottest fuel pin (Rod 4, opposite the ALIP). The three pins opposite the ALIP have equivalent thermal histories; the thermal history of only one (Rod 4) was calculated. Cladding rupture in any of these three pins corresponds to a fuel enthalpy of 835 ± 20 J/g. As each of the remaining pins reaches this enthalpy (Rod 3 is one of two average edge pins between the hodoscope slot and the ALIP, Rod 1 is the central pin, and Rod 2 is the coldest pin nearest the ALIP), there is a corresponding flow surge. At the bottom of the figure, the timing of the eight flow events is compared against the radially averaged fuel enthalpies calculated for the hottest axial zone of each of the four pin cases. These data can be interpreted as indicating a failure-criterion band of about 834 ± 20 J/g for the rupture of all the pins.

The series of ripples on the inlet flow after 7.515 s are interpreted as local thermal reactions between molten cladding and the lower liquid slug. During the 55-ms period from 7.505 s to reverse inlet flow, the void grew from a small region at or above the tops of the fuel columns to the entire length of the fuel columns.

Calculations for the hottest pins showed that the melt front had advanced 0.5 mm into the columnar grains at 7.453 s (the time of cladding rupture) and had just reached the unrestructured grain region at 7.56 s (the time of complete channel voiding). Cladding temperatures were calculated not to reach the sodium saturation temperature until after 7.6 s.

Posttest examinations of the blockages revealed a preponderance of steel at the far ends of the plugs and of fuel at the ends nearest the original fuel columns. We conclude that molten cladding both slumped toward the inlet and was swept out toward the flow-channel exit during the interval from 7.51 to 7.56 s, and that fuel motion was relatively slow and predominantly outward from 7.56 to 7.72 s. Following each cladding rupture, local film dry-out, followed by clad melting, probably occurred. The rate of average motion of the liquid-vapor interface after 7.51 s suggests an axial propagation of the cladding melt front from 7.51 to 7.56 s, when the channel was completely voided.

Further, the lack of hodoscope evidence for clear axial or radial motion of the approximately 50% melted fuel during this interval would indicate that gross fuel swelling had occurred, and that by 7.56 s the two-phase mixture of swollen and molten fuel had filled the entire flow channel. The gradual nature of all the observed fuel motions and the absence of significant pressure pulses and flow slugs supports a fuel-swelling concept. The outer and colder surface of unrestructured fuel appeared to have formed a crust or shell within which the molten fuel was contained. At 7.72 s, vapor pressure could have pushed the molten or slushy fuel upward and outward (through cracks in the crust). Examination of this crust during the posttest operations revealed that the crust was porous and spongy, and probably had not undergone significant melting except near the axial midpoint.

B. Fuel-failure Criteria

According to the correlation between experiment and calculation reported by Baars, Scott, and Culley,³ irradiated fuel fails when the damage parameter reaches a value of 3.8×10^{-3} . On this basis, failure of pin 4 (the hottest) is predicted at 7.5 s (see Fig. 101), pin 3 at 7.51 s (see Fig. 100), the central pin at 7.51 s (see Fig. 98), and the coldest pin (toward the pump) at 7.55 s (see Fig. 99). The earliest time that the hodoscope saw fuel motion (indicative of ex-pin fuel movement rather than pin bowing) was at 7.59 s (see Fig. 53). There is some evidence of hot fuel/slush contact with the coolant in the very low-pressure events (see Figs. 44 and 46) at 7.552 and 7.565 s. Nevertheless, the combined results suggest that fuel failure resulting in fuel motion and contact with the coolant began after 7.55 s. Use of the damage parameter predicts conditions producing cladding rupture, but does not necessarily predict the timing for the onset of ex-cladding fuel movement.

C. Flow-channel Voiding

In comparing the various flow bursts in Fig. 102 from 7.45 to 7.55 s, we note that accelerations of successive outlet surges are increasing slower than the corresponding inlet accelerations. This supports the previous conclusion that gas remained in the upper liquid slug. Any noncondensable gas in the upper slug would cushion the mechanical accelerations caused by the gas-release impulses. Peak cladding temperatures at this time (see Figs. 93 and 96) were calculated to be below the sodium saturation temperature. By 7.55 s, the total void volume was 33.5 cm^3 and probably consisted of the $13\text{--}20 \text{ cm}^3$ due to gas releases (see Table IX). Values of the damage parameter indicate cladding rupture near the top of the pin, so that it can be assumed that the lower slug contains no gas bubbles and extends from the inlet to the lowest cladding-rupture point.

After 7.505 s, we postulate that the cladding melting propagates downward from the rupture point. The wiggles observed on the inlet-flow data (at 7.53, 7.54, 7.56 s, etc.; see Fig. 102) represent successive contact of molten clad with the lower liquid slug. By the time fuel moves into the flow channel (after 7.55 s), the void volume effectively absorbs any pressure pulses that may be generated.

D. Early Fuel and Cladding Motion after Cladding Rupture

Detailed plots of the test data from 7.5 to 7.8 s are shown in Figs. 103-109. From these figures, we make the following observations and conclusions:

1. Figure 103. Hot material approaches the inlet at 7.61 s and causes a slight heating effect for the next 50 ms. At 7.66 s, the material is deposited on the inlet-thermocouple junction and causes it to fail by melting. Response of TC1 after 7.66 s is characteristic of out-of-pile experiments in which a junction was melted by an oxyacetylene torch.

In the posttest examination, the lower blockage was only 12 mm thick. Material found below the blockage had not reacted with the structure and was limited in its downward motion by the roll pins used to hold the fuel pins in place. This can only mean that the hot material that moved downward, solidified in the lower insulator region. Cooling stresses may have broken off chunks of the blockage debris, most of which ended up in the lower bend.

2. Figure 104. Outlet thermocouple TC3 and one of the inlet thermocouples TC2 fail within 5 ms of each other by meltthrough of the sheath at a point far from the junction. It is concluded that the mechanism for producing this effect is a deposit of hot or molten fuel on the sheath at or before 7.767 s. Although molten fuel penetrated the space between the holder walls at this time (see discussion in connection with Fig. 108) and is the likely source of failure in TC2, no reasonable explanation of the nearly simultaneous failure of the outlet thermocouple TC3 is convenient.

3. Figure 105. A nearly linear rise in outlet temperature during the 300-ms period after 7.5 s reflects the response to continued heating of the upper slug, either by the outlet blockage or by finite through-flow. A tendency to cool after 7.7 s is evidence that no hot material (such as an outlet blockage or massive fuel sweepout) exists in the vicinity of the outlet thermocouple (see Fig. 8).

4. Figure 106. Temperatures of sodium returning to the pump (measured by TC6 and TC7) remain relatively constant, confirming the absence of hot material this high up in the flow channel. Cooling of TC5 after 7.6 s is due to monitoring the colder sodium in the pump during reverse flow.

5. Figure 107. Thermocouples on the top (TC8) and bottom (TC7) of the upper sodium-free surface show the liquid-slug ejection began at 7.5 s (see Fig. 32). The 110°C difference in temperature at the elevation of TC8 and in the upper head before slug ejection reflects the magnitude of the heat sink formed by the upper layout structure.

6. Figure 108. The sudden drop in outlet flow and the deceleration of the inlet flow from 7.58 to 7.60 s suggests either that the holder wall has ruptured to relieve the pressures that accelerate the upper and lower slugs, or that a significant quantity of vapor condensed. Hodoscope data indicate that the holder wall probably ruptured during the time interval from 7.63 to 7.77 s (see Fig. 57), but not likely during the overlap period from 7.59 to 7.72 s (see Fig. 55). The evidence was that the holder wall ruptured at 7.72 s, about 30 ms earlier than suggested by the failure of TC2 (see Fig. 104). From these observations, the conclusion is that the holder wall probably ruptured at 7.75 s. During the relatively "quiet" period from 7.5 to 7.75 s, the entire flow channel was voided (see Fig. 43) and small amounts of fuel were moving toward the lower pin region (see Fig. 57).

The threshold sensitivity of the hodoscope was reported as 5% of the fuel in any channel (see Sec. VI.E.3). A typical edge channel (Column 11, Fig. 51) views about 7 g of fuel, so that the threshold sensitivity is about 0.5 g.

As pointed out, however, isolated changes larger than 0.5 g in single isolated channels may be "noise." Thus the quantity of fuel that could have been released to melt the holder wall initially may have been as large as the order of several grams. From the R/P plots in Fig. 58 for Channel 13 (Scalers 58 and 88), there is a gradual but measurable trend toward increased counting rates from 7.58 to 7.65 s in the region of the upper holder wall away from the pump.

7. Figure 109. Pressure pulses (from 7.55 to 7.60 s) are too small to be caused by an FCI and therefore must be due to coolant-cladding reactions. This is consistent with the flow (see Fig. 108) and temperature (see Fig. 103) data.

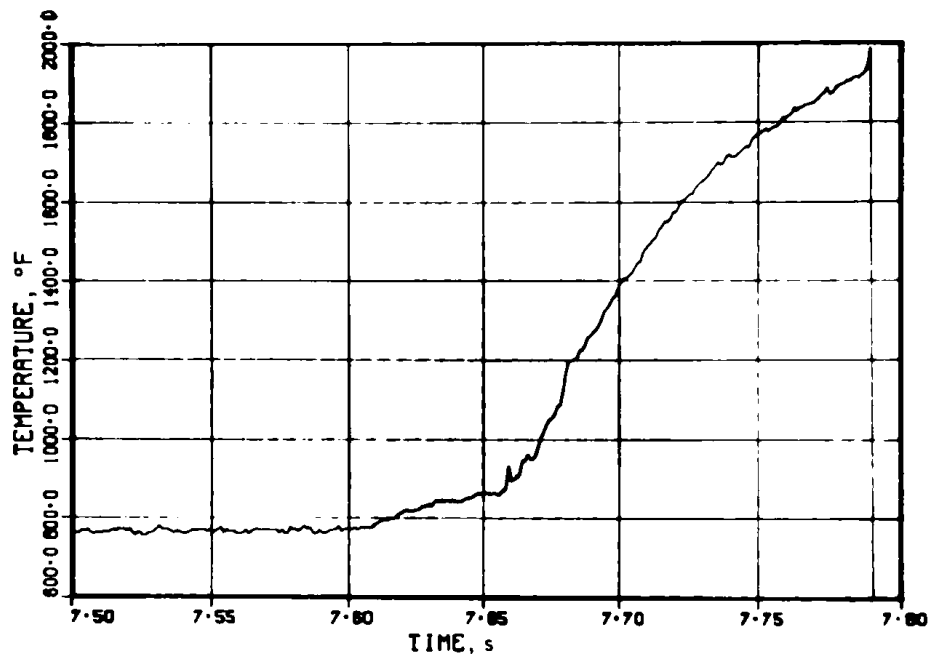


Fig. 103. Response of Inlet Thermocouple TC1 at Failure.

Conversion Factor: $t (^{\circ}\text{C}) = [t (^{\circ}\text{F}) - 32]/1.8$.

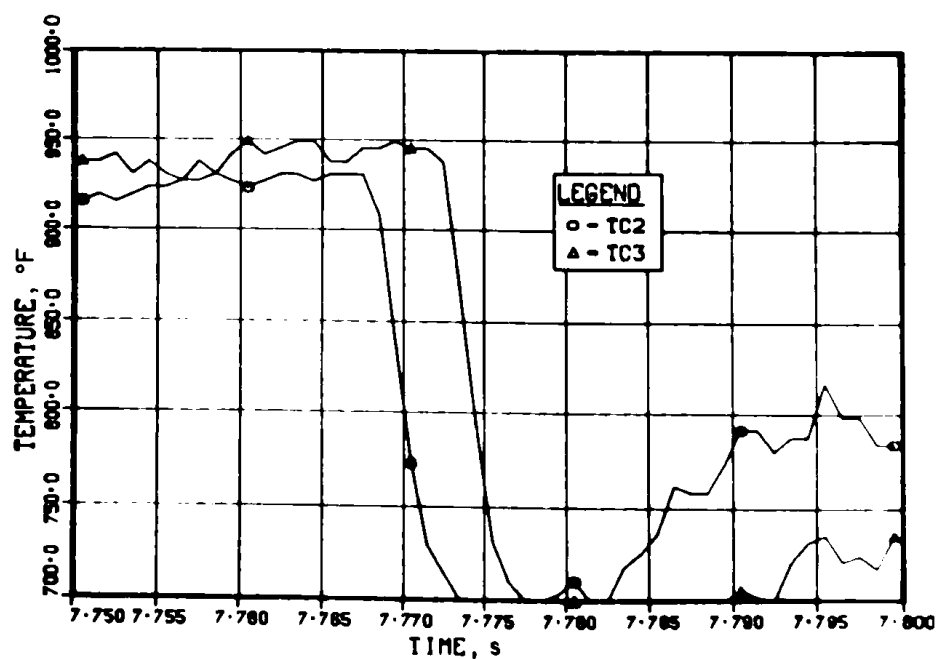


Fig. 104. Responses of Inlet Thermocouple TC2 and Outlet Thermocouple TC3 at Failure. Conversion Factor: $t (^{\circ}\text{C}) = [t (^{\circ}\text{F}) - 32]/1.8$.

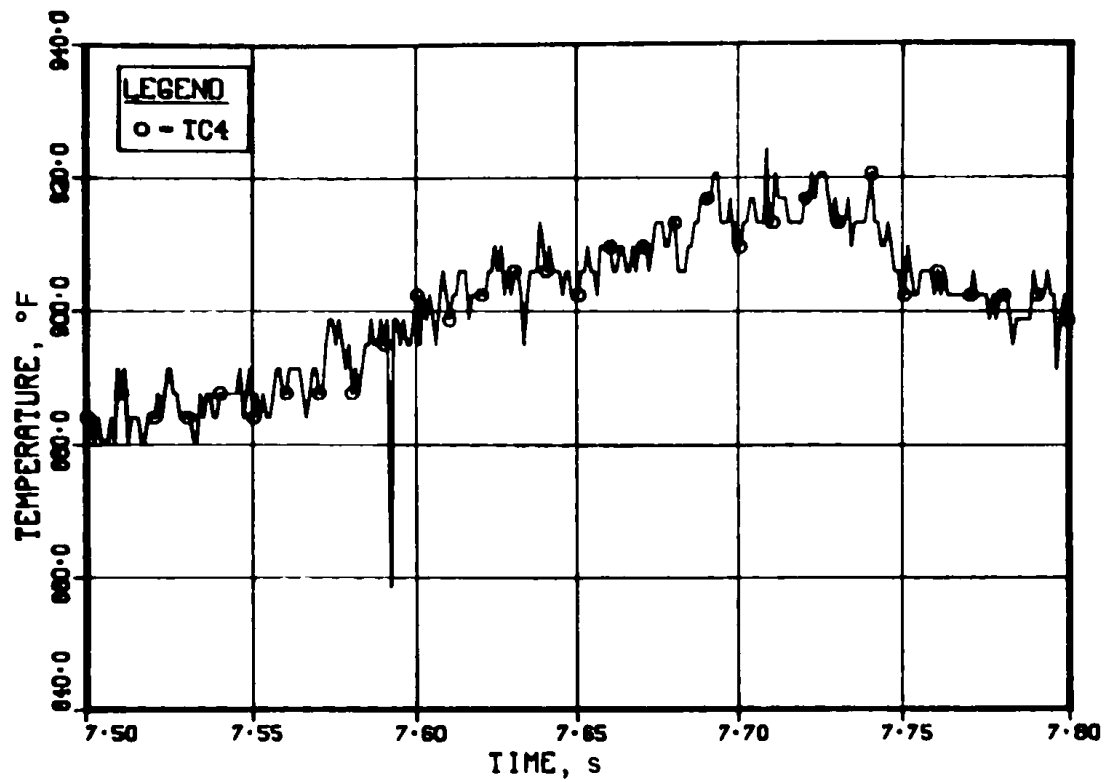


Fig. 105. Response of Outlet Thermocouple TC4 during Failure

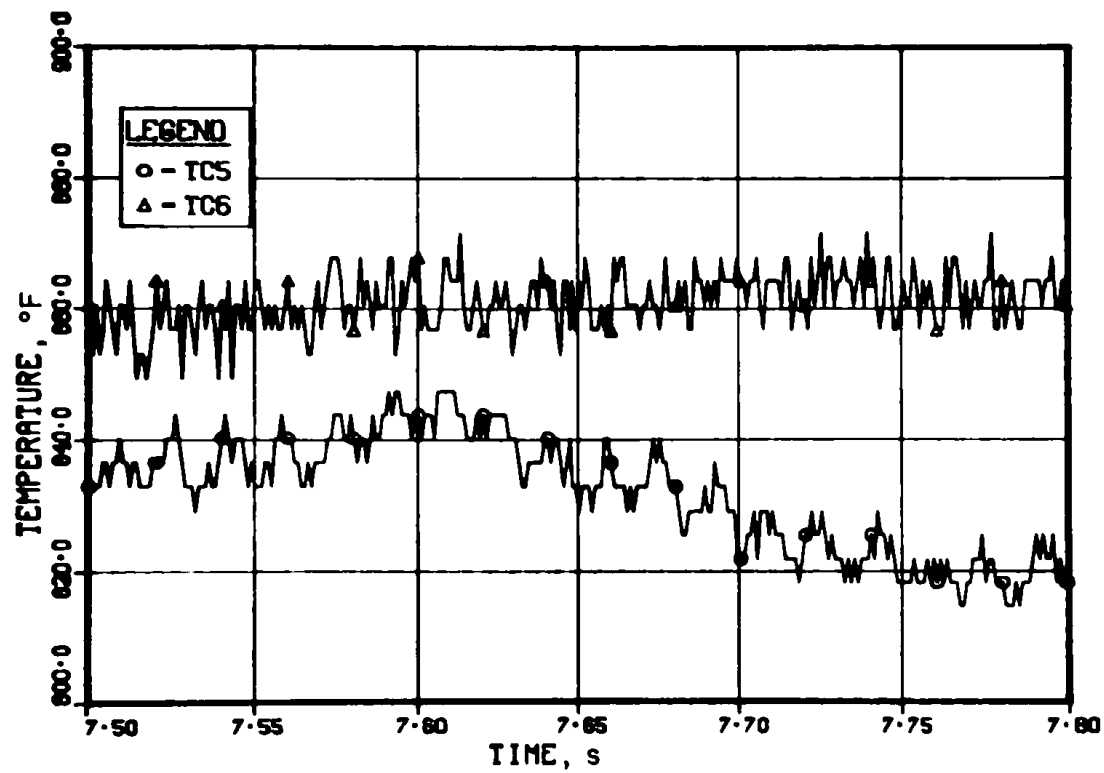


Fig. 106. Temperature History of Return Flow during Failure.
Conversion Factor: $t (^{\circ}\text{C}) = [t (^{\circ}\text{F}) - 32]/1.8$.

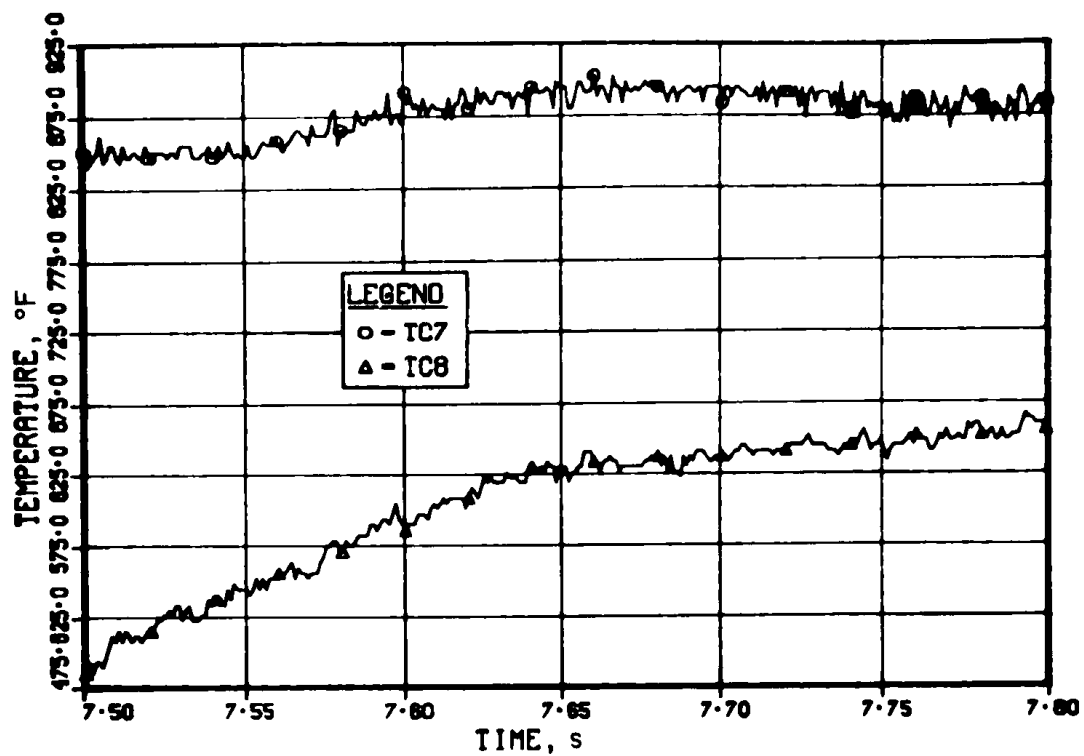


Fig. 107. Temperature History above and below Sodium-free Surface during Failure. Conversion Factor: $t (^{\circ}\text{C}) = [t (^{\circ}\text{F}) - 32]/1.8$.

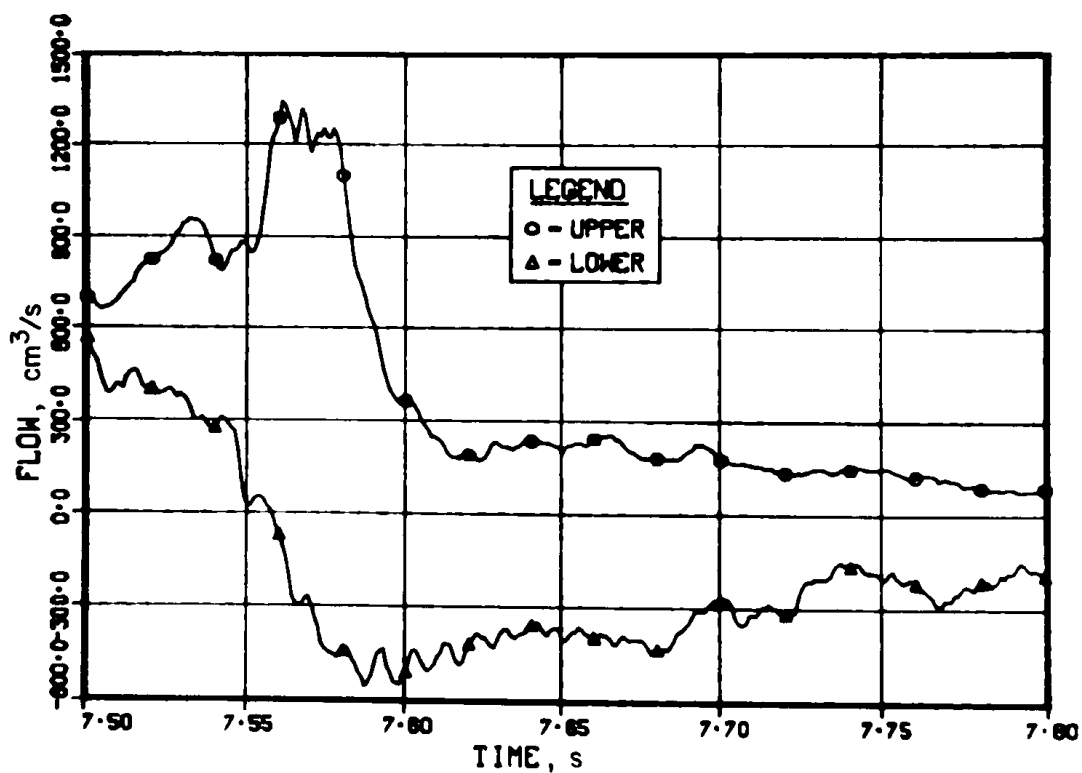


Fig. 108. Inlet and Outlet Flow during Fuel-rod Failure

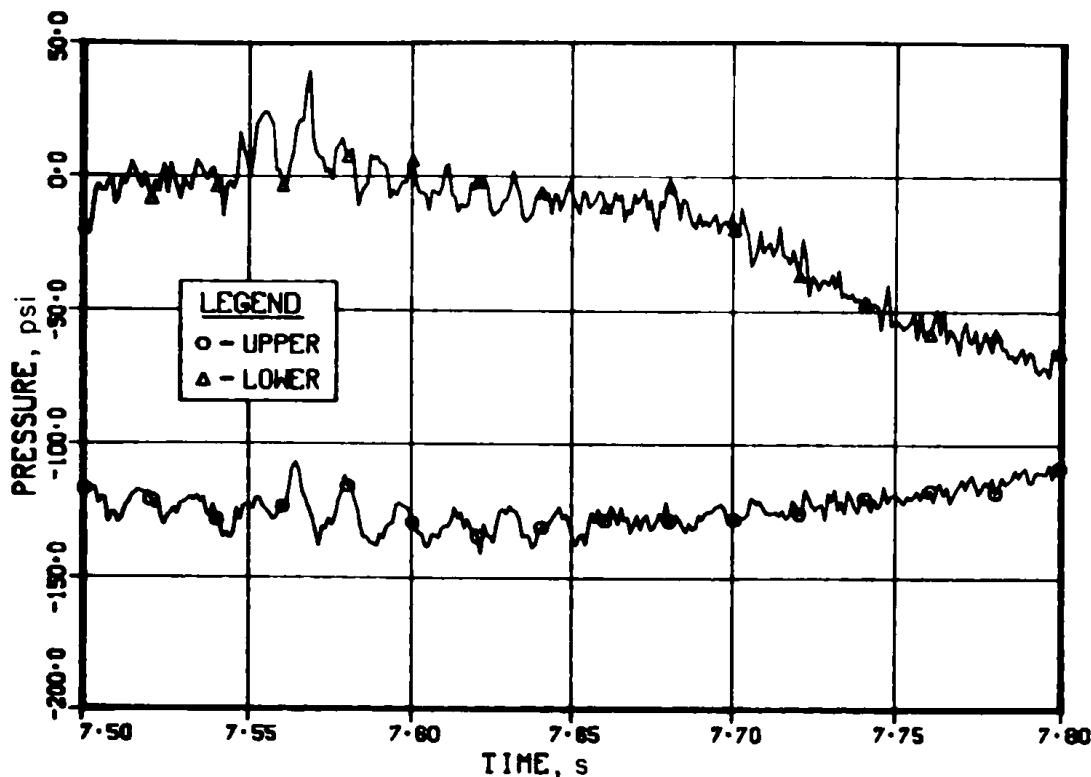


Fig. 109. Inlet and Outlet Pressure during Fuel-rod Failure.

Conversion Factor: 1 psi = 6.895 kPa.

E. Fuel Motion after Holder Rupture

Absence of any significant flow and pressure activity from 7.6 to 7.8 s and the general outward fuel motion observed by the hodoscope (see Fig. 58) support the concept of fuel-slush swelling and expansion. All the fuel elements failed, and the expansion appeared to occur over the entire cluster. Material near or in contact with the colder holder wall remained as a crust that formed a containment shell. Slush froze to the shell on the inside surface and was pushed generally in an upward direction, where it froze to the bottom region of the outlet blockage.

During the interval from 7.8 to 8.4 s, some heat energy was still being added to the crust (see Fig. 48). If a cosine axial power distribution in TREAT is assumed, the center of the crust (Rows 7 and 8, Fig. 63) is the hottest and more mobile than regions above and below Rows 7 and 8. This would cause the axial center of the crust to move, creating the void observed in the radiography (see Fig. 64) and the posttest examination (see Fig. 69).

F. Late Fuel Motion

Clearly, an interaction of significant magnitude and extremely short duration occurred in the inlet region at 7.834 s (see Figs. 35 and 36). Absence of any corresponding pressure pulses can be explained by vapor cushioning of the pressure transducers. Boiling at the inlet was clearly evident (see Fig. 37) from 8.5 to 9 s and from 10.5 to 12.5 s. A second event at 10.95 s (see Fig. 39)

showed many of the flow features of the 7.834-s event, but this one was accompanied by measurable pressure pulses (see Fig. 45). Finally, a small heat source approached the inlet at 17 s (see Fig. 17), but did not pass through the outlet, because there was no corresponding response on any other instrument and because the outlet blockage was formed and frozen by this time. At the times of these late events, the flow channel was completely voided (see Fig. 43), and instrument response was subject to larger uncertainties. The first two events (at 7.834 and 10.95 s) were probably fuel-coolant interactions (FCI's), the later occurring closer to the inlet than the former. Neither FCI relocated sufficient masses of fuel to be seen by the hodoscope.

In a quantitative way, most, but not all, of the fuel motion observed in the posttest radiograph and examinations is accounted for by the hodoscope during the time interval from 7.6 to 7.8 s. The remaining fuel relocation could be due to an interaction between the hot slush forming the inlet blockage and the lower liquid slug at 10.95 s. This interaction would blow out the loose debris at the inlet to produce the observed (posttest) fuel debris in the lower bend. The FCI at 7.834 s does not appear to have much effect on fuel relocation.

G. Chronology of Events

Table X lists the chronology of events associated with Test E7.

H. Conclusions

A failure sequence and details of early fuel movement as inferred from the E7 test data are:

Initial pin failure (at 7.453 s) was by a series of incoherent cladding ruptures and the release of $\sim 10 \text{ cm}^3$ of fission gas. Threshold fuel enthalpy for rupture is $837 \pm 21 \text{ J/g}$ ($200 \pm 5 \text{ cal/g}$). The fuel-solidus front propagated radially outward at an exponential rate with a time constant of 39 ms until 7.450 s and was into the columnar-grain region during rupture process.

Cladding melting began near the rupture point (top of fuel column) and propagated axially. Some molten cladding was carried upward by the liquid/vapor/fission-gas flow stream to start the outlet blockages (at 7.46-7.49 s). Thermal reactions of small magnitude occurred (at 7.50-7.55 s) between hot cladding and the liquid-sodium flow stream containing both condensable and noncondensable gas. A small amount of cladding dripped or flowed to the lower insulator region and froze.

Channel voiding extended over most of the fuel column by 100 ms (at 7.55 s). Small spurts of fuel were ejected from the fuel columns (at 7.58-7.76 s) to burn through the holder wall. Massive wall rupture occurred at 7.75 s. The melt front propagated with a time constant of 195 ms (at 7.45-7.58 s), about the same as the rate of increase of reactor power.

TABLE X. Chronology of Events in Test E7

Time, s	Event
7.4	Start of detectable pin bowing (see Fig. 53).
7.42	Melting begins in hottest pins (see Fig. 95).
7.453	First cladding rupture and fission-gas release (see Fig. 102).
7.46-7.49	Incoherent cladding ruptures and gas release (see Fig. 102). Same cladding carried upward (see Sec. IX.A).
7.49	First coolant-vapor bubble collapse (see Fig. 102).
7.50	Solidus front reaches equiaxed grains (see Fig. 95).
7.505-7.555	Cladding melting propagates downward (see Sec. IX.A).
7.52	Liquidus front begins in columnar grains (see Fig. 95).
7.54	Pin swelling begins (see Sec. IX.A).
7.55	Probable start of outlet blockage formation by frozen steel.
7.558	Reverse inlet flow begins (see Fig. 108).
7.56	Solidus front reaches unrestructured grains (see Fig. 95).
7.56-7.58	Individual pin swelling (see Fig. 53).
7.58	Major vapor-bubble collapse (see Fig. 108); peak reactor power (see Fig. 20).
7.59-7.72	Fuel motion toward pump and downward (see Fig. 58).
7.61	Hot debris approaches inlet (see Fig. 103).
7.62-7.75	Cluster swelling to form crust on holder wall (see Sec. IX.E).
7.66	Hot debris burns out TC1 at inlet (see Fig. 103).
7.72	Small amount of fuel moves toward blockages (see Figs. 54 and 56).
7.75-7.77	Contortion starts in the upper half of fuel column (see Sec. VI.E.3). Holder-wall rupture (see Sec. IX.D).
7.767	TC2 and TC3 failure by sheath burnthrough (see Fig. 104).
7.80	Fuel crust formed on holder wall (see Sec. VI.E.3).
7.8-8.4	Melting and relocation of fuel-crust center (Sec. IX.E).
7.81-8.05	Continued fuel churning (see Sec. VI.E.3).
7.834	FCI in central region, isolated from inlet and outlet by vapor/gas cushion (see Figs. 35 and 36).
8.05-8.41	Gradual fuel motion outward and upward (see Sec. VI.E.3).
10.95	FCI near inlet region (see Figs. 39 and 45).
17	Hot debris displaced toward outlet (see Fig. 17).

Fission gas is expected to produce fuel swelling as the melt front approaches unrestructured fuel grains (the melt front was calculated to reach this region at 7.54 s). Individual pins, with molten cores, swelled until they contacted neighboring pins. After contact, the cluster swelled as a whole to form a crust on the fluted tube. Swelling of individual pins and of the cluster as a whole was accompanied by continuous evolution of fission gas. Both processes served to displace sodium and to void the flow channel.

The dynamics of formation and transport of fission-gas bubbles that lead to fuel-element swelling and gas release has been studied in detail by Gruber.²³ Some slush oozed through the shell to add to the channel blockages. Fuel motion was characterized as being slow and predominantly outward, with some, generally later, upward and downward motion.

Slush-coolant interactions occurred after the initial failures (at 7.834, 10.950, and 16 s) and may have resulted in some redistribution of fuel. No significant pressure pulses were recorded during the entire failure sequence. After refreezing, the slush was very porous in nature. Molten cladding is extremely mobile and penetrated all available space along fuel-grain boundaries.

X. RELATION OF TEST E7 TO LMFBR CONDITIONS

Several parameters of the Test E7 are compared to the corresponding design values for the CRBR²⁴ in Table XI. For a given size of fuel pin, a

TABLE XI. Comparison of Parameters in Test E7 to Reference Design Values of CRBR

Parameters	CRBR Ref Design	Test E7
Lattice pitch, mm	7.26	6.98
Flow area per pin, mm ²	297.0	211.0
Hydraulic diameter, mm	2.72	1.68
Wall surface per pin, mm	4.45	13.5
Fuel-column length, m	0.91	0.34
Inlet pressure, MPa	0.848	0.2 ^a
Fuel Pin		
Diameter, mm	5.84	5.84
Uranium enrichment, %	0.7	77.0
Pu/(Pu + U), %	18.7, 27.1 ^b	25.0
Average burnup, MWd/t	80,000-150,000	450,000
Total rod length, mm	2.91	1.55
Spacer-wire OD, mm	1.42	1.02
Cladding midwall temperature, K	955-985	775 ^c
Flow rate, kg/s	0.437 ^d	0.481
Inlet Temperature, K	655.0	655.0

^aEstimate.

^bInner and outer regions, respectively, for first core loading.

^cDuring preconditioning irradiation in EBR-II.

^dReference value of 23.2 kg/s (184280 lb/h) in Zone 1 assumed equally divided among the 108 subassemblies and 217-pin subassembly. Value listed is for seven pins.

small value for the lattice pitch, the hydraulic diameter, and the flow area per pin tend to restrict or resist axial fuel sweepout. The wall surface per pin is a measure of the propensity for local freezing of molten debris. For all these parameters, the values are such as to indicate that axial fuel motion in Test E7 is more restricted than in the CRBR. However, the test conclusions are that radial motion due to fuel swelling would probably predominate over axial fuel sweepout because of early channel voiding and crust formation on the test-region boundaries. The shorter fuel-column length in the test offers less resistance to through-flow and may partially compensate for the hydraulic restrictions.

The low inlet pressure of the test results in a low inlet-flow inertia. During a fuel- or cladding-coolant interaction, the vapor-produced impulse can more easily reverse the inlet flow, and ultimately lead to dryout and failure of the fuel-pin region below the original failure site. The thin wall of the holder may partially compensate for this effect by yielding under large impulse pressures. Since no significant coolant interactions were observed during Test E7, the holder wall failed by meltthrough several hundred milliseconds after fuel failure.

Test-fuel burnup and enrichment were higher than in the CRBR reference design. Average linear power in the design fuel is 23 kW/m; that of the test fuel during preconditioning was 34 kW/m. The test fuel contained a central void, due to prior irradiation, of about 5% of the cross-sectional area. Little or no void is expected in CRBR fuel. Depending on the details of the failure model used, the void may have an important role in determining internal flow dynamics of molten fuel and fission-gas-pressure relief during the approach to failure. More importantly, the higher enrichment of the test fuel results in a lower cladding fluence at a given burnup. The resulting differences in cladding yield strength, ductility, brittleness, and fission-product-induced faults might lead to earlier cladding failure and gas release in the test.

At the end of the preheat and during the approach to failure, the thermal and hydraulic conditions of the test were prototypic of a \$3/s CRBR TOP accident. The central void in the test fuel probably reduced local cladding loading due to fission-gas release, but the effect is believed small compared to cladding loading by fuel swelling. No measurable amount of prefailure axial fuel movement was observed, although the thermal calculations indicate enough fuel reached the solidus before failure so that such axial flow along the central voids might have been possible.

Overall, it can be concluded that the timing of failure of one or several high-power pins in a CRBR TOP accident can be reasonably well predicted from Test E7. Additional information is needed on the relation between fluence and cladding failure, and between a higher and more prototypic inlet-flow inertia as well as the axial extent of fuel-pin failure. No definitive conclusions can be drawn from this test relating to the extent or rate of failure propagation among pins in a subassembly.

APPENDIX A

Tabulation of Test Data

The test data are tabulated in Tables A.1 and A.2. Thermocouple signals were set to zero after their failure. UP and LP refer to upper and lower pressure, respectively, and UF and LF refer to the upper and lower flow, respectively. SAF1 is the TREAT power as monitored by safety No. 1, and ISAF is the time-integrated value of SAF1. Data as listed have been conditioned as described in Sec. V and integrated over 50-ms time increments.

TABLE A.1. Instrument Signals^a

TEST E7: TREAT TRANSIENT 1499

TIME	TC1	TC2	TC3	TC4	TC5	TC6	TC7	TC8	UP	LF	UP	SAF1	ISAF
SEC	DEGC	DEGC	DEGC	DEGC	DEGC	DEGC	DEGC	DEGC	PSI	CC/S	CC/S	MM	HJ
2.725	391.	390.	396.	387.	390.	391.	397.	251.	3.	6.	579.	1.	0.
2.775	390.	391.	397.	388.	391.	391.	397.	250.	2.	6.	577.	1.	0.
2.825	390.	391.	398.	388.	391.	391.	397.	251.	4.	6.	579.	2.	0.
2.875	391.	391.	399.	388.	391.	392.	398.	252.	4.	7.	581.	2.	0.
2.925	391.	391.	399.	388.	391.	392.	398.	252.	4.	7.	581.	2.	0.
2.975	390.	392.	397.	389.	392.	391.	397.	251.	3.	5.	579.	1.	0.
3.025	391.	392.	398.	389.	392.	392.	397.	251.	5.	6.	578.	2.	0.
3.075	392.	392.	399.	389.	392.	392.	397.	252.	5.	7.	581.	2.	0.
3.125	391.	391.	399.	389.	391.	392.	397.	251.	4.	6.	582.	2.	0.
3.175	390.	391.	397.	388.	391.	391.	397.	251.	2.	5.	580.	2.	0.
3.225	390.	392.	398.	388.	391.	391.	397.	250.	3.	5.	578.	2.	0.
3.275	391.	391.	399.	389.	391.	392.	398.	251.	4.	7.	582.	3.	0.
3.325	391.	391.	398.	388.	391.	391.	397.	251.	4.	6.	580.	3.	0.
3.375	390.	392.	398.	389.	392.	391.	396.	250.	4.	6.	578.	0.	0.
3.425	391.	391.	398.	388.	391.	391.	397.	250.	3.	6.	577.	1.	0.
3.475	392.	392.	399.	388.	391.	392.	398.	252.	6.	8.	581.	2.	0.
3.525	391.	391.	399.	388.	391.	391.	397.	251.	3.	7.	579.	2.	0.
3.575	391.	391.	398.	388.	391.	391.	397.	250.	3.	6.	577.	2.	0.
3.625	390.	391.	398.	388.	391.	392.	398.	250.	3.	6.	578.	2.	0.
3.675	391.	391.	399.	388.	391.	391.	398.	251.	4.	7.	581.	3.	0.
3.725	392.	391.	399.	388.	391.	392.	398.	251.	4.	8.	579.	2.	0.
3.775	390.	391.	398.	388.	391.	391.	397.	251.	2.	6.	578.	3.	0.
3.825	391.	391.	398.	388.	391.	391.	397.	250.	2.	8.	577.	2.	0.
3.875	391.	391.	399.	388.	391.	392.	399.	251.	3.	9.	580.	4.	0.
3.925	391.	391.	399.	388.	391.	392.	398.	251.	4.	8.	581.	6.	0.
3.975	390.	390.	398.	387.	390.	391.	396.	250.	2.	8.	576.	4.	0.
4.025	391.	390.	398.	387.	391.	391.	397.	250.	-1.	9.	579.	4.	0.
4.075	392.	390.	399.	387.	390.	392.	398.	251.	0.	11.	579.	9.	0.
4.125	392.	390.	399.	387.	390.	392.	397.	251.	1.	11.	579.	11.	0.
4.175	390.	390.	398.	388.	391.	391.	396.	250.	-2.	12.	578.	11.	0.
4.225	390.	390.	397.	387.	390.	391.	397.	251.	-3.	14.	577.	17.	0.
4.275	391.	390.	399.	387.	390.	392.	398.	252.	-3.	17.	582.	23.	0.
4.325	392.	390.	399.	387.	390.	392.	397.	252.	-6.	19.	580.	29.	0.
4.375	390.	389.	398.	387.	390.	392.	397.	251.	-10.	20.	575.	35.	0.
4.425	391.	389.	398.	386.	389.	391.	396.	251.	-14.	22.	578.	44.	0.
4.475	391.	389.	399.	386.	389.	393.	398.	253.	-14.	28.	580.	57.	3.
4.525	391.	390.	399.	386.	389.	392.	397.	251.	-20.	31.	580.	72.	6.
4.575	391.	390.	398.	386.	389.	391.	397.	250.	-26.	32.	576.	89.	10.
4.625	391.	389.	398.	386.	389.	392.	397.	251.	-32.	34.	578.	111.	15.
4.675	392.	389.	400.	386.	389.	393.	398.	253.	-37.	36.	581.	145.	21.
4.725	392.	390.	399.	387.	389.	393.	398.	251.	-39.	34.	580.	147.	29.
4.775	391.	390.	399.	387.	390.	392.	398.	251.	-41.	35.	579.	153.	36.
4.825	391.	389.	399.	386.	389.	392.	397.	251.	-41.	32.	578.	147.	44.
4.875	392.	390.	400.	387.	389.	393.	398.	252.	-38.	31.	581.	145.	51.
4.925	392.	390.	400.	388.	390.	393.	398.	252.	-38.	32.	579.	138.	58.
4.975	392.	390.	399.	388.	390.	392.	398.	251.	-38.	27.	578.	135.	65.
5.025	392.	391.	400.	388.	390.	393.	398.	252.	-39.	26.	580.	143.	72.
5.075	393.	391.	401.	388.	390.	394.	399.	252.	-39.	26.	581.	146.	79.
5.125	393.	392.	402.	389.	391.	394.	400.	252.	-39.	23.	582.	145.	86.
5.175	392.	393.	402.	390.	392.	394.	398.	252.	-39.	21.	578.	139.	93.

^aConversion factor: 1 psi = 6.895 kPa.

TABLE A.1 (Contd.)

TEST E7: TREAT TRANSIENT 1499

TIME SEC	TC1 DEGC	TC2 DEGC	TC3 DEGC	TC4 DEGC	TC5 DEGC	TC6 DEGC	TC7 DEGC	TC8 DEGC	UP PSI	LP PSI	LF CC/S	UF CC/S	SAF1 MW	ISAF MJ
5.225	393.	393.	403.	390.	392.	395.	400.	252.	-38.	18.	580.	579.	135.	100.
5.275	393.	394.	405.	391.	392.	396.	401.	252.	-38.	19.	582.	542.	138.	107.
5.325	393.	396.	406.	392.	392.	397.	402.	252.	-40.	19.	580.	580.	144.	114.
5.375	392.	396.	406.	394.	393.	397.	402.	252.	-39.	15.	578.	579.	143.	121.
5.425	393.	399.	408.	396.	394.	398.	403.	253.	-39.	13.	579.	580.	138.	128.
5.475	394.	400.	411.	397.	395.	400.	405.	253.	-37.	14.	581.	541.	136.	135.
5.525	394.	402.	412.	400.	396.	401.	405.	252.	-39.	11.	581.	542.	144.	142.
5.575	393.	404.	413.	403.	397.	401.	405.	252.	-38.	7.	579.	541.	139.	149.
5.625	394.	405.	414.	404.	398.	403.	406.	252.	-38.	7.	580.	542.	138.	156.
5.675	395.	407.	417.	406.	399.	405.	407.	253.	-37.	8.	580.	542.	137.	163.
5.725	395.	408.	418.	407.	400.	406.	407.	253.	-39.	4.	579.	541.	137.	170.
5.775	394.	411.	418.	410.	402.	407.	406.	252.	-41.	3.	577.	540.	137.	177.
5.825	394.	412.	421.	412.	403.	409.	409.	253.	-39.	2.	580.	542.	139.	184.
5.875	396.	413.	423.	414.	404.	411.	413.	253.	-37.	1.	581.	544.	138.	190.
5.925	395.	414.	424.	417.	406.	412.	415.	254.	-38.	-0.	580.	544.	138.	197.
5.975	395.	416.	424.	419.	408.	412.	415.	252.	-38.	-2.	577.	541.	138.	204.
6.025	395.	416.	426.	422.	410.	414.	417.	253.	-38.	-3.	576.	543.	137.	211.
6.075	396.	419.	428.	424.	411.	416.	419.	253.	-37.	-4.	580.	545.	138.	218.
6.125	396.	418.	430.	426.	412.	417.	422.	254.	-39.	-6.	580.	545.	139.	225.
6.175	395.	422.	430.	428.	414.	417.	422.	252.	-40.	-7.	577.	542.	137.	232.
6.225	396.	423.	432.	430.	415.	420.	422.	253.	-40.	-11.	578.	543.	137.	239.
6.275	397.	425.	435.	432.	417.	422.	425.	253.	-37.	-9.	580.	546.	137.	245.
6.325	396.	426.	435.	434.	418.	424.	426.	254.	-39.	-11.	580.	546.	137.	252.
6.375	396.	428.	436.	437.	419.	424.	425.	252.	-42.	-14.	579.	545.	138.	259.
6.425	396.	429.	437.	438.	420.	427.	425.	253.	-39.	-16.	576.	543.	137.	266.
6.475	397.	430.	439.	440.	422.	429.	427.	254.	-37.	-15.	579.	546.	139.	273.
6.525	398.	431.	441.	440.	423.	431.	429.	254.	-39.	-18.	579.	546.	139.	280.
6.575	397.	432.	441.	441.	424.	431.	429.	253.	-39.	-20.	577.	545.	135.	287.
6.625	398.	434.	442.	444.	426.	432.	428.	253.	-39.	-22.	577.	545.	135.	293.
6.675	399.	434.	444.	446.	426.	434.	429.	254.	-37.	-22.	579.	547.	137.	300.
6.725	399.	436.	445.	447.	427.	436.	430.	254.	-39.	-24.	580.	547.	139.	307.
6.775	398.	437.	445.	449.	429.	436.	431.	253.	-41.	-25.	576.	544.	136.	314.
6.825	399.	434.	447.	450.	430.	438.	433.	254.	-41.	-27.	576.	545.	134.	321.
6.875	400.	440.	449.	452.	431.	440.	435.	255.	-39.	-28.	577.	546.	135.	327.
6.925	400.	440.	450.	454.	432.	441.	435.	255.	-40.	-29.	578.	546.	136.	334.
6.975	399.	441.	450.	455.	433.	441.	437.	253.	-41.	-31.	576.	545.	134.	341.
7.025	400.	443.	452.	457.	435.	443.	441.	254.	-39.	-34.	577.	546.	140.	348.
7.075	401.	444.	455.	458.	436.	444.	443.	255.	-44.	-31.	578.	547.	149.	355.
7.125	401.	446.	456.	459.	438.	445.	443.	255.	-58.	-33.	574.	544.	203.	364.
7.175	401.	447.	456.	462.	438.	446.	445.	254.	-71.	-34.	572.	542.	288.	376.
7.225	402.	448.	457.	463.	-39.	447.	446.	254.	-80.	-35.	573.	543.	370.	392.
7.275	403.	450.	460.	465.	441.	450.	449.	255.	-90.	-34.	573.	543.	487.	413.
7.325	404.	451.	461.	467.	440.	451.	448.	255.	-98.	-29.	573.	544.	652.	442.
7.375	403.	453.	461.	467.	443.	452.	448.	255.	-106.	-25.	570.	604.	867.	479.
7.425	406.	455.	464.	469.	443.	454.	448.	256.	-112.	-19.	561.	621.	1141.	529.
7.475	407.	456.	468.	470.	447.	456.	450.	256.	-115.	-12.	538.	657.	1489.	595.
7.525	408.	459.	470.	473.	447.	458.	452.	259.	-124.	-11.	452.	717.	1915.	680.
7.575	409.	463.	472.	475.	447.	459.	457.	285.	-126.	4.	93.	986.	2327.	786.
7.625	418.	467.	477.	481.	451.	461.	470.	312.	-133.	-3.	-472.	566.	2427.	907.
7.675	475.	470.	481.	486.	447.	461.	477.	331.	-134.	-11.	-388.	215.	2098.	1021.

TABLE A.1 (Contd.)

TEST E7: TREAT TRANSIENT 1499

TIME	TC1	TC2	TC3	TC4	TC5	TC6	TC7	TC8	UP	LP	LF	UF	SAF1	ISAF
SEC	DEGC	DEGC	DEGC	DEGC	DEGC	DEGC	DEGC	DEGC	PSI	PSI	CC/S	CC/S	MW	MJ
7.725	743.	478.	487.	490.	442.	462.	478.	337.	-129.	-21.	-341.	171.	1644.	1115.
7.775	961.	480.	498.	487.	438.	462.	472.	341.	-124.	-50.	-212.	129.	1165.	1185.
7.825	313.	345.	349.	482.	439.	461.	471.	348.	-114.	-73.	-268.	79.	786.	1233.
7.875	0.	0.	0.	481.	446.	459.	470.	351.	-103.	-98.	222.	60.	531.	1266.
7.925	0.	0.	0.	480.	449.	458.	469.	349.	-94.	-117.	97.	-3.	377.	1288.
7.975	0.	0.	0.	480.	451.	459.	466.	346.	-86.	-139.	-39.	-36.	283.	1304.
8.025	0.	0.	0.	481.	452.	459.	462.	342.	-76.	-157.	169.	-11.	229.	1317.
8.075	0.	0.	0.	477.	454.	461.	457.	349.	-70.	-169.	203.	-23.	200.	1328.
8.125	0.	0.	0.	473.	455.	462.	453.	334.	-66.	-178.	204.	53.	179.	1337.
8.175	0.	0.	0.	474.	454.	459.	449.	317.	-62.	-186.	210.	98.	163.	1346.
8.225	0.	0.	0.	474.	454.	458.	448.	311.	-59.	-190.	168.	-9.	153.	1354.
8.275	0.	0.	0.	476.	456.	459.	443.	310.	-58.	-194.	67.	-54.	145.	1361.
8.325	0.	0.	0.	477.	455.	458.	439.	311.	-57.	-199.	58.	-39.	139.	1368.
8.375	0.	0.	0.	478.	452.	457.	436.	310.	-57.	-197.	-12.	-53.	134.	1375.
8.425	0.	0.	0.	479.	450.	456.	434.	309.	-53.	-207.	38.	11.	127.	1381.
8.475	0.	0.	0.	479.	449.	457.	435.	312.	-50.	-202.	138.	-19.	125.	1388.
8.525	0.	0.	0.	477.	448.	457.	436.	298.	-52.	-207.	98.	-42.	132.	1394.
8.575	0.	0.	0.	474.	449.	456.	430.	290.	-53.	-210.	34.	-59.	115.	1400.
8.625	0.	0.	0.	471.	447.	458.	419.	290.	-49.	-211.	94.	-42.	114.	1406.
8.675	0.	0.	0.	468.	449.	459.	414.	289.	-31.	-219.	71.	-31.	89.	1411.
8.725	0.	0.	0.	463.	450.	458.	413.	283.	5.	-245.	92.	-5.	31.	1414.
8.775	0.	0.	0.	460.	450.	455.	407.	280.	17.	-269.	52.	9.	6.	1415.
8.825	0.	0.	0.	458.	448.	455.	409.	281.	18.	-271.	105.	22.	6.	1415.
8.875	0.	0.	0.	456.	449.	456.	407.	283.	19.	-268.	23.	15.	7.	1416.
8.925	0.	0.	0.	459.	448.	456.	399.	283.	19.	-270.	72.	36.	5.	1416.
8.975	0.	0.	0.	460.	448.	454.	395.	282.	17.	-269.	86.	45.	5.	1416.
9.025	0.	0.	0.	459.	449.	454.	397.	283.	17.	-267.	44.	47.	4.	1416.
9.075	0.	0.	0.	461.	449.	453.	400.	293.	17.	-266.	37.	32.	6.	1417.
9.125	0.	0.	0.	462.	449.	452.	400.	283.	18.	-265.	19.	50.	6.	1417.
9.175	0.	0.	0.	464.	449.	450.	400.	281.	17.	-264.	27.	54.	4.	1417.
9.225	0.	0.	0.	463.	449.	450.	400.	283.	17.	-263.	41.	55.	5.	1417.
9.275	0.	0.	0.	461.	449.	450.	400.	288.	18.	-261.	44.	58.	6.	1418.
9.325	0.	0.	0.	459.	448.	450.	399.	262.	17.	-260.	52.	45.	6.	1418.
9.375	0.	0.	0.	458.	448.	448.	397.	265.	15.	-258.	54.	54.	4.	1418.
9.425	0.	0.	0.	457.	448.	448.	397.	276.	15.	-257.	55.	50.	4.	1418.
9.475	0.	0.	0.	456.	447.	447.	398.	275.	16.	-256.	59.	62.	5.	1419.
9.525	0.	0.	0.	456.	447.	445.	397.	270.	15.	-254.	69.	55.	36.	1419.
9.575	0.	0.	0.	455.	447.	443.	395.	263.	14.	-252.	57.	62.	3.	1421.
9.625	0.	0.	0.	454.	446.	443.	393.	262.	13.	-250.	57.	59.	4.	1421.
9.675	0.	0.	0.	454.	446.	442.	392.	266.	14.	-248.	57.	59.	5.	1421.
9.725	0.	0.	0.	453.	445.	442.	393.	271.	16.	-246.	56.	54.	4.	1421.
9.775	0.	0.	0.	453.	445.	439.	394.	268.	14.	-245.	59.	63.	4.	1421.
9.825	0.	0.	0.	451.	445.	438.	395.	255.	13.	-244.	72.	60.	4.	1422.
9.875	0.	0.	0.	451.	444.	438.	395.	249.	13.	-242.	85.	68.	5.	1422.
9.925	0.	0.	0.	450.	443.	438.	393.	247.	13.	-241.	92.	65.	4.	1422.
9.975	0.	0.	0.	449.	443.	436.	389.	246.	11.	-240.	98.	66.	3.	1422.
10.025	0.	0.	0.	448.	443.	436.	387.	248.	11.	-240.	103.	76.	4.	1422.
10.075	0.	0.	0.	447.	442.	437.	386.	250.	10.	-237.	108.	75.	5.	1422.
10.125	0.	0.	0.	446.	442.	436.	386.	253.	11.	-235.	113.	72.	3.	1423.
10.175	0.	0.	0.	444.	442.	436.	385.	255.	10.	-234.	118.	73.	3.	1423.

TABLE A.1 (Contd.)

TEST E7: TREAT TRANSIENT 1499

TIME SEC	TC1 DEGC	TC2 DEGC	TC3 DEGC	TC4 DEGC	TC5 DEGC	TC6 DEGC	TC7 DEGC	TC8 DEGC	UP PSI	LP PSI	LF CC/S	UF CC/S	SAF1 MW	ISAF MJ
10.225	0.	0.	0.	439.	441.	436.	384.	253.	10.	-234.	124.	69.	3.	1423.
10.275	0.	0.	0.	432.	441.	437.	384.	253.	10.	-230.	132.	71.	4.	1423.
10.325	0.	0.	0.	427.	441.	436.	383.	252.	11.	-229.	129.	78.	5.	1423.
10.375	0.	0.	0.	424.	441.	435.	382.	251.	9.	-229.	120.	79.	3.	1424.
10.425	0.	0.	0.	422.	440.	435.	383.	251.	9.	-227.	126.	69.	4.	1424.
10.475	0.	0.	0.	424.	440.	435.	385.	252.	10.	-222.	68.	59.	4.	1424.
10.525	0.	0.	0.	425.	439.	435.	388.	252.	10.	-220.	-135.	74.	3.	1424.
10.575	0.	0.	0.	425.	438.	435.	391.	250.	8.	-223.	-35.	58.	3.	1424.
10.625	0.	0.	0.	426.	439.	436.	396.	251.	9.	-221.	154.	76.	3.	1424.
10.675	0.	0.	0.	424.	440.	435.	393.	251.	8.	-219.	193.	76.	4.	1425.
10.725	0.	0.	0.	420.	440.	434.	391.	251.	8.	-217.	183.	73.	3.	1425.
10.775	0.	0.	0.	416.	439.	431.	387.	252.	7.	-218.	171.	69.	3.	1425.
10.825	0.	0.	0.	416.	438.	430.	385.	253.	7.	-215.	138.	49.	4.	1425.
10.875	0.	0.	0.	419.	439.	428.	385.	253.	9.	-212.	70.	75.	3.	1425.
10.925	0.	0.	0.	420.	439.	427.	384.	253.	8.	-212.	89.	79.	4.	1425.
10.975	0.	0.	0.	421.	439.	426.	384.	252.	7.	-198.	-118.	51.	2.	1426.
11.025	0.	0.	0.	421.	438.	428.	390.	251.	9.	-214.	-336.	68.	6.	1426.
11.075	0.	0.	0.	420.	440.	434.	400.	252.	10.	-207.	-58.	92.	3.	1426.
11.125	0.	0.	0.	421.	440.	435.	405.	252.	10.	-207.	149.	93.	4.	1426.
11.175	0.	0.	0.	419.	439.	433.	405.	251.	7.	-206.	214.	46.	3.	1426.
11.225	0.	0.	0.	415.	439.	432.	401.	253.	6.	-206.	219.	46.	3.	1426.
11.275	0.	0.	0.	413.	440.	431.	400.	254.	8.	-202.	202.	55.	4.	1427.
11.325	0.	0.	0.	412.	440.	429.	396.	254.	7.	-202.	188.	62.	3.	1427.
11.375	0.	0.	0.	409.	439.	426.	394.	253.	6.	-201.	158.	62.	2.	1427.
11.425	0.	0.	0.	409.	437.	425.	393.	253.	5.	-198.	42.	62.	3.	1427.
11.475	0.	0.	0.	412.	436.	425.	393.	255.	7.	-198.	37.	67.	4.	1427.
11.525	0.	0.	0.	413.	437.	425.	393.	254.	7.	-197.	109.	67.	4.	1427.
11.575	0.	0.	0.	414.	436.	429.	391.	254.	5.	-195.	137.	67.	2.	1428.
11.625	0.	0.	0.	413.	435.	423.	391.	254.	6.	-193.	81.	60.	4.	1428.
11.675	0.	0.	0.	414.	435.	423.	393.	255.	6.	-189.	-90.	67.	3.	1428.
11.725	0.	0.	0.	413.	436.	423.	394.	253.	6.	-191.	-29.	72.	4.	1428.
11.775	0.	0.	0.	413.	437.	422.	393.	253.	6.	-194.	94.	63.	2.	1428.
11.825	0.	0.	0.	412.	437.	423.	394.	254.	6.	-190.	167.	65.	3.	1428.
11.875	0.	0.	0.	410.	437.	422.	395.	254.	5.	-188.	185.	71.	5.	1429.
11.925	0.	0.	0.	407.	436.	422.	395.	255.	5.	-187.	164.	49.	2.	1429.
11.975	0.	0.	0.	408.	435.	420.	395.	254.	6.	-185.	53.	43.	2.	1429.
12.025	0.	0.	0.	409.	436.	419.	396.	254.	5.	-186.	41.	47.	1.	1429.
12.075	0.	0.	0.	408.	436.	420.	399.	255.	4.	-183.	101.	70.	4.	1429.
12.125	0.	0.	0.	406.	436.	420.	399.	255.	5.	-182.	128.	70.	4.	1429.
12.175	0.	0.	0.	408.	436.	418.	397.	255.	5.	-180.	82.	63.	2.	1429.
12.225	0.	0.	0.	408.	435.	418.	398.	254.	3.	-180.	60.	63.	3.	1429.
12.275	0.	0.	0.	409.	436.	416.	399.	255.	4.	-178.	96.	59.	3.	1430.
12.325	0.	0.	0.	410.	436.	417.	399.	255.	5.	-177.	116.	59.	3.	1430.
12.375	0.	0.	0.	411.	436.	417.	398.	254.	3.	-176.	95.	63.	2.	1430.
12.425	0.	0.	0.	413.	436.	418.	398.	254.	4.	-175.	66.	60.	2.	1430.
12.475	0.	0.	0.	414.	436.	420.	400.	255.	5.	-173.	103.	64.	3.	1430.
12.525	0.	0.	0.	414.	436.	420.	399.	255.	4.	-172.	121.	73.	3.	1430.
12.575	0.	0.	0.	414.	437.	420.	398.	255.	4.	-172.	106.	66.	2.	1430.
12.625	0.	0.	0.	414.	438.	420.	398.	255.	5.	-171.	93.	63.	1.	1430.
12.675	0.	0.	0.	414.	437.	420.	400.	256.	5.	-168.	95.	64.	4.	1431.

TABLE A.1 (Contd.)

TEST E7: TREAT TRANSIENT 1499

TIME SEC	TC1 DEGC	TC2 DEGC	TC3 DEGC	TC4 DEGC	TC5 DEGC	TC6 DEGC	TC7 DEGC	TC8 DEGC	UP PSI	LP PSI	LF CC/S	UF CC/S	SAF1 MW	ISAF MJ
12.725	0.	0.	0.	414.	438.	419.	400.	255.	4.	-168.	95.	58.	3.	1431.
12.775	0.	0.	0.	415.	439.	417.	399.	255.	4.	-167.	94.	61.	2.	1431.
12.825	0.	0.	0.	415.	439.	417.	399.	255.	4.	-167.	95.	66.	3.	1431.
12.875	0.	0.	0.	414.	440.	417.	400.	256.	5.	-164.	99.	71.	4.	1431.
12.925	0.	0.	0.	414.	441.	418.	400.	256.	6.	-164.	103.	80.	3.	1431.
12.975	0.	0.	0.	414.	443.	416.	399.	255.	3.	-163.	102.	79.	2.	1431.
13.025	0.	0.	0.	415.	444.	417.	400.	255.	5.	-162.	104.	74.	1.	1431.
13.075	0.	0.	0.	414.	444.	418.	401.	256.	4.	-160.	105.	81.	3.	1432.
13.125	0.	0.	0.	415.	444.	419.	401.	256.	4.	-159.	107.	80.	3.	1432.
13.175	0.	0.	0.	415.	443.	419.	399.	255.	2.	-159.	106.	84.	2.	1432.
13.225	0.	0.	0.	415.	443.	421.	399.	255.	3.	-157.	107.	88.	2.	1432.
13.275	0.	0.	0.	415.	443.	422.	401.	256.	5.	-154.	107.	91.	3.	1432.
13.325	0.	0.	0.	414.	441.	422.	400.	256.	4.	-154.	109.	85.	3.	1432.
13.375	0.	0.	0.	415.	443.	421.	400.	256.	3.	-155.	108.	87.	2.	1432.
13.425	0.	0.	0.	415.	445.	420.	400.	256.	3.	-153.	107.	95.	2.	1432.
13.475	0.	0.	0.	415.	446.	422.	401.	256.	5.	-151.	110.	98.	3.	1433.
13.525	0.	0.	0.	415.	447.	421.	401.	256.	5.	-151.	108.	94.	3.	1433.
13.575	0.	0.	0.	415.	447.	421.	400.	256.	2.	-149.	109.	81.	2.	1433.
13.625	0.	0.	0.	415.	447.	421.	400.	255.	1.	-150.	111.	82.	2.	1433.
13.675	0.	0.	0.	415.	446.	422.	401.	255.	5.	-146.	112.	94.	3.	1433.
13.725	0.	0.	0.	415.	445.	422.	401.	256.	4.	-146.	115.	95.	3.	1433.
13.775	0.	0.	0.	415.	443.	422.	400.	255.	2.	-146.	114.	95.	2.	1433.
13.825	0.	0.	0.	416.	441.	423.	400.	255.	3.	-144.	113.	88.	3.	1433.
13.875	0.	0.	0.	415.	439.	424.	401.	256.	4.	-143.	116.	82.	4.	1434.
13.925	0.	0.	0.	415.	438.	424.	401.	256.	4.	-141.	115.	86.	2.	1434.
13.975	0.	0.	0.	415.	437.	424.	400.	255.	2.	-141.	114.	72.	1.	1434.
14.025	0.	0.	0.	415.	439.	426.	400.	255.	4.	-141.	113.	78.	3.	1434.
14.075	0.	0.	0.	416.	440.	427.	401.	256.	5.	-140.	116.	84.	3.	1434.
14.125	0.	0.	0.	415.	442.	428.	401.	256.	4.	-138.	117.	83.	4.	1434.
14.175	0.	0.	0.	415.	443.	427.	400.	255.	2.	-138.	111.	77.	2.	1434.
14.225	0.	0.	0.	415.	444.	428.	401.	256.	3.	-136.	113.	84.	2.	1434.
14.275	0.	0.	0.	415.	444.	430.	401.	256.	4.	-135.	118.	83.	3.	1435.
14.325	0.	0.	0.	416.	445.	429.	401.	256.	4.	-133.	117.	76.	3.	1435.
14.375	0.	0.	0.	416.	444.	429.	400.	255.	2.	-134.	119.	76.	2.	1435.
14.425	0.	0.	0.	415.	444.	430.	400.	255.	3.	-132.	119.	71.	1.	1435.
14.475	0.	0.	0.	416.	444.	431.	401.	256.	5.	-131.	119.	67.	3.	1435.
14.525	0.	0.	0.	416.	444.	432.	401.	255.	3.	-129.	120.	63.	3.	1435.
14.575	0.	0.	0.	416.	444.	431.	400.	255.	4.	-130.	116.	51.	1.	1435.
14.625	0.	0.	0.	415.	443.	432.	400.	255.	2.	-130.	117.	50.	2.	1435.
14.675	0.	0.	0.	415.	445.	433.	401.	256.	4.	-126.	119.	48.	3.	1435.
14.725	0.	0.	0.	415.	447.	434.	401.	256.	5.	-126.	118.	40.	3.	1435.
14.775	0.	0.	0.	415.	446.	433.	400.	255.	4.	-126.	118.	36.	3.	1436.
14.825	0.	0.	0.	415.	446.	434.	400.	256.	3.	-125.	119.	31.	2.	1436.
14.875	0.	0.	0.	415.	446.	434.	401.	256.	3.	-122.	122.	25.	4.	1436.
14.925	0.	0.	0.	415.	447.	435.	401.	256.	4.	-122.	121.	22.	4.	1436.
14.975	0.	0.	0.	414.	448.	435.	400.	255.	3.	-122.	120.	22.	2.	1436.
15.025	0.	0.	0.	414.	448.	436.	400.	255.	4.	-121.	121.	23.	3.	1436.
15.075	0.	0.	0.	414.	450.	438.	401.	256.	3.	-119.	121.	22.	3.	1436.
15.125	0.	0.	0.	414.	452.	438.	401.	256.	5.	-118.	120.	17.	3.	1437.
15.175	0.	0.	0.	414.	450.	438.	400.	255.	3.	-117.	118.	19.	2.	1437.

TABLE A.1 (Contd.)

TEST E71 TREAT TRANSIENT 1499

TIME SEC	TC1 DEGC	TC2 DEGC	TC3 DEGC	TC4 DEGC	TC5 DEGC	TC6 DEGC	TC7 DEGC	TC8 DEGC	UP PSI	LP PSI	LF CC/S	UP CC/S	SAF1 MW	ISAF MJ
15.225	0.	0.	0.	414.	449.	439.	400.	255.	4.	-118.	118.	17.	2.	1437.
15.275	0.	0.	0.	414.	449.	439.	401.	255.	3.	-115.	117.	21.	2.	1437.
15.325	0.	0.	0.	414.	448.	439.	401.	255.	5.	-116.	117.	21.	2.	1437.
15.375	0.	0.	0.	414.	447.	439.	401.	255.	3.	-115.	117.	24.	2.	1437.
15.425	0.	0.	0.	414.	446.	440.	401.	255.	6.	-115.	117.	30.	2.	1437.
15.475	0.	0.	0.	413.	446.	441.	402.	256.	4.	-110.	119.	27.	2.	1437.
15.525	0.	0.	0.	413.	449.	441.	401.	256.	5.	-113.	117.	32.	2.	1437.
15.575	0.	0.	0.	414.	453.	441.	400.	256.	2.	-113.	115.	25.	2.	1437.
15.625	0.	0.	0.	413.	457.	442.	400.	255.	2.	-110.	115.	32.	3.	1438.
15.675	0.	0.	0.	413.	460.	442.	402.	256.	3.	-109.	118.	33.	3.	1438.
15.725	0.	0.	0.	413.	461.	441.	401.	255.	4.	-109.	119.	33.	3.	1438.
15.775	0.	0.	0.	413.	463.	440.	401.	255.	3.	-108.	116.	43.	2.	1438.
15.825	0.	0.	0.	412.	464.	440.	401.	255.	5.	-107.	119.	36.	2.	1438.
15.875	0.	0.	0.	412.	467.	441.	402.	256.	4.	-104.	119.	38.	4.	1438.
15.925	0.	0.	0.	412.	469.	441.	402.	256.	5.	-105.	117.	37.	3.	1438.
15.975	0.	0.	0.	412.	472.	440.	401.	255.	4.	-106.	115.	44.	2.	1438.
16.025	0.	0.	0.	412.	473.	440.	401.	255.	5.	-104.	117.	44.	3.	1439.
16.075	0.	0.	0.	412.	475.	442.	402.	256.	5.	-101.	120.	50.	3.	1439.
16.125	0.	0.	0.	412.	476.	443.	402.	256.	4.	-102.	117.	54.	4.	1439.
16.175	0.	0.	0.	412.	476.	444.	401.	255.	3.	-102.	116.	55.	2.	1439.
16.225	0.	0.	0.	412.	477.	447.	401.	255.	3.	-102.	117.	61.	2.	1439.
16.275	0.	0.	0.	412.	478.	448.	402.	256.	6.	-99.	118.	62.	4.	1439.
16.325	0.	0.	0.	411.	477.	448.	402.	256.	5.	-97.	117.	62.	3.	1439.
16.375	0.	0.	0.	411.	476.	448.	401.	255.	3.	-100.	113.	46.	2.	1440.
16.425	0.	0.	0.	411.	477.	448.	401.	255.	4.	-98.	114.	32.	1.	1440.
16.475	0.	0.	0.	411.	476.	448.	402.	255.	5.	-96.	114.	15.	3.	1440.
16.525	0.	0.	0.	412.	469.	449.	401.	255.	4.	-96.	114.	6.	2.	1440.
16.575	0.	0.	0.	412.	468.	448.	400.	254.	3.	-97.	111.	-4.	1.	1440.
16.625	0.	0.	0.	412.	469.	449.	402.	256.	4.	-96.	112.	-18.	1.	1440.
16.675	0.	0.	0.	411.	473.	451.	401.	256.	5.	-93.	114.	-40.	3.	1440.
16.725	0.	0.	0.	412.	472.	451.	402.	256.	4.	-92.	113.	-43.	2.	1440.
16.775	0.	0.	0.	411.	469.	450.	400.	255.	5.	-94.	109.	-52.	2.	1440.
16.825	0.	0.	0.	411.	469.	451.	401.	255.	3.	-94.	112.	-59.	2.	1440.
16.875	0.	0.	0.	411.	471.	452.	402.	256.	4.	-90.	113.	-67.	2.	1440.
16.925	0.	0.	0.	411.	473.	452.	402.	256.	4.	-91.	109.	-80.	2.	1441.
16.975	0.	0.	0.	411.	474.	452.	401.	255.	3.	-90.	110.	-83.	2.	1441.
17.025	0.	0.	0.	411.	475.	452.	401.	256.	3.	-89.	109.	-85.	2.	1441.
17.075	0.	0.	0.	411.	475.	454.	402.	257.	5.	-85.	109.	-83.	2.	1441.
17.125	0.	0.	0.	414.	478.	454.	402.	257.	3.	-87.	109.	-91.	3.	1441.
17.175	0.	0.	0.	434.	480.	454.	401.	255.	4.	-88.	107.	-90.	1.	1441.
17.225	0.	0.	0.	446.	481.	455.	401.	256.	5.	-87.	109.	-103.	2.	1441.
17.275	0.	0.	0.	454.	484.	457.	402.	256.	4.	-84.	110.	-105.	3.	1441.
17.325	0.	0.	0.	461.	488.	460.	402.	256.	6.	-84.	110.	-105.	2.	1441.
17.375	0.	0.	0.	464.	491.	461.	401.	255.	5.	-86.	109.	-107.	1.	1441.
17.425	0.	0.	0.	467.	494.	464.	401.	255.	3.	-85.	107.	-111.	1.	1441.
17.475	0.	0.	0.	470.	496.	466.	403.	256.	4.	-82.	108.	-123.	3.	1442.
17.525	0.	0.	0.	472.	498.	466.	402.	256.	5.	-82.	106.	-108.	2.	1442.
17.575	0.	0.	0.	475.	500.	466.	401.	255.	2.	-81.	104.	-118.	2.	1442.
17.625	0.	0.	0.	476.	500.	467.	401.	255.	4.	-79.	107.	-118.	2.	1442.
17.675	0.	0.	0.	476.	497.	469.	402.	257.	5.	-80.	108.	-114.	2.	1442.

TABLE A.1 (Contd.)

TEST E7: TREAT TRANSIENT 1499

TIME SEC	TC1 DEGC	TC2 DEGC	TC3 DEGC	TC4 DEGC	TC5 DEGC	TC6 DEGC	TC7 DEGC	TC8 DEGC	UP PSI	LD PSI	LF CC/S	UF CC/S	SAF1 MW	ISAF MJ
17.725	0.	0.	0.	479.	496.	470.	402.	256.	6.	-79.	106.	-121.	2.	1442.
17.775	0.	0.	0.	481.	497.	470.	401.	255.	4.	-80.	106.	-125.	1.	1442.
17.825	0.	0.	0.	484.	500.	472.	402.	255.	4.	-79.	108.	-119.	2.	1442.
17.875	0.	0.	0.	487.	504.	473.	402.	257.	6.	-77.	110.	-124.	3.	1442.
17.925	0.	0.	0.	488.	507.	474.	402.	256.	5.	-77.	109.	-120.	2.	1442.
17.975	0.	0.	0.	491.	509.	474.	401.	256.	4.	-77.	106.	-116.	2.	1443.
18.025	0.	0.	0.	493.	510.	476.	401.	256.	5.	-76.	108.	-117.	2.	1443.
18.075	0.	0.	0.	494.	511.	477.	402.	256.	5.	-75.	106.	-123.	2.	1443.
18.125	0.	0.	0.	496.	511.	479.	402.	257.	5.	-73.	104.	-119.	3.	1443.
18.175	0.	0.	0.	497.	510.	478.	401.	256.	4.	-73.	102.	-123.	1.	1443.
18.225	0.	0.	0.	498.	512.	480.	401.	256.	4.	-73.	102.	-127.	2.	1443.
18.275	0.	0.	0.	501.	513.	482.	403.	256.	7.	-71.	104.	-132.	2.	1443.
18.325	0.	0.	0.	502.	513.	483.	402.	257.	6.	-72.	104.	-131.	3.	1443.
18.375	0.	0.	0.	503.	513.	483.	401.	256.	6.	-73.	103.	-135.	2.	1443.
18.425	0.	0.	0.	504.	513.	484.	402.	256.	5.	-71.	104.	-140.	3.	1443.
18.475	0.	0.	0.	507.	516.	486.	402.	257.	7.	-70.	107.	-137.	4.	1444.
18.525	0.	0.	0.	510.	519.	486.	403.	256.	5.	-68.	107.	-137.	2.	1444.
18.575	0.	0.	0.	510.	520.	486.	401.	255.	4.	-68.	103.	-139.	2.	1444.
18.625	0.	0.	0.	509.	520.	488.	401.	256.	4.	-68.	103.	-144.	1.	1444.
18.675	0.	0.	0.	510.	520.	489.	403.	256.	6.	-66.	106.	-137.	3.	1444.
18.725	0.	0.	0.	512.	519.	489.	403.	257.	6.	-66.	104.	-139.	3.	1444.
18.775	0.	0.	0.	513.	517.	490.	402.	255.	6.	-67.	103.	-136.	0.	1444.
18.825	0.	0.	0.	516.	516.	491.	402.	255.	5.	-66.	103.	-131.	1.	1444.
18.875	0.	0.	0.	517.	513.	492.	402.	256.	6.	-65.	105.	-128.	2.	1444.
18.925	0.	0.	0.	518.	514.	493.	403.	257.	6.	-64.	103.	-131.	3.	1444.
18.975	0.	0.	0.	518.	514.	493.	402.	255.	4.	-65.	98.	-127.	2.	1445.
19.025	0.	0.	0.	518.	513.	495.	401.	256.	4.	-63.	101.	-125.	2.	1445.
19.075	0.	0.	0.	519.	515.	496.	402.	257.	6.	-61.	101.	-129.	3.	1445.
19.125	0.	0.	0.	520.	519.	497.	402.	256.	5.	-62.	101.	-123.	2.	1445.
19.175	0.	0.	0.	520.	522.	497.	402.	255.	4.	-62.	100.	-117.	2.	1445.
19.225	0.	0.	0.	522.	523.	499.	402.	255.	6.	-62.	102.	-122.	1.	1445.
19.275	0.	0.	0.	523.	524.	499.	403.	256.	6.	-59.	106.	-116.	3.	1445.
19.325	0.	0.	0.	523.	525.	500.	403.	256.	6.	-59.	104.	-118.	2.	1445.
19.375	0.	0.	0.	522.	523.	500.	402.	255.	4.	-61.	100.	-123.	2.	1445.
19.425	0.	0.	0.	524.	523.	502.	402.	255.	4.	-60.	98.	-117.	2.	1446.
19.475	0.	0.	0.	527.	523.	504.	402.	256.	4.	-57.	102.	-114.	3.	1446.
19.525	0.	0.	0.	528.	522.	505.	402.	256.	5.	-57.	101.	-119.	3.	1446.
19.575	0.	0.	0.	529.	521.	505.	402.	255.	4.	-58.	99.	-117.	2.	1446.
19.625	0.	0.	0.	529.	524.	505.	402.	256.	4.	-57.	98.	-115.	2.	1446.
19.675	0.	0.	0.	530.	527.	506.	403.	257.	6.	-56.	102.	-116.	3.	1446.
19.725	0.	0.	0.	531.	529.	506.	403.	256.	5.	-55.	101.	-117.	2.	1446.
19.775	0.	0.	0.	530.	531.	505.	402.	255.	5.	-56.	101.	-116.	2.	1446.
19.825	0.	0.	0.	528.	535.	507.	402.	255.	4.	-56.	99.	-117.	1.	1446.
19.875	0.	0.	0.	526.	534.	510.	403.	257.	7.	-53.	103.	-114.	3.	1447.
19.925	0.	0.	0.	528.	532.	511.	403.	256.	5.	-52.	102.	-115.	3.	1447.
19.975	0.	0.	0.	531.	529.	511.	402.	255.	6.	-53.	98.	-120.	2.	1447.
20.025	0.	0.	0.	532.	526.	513.	402.	256.	6.	-53.	97.	-112.	1.	1447.
20.075	0.	0.	0.	533.	524.	515.	403.	257.	5.	-51.	97.	-115.	3.	1447.
20.125	0.	0.	0.	533.	523.	515.	402.	256.	5.	-50.	96.	-114.	3.	1447.
20.175	0.	0.	0.	533.	522.	514.	402.	255.	3.	-52.	95.	-112.	2.	1447.

TABLE A.1 (Contd.)

TEST E7: TREAT TRANSIENT 1499

TIME SEC	TC1 DEGC	TC2 DEGC	TC3 DEGC	TC4 DEGC	TC5 DEGC	TC6 DEGC	TC7 DEGC	TC8 DEGC	UP PSI	LP PSI	LF CC/S	UF CC/S	SAF1 MW	ISAF MJ
20.225	0.	0.	0.	532.	522.	516.	402.	256.	5.	-50.	94.	-112.	2.	1447.
20.275	0.	0.	0.	535.	523.	518.	403.	256.	6.	-50.	94.	-109.	3.	1447.
20.325	0.	0.	0.	538.	528.	519.	403.	257.	5.	-48.	94.	-113.	2.	1448.
20.375	0.	0.	0.	538.	532.	518.	402.	256.	4.	-50.	90.	-107.	1.	1448.
20.425	0.	0.	0.	538.	534.	519.	402.	256.	5.	-49.	91.	-115.	1.	1448.
20.475	0.	0.	0.	536.	537.	521.	403.	257.	6.	-47.	92.	-109.	2.	1448.
20.525	0.	0.	0.	538.	541.	521.	403.	257.	5.	-47.	94.	-105.	3.	1448.
20.575	0.	0.	0.	538.	543.	521.	402.	256.	5.	-48.	94.	-107.	2.	1448.
20.625	0.	0.	0.	536.	544.	522.	402.	256.	5.	-48.	92.	-106.	1.	1448.
20.675	0.	0.	0.	539.	546.	523.	403.	256.	6.	-46.	95.	-110.	3.	1448.
20.725	0.	0.	0.	539.	548.	524.	403.	257.	7.	-44.	95.	-107.	3.	1448.
20.775	0.	0.	0.	539.	549.	524.	401.	255.	5.	-46.	93.	-103.	1.	1448.
20.825	0.	0.	0.	540.	550.	525.	402.	256.	4.	-44.	94.	-109.	3.	1448.
20.875	0.	0.	0.	540.	550.	527.	403.	256.	7.	-44.	92.	-106.	3.	1449.
20.925	0.	0.	0.	539.	549.	527.	403.	256.	6.	-44.	92.	-98.	2.	1449.
20.975	0.	0.	0.	537.	546.	526.	402.	255.	4.	-44.	90.	-100.	2.	1449.
21.025	0.	0.	0.	533.	542.	528.	402.	256.	6.	-43.	90.	-104.	2.	1449.
21.075	0.	0.	0.	531.	541.	530.	403.	256.	6.	-41.	93.	-97.	3.	1449.
21.125	0.	0.	0.	529.	541.	531.	403.	256.	6.	-42.	94.	-91.	2.	1449.
21.175	0.	0.	0.	526.	537.	530.	402.	255.	5.	-42.	89.	-88.	1.	1449.
21.225	0.	0.	0.	526.	532.	532.	402.	255.	4.	-42.	89.	-93.	2.	1449.
21.275	0.	0.	0.	536.	528.	533.	403.	257.	7.	-40.	92.	-93.	3.	1449.
21.325	0.	0.	0.	541.	528.	535.	403.	256.	6.	-41.	89.	-89.	2.	1450.
21.375	0.	0.	0.	542.	526.	534.	402.	255.	6.	-41.	89.	-92.	2.	1450.
21.425	0.	0.	0.	541.	523.	532.	402.	256.	4.	-40.	91.	-88.	2.	1450.
21.475	0.	0.	0.	542.	522.	537.	403.	256.	5.	-38.	89.	-91.	2.	1450.
21.525	0.	0.	0.	543.	521.	537.	403.	257.	5.	-37.	90.	-89.	3.	1450.
21.575	0.	0.	0.	541.	522.	537.	402.	256.	6.	-38.	90.	-91.	2.	1450.
21.625	0.	0.	0.	538.	523.	538.	403.	256.	5.	-39.	91.	-88.	2.	1450.
21.675	0.	0.	0.	535.	524.	539.	403.	257.	7.	-37.	93.	-85.	2.	1450.
21.725	0.	0.	0.	532.	525.	540.	403.	256.	6.	-36.	90.	-89.	3.	1450.
21.775	0.	0.	0.	530.	525.	539.	402.	255.	5.	-37.	80.	-86.	2.	1451.
21.825	0.	0.	0.	527.	525.	541.	402.	256.	5.	-36.	86.	-87.	2.	1451.
21.875	0.	0.	0.	525.	527.	541.	403.	256.	7.	-35.	90.	-80.	3.	1451.
21.925	0.	0.	0.	523.	531.	542.	403.	257.	6.	-35.	89.	-79.	3.	1451.
21.975	0.	0.	0.	521.	535.	542.	403.	256.	4.	-35.	88.	-77.	1.	1451.
22.025	0.	0.	0.	520.	535.	543.	402.	255.	5.	-34.	86.	-79.	2.	1451.
22.075	0.	0.	0.	518.	533.	544.	404.	257.	6.	-33.	89.	-69.	3.	1451.
22.125	0.	0.	0.	517.	536.	544.	403.	256.	6.	-34.	86.	-78.	3.	1451.
22.175	0.	0.	0.	515.	540.	544.	402.	255.	6.	-34.	86.	-80.	2.	1451.
22.225	0.	0.	0.	513.	541.	546.	403.	256.	6.	-34.	87.	-73.	2.	1452.
22.275	0.	0.	0.	511.	543.	546.	404.	256.	6.	-31.	87.	-76.	3.	1452.
22.325	0.	0.	0.	511.	543.	546.	403.	256.	6.	-31.	85.	-68.	2.	1452.
22.375	0.	0.	0.	509.	539.	546.	402.	255.	4.	-33.	84.	-73.	1.	1452.
22.425	0.	0.	0.	508.	539.	547.	402.	256.	3.	-31.	85.	-66.	1.	1452.
22.475	0.	0.	0.	507.	538.	549.	404.	256.	7.	-30.	88.	-61.	3.	1452.
22.525	0.	0.	0.	506.	535.	549.	404.	256.	6.	-29.	86.	-54.	2.	1452.
22.575	0.	0.	0.	504.	534.	549.	403.	256.	5.	-30.	86.	-60.	2.	1452.
22.625	0.	0.	0.	503.	532.	550.	403.	256.	5.	-30.	87.	-67.	2.	1452.
22.675	0.	0.	0.	502.	532.	551.	404.	257.	6.	-28.	86.	-53.	3.	1452.

TABLE A.1 (Contd.)

TEST E7: TREAT TRANSIENT 1499

TIME SEC	TC1 DEGC	TC2 DEGC	TC3 DEGC	TC4 DEGC	TC5 DEGC	TC6 DEGC	TC7 DEGC	TC8 DEGC	UP PSI	LP PSI	LF CC/S	UF CC/S	SAF1 MW	ISAF MJ
22.725	0.	0.	0.	502.	534.	551.	404.	256.	5.	-29.	88.	-57.	2.	1453.
22.775	0.	0.	0.	500.	533.	551.	402.	256.	5.	-29.	86.	-53.	1.	1453.
22.825	0.	0.	0.	499.	533.	552.	403.	255.	6.	-28.	84.	-52.	2.	1453.
22.875	0.	0.	0.	498.	533.	553.	404.	257.	6.	-28.	86.	-47.	3.	1453.
22.925	0.	0.	0.	497.	533.	553.	403.	256.	5.	-27.	83.	-48.	2.	1453.
22.975	0.	0.	0.	496.	533.	553.	402.	256.	3.	-28.	83.	-36.	2.	1453.
23.025	0.	0.	0.	496.	531.	553.	403.	256.	5.	-27.	82.	-36.	2.	1453.
23.075	0.	0.	0.	495.	532.	554.	404.	257.	7.	-25.	84.	-37.	2.	1453.
23.125	0.	0.	0.	494.	533.	556.	404.	257.	7.	-25.	84.	-39.	3.	1453.
23.175	0.	0.	0.	493.	534.	555.	403.	256.	5.	-26.	81.	-33.	2.	1454.
23.225	0.	0.	0.	492.	536.	555.	403.	256.	7.	-25.	82.	-28.	2.	1454.
23.275	0.	0.	0.	492.	536.	554.	405.	257.	8.	-24.	85.	-26.	3.	1454.
23.325	0.	0.	0.	491.	539.	556.	404.	256.	8.	-25.	82.	-26.	2.	1454.
23.375	0.	0.	0.	490.	541.	556.	402.	255.	6.	-24.	82.	-29.	2.	1454.
23.425	0.	0.	0.	490.	543.	557.	403.	256.	5.	-24.	84.	-24.	2.	1454.
23.475	0.	0.	0.	488.	545.	557.	404.	256.	6.	-23.	83.	-25.	2.	1454.
23.525	0.	0.	0.	488.	547.	558.	404.	257.	7.	-22.	83.	-24.	2.	1454.
23.575	0.	0.	0.	487.	547.	558.	402.	255.	5.	-23.	80.	-20.	2.	1454.
23.625	0.	0.	0.	486.	547.	557.	403.	256.	6.	-23.	80.	-18.	2.	1454.
23.675	0.	0.	0.	486.	549.	560.	404.	256.	8.	-21.	79.	-14.	2.	1455.
23.725	0.	0.	0.	485.	550.	559.	404.	257.	7.	-21.	82.	-13.	3.	1455.
23.775	0.	0.	0.	485.	549.	559.	403.	256.	4.	-21.	77.	-13.	1.	1455.
23.825	0.	0.	0.	485.	552.	559.	403.	256.	6.	-21.	80.	-12.	1.	1455.
23.875	0.	0.	0.	483.	554.	560.	404.	257.	7.	-20.	82.	-8.	2.	1455.
23.925	0.	0.	0.	483.	557.	561.	403.	256.	8.	-21.	80.	-4.	3.	1455.
23.975	0.	0.	0.	483.	557.	561.	402.	256.	6.	-20.	78.	-6.	2.	1455.
24.025	0.	0.	0.	481.	553.	561.	404.	256.	7.	-20.	80.	-6.	1.	1455.
24.075	0.	0.	0.	481.	546.	562.	403.	257.	9.	-18.	81.	-2.	3.	1455.
24.125	0.	0.	0.	481.	544.	562.	404.	256.	5.	-19.	80.	-1.	2.	1455.
24.175	0.	0.	0.	480.	542.	561.	403.	255.	6.	-20.	78.	-1.	2.	1456.
24.225	0.	0.	0.	480.	541.	563.	404.	256.	7.	-19.	81.	0.	2.	1456.
24.275	0.	0.	0.	479.	541.	564.	404.	257.	7.	-17.	80.	6.	3.	1456.
24.325	0.	0.	0.	479.	542.	563.	404.	257.	7.	-17.	82.	5.	2.	1456.
24.375	0.	0.	0.	478.	542.	563.	403.	256.	4.	-18.	78.	7.	2.	1456.
24.425	0.	0.	0.	477.	541.	563.	403.	255.	6.	-18.	79.	9.	2.	1456.
24.475	0.	0.	0.	477.	541.	565.	404.	256.	7.	-15.	81.	14.	2.	1456.
24.525	0.	0.	0.	476.	542.	565.	404.	256.	7.	-15.	81.	13.	3.	1456.
24.575	0.	0.	0.	476.	543.	565.	403.	256.	5.	-17.	80.	8.	1.	1456.
24.625	0.	0.	0.	476.	542.	565.	403.	256.	4.	-16.	81.	12.	2.	1456.
24.675	0.	0.	0.	475.	541.	567.	404.	256.	7.	-14.	82.	15.	3.	1457.
24.725	0.	0.	0.	475.	542.	566.	404.	257.	7.	-15.	82.	14.	1.	1457.
24.775	0.	0.	0.	475.	546.	566.	404.	255.	7.	-15.	79.	14.	2.	1457.
24.825	0.	0.	0.	474.	549.	567.	404.	256.	6.	-14.	79.	13.	2.	1457.
24.875	0.	0.	0.	474.	552.	568.	404.	257.	8.	-13.	82.	15.	3.	1457.
24.925	0.	0.	0.	475.	557.	567.	404.	257.	7.	-13.	81.	15.	3.	1457.
24.975	0.	0.	0.	474.	559.	567.	404.	255.	6.	-14.	79.	15.	1.	1457.
25.025	0.	0.	0.	0.	0.	0.	0.	0.	0.	0.	0.	0.	0.	0.
25.075	0.	0.	0.	0.	0.	0.	0.	0.	0.	0.	0.	0.	0.	0.
25.125	0.	0.	0.	0.	0.	0.	0.	0.	0.	0.	0.	0.	0.	0.
25.175	0.	0.	0.	0.	0.	0.	0.	0.	0.	0.	0.	0.	0.	0.

TABLE A.2. Inlet and Outlet Flow Rates and Integrals, and Void

TEST E7: VOID CALCULATIONS

TIME	INLET FLOW		OUTLET FLOW		INT. INLET		INT. OUTLET		VOID	
SEC	CC/SEC	G/SEC	CC/SEC	G/SEC	CC	GRAMS	CC	GRAMS	CC	GRAMS
5.002	583.6	500.2	582.8	500.4	0.0	0.0	0.0	0.0	0.0	0.0
5.007	584.9	501.2	584.1	501.4	2.9	2.5	2.9	2.5	0.0	0.0
5.012	584.4	501.0	584.1	501.4	5.8	5.0	5.8	5.0	0.0	0.0
5.017	584.9	501.4	583.9	501.4	8.8	7.5	8.8	7.5	0.0	0.0
5.022	583.9	500.4	583.3	500.6	11.7	10.0	11.7	10.0	0.0	0.0
5.027	587.2	503.4	586.3	503.4	14.6	12.5	14.6	12.5	0.0	0.0
5.032	588.1	504.0	587.4	504.3	17.6	15.0	17.5	15.1	0.0	0.0
5.037	588.8	504.8	588.0	504.8	20.5	17.6	20.5	17.6	0.0	0.0
5.042	584.9	501.1	583.9	501.3	23.4	20.1	23.4	20.1	0.0	0.0
5.047	587.3	503.5	586.2	503.4	26.4	22.6	26.3	22.6	0.0	0.0
5.052	585.6	501.8	584.8	502.1	29.3	25.1	29.3	25.1	0.0	0.0
5.057	588.4	504.3	587.5	504.3	32.2	27.6	32.2	27.6	0.0	0.0
5.062	586.0	502.1	585.6	502.7	35.2	30.1	35.1	30.2	0.0	0.0
5.067	586.9	503.1	586.2	503.2	38.1	32.7	38.1	32.7	0.0	0.0
5.072	585.9	502.2	585.3	502.2	41.0	35.2	41.0	35.2	0.0	0.0
5.077	588.3	504.3	587.6	504.3	44.0	37.7	43.9	37.7	0.0	0.0
5.082	585.1	501.3	584.1	501.4	46.9	40.2	46.8	40.2	0.0	0.0
5.087	585.8	502.0	585.1	502.1	49.8	42.7	49.8	42.7	0.0	0.0
5.092	585.9	502.2	584.7	502.0	52.8	45.2	52.7	45.2	0.0	0.0
5.097	588.8	504.5	588.0	504.8	55.7	47.7	55.6	47.7	0.0	0.0
5.102	585.0	501.4	584.5	501.4	58.6	50.2	58.6	50.3	0.0	0.0
5.107	585.3	501.6	584.6	501.5	61.6	52.8	61.5	52.8	0.0	0.0
5.112	583.7	500.2	583.0	500.5	64.5	55.3	64.4	55.3	0.0	0.0
5.117	583.7	500.3	583.0	500.5	67.4	57.8	67.3	57.8	0.0	0.0
5.122	580.2	497.1	579.8	497.3	70.3	60.3	70.3	60.3	0.0	0.0
5.127	581.9	498.9	581.7	499.2	73.2	62.7	73.1	62.8	0.0	0.0
5.132	586.9	503.1	586.1	503.1	76.1	65.2	76.0	65.3	0.0	0.0
5.137	584.9	501.4	584.7	501.5	79.0	67.8	79.0	67.8	0.0	0.0
5.142	581.9	498.6	581.8	499.1	82.0	70.3	81.9	70.3	0.0	0.0
5.147	588.1	503.9	587.7	504.4	84.9	72.8	84.8	72.8	0.0	0.0
5.152	583.0	499.7	582.7	500.0	87.8	75.3	87.8	75.3	0.0	0.0
5.157	581.5	498.4	581.0	498.4	90.7	77.8	90.7	77.8	0.0	0.0
5.162	582.6	499.3	582.7	500.0	93.7	80.3	93.6	80.3	0.0	0.0
5.167	584.0	500.5	583.4	500.8	96.6	82.8	96.4	82.8	0.0	0.0
5.172	579.8	496.8	579.3	496.8	99.5	85.3	99.5	85.3	0.0	0.0
5.177	582.7	499.5	582.6	499.9	102.4	87.7	102.3	87.8	0.0	0.0
5.182	583.7	500.4	583.2	500.6	105.3	90.2	105.2	90.3	0.0	0.0
5.187	583.4	500.2	582.9	500.0	108.2	92.7	108.2	92.8	0.0	0.0
5.192	581.7	498.7	581.7	499.1	111.1	95.2	111.0	95.3	0.0	0.0
5.197	590.1	505.5	589.4	505.9	114.1	97.8	113.9	97.8	0.0	0.0
5.202	586.9	502.9	586.3	503.1	117.0	100.3	116.9	100.3	0.0	0.0
5.207	584.8	501.0	584.1	501.2	120.0	102.8	119.8	102.8	0.0	0.0
5.212	585.1	501.2	584.5	501.7	122.9	105.3	122.7	105.3	0.0	0.0
5.217	585.8	501.9	585.4	502.3	125.8	107.8	125.7	107.8	0.1	0.0
5.222	579.9	496.4	579.1	496.8	128.8	110.3	128.6	110.3	0.1	0.0
5.227	583.1	499.6	583.2	500.2	131.6	112.8	131.6	112.8	0.1	0.0
5.232	587.8	503.7	587.3	503.9	134.5	115.3	134.4	115.3	0.1	0.0
5.237	588.4	504.0	588.0	504.3	137.6	117.8	137.4	117.9	0.1	0.1
5.242	585.0	501.0	584.8	501.6	140.5	120.3	140.3	120.4	0.1	0.1
5.247	592.5	507.7	591.8	507.7	143.4	122.8	143.2	122.9	0.1	0.1

TABLE A.2 (Contd.)

TEST E7: VOID CALCULATIONS

TIME SEC	INLET FLOW		OUTLET FLOW		INT. INLET		INT. OUTLET		VOID	
	CC/SEC	G/SEC	CC/SEC	G/SEC	CC	GRAMS	CC	GRAMS	CC	GRAMS
5.252	589.1	504.4	588.7	504.9	146.4	125.4	146.3	125.4	0.1	0.1
5.257	585.3	501.4	585.0	501.6	149.3	127.9	149.2	128.0	0.1	0.1
5.262	587.1	502.8	586.8	503.3	152.3	130.4	152.1	130.5	0.1	0.1
5.267	589.5	505.0	589.1	505.4	155.2	132.9	155.0	133.0	0.1	0.1
5.272	581.8	498.4	581.4	498.6	158.1	135.4	158.0	135.5	0.1	0.1
5.277	584.9	500.9	585.0	501.6	161.1	137.9	160.9	138.0	0.1	0.1
5.282	587.1	502.9	586.9	503.4	164.0	140.4	163.8	140.5	0.1	0.1
5.287	586.1	501.9	585.5	502.0	166.9	143.0	166.8	143.0	0.1	0.1
5.292	583.9	499.9	584.4	500.9	169.9	145.5	169.8	145.5	0.1	0.1
5.297	589.2	504.7	588.9	505.1	172.7	148.0	172.6	148.0	0.1	0.1
5.302	585.7	501.5	585.6	502.1	175.7	150.5	175.6	150.6	0.1	0.1
5.307	581.6	498.0	581.5	498.4	178.7	153.0	178.6	153.1	0.1	0.1
5.312	583.3	499.2	583.0	500.1	181.7	155.5	181.4	155.6	0.1	0.1
5.317	586.3	501.9	586.1	502.6	184.5	158.0	184.3	158.1	0.1	0.1
5.322	580.1	496.8	579.8	497.0	187.4	160.5	187.3	160.6	0.1	0.1
5.327	583.1	499.2	583.7	500.4	190.4	163.0	190.2	163.1	0.1	0.1
5.332	583.2	499.6	583.4	500.2	193.1	165.5	193.1	165.6	0.1	0.1
5.337	581.8	498.3	581.3	498.4	196.1	168.0	196.0	168.1	0.1	0.1
5.342	582.3	498.4	583.0	499.6	199.1	170.4	199.0	170.6	0.1	0.1
5.347	588.0	503.8	588.3	504.4	201.9	173.0	201.8	173.1	0.1	0.1
5.352	584.2	500.2	584.0	500.4	204.9	175.5	204.9	175.6	0.1	0.1
5.357	581.6	497.9	582.5	498.9	207.9	178.0	207.9	178.1	0.1	0.1
5.362	583.7	500.0	583.9	500.5	210.6	180.5	210.7	180.6	0.1	0.1
5.367	586.2	501.9	586.4	502.6	213.7	183.0	213.6	183.1	0.1	0.1
5.372	580.2	496.8	580.4	497.2	216.6	185.5	216.6	185.6	0.1	0.1
5.377	583.1	499.6	583.9	500.3	219.4	187.9	219.5	188.1	0.1	0.1
5.382	587.5	503.0	588.2	504.0	222.4	190.5	222.4	190.6	0.2	0.1
5.387	585.5	501.5	585.4	501.4	225.3	193.0	225.4	193.1	0.2	0.1
5.392	579.9	496.5	581.2	497.6	228.3	195.5	228.5	195.6	0.2	0.1
5.397	590.1	505.3	591.3	506.5	231.2	198.0	231.3	198.1	0.2	0.1
5.402	585.4	501.1	585.3	501.4	234.2	200.5	234.2	200.6	0.2	0.1
5.407	581.0	497.2	582.1	498.3	237.2	203.0	237.3	203.1	0.2	0.1
5.412	584.5	500.2	584.9	501.2	240.1	205.5	240.0	205.6	0.2	0.2
5.417	588.9	503.9	589.0	504.5	243.0	208.0	243.0	208.1	0.2	0.2
5.422	580.0	496.4	580.6	497.0	245.9	210.5	246.1	210.6	0.2	0.2
5.427	584.9	500.5	585.6	501.5	248.9	213.0	248.8	213.1	0.2	0.2
5.432	587.3	502.5	587.8	503.4	251.8	215.5	251.8	215.6	0.2	0.2
5.437	585.0	500.7	584.7	500.8	254.7	218.0	254.7	218.2	0.2	0.2
5.442	584.8	500.2	585.6	501.4	257.8	220.5	257.7	220.7	0.2	0.2
5.447	593.4	508.0	594.3	508.9	260.5	223.0	260.6	223.2	0.2	0.2
5.452	588.9	504.0	588.9	504.3	263.6	225.5	263.6	225.7	0.2	0.2
5.457	583.1	498.7	584.0	499.8	266.6	228.0	266.7	228.2	0.2	0.2
5.462	585.8	501.3	586.9	502.5	269.4	230.5	269.5	230.7	0.2	0.2
5.467	589.7	504.3	589.9	505.1	272.5	233.1	272.4	233.3	0.2	0.2
5.472	580.3	496.3	580.6	496.9	275.4	235.6	275.5	235.8	0.2	0.2
5.477	583.2	498.9	584.4	500.1	278.3	238.0	278.4	238.3	0.2	0.2
5.482	590.2	504.8	590.9	505.9	281.3	240.6	281.3	240.8	0.2	0.2
5.487	584.4	500.1	584.6	500.3	284.1	243.1	284.3	243.3	0.3	0.2
5.492	580.8	496.7	581.9	498.0	287.1	245.6	287.2	245.8	0.3	0.2
5.497	591.7	505.9	593.1	507.5	290.1	248.1	290.2	248.3	0.3	0.2

TABLE A.2 (Contd.)

TEST E71 VOID CALCULATIONS

TIME SEC	INLET FLOW		OUTLET FLOW		INT. INLET		INT. OUTLET		VOID CC	GRAMS
	CC/SEC	G/SEC	CC/SEC	G/SEC	CC	GRAMS	CC	GRAMS		
4.502	581.7	497.7	585.3	500.8	292.9	250.6	293.2	250.8	0.3	0.2
4.507	592.4	506.6	593.2	507.4	295.9	253.1	296.2	253.3	0.3	0.2
4.512	580.3	496.3	579.3	495.5	298.8	255.6	299.1	255.8	0.3	0.2
4.517	578.5	494.9	581.1	497.2	301.7	258.1	301.9	259.3	0.3	0.3
4.522	588.1	502.8	590.7	505.2	304.8	260.6	305.0	260.8	0.3	0.3
4.527	586.2	501.4	584.8	500.1	307.6	263.1	307.9	263.3	0.3	0.3
4.532	574.8	491.7	576.1	492.7	310.5	265.6	310.8	265.8	0.3	0.3
4.537	586.8	502.2	590.5	504.8	313.2	268.0	313.8	268.3	0.3	0.3
4.542	590.1	504.7	589.9	504.4	316.3	270.6	316.7	270.8	0.3	0.3
4.547	579.5	495.6	580.2	496.0	319.3	273.1	319.7	273.3	0.3	0.3
4.552	579.7	495.9	583.5	498.8	322.1	275.5	322.7	275.8	0.3	0.3
4.557	590.5	505.0	592.0	505.9	325.1	278.0	325.7	279.3	0.4	0.3
4.562	581.3	497.0	581.0	496.7	328.1	280.5	328.5	280.8	0.4	0.3
4.567	578.7	495.0	581.8	497.5	330.9	283.0	331.3	283.3	0.4	0.3
4.572	589.5	504.0	592.5	506.3	333.9	285.5	334.5	285.8	0.4	0.3
4.577	587.2	502.3	586.9	501.5	336.7	288.0	337.4	288.4	0.4	0.3
4.582	576.9	493.4	578.6	494.6	339.7	290.5	340.2	290.9	0.4	0.3
4.587	587.1	501.9	591.2	505.1	342.8	293.0	343.4	293.4	0.4	0.3
4.592	589.5	504.0	589.6	503.9	345.7	295.5	346.2	295.9	0.4	0.3
4.597	581.7	497.2	582.2	497.6	348.7	298.0	349.1	298.4	0.4	0.3
4.602	585.0	500.1	589.1	503.4	351.5	300.5	352.1	300.9	0.4	0.4
4.607	595.1	509.5	596.7	509.8	354.6	303.1	355.2	303.4	0.4	0.4
4.612	582.3	497.6	582.2	497.5	357.6	305.6	358.0	305.9	0.4	0.4
4.617	580.2	495.8	583.3	498.5	360.5	308.0	360.9	309.4	0.4	0.4
4.622	588.7	503.0	591.6	505.4	363.4	310.5	364.0	310.9	0.5	0.4
4.627	588.0	502.4	587.9	502.2	366.4	313.1	367.0	313.5	0.5	0.4
4.632	580.4	496.1	581.9	497.2	369.2	315.6	369.8	315.9	0.5	0.4
4.637	589.1	503.3	593.1	506.8	372.3	318.1	372.7	318.5	0.5	0.4
4.642	590.1	504.5	590.3	504.3	375.0	320.6	375.7	321.0	0.5	0.4
4.647	583.5	498.5	584.2	498.9	378.2	323.1	379.8	323.5	0.5	0.4
4.652	584.9	499.6	589.2	503.2	381.1	325.6	381.7	326.0	0.5	0.4
4.657	593.0	506.5	594.5	507.9	384.1	328.1	384.6	328.5	0.5	0.4
4.662	583.0	498.0	582.9	497.8	387.0	330.6	387.6	331.0	0.5	0.4
4.667	580.1	495.8	583.7	498.5	389.7	333.1	390.6	333.5	0.5	0.4
4.672	589.0	503.0	591.9	505.4	392.9	335.6	393.5	336.0	0.5	0.5
4.677	586.1	500.5	586.3	500.8	395.9	338.1	396.6	338.6	0.5	0.5
4.682	577.2	493.3	579.3	494.7	398.5	340.6	399.3	341.0	0.5	0.5
4.687	586.8	501.3	590.8	504.4	401.6	343.1	402.4	343.5	0.5	0.5
4.692	588.0	502.4	588.4	502.5	404.5	345.6	405.2	346.1	0.6	0.5
4.697	581.3	496.5	581.9	497.0	407.5	348.1	408.1	348.6	0.6	0.5
4.702	580.0	495.1	584.6	498.9	410.7	350.5	411.3	351.0	0.6	0.5
4.707	590.2	504.0	592.0	505.4	413.4	353.0	414.1	353.6	0.6	0.5
4.712	580.6	495.8	580.2	495.5	416.3	355.5	416.9	356.1	0.6	0.5
4.717	578.1	493.8	582.0	496.8	419.1	358.0	420.0	358.5	0.6	0.5
4.722	585.1	499.5	588.4	502.2	422.3	360.5	423.0	361.0	0.6	0.5
4.727	585.3	499.8	586.0	500.1	425.1	363.0	426.0	363.5	0.6	0.5
4.732	577.1	493.0	579.5	494.8	427.9	365.5	429.7	366.0	0.6	0.5
4.737	587.3	501.5	591.8	504.9	430.9	368.0	432.0	368.5	0.7	0.6
4.742	587.2	501.3	588.7	502.3	433.9	370.5	434.9	371.0	0.7	0.6
4.747	582.0	497.0	583.1	497.7	436.8	373.0	437.6	373.5	0.7	0.6

TABLE A.2 (Contd.)

TEST E7: VOID CALCULATIONS

TIME	INLET FLOW		OUTLET FLOW		INT. INLET		INT. OUTLET		VOID	
SEC	CC/SEC	G/SEC	CC/SEC	G/SEC	CC	GRAMS	CC	GRAMS	CC	GRAMS
5.752	584.6	499.0	589.6	502.8	439.9	375.5	441.0	376.0	0.7	0.6
5.757	590.6	504.5	593.1	506.0	442.5	378.0	443.7	378.6	0.7	0.6
5.762	579.4	494.7	580.0	495.0	445.6	380.5	446.5	381.1	0.7	0.6
5.767	576.9	492.6	581.2	495.9	448.4	382.9	449.5	383.6	0.7	0.6
5.772	586.2	500.4	589.7	503.0	451.5	385.4	452.6	386.0	0.7	0.6
5.777	585.4	499.7	586.3	500.1	454.4	387.9	455.6	388.6	0.7	0.6
5.782	578.7	494.0	581.7	496.4	457.3	390.4	458.3	391.0	0.8	0.6
5.787	588.1	502.0	592.6	505.4	460.3	392.9	461.5	393.6	0.8	0.7
5.792	589.1	502.7	591.2	504.0	463.4	395.4	464.6	396.1	0.8	0.7
5.797	583.1	497.8	584.9	499.0	466.1	397.9	467.3	398.6	0.8	0.7
5.802	583.9	499.2	588.7	501.9	469.3	400.4	470.5	401.1	0.8	0.7
5.807	594.4	507.3	597.6	509.3	472.1	402.9	473.6	403.6	0.8	0.7
5.812	582.4	497.2	583.3	497.4	474.9	405.4	476.3	406.1	0.8	0.7
5.817	583.0	497.5	587.3	500.8	478.1	407.9	479.2	408.6	0.8	0.7
5.822	590.8	504.0	594.5	506.9	481.1	410.4	482.3	411.1	0.9	0.7
5.827	587.3	501.0	588.4	501.6	484.1	412.9	485.3	413.7	0.9	0.7
5.832	580.4	495.3	583.4	497.5	486.7	415.4	488.1	416.2	0.9	0.7
5.837	590.9	504.2	595.4	507.6	489.7	417.9	491.1	418.7	0.9	0.8
5.842	590.2	503.3	592.3	504.7	493.1	420.4	494.3	421.2	0.9	0.8
5.847	584.2	498.7	586.2	499.7	495.5	422.9	497.1	423.7	0.9	0.8
5.852	584.2	498.3	589.1	502.1	498.8	425.4	500.1	426.2	0.9	0.8
5.857	592.7	505.5	595.9	507.7	501.7	427.9	503.2	428.7	0.9	0.8
5.862	581.6	496.0	582.7	496.6	504.8	430.4	506.0	431.3	1.0	0.8
5.867	580.5	495.0	584.7	498.4	507.7	432.9	508.9	433.7	1.0	0.8
5.872	587.6	501.2	591.8	504.2	510.5	435.4	512.1	436.2	1.0	0.8
5.877	587.2	500.8	588.3	501.2	513.5	437.9	514.9	438.8	1.0	0.8
5.882	580.4	494.9	584.0	497.6	515.5	440.4	517.9	441.3	1.0	0.9
5.887	590.6	503.6	595.3	507.4	519.4	442.9	520.7	443.8	1.0	0.9
5.892	588.4	501.7	590.9	503.1	522.4	445.4	524.2	446.3	1.0	0.9
5.897	583.2	497.4	586.0	499.2	525.2	447.9	526.8	448.8	1.0	0.9
5.902	584.3	498.4	589.5	502.0	528.1	450.4	530.0	451.3	1.1	0.9
5.907	589.7	502.7	593.3	505.2	531.3	452.9	533.0	453.8	1.1	0.9
5.912	584.0	497.9	585.9	499.0	534.2	455.4	535.8	456.3	1.1	0.9
5.917	580.6	495.0	585.2	498.2	537.0	457.9	539.0	458.8	1.1	0.9
5.922	587.8	501.3	592.4	504.0	539.8	460.4	542.2	461.3	1.1	1.0
5.927	585.0	498.8	586.9	499.8	542.9	462.9	544.7	463.8	1.1	1.0
5.932	580.4	494.9	584.5	497.5	545.8	465.4	547.8	465.3	1.1	1.0
5.937	588.3	501.8	593.6	505.2	548.5	467.9	550.9	468.8	1.2	1.0
5.942	587.7	501.2	590.7	502.7	551.6	470.4	553.9	471.4	1.2	1.0
5.947	582.7	497.2	586.0	498.7	554.2	472.9	556.8	473.9	1.2	1.0
5.952	584.6	498.6	590.0	502.1	557.3	475.3	559.8	476.4	1.2	1.0
5.957	586.2	499.7	590.3	502.1	560.6	477.8	563.0	478.9	1.2	1.0
5.962	579.1	493.9	581.9	495.1	563.2	480.3	565.6	481.4	1.2	1.0
5.967	579.7	494.2	584.3	497.7	566.3	482.8	568.6	483.9	1.2	1.1
5.972	586.3	499.8	591.5	502.9	569.3	485.3	572.1	486.4	1.3	1.1
5.977	584.4	498.3	587.1	499.5	572.1	487.8	574.7	488.9	1.3	1.1
5.982	578.1	492.7	582.3	495.6	575.2	490.3	577.3	491.3	1.3	1.1
5.987	586.0	499.3	591.7	503.2	578.3	492.7	580.6	493.8	1.3	1.1
5.992	588.8	502.0	592.3	503.6	580.9	495.2	583.7	496.4	1.3	1.1
5.997	585.6	499.3	589.6	501.4	583.8	497.7	586.6	498.9	1.3	1.1

TABLE A.2 (Contd.)

TEST E7: VOID CALCULATIONS

TIME SEC	INLET FLOW		OUTLET FLOW		INT. INLET		INT. OUTLET		VOID	
	CC/SEC	G/SEC	CC/SEC	G/SEC	CC	GRAMS	CC	GRAMS	CC	GRAMS
6.002	582.8	496.7	588.6	500.6	586.9	500.2	589.6	501.4	1.6	1.1
6.007	589.2	502.0	593.9	504.5	590.1	502.7	593.2	503.9	1.4	1.2
6.012	583.3	497.2	586.9	499.0	592.7	505.2	595.5	506.4	1.4	1.2
6.017	582.5	496.5	587.9	499.9	595.6	507.7	598.5	508.9	1.4	1.2
6.022	588.9	501.7	594.5	505.3	598.9	510.2	601.7	511.4	1.4	1.2
6.027	586.2	499.5	589.4	501.0	601.7	512.7	604.7	513.9	1.4	1.2
6.032	582.0	495.9	586.4	498.6	604.6	515.2	607.3	516.4	1.4	1.2
6.037	589.8	502.4	595.7	506.3	607.7	517.7	610.5	518.9	1.5	1.2
6.042	587.0	500.1	590.8	502.1	610.6	520.2	613.5	521.5	1.5	1.3
6.047	585.8	499.1	590.3	501.5	613.5	522.7	616.8	524.0	1.5	1.3
6.052	587.2	500.3	593.2	504.1	616.4	525.2	619.5	526.5	1.5	1.3
6.057	589.4	502.0	594.1	504.7	619.7	527.7	622.7	529.0	1.5	1.3
6.062	584.1	497.6	587.9	499.7	622.4	530.2	625.4	531.5	1.5	1.3
6.067	580.8	494.9	586.2	498.2	625.1	532.7	628.4	534.0	1.6	1.3
6.072	588.4	500.9	594.3	504.5	628.6	535.2	632.0	536.5	1.6	1.3
6.077	585.2	498.8	589.0	500.3	630.8	537.7	634.6	539.0	1.6	1.4
6.082	582.6	496.2	587.2	499.1	634.2	540.2	637.1	541.5	1.6	1.4
6.087	587.9	500.9	594.0	504.6	637.0	542.6	640.3	544.0	1.6	1.4
6.092	586.2	499.1	590.2	501.4	640.2	545.1	643.3	546.5	1.7	1.4
6.097	583.5	496.9	587.9	499.3	643.1	547.6	646.4	549.0	1.7	1.4
6.102	583.0	496.4	589.1	500.5	646.0	550.1	649.2	551.5	1.7	1.4
6.107	589.4	501.8	594.2	504.5	649.1	552.6	652.6	554.1	1.7	1.4
6.112	583.7	496.8	588.1	499.5	652.1	555.1	655.3	556.6	1.7	1.5
6.117	582.1	495.7	588.1	499.4	654.8	557.6	658.4	559.1	1.7	1.5
6.122	587.4	499.0	593.1	503.5	658.1	560.1	661.5	561.6	1.8	1.5
6.127	586.1	499.0	590.8	501.4	660.7	562.6	664.6	564.1	1.8	1.5
6.132	578.4	492.6	583.5	495.6	663.5	565.1	667.1	566.6	1.8	1.5
6.137	586.3	499.2	592.5	503.1	666.5	567.5	670.2	569.1	1.8	1.5
6.142	587.1	499.9	591.6	502.3	669.5	570.0	673.1	571.6	1.8	1.5
6.147	583.0	496.3	587.4	498.8	672.5	572.5	676.1	574.1	1.8	1.5
6.152	584.5	497.6	591.3	501.4	675.4	575.0	679.4	576.5	1.9	1.4
6.157	589.9	502.3	595.5	505.2	678.2	577.5	682.6	579.1	1.9	1.4
6.162	582.3	495.8	586.7	498.2	681.2	580.0	684.9	581.6	1.9	1.4
6.167	580.9	494.6	587.4	498.5	684.1	582.5	688.3	584.1	1.9	1.4
6.172	584.5	497.6	590.4	501.1	687.2	585.0	691.1	586.6	1.9	1.4
6.177	583.5	496.5	583.4	499.2	690.4	587.4	694.3	589.1	2.0	1.7
6.182	579.0	492.9	584.3	496.2	693.0	589.9	696.7	591.5	2.0	1.7
6.187	585.6	498.5	592.0	502.5	696.0	592.4	700.0	594.1	2.0	1.7
6.192	585.8	498.5	591.2	501.5	699.0	594.9	703.3	596.6	2.0	1.7
6.197	585.5	498.2	590.3	501.1	702.1	597.4	705.8	599.1	2.0	1.7
6.202	583.0	496.0	589.6	500.3	705.1	599.9	709.1	601.6	2.1	1.7
6.207	585.6	498.3	591.3	501.4	707.9	602.4	712.4	604.1	2.1	1.8
6.212	582.5	495.4	587.3	498.2	711.1	604.8	715.2	606.6	2.1	1.8
6.217	581.7	495.0	588.3	499.0	713.7	607.3	718.2	609.1	2.1	1.8
6.222	586.9	499.2	593.3	502.9	717.0	609.8	721.5	611.6	2.1	1.8
6.227	586.5	498.9	591.8	501.7	719.8	612.3	724.4	614.1	2.2	1.8
6.232	580.6	493.7	586.3	497.4	722.9	614.8	726.8	616.6	2.2	1.8
6.237	588.9	501.0	595.4	505.1	725.7	617.3	729.9	619.1	2.2	1.9
6.242	586.8	499.1	592.4	502.1	728.7	619.8	733.5	621.6	2.2	1.9
6.247	585.9	498.5	590.8	501.1	731.3	622.3	735.8	624.2	2.2	1.9

TABLE A.2 (Contd.)

TEST E7: VOID CALCULATIONS

TIME SEC	INLET FLOW		OUTLET FLOW		INT. INLET		INT. OUTLET		VOID	
	CC/SEC	G/SEC	CC/SEC	G/SEC	CC	GRAMS	CC	GRAMS	CC	GRAMS
A.252	585.8	498.1	592.6	502.8	734.7	624.7	739.1	626.7	2.3	1.9
A.257	588.3	500.1	594.1	503.6	737.9	627.2	742.2	629.2	2.3	1.9
A.262	584.8	497.3	589.6	500.0	740.6	629.7	744.8	631.7	2.3	2.0
A.267	582.3	495.2	588.9	499.4	743.4	632.2	747.9	634.2	2.3	2.0
A.272	587.4	499.3	593.7	503.4	746.8	634.7	751.0	636.7	2.4	2.0
A.277	586.7	498.6	592.0	501.8	749.9	637.2	754.1	639.2	2.4	2.0
A.282	580.6	493.7	586.9	497.6	752.3	639.7	756.8	641.7	2.4	2.0
A.287	586.4	498.5	593.0	502.8	755.4	642.2	759.8	644.2	2.4	2.1
A.292	586.5	498.5	592.2	501.9	758.4	644.6	763.1	646.7	2.4	2.1
A.297	581.5	494.3	586.6	497.4	761.4	647.1	765.7	649.2	2.5	2.1
A.302	582.9	495.4	589.7	499.7	764.3	649.6	768.8	651.7	2.5	2.1
A.307	587.1	499.1	593.2	502.7	767.0	652.1	771.9	654.2	2.5	2.1
A.312	582.1	494.7	587.4	497.3	770.3	654.6	775.0	656.7	2.5	2.1
A.317	580.3	493.2	587.1	497.7	773.1	657.0	777.6	659.2	2.5	2.2
A.322	583.9	496.3	590.6	500.3	776.0	659.5	781.1	661.7	2.6	2.2
A.327	583.4	495.8	589.2	499.1	779.1	662.0	784.2	664.2	2.6	2.2
A.332	579.9	492.7	586.7	497.0	782.1	664.5	787.0	666.7	2.6	2.2
A.337	583.6	496.0	590.5	500.3	784.7	666.9	789.9	669.2	2.6	2.2
A.342	585.5	497.7	592.4	501.5	787.6	669.4	793.5	671.7	2.7	2.3
A.347	583.1	495.8	589.6	499.4	790.2	671.9	796.0	674.2	2.7	2.3
A.352	582.0	494.6	589.3	499.0	793.5	674.4	799.1	676.7	2.7	2.3
A.357	587.6	499.4	594.6	503.3	796.4	676.9	802.3	679.2	2.7	2.3
A.362	582.2	494.7	587.9	498.1	799.4	679.4	804.7	681.7	2.8	2.3
A.367	581.3	493.9	583.5	498.3	802.4	681.8	808.0	684.2	2.8	2.4
A.372	585.1	497.0	592.1	501.4	805.6	684.3	810.9	686.7	2.8	2.4
A.377	582.4	494.7	588.5	498.3	808.5	686.8	814.0	689.2	2.8	2.4
A.382	578.3	491.3	585.0	495.8	811.2	689.2	816.7	691.7	2.9	2.4
A.387	585.1	497.0	592.3	501.5	814.3	691.7	819.8	694.2	2.9	2.4
A.392	586.4	497.9	593.4	502.3	817.5	694.2	823.1	696.7	2.9	2.5
A.397	582.7	494.8	589.1	499.0	820.5	696.7	825.5	699.2	2.9	2.5
A.402	582.3	494.6	589.8	499.3	823.2	699.2	828.9	701.7	3.0	2.5
A.407	583.0	494.9	589.8	499.0	826.6	701.6	832.2	704.2	3.0	2.5
A.412	581.2	493.6	587.6	497.5	829.2	704.1	834.8	706.7	3.0	2.5
A.417	582.5	494.5	589.7	499.3	832.4	706.6	837.6	709.1	3.0	2.6
A.422	583.1	494.9	590.5	499.6	835.3	709.0	841.1	711.6	3.1	2.6
A.427	584.6	496.3	590.6	499.8	838.1	711.5	843.8	714.1	3.1	2.6
A.432	582.2	494.4	589.4	498.9	840.9	714.0	846.6	716.6	3.1	2.6
A.437	585.5	497.1	592.8	501.7	843.9	716.5	849.8	719.1	3.1	2.7
A.442	585.4	496.8	591.9	500.7	847.2	719.0	852.9	721.6	3.2	2.7
A.447	584.5	496.1	591.6	500.6	850.0	721.4	855.8	724.1	3.2	2.7
A.452	583.2	494.8	590.5	499.8	853.2	723.9	858.6	726.6	3.2	2.7
A.457	585.9	496.9	593.0	501.5	856.4	726.4	862.1	729.2	3.2	2.7
A.462	583.1	494.9	589.6	498.9	858.9	728.9	864.6	731.7	3.3	2.8
A.467	582.6	494.2	590.0	499.3	862.2	731.4	867.6	734.1	3.3	2.8
A.472	588.8	499.3	596.4	504.3	865.3	733.8	871.1	736.7	3.3	2.8
A.477	584.2	495.7	590.8	499.7	867.7	736.3	874.0	739.2	3.4	2.8
A.482	582.1	493.7	588.9	498.4	871.0	738.8	876.4	741.7	3.4	2.9
A.487	585.6	496.9	593.2	501.8	873.7	741.3	879.6	744.2	3.4	2.9
A.492	583.7	495.1	590.8	499.5	877.0	743.8	883.1	746.7	3.4	2.9
A.497	583.1	494.6	590.1	499.1	879.8	746.2	885.8	749.2	3.5	2.9

TABLE A.2 (Contd.)

TEST E7: VOID CALCULATIONS

TIME SEC	INLET FLOW		OUTLET FLOW		INT. INLET		INT. OUTLET		VOID	
	CC/SEC	G/SEC	CC/SEC	G/SEC	CC	GRAMS	CC	GRAMS	CC	GRAMS
6.502	582.9	494.6	590.3	499.4	882.3	748.7	888.5	751.7	3.5	3.0
6.507	582.5	494.2	589.5	498.7	885.4	751.2	891.6	754.2	3.5	3.0
6.512	580.9	492.8	587.5	497.1	888.4	753.6	894.2	756.6	3.5	3.0
6.517	580.5	492.5	587.6	497.4	891.1	756.1	896.7	759.1	3.6	3.0
6.522	583.0	494.5	590.4	499.4	894.5	758.6	900.4	761.6	3.6	3.0
6.527	583.0	494.6	589.7	498.9	897.1	761.0	903.1	764.1	3.6	3.0
6.532	579.4	491.6	586.3	496.2	899.9	763.5	905.7	766.6	3.7	3.0
6.537	584.9	496.2	592.4	501.4	903.0	766.0	908.7	769.1	3.7	3.1
6.542	583.6	495.1	590.6	499.5	905.8	768.5	912.4	771.6	3.7	3.1
6.547	583.5	494.8	591.0	499.9	909.2	770.9	915.3	774.1	3.7	3.2
6.552	583.2	494.6	590.9	499.9	912.0	773.4	918.0	776.6	3.8	3.2
6.557	584.3	495.6	591.4	500.1	914.8	775.9	921.3	779.1	3.8	3.2
6.562	581.6	493.5	588.8	498.0	917.3	778.4	924.1	781.6	3.8	3.2
6.567	581.8	493.6	589.4	498.6	920.4	780.8	927.0	784.1	3.9	3.2
6.572	583.5	494.6	590.9	499.7	924.0	783.3	930.2	786.6	3.9	3.2
6.577	582.1	493.8	589.5	498.3	926.2	785.8	933.5	789.1	3.9	3.3
6.582	581.1	492.6	588.4	497.6	929.7	788.2	935.9	791.6	3.9	3.3
6.587	583.7	495.1	591.6	499.9	932.2	790.7	939.6	794.1	4.0	3.4
6.592	582.0	493.9	589.5	498.1	934.6	793.2	942.7	796.6	4.0	3.4
6.597	586.3	496.9	593.7	501.8	938.7	795.6	945.5	799.1	4.0	3.4
6.602	584.4	495.5	592.4	500.6	941.3	798.1	948.6	801.6	4.1	3.4
6.607	583.5	494.7	590.8	499.3	944.2	800.6	951.3	804.1	4.1	3.5
6.612	582.0	493.4	589.7	498.2	947.3	803.1	954.6	806.6	4.1	3.5
6.617	582.2	493.6	590.3	498.9	950.3	805.5	957.3	809.0	4.1	3.5
6.622	583.9	494.8	591.6	499.7	953.6	808.0	960.7	811.5	4.2	3.5
6.627	584.0	495.1	592.1	500.0	956.0	810.5	963.9	814.0	4.2	3.4
6.632	583.9	494.9	591.4	499.9	959.0	813.0	966.0	816.5	4.2	3.4
6.637	585.9	496.5	593.9	501.7	962.3	815.4	969.5	819.0	4.3	3.6
6.642	585.9	496.6	593.7	501.2	965.0	817.9	973.1	821.6	4.3	3.6
6.647	585.6	496.2	593.2	501.0	968.1	820.4	975.6	824.1	4.3	3.7
6.652	583.0	494.3	591.2	499.2	970.6	822.9	979.0	826.6	4.4	3.7
6.657	585.3	496.0	593.0	500.6	973.9	825.4	981.9	829.1	4.4	3.7
6.662	582.4	493.3	589.9	498.2	977.4	827.8	984.7	831.6	4.4	3.7
6.667	581.4	492.8	589.5	498.0	979.6	830.3	987.4	834.0	4.4	3.7
6.672	584.4	495.0	592.0	500.0	983.1	832.8	990.6	836.5	4.5	3.8
6.677	583.6	494.2	591.7	499.6	986.4	835.2	993.6	839.0	4.5	3.8
6.682	581.8	493.1	589.1	498.0	988.5	837.7	995.6	841.5	4.5	3.8
6.687	585.3	495.8	593.3	501.0	991.9	840.2	999.5	844.0	4.6	3.8
6.692	584.3	495.2	592.6	500.1	994.3	842.7	1003.0	846.5	4.6	3.7
6.697	584.9	495.5	592.5	500.4	997.6	845.1	1005.4	849.0	4.6	3.9
6.702	583.5	494.2	591.7	499.6	1000.7	847.6	1009.7	851.5	4.7	3.9
6.707	582.9	493.8	590.8	498.8	1003.4	850.1	1011.6	854.0	4.7	4.0
6.712	580.5	491.5	587.9	496.5	1007.0	852.5	1014.2	856.5	4.7	4.0
6.717	581.4	492.4	590.0	498.0	1009.4	855.0	1017.6	859.0	4.7	4.0
6.722	580.9	492.2	588.7	496.9	1012.1	857.5	1020.6	861.5	4.8	4.0
6.727	581.0	492.1	589.6	497.4	1015.2	859.9	1024.2	864.0	4.8	4.1
6.732	579.1	490.8	587.3	495.8	1017.4	862.4	1026.2	866.5	4.8	4.1
6.737	581.1	492.2	589.2	497.3	1021.0	864.8	1029.4	868.9	4.9	4.1
6.742	581.5	492.4	590.2	498.0	1024.2	867.3	1032.8	871.4	4.9	4.1
6.747	582.1	493.1	590.5	498.4	1026.7	869.8	1035.3	873.9	4.9	4.2

TABLE A.2 (Contd.)

TEST E7: VOID CALCULATIONS

TIME SEC	INLET FLOW		OUTLET FLOW		INT. INLET		INT. OUTLET		VOID	
	CC/SEC	G/SEC	CC/SEC	G/SEC	CC	GRAMS	CC	GRAMS	CC	GRAMS
6.752	581.8	492.7	590.3	497.9	1030.0	872.2	1039.0	876.4	5.0	4.2
6.757	582.2	493.0	590.4	498.2	1032.8	874.7	1041.7	878.9	5.0	4.2
6.762	579.2	490.6	587.5	495.9	1035.7	877.1	1044.3	881.4	5.0	4.2
6.767	582.1	492.9	591.0	498.7	1038.7	879.6	1047.4	883.9	5.1	4.3
6.772	579.7	490.9	587.7	496.0	1041.6	882.1	1050.2	886.4	5.1	4.3
6.777	582.8	493.3	591.6	499.0	1045.0	884.5	1053.7	888.8	5.1	4.3
6.782	578.5	489.9	586.8	495.3	1047.3	887.0	1055.9	891.3	5.2	4.3
6.787	582.9	493.6	591.1	498.7	1050.3	889.4	1059.5	893.8	5.2	4.4
6.792	582.7	493.4	591.1	498.8	1053.4	891.9	1062.3	896.3	5.2	4.4
6.797	584.2	494.7	592.3	500.2	1056.2	894.4	1065.1	898.8	5.2	4.4
6.802	583.8	494.0	592.2	499.7	1059.8	896.9	1068.2	901.3	5.3	4.4
6.807	582.8	493.2	591.5	498.9	1062.6	899.3	1071.8	903.8	5.3	4.5
6.812	582.4	493.0	590.4	498.2	1065.3	901.8	1073.9	906.3	5.3	4.5
6.817	583.8	494.2	592.7	499.9	1068.3	904.3	1077.5	908.8	5.4	4.5
6.822	582.8	493.3	591.3	498.5	1071.2	906.7	1081.0	911.3	5.4	4.6
6.827	585.5	495.5	593.9	500.9	1074.4	909.2	1083.5	913.8	5.4	4.6
6.832	583.0	493.4	592.3	499.4	1077.2	911.7	1086.6	916.3	5.5	4.6
6.837	585.9	495.7	594.1	501.1	1080.4	914.1	1089.2	918.8	5.5	4.6
6.842	585.7	495.5	594.8	501.2	1083.4	916.6	1093.3	921.3	5.6	4.7
6.847	585.4	495.3	594.0	500.9	1086.4	919.1	1095.5	923.8	5.6	4.7
6.852	582.4	492.8	590.8	498.2	1089.2	921.6	1098.5	926.3	5.6	4.7
6.857	580.8	491.3	589.7	497.0	1092.4	924.0	1102.1	928.8	5.6	4.8
6.862	581.2	491.7	589.8	497.5	1095.1	926.5	1104.1	931.3	5.7	4.8
6.867	581.6	491.9	590.3	497.6	1098.4	928.9	1107.6	933.8	5.7	4.8
6.872	581.4	491.9	590.3	497.5	1100.9	931.4	1110.8	936.2	5.7	4.8
6.877	580.7	491.2	589.5	496.9	1104.1	933.9	1113.6	938.7	5.8	4.9
6.882	581.6	491.9	590.4	497.7	1107.0	936.3	1116.6	941.2	5.8	4.9
6.887	582.1	492.4	590.5	497.9	1109.7	938.8	1119.1	943.7	5.8	4.9
6.892	580.3	490.7	589.4	496.6	1113.2	941.2	1123.0	946.2	5.9	5.0
6.897	584.0	493.9	593.1	499.9	1115.8	943.7	1125.5	948.7	5.9	5.0
6.902	580.3	490.8	588.9	496.6	1118.7	946.2	1128.1	951.2	6.0	5.0
6.907	583.7	493.4	593.0	499.6	1122.3	948.6	1132.1	953.7	6.0	5.0
6.912	580.9	491.2	589.4	496.9	1124.7	951.1	1134.1	956.2	6.0	5.1
6.917	580.6	491.1	589.4	496.8	1127.3	953.5	1137.5	958.6	6.1	5.1
6.922	579.9	490.6	588.9	496.0	1130.1	956.0	1141.1	961.1	6.1	5.1
6.927	583.2	493.3	592.5	499.2	1133.0	958.4	1143.8	963.6	6.1	5.2
6.932	583.2	493.3	592.3	499.2	1136.1	960.9	1146.3	966.1	6.2	5.2
6.937	581.5	491.9	590.1	497.4	1138.8	963.4	1149.0	968.6	6.2	5.2
6.942	580.1	490.6	590.2	497.0	1142.0	965.8	1153.3	971.1	6.2	5.3
6.947	581.3	491.7	590.6	497.7	1144.9	968.3	1155.2	973.6	6.3	5.3
6.952	580.2	490.9	589.0	496.4	1147.4	970.7	1158.1	976.1	6.3	5.3
6.957	579.4	490.0	588.5	495.8	1150.7	973.2	1161.5	978.5	6.3	5.3
6.962	578.9	489.9	588.5	495.8	1152.9	975.6	1164.4	981.0	6.4	5.4
6.967	577.4	488.5	586.4	494.1	1156.0	978.1	1167.1	983.5	6.4	5.4
6.972	578.4	489.0	587.6	494.8	1159.7	980.5	1170.8	986.0	6.4	5.4
6.977	576.4	487.4	586.0	493.4	1162.5	983.0	1173.8	988.4	6.5	5.5
6.982	581.0	491.3	590.3	497.3	1165.4	985.4	1176.3	990.9	6.5	5.5
6.987	581.0	491.3	590.1	496.9	1168.1	987.9	1179.7	993.4	6.5	5.5
6.992	579.9	490.3	589.6	496.4	1171.4	990.3	1183.0	995.9	6.6	5.5
6.997	587.8	497.0	597.9	503.4	1174.2	992.8	1185.9	998.4	6.6	5.6

TABLE A.2 (Contd.)

TEST E7: VOID CALCULATIONS

TIME SEC	INLET FLOW		OUTLET FLOW		INT. INLET		INT. OUTLET		VOID	
	CC/SEC	G/SEC	CC/SEC	G/SEC	CC	GRAMS	CC	GRAMS	CC	GRAMS
7.002	592.0	500.5	601.5	506.4	1177.2	995.3	1188.7	1000.9	6.7	5.5
7.007	583.1	493.0	592.5	498.9	1180.0	997.8	1191.7	1003.4	6.7	5.4
7.012	583.1	492.3	593.1	499.3	1183.5	1000.2	1194.9	1005.9	6.7	5.7
7.017	580.8	490.8	589.8	496.7	1186.4	1002.7	1197.5	1008.4	6.9	5.7
7.022	582.2	491.9	591.5	497.7	1189.7	1005.2	1201.5	1010.9	6.8	5.7
7.027	583.8	493.6	593.7	499.8	1191.8	1007.6	1203.9	1013.4	6.8	5.8
7.032	581.6	491.6	590.9	497.5	1195.0	1010.1	1206.5	1015.9	6.9	5.9
7.037	584.3	493.7	593.3	499.5	1198.2	1012.5	1209.6	1018.4	6.9	5.8
7.042	579.2	489.6	588.8	495.4	1200.7	1015.0	1213.2	1020.8	6.9	5.8
7.047	584.8	494.1	594.5	500.5	1204.2	1017.5	1215.6	1023.3	7.0	5.9
7.052	582.0	491.9	591.2	497.6	1206.8	1019.9	1218.7	1025.8	7.0	5.9
7.057	580.9	490.9	590.1	496.6	1210.0	1022.4	1221.8	1028.3	7.0	5.9
7.062	582.2	491.6	592.4	498.5	1213.7	1024.8	1224.9	1030.8	7.1	6.0
7.067	582.2	492.1	591.4	497.9	1215.5	1027.3	1227.3	1033.3	7.1	6.0
7.072	578.1	488.5	587.2	494.1	1218.7	1029.8	1231.0	1035.8	7.2	6.0
7.077	583.0	492.5	593.2	499.1	1221.7	1032.2	1233.9	1038.3	7.2	6.1
7.082	579.2	489.5	588.1	495.2	1224.4	1034.7	1235.9	1040.7	7.2	6.1
7.087	580.2	490.4	589.6	495.9	1227.1	1037.1	1240.3	1043.2	7.3	6.1
7.092	578.0	488.5	587.8	494.5	1230.2	1039.6	1243.1	1045.7	7.3	6.1
7.097	581.2	491.0	590.8	497.2	1233.3	1042.0	1245.4	1048.2	7.3	6.2
7.102	577.2	487.7	586.6	493.5	1236.1	1044.5	1248.7	1050.7	7.4	6.2
7.107	579.5	489.5	588.8	495.3	1239.4	1046.9	1251.9	1053.1	7.4	6.2
7.112	578.8	489.2	588.8	495.5	1241.6	1049.3	1254.4	1055.6	7.4	6.3
7.117	580.5	490.5	589.8	496.3	1244.9	1051.8	1257.4	1058.1	7.5	6.3
7.122	575.7	486.1	585.0	492.1	1248.4	1054.2	1260.7	1060.6	7.5	6.3
7.127	579.9	489.9	590.7	496.7	1250.8	1056.7	1264.4	1063.0	7.6	6.4
7.132	576.8	487.4	586.4	493.4	1253.3	1059.1	1266.2	1065.5	7.6	6.4
7.137	578.4	488.8	587.8	494.3	1256.2	1061.6	1270.0	1068.0	7.6	6.4
7.142	578.0	489.4	588.4	494.9	1259.4	1064.0	1272.8	1070.4	7.7	6.4
7.147	580.9	490.6	591.3	497.3	1262.9	1066.4	1275.7	1072.9	7.7	6.5
7.152	580.9	490.6	590.4	496.4	1265.8	1068.9	1279.0	1075.4	7.7	6.5
7.157	576.5	487.1	586.4	492.9	1267.9	1071.3	1282.3	1077.9	7.8	6.5
7.162	575.9	486.4	586.7	493.2	1271.4	1073.8	1285.1	1080.3	7.8	6.5
7.167	576.5	487.1	586.5	492.9	1273.7	1076.2	1288.4	1082.8	7.9	6.5
7.172	574.9	485.5	584.3	491.2	1277.3	1078.6	1291.0	1085.3	7.9	6.4
7.177	574.3	485.1	585.5	492.1	1280.0	1081.1	1294.2	1087.7	7.9	6.7
7.182	578.1	488.4	587.6	494.4	1282.5	1083.5	1295.8	1090.2	8.0	6.7
7.187	578.0	488.0	587.1	493.6	1286.2	1085.9	1299.8	1092.7	8.0	6.7
7.192	577.2	487.4	587.8	494.1	1288.8	1088.4	1302.9	1095.1	8.0	6.8
7.197	581.5	491.1	591.6	497.4	1291.7	1090.8	1305.4	1097.6	8.1	6.8
7.202	577.7	487.9	587.1	493.6	1294.5	1093.3	1308.5	1100.1	8.1	6.8
7.207	577.9	487.8	587.7	493.9	1298.0	1095.7	1312.0	1102.6	8.1	6.8
7.212	577.5	487.5	586.7	493.3	1301.0	1098.2	1314.2	1105.0	8.2	6.9
7.217	581.2	490.6	587.2	493.5	1303.9	1100.6	1317.7	1107.5	8.2	6.9
7.222	577.2	487.3	588.0	494.2	1306.5	1103.0	1320.8	1110.0	8.2	6.9
7.227	579.5	489.1	589.1	494.9	1309.8	1105.5	1324.2	1112.4	8.3	7.0
7.232	577.1	487.2	587.5	493.8	1312.4	1107.9	1326.6	1114.9	8.3	7.0
7.237	581.0	490.2	590.1	495.8	1316.1	1110.4	1329.8	1117.4	8.4	7.0
7.242	580.9	490.2	589.1	494.9	1318.7	1112.8	1333.2	1119.9	8.4	7.0
7.247	582.1	491.4	586.7	493.0	1321.3	1115.3	1335.7	1122.3	8.4	7.1

TABLE A.2 (Contd.)

TEST E7: VOID CALCULATIONS

TIME SEC	INLET FLOW		OUTLET FLOW		INT. INLET		INT. OUTLET		VOID	
	CC/SEC	G/SEC	CC/SEC	G/SEC	CC	GRAMS	CC	GRAMS	CC	GRAMS
7.252	577.6	487.1	587.6	493.6	1325.3	1117.7	1338.9	1124.8	8.4	7.1
7.257	577.1	487.1	588.0	493.7	1327.2	1120.2	1342.6	1127.3	8.5	7.1
7.262	578.0	487.5	588.4	494.4	1330.9	1122.6	1344.7	1129.7	8.5	7.1
7.267	577.9	487.6	586.3	492.5	1333.3	1125.0	1347.6	1132.2	8.5	7.2
7.272	576.5	486.3	587.9	493.8	1336.5	1127.5	1350.8	1134.7	8.6	7.2
7.277	575.3	485.2	584.7	490.9	1339.5	1129.9	1354.4	1137.1	8.6	7.2
7.282	580.1	489.4	584.6	491.2	1342.1	1132.3	1356.4	1139.6	8.6	7.3
7.287	577.4	486.9	585.4	491.7	1345.6	1134.8	1359.8	1142.0	8.7	7.3
7.292	575.3	485.1	586.8	492.7	1348.8	1137.2	1363.0	1144.5	8.7	7.3
7.297	577.7	487.5	589.8	495.5	1350.3	1139.6	1365.5	1147.0	8.7	7.3
7.302	577.3	486.6	588.0	493.9	1354.7	1142.1	1368.4	1149.4	8.8	7.4
7.307	574.2	484.4	590.2	495.4	1356.8	1144.5	1372.3	1151.9	8.8	7.4
7.312	574.5	484.5	588.6	494.4	1360.0	1146.9	1374.3	1154.4	8.9	7.5
7.317	573.6	483.7	590.5	495.8	1363.1	1149.3	1377.9	1156.9	9.0	7.5
7.322	570.7	481.3	594.6	499.1	1365.6	1151.7	1381.0	1159.4	9.1	7.6
7.327	571.4	481.9	596.7	500.8	1368.5	1154.2	1384.3	1161.9	9.2	7.7
7.332	573.8	484.0	596.6	501.2	1371.2	1156.6	1386.2	1164.4	9.3	7.8
7.337	575.3	485.3	604.5	507.8	1373.9	1159.0	1389.2	1166.9	9.4	7.9
7.342	573.3	483.4	608.5	510.7	1377.4	1161.4	1393.3	1169.4	9.6	8.0
7.347	577.1	486.4	608.6	511.0	1380.7	1163.8	1395.9	1172.0	9.7	8.1
7.352	572.0	482.3	613.9	515.5	1383.0	1166.3	1398.6	1174.5	9.9	8.3
7.357	574.3	484.2	614.6	516.1	1386.0	1168.7	1401.9	1177.1	10.1	8.5
7.362	570.8	481.2	617.2	518.1	1389.0	1171.1	1405.3	1179.7	10.3	8.6
7.367	573.5	483.5	621.4	521.9	1391.9	1173.5	1407.7	1182.3	10.5	8.8
7.372	570.1	480.7	625.4	524.7	1394.7	1175.9	1412.3	1184.9	10.8	9.0
7.377	569.1	479.6	621.8	521.8	1398.2	1178.3	1415.1	1187.5	11.0	9.2
7.382	575.3	484.7	625.7	525.3	1401.4	1180.7	1417.6	1190.2	11.2	9.4
7.387	573.0	483.0	626.2	525.7	1403.5	1183.1	1420.9	1192.8	11.5	9.6
7.392	573.2	483.1	626.9	526.1	1406.5	1185.6	1424.5	1195.4	11.8	9.9
7.397	571.3	481.6	622.6	522.6	1409.2	1188.0	1427.3	1198.0	12.0	10.1
7.402	546.0	460.1	623.6	523.4	1412.5	1190.3	1430.4	1200.7	12.3	10.3
7.407	586.7	494.2	626.7	526.0	1415.8	1192.7	1433.7	1203.3	12.6	10.6
7.412	590.6	497.7	626.2	525.5	1418.3	1195.2	1437.0	1205.9	12.8	10.7
7.417	547.9	461.5	625.5	525.0	1421.9	1197.6	1440.1	1208.5	13.0	10.9
7.422	567.3	477.8	629.4	527.9	1424.7	1199.9	1444.1	1211.2	13.4	11.2
7.427	598.5	504.5	626.7	526.0	1426.5	1202.4	1446.2	1213.8	13.6	11.4
7.432	559.8	471.6	625.5	524.8	1430.4	1204.8	1449.8	1216.4	13.8	11.6
7.437	556.5	468.8	625.7	525.0	1432.8	1207.2	1452.8	1219.1	14.1	11.9
7.442	594.8	500.9	625.9	524.9	1436.4	1209.6	1456.8	1221.7	14.4	12.1
7.447	576.1	485.1	626.6	525.6	1439.6	1212.1	1459.6	1224.3	14.6	12.2
7.452	532.6	448.8	637.0	534.4	1441.2	1214.4	1462.6	1227.0	15.0	12.5
7.457	549.0	462.5	665.7	558.3	1444.4	1216.7	1466.1	1229.7	15.5	13.0
7.462	469.8	395.7	741.5	621.9	1447.1	1218.8	1469.5	1232.6	16.5	13.8
7.467	453.9	382.3	818.5	686.7	1449.3	1220.8	1473.1	1235.9	18.0	15.1
7.472	514.6	433.3	802.9	673.0	1452.2	1222.8	1478.5	1239.3	19.7	16.5
7.477	503.7	424.1	806.2	676.0	1454.8	1225.0	1482.0	1242.7	21.1	17.7
7.482	448.3	377.5	753.5	631.9	1457.1	1227.0	1485.5	1245.9	22.6	19.0
7.487	467.6	393.9	692.4	580.6	1458.7	1228.9	1489.5	1249.0	24.0	20.1
7.492	365.4	307.7	638.1	534.9	1461.5	1230.6	1493.3	1251.8	25.2	21.1
7.497	587.0	494.2	660.9	554.0	1464.2	1232.6	1496.6	1254.5	26.1	21.8

APPENDIX B

Thermal Constants and Geometry Used in COBRA Calculations

The multichannel COBRA-3M code²⁵ calculates individual pin and coolant temperatures at different axial elevations. Heat transfer between connecting channels is by turbulent mixing and diversion crossflow due to interchannel pressure gradients and the helical wire wraps.

Argonne's 3H version of this code² includes a new gap-conductance model and allows an arbitrary driving function, a wider latitude in the choice of calculational time steps, and various subsidiary results such as average fuel energy density and average coolant outlet temperature.

The code does not calculate the thermal conductance between azimuthal fuel sectors or axial increments. Accordingly, fuel temperatures in zones adjacent to the insulator pellets are overestimated, and large temperature gradients between adjacent azimuthal sectors can result. Interchannel mixing tends to reduce these temperature gradients in the coolant.

Boundary conditions for the calculation include inlet flow and enthalpy. Reverse flow cannot be calculated. Fuel and coolant temperature after boiling and reverse flow begin in the test can be estimated by operating at an artificially high pressure [300 psi (2 MPa)] to suppress early boiling in the calculations.

Conductance across the fuel-cladding gap is inversely proportional to the gap size. At fuel and cladding contact, a small residual or effective gap remains due to the irregularities of the contacting surfaces. The gap conductance used in COBRA-3H is

$$h_{\text{gap}} = \frac{k}{c + \Delta r},$$

where k is the conductivity of the gap gas, c is a parameter reflecting the residual gap (of the order of 0.012 mm), and Δr is the time-dependent gap calculated from differential thermal expansion. A user-supplied maximum value is used to evaluate c .

Values of gap conductance used for the E7 calculations are given in Fig. B.1. A value of 10.88 kW/m²·K (1916 Btu/hr·ft²·°F) was used as the maximum gap conductance. COBRA calculates the fuel-pin thermal expansion without regard to the restricting boundary of the cladding-fuel interface. Expansion of fuel exceeding that of the cladding leads to a negative gap as shown in Fig. B.1.

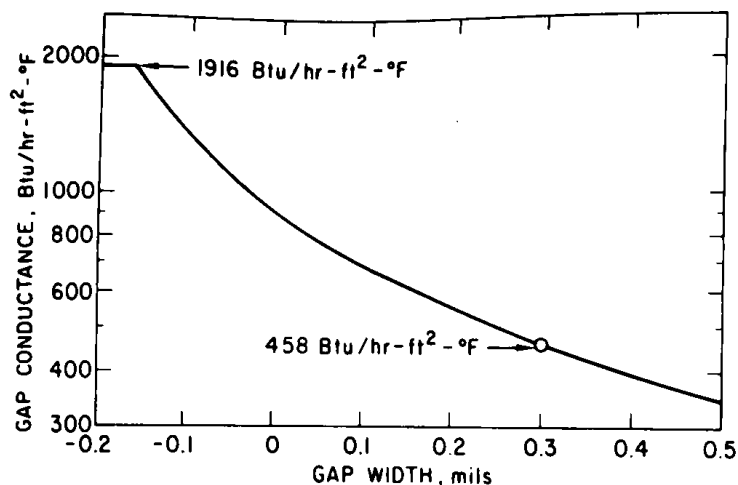


Fig. B.1. Gap Conductance Used in COBRA Calculations. Conversion factors: 1 Btu/h·ft²·°F = 5.679 W/m²·°C; 1 mil = 0.0254 mm.

Input data to COBRA include tabular listings of the thermodynamic properties of sodium, cladding and duct-wall material, and the mixed-oxide fuel. These are listed in Tables B.1-B.3, respectively. Input values for the hydraulic parameters are listed in Table B.4, and the fuel-rod and channel geometry are shown in Fig. B.2. Forcing functions for the power and inlet enthalpy are listed in Table B.5. Relative axial and radial power shapes within the fuel pins are listed in Table IV. Miscellaneous input data are listed in Table B.6.

TABLE B.1. Thermal Properties of Sodium^a

Pressure, psi	Temp, °F	Liquid Specific Volume, ft ³ /lb	Vapor Specific Volume, ft ³ /lb	Liquid Enthalpy, Btu/lb	Vapor Enthalpy, Btu/lb	Liquid Viscosity, lb/h·ft	Liquid Thermal Conductivity, Btu/h·ft·°F	Liquid Surface Tension, lb/ft
0.000	590	0.01825	999999.00	331.90	2220.52	0.81430	43.95000	0.01204
0.001	650	0.01842	409866.00	350.49	2227.58	0.75580	42.98000	0.01181
0.003	700	0.01856	178122.00	365.88	2234.13	0.71380	42.17999	0.01162
0.007	750	0.01870	83102.00	381.19	2240.18	0.67670	41.39000	0.01143
0.014	800	0.01885	41266.00	396.43	2245.77	0.64370	40.62000	0.01124
0.024	840	0.01897	24533.00	408.58	2249.94	0.61980	40.00000	0.01109
0.040	880	0.01909	15060.00	420.69	2253.87	0.59800	39.39000	0.01094
0.065	920	0.01921	9519.00	432.77	2257.57	0.57750	38.78999	0.01078
0.082	940	0.01927	7645.00	438.80	2259.35	0.56830	38.50000	0.01071
0.100	960	0.01933	6180.00	444.83	2261.09	0.55920	38.20000	0.01063
0.130	980	0.01940	5026.00	450.85	2262.78	0.55040	37.90999	0.01056
0.160	1000	0.01946	4111.00	456.86	2264.44	0.54190	37.60999	0.01048
0.200	1020	0.01952	3382.00	462.87	2266.06	0.53380	37.42000	0.01040
0.240	1040	0.01959	2798.00	468.88	2267.65	0.52590	37.03000	0.01033
0.290	1060	0.01965	2326.00	474.88	2269.22	0.51830	36.73999	0.01025
0.350	1080	0.01971	1944.00	480.88	2270.75	0.51100	36.45999	0.01017
0.470	1100	0.01978	1632.00	486.88	2272.27	0.50390	36.17000	0.01010
0.540	1120	0.01985	1376.00	492.87	2273.76	0.49700	35.89000	0.01002
0.610	1140	0.01991	1166.00	498.87	2275.24	0.49040	35.60999	0.00995
0.720	1160	0.01998	992.00	504.86	2276.70	0.48400	35.32999	0.00987
0.850	1180	0.02005	847.00	510.86	2278.15	0.47780	35.04999	0.00979
1.000	1200	0.02011	727.00	516.85	2279.60	0.47170	34.78000	0.00972
2.100	1300	0.02046	356.00	546.85	2286.72	0.44420	33.42000	0.00934
4.200	1400	0.02082	189.10	576.95	2293.86	0.42040	32.10999	0.00896
7.800	1500	0.02119	107.40	607.21	2301.10	0.39950	30.84000	0.00857
14.000	1600	0.02157	64.63	637.70	2308.47	0.38110	29.60999	0.00819
22.000	1700	0.02197	41.25	668.49	2316.95	0.36470	28.42000	0.00781
34.000	1800	0.02238	27.40	699.65	2325.24	0.35010	27.26999	0.00743
51.000	1900	0.02281	18.87	731.24	2333.38	0.33680	26.17000	0.00705
320.000	2500	0.02575	3.44	933.78	2371.86	0.27850	20.42000	0.00476

^aConversion factors: 1 psi = 6.895 kPa; $t(^{\circ}\text{C}) = [t(^{\circ}\text{F}) - 32]/1.8$; 1 ft³/lb = 62.3 cm³/g; 1 Btu/lb = 2.3 x 10³ J/kg; 1 lb/h·ft = 4.134 x 10⁻⁴ N·s/m²; 1 Btu/h·ft·°F = 5.678 W/m²·K; 1 lb/ft = 14.59 N/m.

TABLE B.2. Cladding and Duct-wall Thermal Properties^a

Temp, °F	Thermal Conductivity, Btu/h·ft·°F	Heat Capacity, Btu/lb·°F
70	8.32	0.108
300	9.35	0.120
600	10.70	0.128
700	11.15	0.130
800	11.60	0.132
900	12.05	0.134
1000	12.50	0.137
1100	12.95	0.139
1200	13.40	0.141
1300	13.85	0.144
1400	14.30	0.147
2500	14.30	0.147

Cladding expansion coefficient = $9 \times 10^{-6} + 1.17 \times 10^{-9} T$.

^aConversion factors: $t (^{\circ}\text{C}) = [t (^{\circ}\text{F}) - 32]/1.8$;
 $1 \text{ Btu/h}\cdot\text{ft}\cdot^{\circ}\text{F} = 5.678 \text{ W/m}^2\cdot\text{K}$;
 $1 \text{ Btu/lb}\cdot^{\circ}\text{F} = 4187 \text{ J/kg}\cdot\text{K}$.

TABLE B.3. Fuel Thermal Properties^a

Temp, °F	Thermal Conductivity, Btu/h·ft·°F	Heat Capacity, Btu/lb·°F
77	4.10	0.0419
800	2.08	0.0573
1520	1.42	0.0707
2060	1.18	0.0797
2780	1.03	0.0902
3500	0.99	0.0991
4040	1.03	0.1046
4400	1.09	0.1078
4760	1.17	0.1106
5000	1.23	0.1122
5100	1.50	0.1200
8000	1.50	0.1200

Fuel Expansion Coefficient = $3.764 \times 10^{-6} + 9.15 \times 10^{-10} T$.

^aConversion factors: $t (^{\circ}\text{C}) = [t (^{\circ}\text{F}) - 32]/1.8$;
 $1 \text{ Btu/h}\cdot\text{ft}\cdot^{\circ}\text{F} = 5.678 \text{ W/m}^2\cdot\text{K}$;
 $1 \text{ Btu/lb}\cdot^{\circ}\text{F} = 4187 \text{ J/kg}\cdot\text{K}$.

TABLE B.4. Hydraulic Parameters Used in E7 COBRA Calculations

System pressure	2.07 MPa (300 psia)			
Friction factor	$0.316 \text{Re}^{(-0.25)}$			
Crossflow resistance	0.5			
Turbulent mixing factor (β)	0.0125			
Conduction geometry factor	2.0			
Film-coefficient correlation constant	$\text{Nu} = 5.87 + 0.021 \text{Pe}^{0.8}$			
Duct wall				
Thickness	0.89 m (.035 in.)			
Density	7.98 mg/m^3 (498 lb/ft ³)			
Heat transfer to bypass	$113 \text{ W/m}^2\cdot\text{K}$ (20 Btu/hr·ft ² ·°F)			
Bypass temperature	655 K (720°F)			
Wall-section length				
Sections 1, 3, 4, 6, 7, and 9	4.88 mm (.19 in.)			
Sections 2, 5, and 8	2.98 mm (.117 in.)			
Flow channel				
Length	0.68 m (27 in.)			
Number of nodes	14			
	Flow Area, mm ² (in ²)	Wetted Perimeter, mm (in.)	Heated Perimeter, mm (in.)	Hydraulic Diameter, mm (in.)
Channels 1, 2, and 3	7.37 (0.0114)	10.77 (0.42)	9.17 (0.36)	2.74 (0.11)
Channels 4, 6, 7, 9, 10, and 12	5.00 (0.0077)	8.42 (0.33)	3.02 (0.12)	2.37 (0.094)
Channels 5, 8, and 11	7.33 (0.0114)	10.25 (0.40)	6.19 (0.24)	2.86 (0.11)
Cluster flow area	148 mm ² (0.229 in. ²)			
Initial inlet temperature	655 K (720°F)			
Initial inlet flow	$3.824 \text{ g/m}^2\cdot\text{s}$ ($2.82 \times 10^6 \text{ lb h}\cdot\text{ft}^2$)			
Average heat flux	10.56 kW/m^2 ($3.35 \times 10^4 \text{ Btu h}\cdot\text{ft}^2$)			

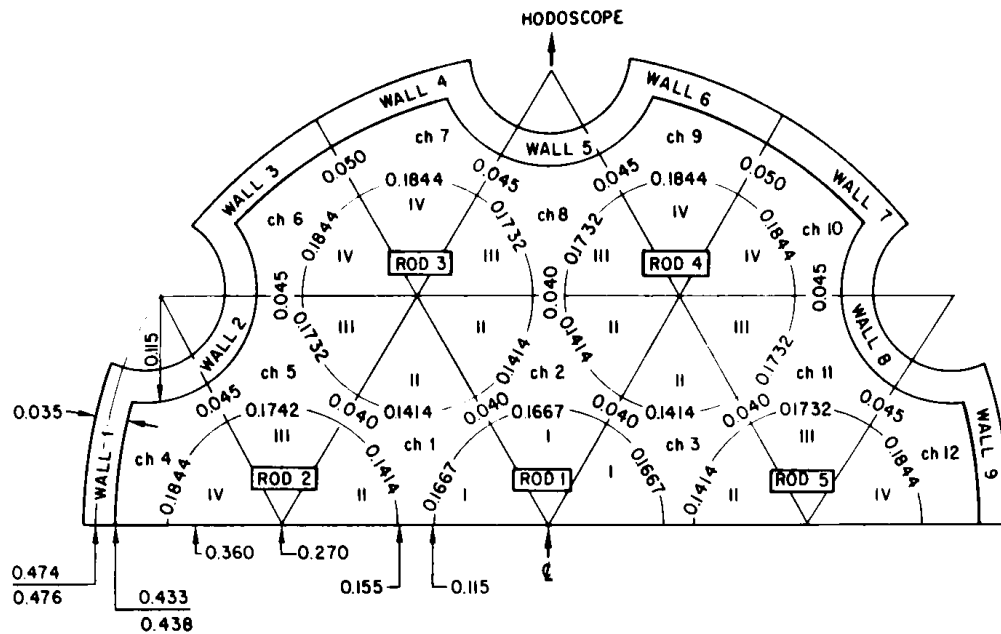


Fig. B.2. Geometric Details Used in COBRA Calculations. All units in inches. Conversion factor: 1 in. = 2.54 cm.

TABLE B.5. Forcing Functions Used in COBRA Calculations

Forcing Function for Power		Forcing Function for Inlet Enthalpy	
Time, s	Power, MW	Time, s	Relative Enthalpy
3.80	1.0	3.80	1.000
4.50	79.0	6.00	1.021
4.60	141.6	7.00	1.036
7.00	141.6	7.10	1.043
7.10	215.0	7.60	1.070
7.20	384.0	7.61	1.117
7.28	581.0	7.63	1.169
7.36	933.0	7.66	1.268
7.42	1293.0	7.67	1.425
7.48	1753.0	7.68	1.646
7.54	2283.0	7.69	1.812
7.56	2416.0	7.70	1.951
7.58	2468.0	7.72	2.194
7.60	2422.0	7.74	2.377
7.62	2306.0	7.76	2.486
7.70	1610.0	7.77	2.558
7.74	1217.0	7.78	2.655
7.78	894.0		
7.82	661.0		
7.86	489.0		
7.90	373.0		
8.00	238.0		
8.10	186.0		
8.50	124.0		
8.60	121.0		
8.80	8.6		

TABLE B.6. Fuel-pin Properties for COBRA Calculations

Diameter:	Fuel OD = cladding ID	0.508 cm (0.200 in.)
	Central void	0.117 cm (0.046 in.)
	Cladding OD	0.584 cm (0.230 in.)
Density:	Fuel	9.95 Mg/m ³ (621 lb/ft ³)
	Cladding	7.98 Mg/m ³ (498 lb/ft ³)
Radial nodes:	Number in fuel	8
	Fuel node type	Equal Δr
	Number in cladding	5
	Cladding node type	Equal Δr
Length		34.29 cm (13.5 in.)
Number of axial nodes in fuel		7
Solidus temperature		2760°C (5000°F)
Liquidus temperature		2816°C (5100°F)
Heat of fusion		274 J/g (118 Btu/lb)
Heat capacity of liquid		503 J/kg·K (0.1202 Btu/lb·°F)
Initial radial gap size:	Central pin	7.62 μ m (0.0003 in.)
	Edge pin	7.62 μ m (0.0003 in.)
Radial jump distance:	Central pin	7.62 μ m (0.0003 in.)
	Edge pin	7.62 μ m (0.0003 in.)
Initial gap conductance:	Central pin	2.55 kW/m ² ·K (450 Btu/h·ft ² ·°F)
	Edge pin	2.55 kW/m ² ·K (450 Btu/h·ft ² ·°F)
Maximum gap conductance:	Central pin	10.88 kW/m ² ·K (1916 Btu/h·ft ² ·°F)
	Edge pin	10.88 kW/m ² ·K (1916 Btu/h·ft ² ·°F)

Five fuel rods and 12 coolant channels were used in the calculations. Rods 4 and 5 gave nearly identical results. Roman numerals associated with the sectors of each rod in Fig. B.2 refer to the type of radial distribution used for that aximuthal zone (from Table IV). Centroid-to-centroid distances are 3.94 mm for the three central channels and 3.76 mm for the outer channels. Channel-to-channel contact lengths are shown in Fig. B.2. Numbers on the surface of each rod in Fig. B.2 are the fractions of total heat energy generated in the fuel rod that can be transferred to the adjacent coolant channel.

ACKNOWLEDGMENTS

We wish to express our appreciation to the many people who made important contributions to Test E7. In particular, we thank C. E. Dickerman, Manager of the In-Pile Experiments Program; R. A. Noland, Manager of In-Pile Engineering Operations, and his staff for fabrication of the test hardware; J. F. Boland and his staff at TREAT for performing the test irradiation; J. H. Cook and his staff at HFEF for pretest and posttest fuel loading and handling operations; L. A. Neimark and D. H. Stahl and their group at MSD for initial planning and support in the posttest examinations; and A. De Volpi and his staff for the special development work needed to analyze the hodoscope data.

REFERENCES

1. R. C. Doerner and A. De Volpi, *A Failure Experiment on High Power FFTF-Type Fuel in a Transient Overpower Accident (Test E7)*, Trans. Am. Nucl. Soc. 18(2), 212 (1974).
2. L. W. Deitrich, R. C. Doerner, A. E. Wright, and T. H. Hughes, *Summary and Evaluation--Fuel Dynamics Transient Overpower Experiments*, ANL-77-44 (June 1977).
3. R. E. Baars, J. H. Scott, G. E. Culley, *Failure Threshold Correlation for Fast Reactor Transient Overpower Accident Analysis*, Trans. Am. Nucl. Soc. 21, 303 (June 1975).
4. J. H. Scott and R. E. Baars, HEDL-SA-946, *IAEA International Working Group on Fast Reactor Specialists Meeting on Fuel Failure Mechanisms*, Richland, Wash. (Nov 19-22, 1974).
5. A. E. Wright et al., "Final Report for The H3 Transient Overpower Failure Threshold Experiment," ANL-75-32 (June 1975).
6. D. Stahl, ANL/MSD, private communication (Oct 1973).
7. *Reactor Development Program Progress Report: October 1971*, ANL-7872, p. 8.8 (Nov 23, 1971).
8. *Reactor Development Program Progress Report: February 1972*, ANL-RDP-2, p. 8.22 (Mar 29, 1972); Ibid.: *March 1972*, p. 8.26 (Apr 27, 1972); Ibid.: *June 1972*, p. 8.24 (July 31, 1972).
9. *Reactor Development Program Progress Report: September 1971*, ANL-7861, p. 8.6 (Oct 26, 1971).
10. *Reactor Development Program Progress Report: July 1972*, ANL-RDP-7, p. 9.14 (Aug 29, 1972); Ibid.: *August 1972*, ANL-RDP-8, p. 9.26 (Oct 10, 1972); Ibid.: *September 1972*, ANL-RDP-9, p. 9.27 (Oct 20, 1972).
11. *Reactor Development Program Progress Report: July 1971*, ANL-7845, p. 8.9 (Aug 20, 1971).
12. J. Ingram, HEDL, to R. C. Doerner, ANL, private communication (Aug 1973).

13. L. E. Robinson, R. T. Purviance, and K. J. Schmidt, *The Mark-II Integral Sodium TREAT Loop*, Trans. Am. Nucl. Soc. 13(1), 354 (1970).
14. G. A. Freund et al., *Design Summary Report on the Transient Reactor Test Facility (TREAT)*, ANL-6034 (June 1960).
15. A. De Volpi and C. H. Freese, *Fast Neutron Transient Detection Hodoscope for Reactor Fuel Meltdown Studies*, IEEE Trans. Nucl. Sci., NS-13 (1), 623 (Feb 1966).
16. A. De Volpi et al., *Preliminary Performance Data from Fast-Neutron Hodoscope at TREAT*, Trans. Am. Nucl. Soc. 12(2), 868 (1969).
17. *Reactor Development Program Progress Report: September 1971*, ANL-7861, p. 8.26 (Oct 26, 1971).
18. *Reactor Development Program Progress Report: November 1971*, ANL-7887, p. 8.10 (Dec 29, 1971).
19. R. C. Doerner et al., *Beyond-Failure Transient Test of a Prototypical FFTF Fuel Element*, Trans. Am. Nucl. Soc. 14, 279 (1971).
20. R. W. Ostensen et al., *Fuel Flow and Freezing in the Upper Subassembly Structure Following an LMFBR Disassembly*, Trans. Am. Nucl. Soc. 18, 214 (June 1974).
21. D. R. Ferguson to R. C. Doerner, private communication (Aug 15, 1975).
22. *Nuclear Systems Materials Handbook*, Vol. 1, Design Data, TID-26666.
23. E. E. Gruber, "A Generalized Parametric Model for Transient Gas Release and Swelling in Oxide Fuels," ANL-77-2 (Jan 1977).
24. Clinch River Breeder Reactor Project, *Preliminary Safety Analysis Report*, Vol. 5, Sections 4 and 5, Project Management Corporation (Jan 1976).
25. W. W. Marr, *COBRA-3M: A digital Computer Code for Analyzing Thermal-Hydraulic Behavior in Pin Bundles*, ANL-8131 (Mar 1975).

Distribution for ANL-77-25Internal:

J. A. Kyger	R. A. Noland	R. J. Page
A. Amorosi	D. R. Ferguson	D. R. Pedersen
R. Avery	T. T. Anderson	L. W. Person
L. Burris	W. R. Bohl	G. J. Pokorny
S. A. Davis	R. E. Boyar	F. G. Prohammer
B. R. T. Frost	R. O. Brittan	E. A. Rhodes
D. C. Rardin	J. P. Burelbach	L. E. Robinson
R. G. Staker	N. J. Carson	A. B. Rothman
R. J. Teunis	W. L. Chen	L. Semenza
C. E. Till	D. H. Cho	R. Simms
R. S. Zeno	D. J. Dever	B. W. Spencer
D. W. Cissel	A. De Volpi	G. S. Stanford (5)
C. E. Dickerman	R. C. Doerner (5)	M. E. Stephenson
H. K. Fauske	F. E. Dunn	R. R. Stewart
S. Fistedis	J. J. English	F. J. Tebo
B. D. LaMar	C. L. Fink	J. H. Tessier
J. F. Marchaterre	J. R. Folkrod	J. P. Tylka
R. Sevy	P. H. Froehle (5)	J. B. van Erp
A. J. Goldman	E. E. Gruber	H. Wider
E. L. Martinec	T. J. Heames	A. E. Wright
I. Bornstein	T. H. Hughes	P. I. Parks (2)
D. Rose	A. J. Klickman	W. F. Murphy
P. A. Lottes	R. N. Koopman	R. E. Henry
B. A. Korelc (2)	J. Kramer	M. A. Grolmes
D. H. Lennox	R. K. Lo	A. B. Krisciunas
L. W. Deitrich	W. W. Marr	ANL Contract File
M. J. McDaniel	C. C. Meek	ANL Libraries (3)
L. Baker		TIS Files (2)

External:

ERDA-TIC, for distribution per UC-79p (282)
 Manager, Chicago Operations Office
 Chief, Chicago Patent Group
 Director, ERDA-RDD (2)
 Director, Reactor Programs Div., ERDA-CH
 Director, CH-INEL
 President, Argonne Universities Association
 Reactor Analysis and Safety Division Review Committee:
 D. D. Glower, Ohio State U.
 W. Kerr, U. Michigan
 M. Levenson, Electric Power Research Inst.
 S. Levy, General Electric Co., San Jose
 R. B. Nicholson, Exxon Nuclear Co., Inc.
 D. Okrent, U. California, Los Angeles

ARGONNE NATIONAL LAB WEST



3 4444 00011115 3